A Study of Transverse Momentum and Jets Using Forward Hadrons and Photons in Deep Inelastic Muon Scattering at 490 GeV/c

A thesis presented

by

Douglas Grant Michael

to

The Department of Physics

in partial fulfillment of the requirements
for the degree of
Doctor of Philosophy
in the subject of
Physics

Harvard University
Cambridge, Massachusetts

April, 1990

Abstract

The transverse momentum and energy-flow properties of forward ($x_F > 0$) charged hadrons and photons in deep inelastic muon scattering at $490 GeV/c$ have been studied. Single particle transverse momentum and average transverse momentum as a function of x_{Feynman} are presented. Events are found to have a planar structure and transverse momentum spectra in and out of the event plane are presented. Data in the kinematic range $Q^2 > 3 GeV^2/c^2$ and $20 < W < 30 GeV/c^2$ are used to search for two jets of particles in the forward direction. Energy and particle flow within the hadronic event plane are presented with several different cuts made on the data. A jet reconstruction algorithm is applied and properties of the forward jets are studied. For all plots, comparison is made with predictions from the Lund Monte Carlo tuned in different fashions. It is found that it is necessary to include hard QCD processes (gluon bremsstrahlung and photon-gluon fusion) in order to achieve good agreement between the data and the Monte Carlo. In addition, it is shown that the data have more multi-jet events than predicted by the default version of the Lund (4.3) Monte Carlo. It is suggested that it is necessary to increase the overall 'jettiness' by either increasing the primordial gluon distribution of the nucleon or adjusting the production cross section in the Monte Carlo. The possibility of an increased gluon distribution is presented and compared to data.

Acknowledgements

In eight years as a graduate student in high energy physics, one clearly will have relied heavily on the efforts and assistance of many others. It is my pleasure to acknowledge some of those efforts and assistance.

First, working with Frank Pipkin and Dick Wilson has never been anything but enjoyable. I have learned a lot from both of them. I am particularly pleased to have been able to make use of the calorimeter in my analysis exactly as Frank envisioned 9 years ago in his studies on the subject. Although the 1000 miles between Cambridge and Batavia has prevented a close day-by-day interaction with them over the last five years, when they are around I always benefit from their knowledge and experience. I would have enjoyed having them around more than it was possible. I will certainly miss Dick's stories of his adventures around the globe.

For most of my first 6 years as a graduate student I had the benefit of working closely with Richard Nickerson. I certainly learned a lot *from* Richard during those years and we also learned a lot together at the same time. I am sure that neither of us will ever forget the smell of PVC cement.

Over the years, Hugh Montgomery has occassionally provided wisdom on physics ideas. His continual comment, ' Don't forget about photon-gluon fusion' has proven prophetic. Shuichi Kunori has provided me with many useful suggestions and comments on my analysis in addition to supplying important guidance to the overall offline analysis effort. Jorge Morfin has always been helpful but in particular has helped me to understand what we don't understand with respect to gluon distributions. Thanks to him and Wuki Tung for the 'Jowuki' parton distributions, of which I have made heavy use. I have always enjoyed working with Don Geesaman on the data acquisition system and in recent times he always has good comments to make with regard to my analysis.

Without the tireless efforts of many of my fellow graduate students, it would not have been possible to get the reconstruction code working. Michael Schmitt has spent countless hours of work on general software issues and on understanding the calorimeter and making code work for it. John Ryan's efforts towards general software organization and on tracking down bugs and inefficienies has been invaluable. Anwar Bhatti and Doug Jansen have both contributed major efforts to improving and understanding reconstruction. Alex Salvarani has performed mostly as a one-man-show on getting the track-fitting code to work. Steve Magill invested effort in getting the beam and small angle pattern recognition in order. Silhacen Aid has invested a lot of

time in getting the Monte Carlo organized. Although not graduate students, Harry Melanson and Steve Wolbers have both spent substantial amounts of time in improving and understanding reconstruction and in working on all of the issues associated with getting the data run through all stages of reconstruction. Of course , many others have made contributions as well.

I am indebted to Michael Schmitt and Erik Ramberg for providing me with figures from their studies on calorimeter functionality, some of which appear in chapter 3. Janet Conrad spent untold hours on a number of the general apparatus figures (and table) which appear in Chapter 3.

I would like to acknowledge the efforts of the shop and support personnel at Harvard. The electric and mechanical shop workers really help Harvard to be first-rate in participation in experiments. Much thanks go to Carol Davis for her many favors over the years – not the least of which is that she is helping to take care of the binding of this thesis. At Fermilab, Ruth Pordes, Carmenita Moore and Don Petravick from the Computing Department (Division now) have always been very helpful when working on data acquisition problems. All of the people at PREP have always been very helpful to me as well.

I would like to thank my parents for all of their support over the now (very) many years that I have been a student. They always provided a good environment in which to grow intellectually. I learned a lot from my dad about how to 'get a problem solved somehow' which is invaluable in working on apparatus for high energy physics. My mom has provided lots of 'soul support' over the years. And don't worry Mom, physicists just *love* to argue.

Finally, thanks to Matt for putting up with me over these years.

Contents

Chapter 1

Introduction

The process of scattering leptons from nucleons has been used for about 40 years as a tool to aid in the understanding of the structure of the nucleus and nucleons and of the forces which bind the components together. Throughout, the strength of the technique has been good understanding of the event kinematics due to the ease of measuring the scattered lepton and the high level of understanding of the photon exchange process which is involved. (Of course, deep-inelastic scattering is also done with neutrinos which provides interesting handles not available in the charged lepton scatter but has poorer statistics and understanding of the event kinematics.) Starting in the 1960's, electron scattering experiments demonstrated that the nucleon appeared to have a substructure (see chapter 2 and references therein) and the technique of so-called deep-inelastic lepton scattering is still the best means of determining nucleon structure.

The advent of high energy muon beams (first at Fermilab and then at CERN

in the 1970's) brought about a new round of studies not only of nucleon structure functions but of the resulting hadronic final state as well. During the same period of time, e^+e^- colliders began to demonstrate their considerable strengths in the study of hadronic final states. Of particular importance and relevance to this thesis has been the observation and study of multi-jet events and the understanding of the underlying hard processes which those studies have allowed. Although a clean separation of multi-jet (3 or more jets) events was not possible, the European Muon Collaboration subsequently demonstrated a planar event structure and 'two-lobed' events in the forward direction which was consistent with QCD predictions. However, the center-of-mass (CM) energy was lower than that of the e^+e^- experiments which observed clear multi-jet events.

Experiment 665 at Fermilab makes use of the world's highest energy muon beam (nominally $490GeV$) and a spectrometer which is designed to observe as much of the hadronic final state as possible. The combination of the higher energy, the spectrometer and the ever-present advantage of the knowledge of the virtual photon direction from the muon scatter, allow E665 (for the first time in deep-inelastic scattering) to delve into the realm of multi-jet physics. As will be discussed in chapter 2, the goal will not be simply to redo the same measurements as have already been done in e^+e^- experiments. Rather, we wish to use the unique advantages that deep-inelastic scattering provides in order to further our understanding of QCD

and gluons.

Throughout its history, deep-inelastic scattering has primarily been the study of boson exchange with some charged constituent within the nucleon. At the same time, we know that a large fraction of the momentum of the nucleon must be carried by uncharged gluons. Hard scattering in $p\bar{p}$ collisions at the Tevatron begin to be dominated by gluon-gluon scattering and collisions at the SSC will be totally dominated by this process. As will be demonstrated, the CM energy of 20 to 30 GeV and low Bjorken-x region of the data implies that E665 may be entering the regime where a large fraction of events will be the result of the photon scattering with a gluon via an inter-connecting quark - the photon-gluon fusion process. The high energy allows the resulting $q\bar{q}$ pair to produce noticeably multi-jet events and thus will provide an important new handle on both the fundamental QCD process and the gluon distribution of the nucleon.

Chapter 2 will present a discussion of the general process of hadron production in deep-inelastic scattering. Chapter 3 provides a rather thorough description of the E665 apparatus (not completely inappropriate for somebody who spent six years building it and making it work). Chapter 4 describes the event reconstruction programs, event selection, track selection and Monte Carlo acceptance corrections. In chapter 4, the results of this analysis are presented and compared with Monte Carlo predictions. Discussion of the results is folded in with the presentation for clarity.

Chapter 5 summarizes the conclusions. A list of authors and their institutions which are involved in E665 is given in Appendix A.

Special Note: Throughout this thesis (but not necessarily everywhere) I set the speed of light $c = 1$ in units for mass and momentum which are given in GeV/c^2 or GeV/c respectively.

Chapter 2

Hadron Production in DIS

2.1 Kinematics for DIS

To first order, deep-inelastic scattering of muons on nucleons is dominated by the exchange of a single virtual photon. Figure 2.1 shows the first order Feynman diagram for this process. The kinematics for this interaction are independent (at this order) of the resulting hadronic final state. Here the incoming muon carries 4-momentum $k = (E, \vec{k})$, radiates a virtual photon with momentum $q = (\nu, \vec{q})$ and as a result has a final momentum $k' = k - q = (E', \vec{k'})$. The virtual photon is absorbed by the nucleon which carries initial momentum p (approximately $(M, \vec{0})$ in the lab frame neglecting possible nuclear smearing effects) which subsequently rebounds into an unspecified final state. Two Lorentz scalars can be used to fully characterize the interaction:

$$Q^2 = -q^2 = (k - k')^2 \approx 4EE' \sin^2(\frac{\theta}{2}) \quad \text{(neglects muon mass)} \qquad (2.1)$$

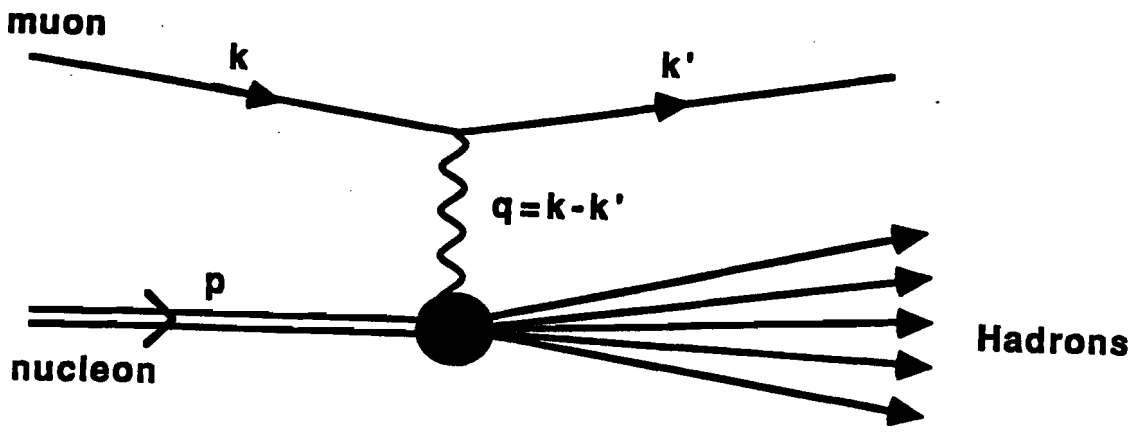

Figure 2.1: Lowest order Feynman diagram for Deep-Inelastic Scattering.

and

$$\nu = \frac{p \cdot q}{M} = E - E' \tag{2.2}$$

where M is the nucleon mass and θ is the angle at which the muon scatters from its original direction in the laboratory. The invariant mass of the hadronic final state is then given by:

$$W'^2 = M^2 - 2M\nu - Q^2. \tag{2.3}$$

This is the variable which corresponds to the square of the center-of-mass energy, ($\hat{s}$), in electron-positron annihilation. The vertex involving the muon can be calculated exactly from first order Quantum Electrodynamics (QED). However, it should not be forgotten that radiative corrections as shown in figure 2.2 will be non-negligible, especially at low Q^2. The vertex between the nucleon and the pho-

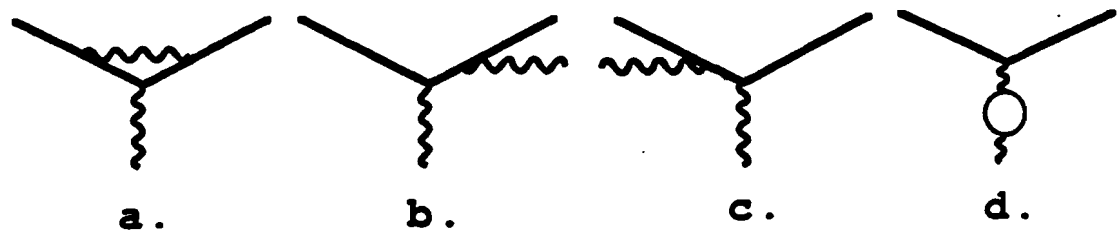

Figure 2.2: Lowest order radiative correction terms to muon-photon vertex.

ton is considerably more complex and difficult (or impossible) to calculate. Instead, an expression for the cross section can be written which allows two independent and arbitrary structure functions for the nucleon $W_1(Q^2,\nu)$ and $W_2(Q^2,\nu)$ which will fully account for possible differences in absorption of transverse and longitudinally polarized virtual photons. Then the cross section is given by (see for example [1.2]:

$$\frac{d^2\sigma}{dQ^2 d\nu} = \frac{4\pi\alpha^2}{Q^4}\frac{E'}{EM}\left[W_2(Q^2,\nu)\cos^2\frac{\theta}{2} + 2W_1(Q^2,\nu)\sin^2\frac{\theta}{2}\right], \qquad (2.4)$$

where α is the electromagnetic fine structure constant. Of course, these structure functions only relate to charged properties of the proton structure but beyond that make no explicit assumptions as to the nature of such functions.

2.2 The Quark-Parton Model

Experiments done at SLAC in the late 1960s [3,4] first demonstrated the effect known as *scaling* which was predicted by Bjorken [5]. Bjorken demonstrated that in the kinematic limit that $Q^2 \to \infty$ and $\nu \to \infty$, then the two structure functions $W_1(Q^2, \nu)$ and $W_2(Q^2, \nu)$ can be reformulated such that:

$$MW_1(Q^2, \nu) \to F_1(\frac{Q^2}{M\nu}) \tag{2.5}$$

$$\nu W_2(Q^2, \nu) \to F_2(\frac{Q^2}{M\nu}) \tag{2.6}$$

as long as F_1 and F_2 remain finite and that F_2 remains non-vanishing as $Q^2 \to \infty$. The Bjorken scaling variable $x_{Bj} \equiv Q^2/2M\nu$ is dimensionless and hence the functions F_1 and F_2 will have no physical scale (referred to as scale invariance). In fact, scaling appears to hold reasonably well even in regions where Q^2 is not *very* large.

The physical interpretation of scale invariance as being the result of point-like scattering of partons was given by Feynman [6]. The parton model provides a particularly simple interpretation of the significance of x_{Bj}. Consider a nucleon moving at large momentum p containing a parton carrying a fraction ξp of the nucleon momentum. In this picture, the DIS process will have the photon scatter elastically from a parton as shown in figure 2.3. The 'elastic' scatter results in the

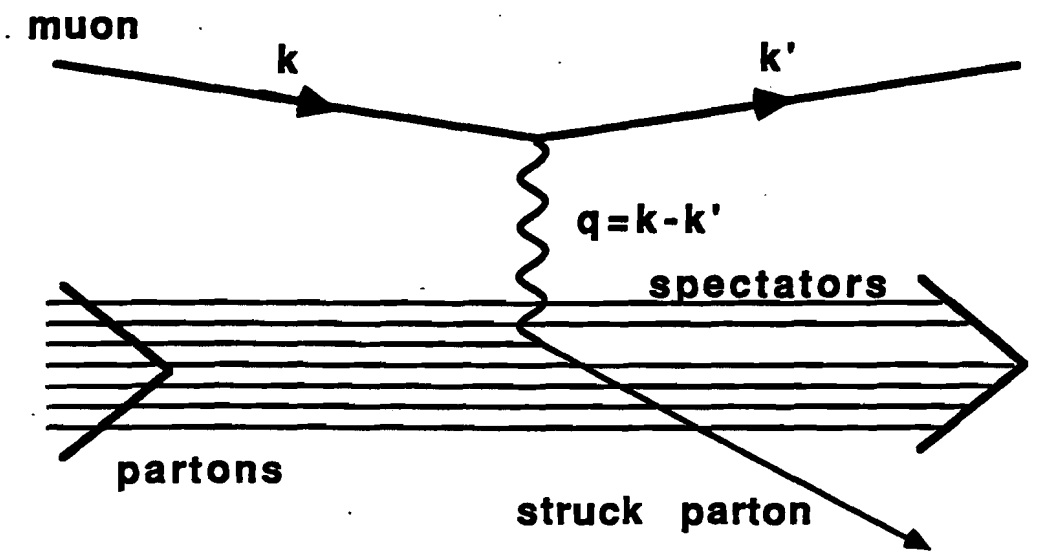

Figure 2.3: Lowest order diagram for DIS in the quark-parton model.

constraint:

$$(\xi p + q)^2 = m^2, \tag{2.7}$$

where m is the mass of the parton. When expanded and rearranged this yields:

$$\xi = \frac{Q^2 + m^2}{M(\nu + \sqrt{\nu^2 + Q^2 + m^2}}. \tag{2.8}$$

Now, if $\nu^2 \gg Q^2 \gg m^2$ then this becomes:

$$\xi = \frac{Q^2}{2M\nu} \equiv x_{Bj}. \tag{2.9}$$

Hence, we see that in this case, x_{Bj} simply becomes the fraction of the total momentum which the parton is carrying. Clearly, care should be taken in applying this interpretation if Q^2 is sufficiently small.

We can now re-write the DIS cross section as:

$$\frac{d^2\sigma}{dQ^2dx} = \frac{4\pi\alpha^2}{Q^4}\left[(1-y)\frac{F_2(x,Q^2)}{x} + y^2F_1(x,Q^2)\right] \tag{2.10}$$

where $y \equiv \nu/E$. Note that the two structure functions have been written such that they retain a dependence on Q^2. Although this is nominally unnecessary for the parton model at sufficiently large momentum transfer, it remains necessary when discussing so called *scaling violations* which result from QCD (or possibly other theories of parton confinement).

It is possible to express the two structure functions directly in terms of the cross section for scattering of transverse and longitudinal polarization virtual photons. This gives:

$$\frac{d^2\sigma}{dQ^2d\nu} = \frac{\alpha}{4\pi}\frac{W^2-M^2}{2mQ^2E^2}\frac{2}{1-\epsilon}(\sigma_T + \epsilon\sigma_L), \tag{2.11}$$

where

$$\epsilon = \left[1 + 2\left(1+\frac{\nu^2}{Q^2}\right)\tan^2\frac{\theta}{2}\right]^{-1}, \tag{2.12}$$

is the polarisation parameter. If all charged partons are spin $\frac{1}{2}$ particles then the longitudinal cross section should vanish at sufficiently high Q^2. In that case, we see that:

$$2xF_1 = F_2 \tag{2.13}$$

which is known as the Callan-Gross relation [7]. Hence, the nucleon portion of the cross section reduces to a dependence on a single structure function. Measurements

(see [1] for a compilation of the data) have shown that the ratio $R \equiv \sigma_l/\sigma_t$ is indeed small but recent analysis has shown that it is probably unwise to completely ignore the effects of a non-zero ratio [8,9]. Still, for many purposes the supposition of a single structure function is valid. In this case, it is possible to express this structure function in terms of the sum of charge-weighted probability distributions for different partons:

$$F_2(x, Q^2) = \sum_i e_i^2 x f_i(x, Q^2) \tag{2.14}$$

where f_i is the probability function for quarks of type i each with a charge e_i in units of the proton charge and the sum is over all types of quarks. Scattering at larger x_{Bj} implies that the struck quark was carrying a large fraction of the total proton momentum and can usually be attributed to scattering from one of the *valence* quarks for the nucleon which are simply the quarks of Gell-Mann [10]. Hence, it should be noted that when charge weights are considered, at higher x_{Bj}, up quarks will dominate the scattering process in both protons and neutrons although less-so in the latter. It is possible to extract information on the relative quantities of up and down valence quarks within nucleons by comparing structure functions measured from hydrogen and deuterium.

At sufficiently small x_{Bj} and large ν it becomes important to account for a non-zero ratio $R \equiv \sigma_L/\sigma_T$. The reason for this is the probability for scattering off

of a gluon which splits into a quark-antiquark pair with non-neglibible transverse momentum becomes relatively large. In other words, scattering will be occurring with relatively large probability off of the gluons and not just quarks. The probability for this process is calculable from QCD. If one assumes R as calculated from QCD it will still be possible to treat the cross section as having a single structure function F_2. More will be said on the relevance of R and the distribution of gluons in section 2.3.2.

2.3 Fragmentation of Quarks into Hadrons

Although partons may be involved in the initial scattering process, liberated, fractionally charged partons have never been observed in any experiment. The observed products of high-energy collisions are always particles of integral electronic charge which (usually) are well known and understood particles. Clearly, some mechanism is at work to make it at least very difficult for quarks to be liberated regardless of the overwhelming evidence for their existence. The process by which partons are turned into hadrons (which may subsequently decay into other particles) is known as *fragmentation* or *hadronization.*

The parton model has nothing at all to say about the forces which cause quarks to be bound together within a nucleon let alone the fragmentation process. The assumption is that the quark which absorbs the virtual photon will fly off in that

direction while the remaining partons will simply act as spectators in the process. If the assumption is made that the struck quark will fragment independently of the rest of the system and that the fragmentation is not related to the production of the quark, then one can hypothesize purely phenomenological functions which will describe the spectrum of produced hadrons. These functions are defined to be of the form $D_q^h(z)$ which is the probability that a hadron of type h will be produced with momentum fraction z of a fragmenting quark q. A most simple model could simply involve the decay of the energy of the system W, into the available phase space of momentum and hadrons. Of course, this still says nothing about the forces which bind the quarks or cause such a decay to occur. On the other hand, such a 'phase space' decay may describe many of the most obvious properties of fragmentation and will certainly be included within any more complex theory. Hence, such analyses can be useful as a vehicle for discerning differences between proposed theories for fragmentation other than simply those arising from simple kinematics. Still, to make any real progress, it is crucial to at least attempt to explain the process in terms of the forces which bind the quarks. The presently reigning champions in this field are those models which are based on Quantum Chromodynamics.

2.3.1 Quantum Chromodynamics

Quantum Chromodynamics (hereafter always to be referred to as QCD) is a local non-abelian gauge theory of the strong interactions through which quarks interact ([11,12,13], reviews given in [14,15,16]). The theory is based on the SU(3) gauge group where the gauge bosons are referred to as *gluons*. Each flavor of quark is assumed to carry a 'color' charge which comes in three varieties so that each flavor of quark will form a triplet in the fundamental representation of SU(3). The gluons also carry color charge so that they transform as an octet in the adjoint representation. The gluons are very analogous to the photon in the electroweak sector but the fact that they carry color charge makes QCD a very different sort of theory. In addition to the two lowest order tree-level Feynman diagrams, which are analogous to QED (figure 2.4a,b), there is an additional diagram (figure 2.4)c which is the self interaction of gluons. When QCD is renormalized, the gluon self interactions are responsible for causing the strength of the coupling to go to zero as the energy scale of the interaction goes to infinity (as long as the number of flavors of quarks is less than 17). The renormalization process will introduce a cutoff scale in the theory which results in a renormalization-group-equation-improved perturbation theory (to leading order) with the perturbative coupling constant given by:

$$\alpha_s(Q^2) \equiv \frac{g^2(Q^2)}{4\pi} = \frac{12\pi}{(33-2f)\ln(Q^2/\Lambda^2)} \tag{2.15}$$

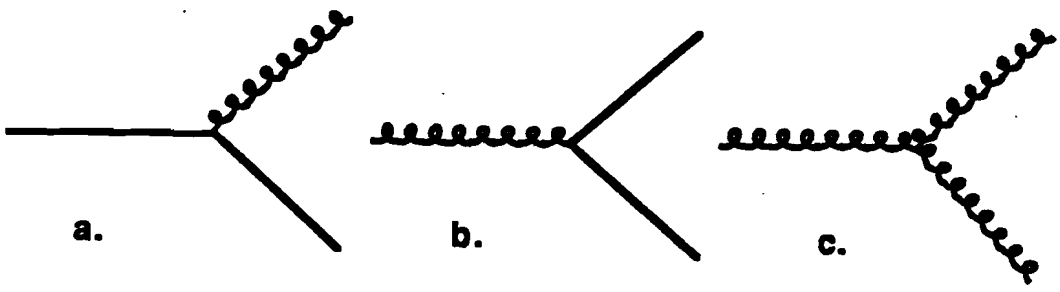

Figure 2.4: Lowest order tree level Feynman diagrams for QCD. a) Gluon emission by a quark, b) gluon splitting into two quarks, c) gluon self interaction.

where g is the actual coupling constant, f is the number of quark flavors and Λ is the 'cutoff' scale for the interaction (see for instance [14] for a nice review treatment). Clearly, perturbative calculations will only be meaningful for $Q^2 \gg \Lambda^2$ for which α_s will be small. The parameter Λ is dependent on the particular prescription used in the renormalization but is truly a free parameter which must be determined by experiment. The particular form of equation 2.15 which appears here comes from what is known as the 'modified minimal-subtraction' prescription for renormalization and the associated Λ is referred to as $\Lambda_{\overline{MS}}$. In fact, what experiments actually end up measuring is the strength of the coupling α_s at a particular energy scale and using equation 2.15 calculate Λ. The *attempt* is made to simultaneously test the legitimacy of the calculation as well as compare the resulting value of Λ

with that from other experiments in hopes of getting it 'right'. Unfortunately, two rather tricky difficulties arise in this process. First, although it is clear what one is measuring in experiments, the interpretation is not necessarily really the same for experiments at very different energy scales or dealing with considerably different initial conditions (e^+e^- versus $p\bar{p}$ for instance). In this case, higher order terms can become important and these terms will necessarily change the apparent value of Λ. There are considerable technical difficulties in calculating the additional terms so that Λ's calculated from different environments can be properly compared. The second problem is that there can be ambiguities in what the correct energy scale really is for a given measurement of α. If you can't get the scale right, its going to be very hard to compare anything! The best demonstration of the running of α using a single *type* of experiment (reducing theoretical uncertainty) comes from multi-jet production in e^+e^- annihilation (see for instance [17,18]). Figure 2.5 shows results from JADE, TASSO and AMY for the three-jet fraction as a function of CM energy. A new measurement from the MARK II using data from the SLC and PEP confirms and extends these results [19]. Although the experimental data clearly support a running coupling constant, it is difficult to consider the question completely closed at this time. It would be interesting to confirm the effect at a different scale (such as the lower Q^2 regime of deep inelastic scattering).

Typical measured (with calculation!) values of Λ are around $150-300MeV$ This

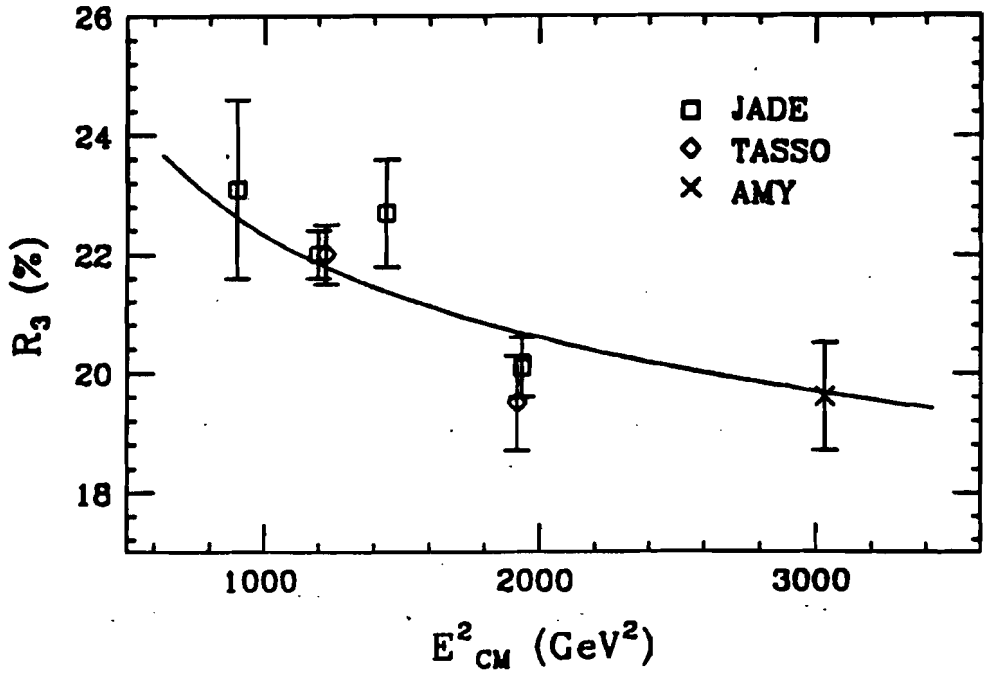

Figure 2.5: Data from JADE, TASSO and AMY for fraction of three-jet events produced in e^+e^- annihilation. Plot is from reference [17]. The Solid line is based on a second-order calculation by Kramer and Lampe [20] and is part of the original plot from [17].

means that for momentum transfers of greater than a few GeV that perturbation theory should be legitimate. In addition, at these momentum transfers, quarks within a nucleon should more-or-less appear to be unbound from the viewpoint of a scattered lepton since the smallness of α_s implies that the quark will tend to interact unilaterally rather than coherently with one or more neighbors. In other words, it will appear as if the quarks are not strongly bound within the nucleon (even though they actually are!). This allows both QCD and the parton model to peacefully co-exist. Indeed, QCD simply acts as an improvement upon the simple quark-parton model.

QCD is still very poorly understood in the regime in which fragmentation occurs. Here, the momentum transfer scales are relatively small and many sets of quark-antiquark pairs are being formed to produce the final state hadrons. It is certainly not yet possible to calculate such terms analytically. Indeed, it will likely require a significantly different approach from pertubartion theory in order to do so. Hence, it is necessary to use some type of model which describes the fragmentation process. QCD may be included as a feature in such models and the perturbative method applied as far as one theoretically reasonably dares and sometimes well beyond that point as long as the data seems to justify such actions. Typically, such models will provide exact calculation of first-order QCD matrix elements (and sometimes next-to-leading order) for generation of partonic initial states combined with some

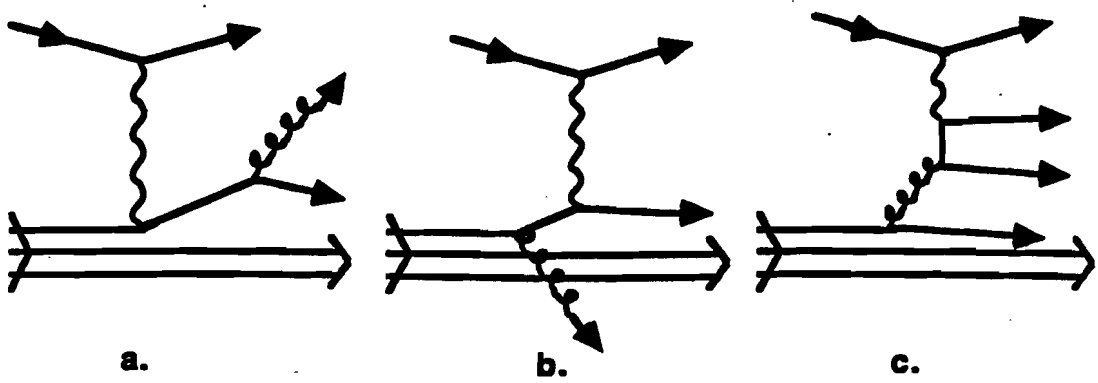

Figure 2.6: Lowest order QCD corrections to the Quark-Parton picture of DIS. a),b) gluon bremsstrahlung, c) photon-gluon fusion.

prescription for turning those partonic states into hadrons.

Hence, to this level, the effects of QCD may be viewed as the quark-parton model with corrections to the structure functions and also with the addition of a few additional graphs in the final state which will change the overall fragmentation. Figure 2.6 shows the additional Feynman diagrams which must be added to the quark-parton picture of DIS to leading order from QCD. The probability for the splitting at each of the purely quark-gluon vertices is that given by Altarelli and Parisi [21]. These diagrams will tend to increase the overall transverse momentum of the final state hadrons with respect to the virtual photon direction. Altarelli and Martinelli [22] have calculated the corrections due to the diagrams in figure 2.6 and find that the average $p_\perp^2$ should be asymptotically proportional to W^2 with a

coefficient which will depend little on either x or y. Measurements from EMC show this to roughly be the case [23,24].

2.3.2 QCD and Jets

The additional $p_\perp$ which results from the leading order hard QCD processes will tend to lie in a single plane due to the fact that two partons will carry equal and opposite additional $p_\perp$. Hence, the first sign of hard QCD processes will be the emergence of events with a distinct planar structure. As the CM energy increases, individual partons will carry more momentum as will the corresponding hadrons. At the same time, the transverse momentum which is produced relative to the direction of the fragmenting parton should remain roughly the same (the fragmentation is still occurring at the same momentum scales as previously). The result will be a cone of particles about the initial parton direction. Once the longitudinal momentum of the hadrons along the parton's direction becomes sufficiently large compared to the transverse momentum which they gain during fragmentation, it will be possible to observe a *jet* of hadrons from that parton. Indeed, this is really the definition of a jet – a group of hadrons all travelling in the same direction within a cone with an opening angle such that the hadrons are *believably* associated with the fragmentation of a particular primordial parton.

A good estimate of what kinds of energies are required for the above definition

to hold can be made using existing experimental data with only minor aid of a fragmentation model (and practically any will do). EMC has measured the average charged multiplicity $\langle N_c \rangle$ as a function of W^2 and reports that the data (for forward hadrons) is well fitted using the parameterization:

$$\langle N_c \rangle = a + b \ln W^2, \tag{2.16}$$

where $a = -0.14$ and $b = 0.73$ [25]. The typical total multiplicity (including neutrals) will be roughly given by $N \simeq 1.3 N_c$. In addition, EMC has measured the part of the typical transverse momentum which is due simply to the fragmentation process (and not to perturbative QCD or primordial $k_\perp$) to be $\sigma_\perp \simeq 0.4 GeV$ [26,23]. Although this measurement is made using the Lund Monte-Carlo to unfold the effects of perturbative QCD, it could just as easily (well almost) be made looking only at particularly non-planar events or at the transverse momentum *out* of the hadronic event plane. Thus the measured value of $\sigma_\perp$ is not terribly dependent on the fragmentation scheme used to measure it. Given these two quantities, it is possible to readily calculate our expectation for identifying events with multiple jets due to extra partons resulting from hard QCD.

Consider a parton i with momentum p_i fragmenting into hadrons as shown in figure 2.7. Given the ansatz that the transverse momentum of the hadrons is limited ($\sigma_\perp$) and that we can define a 'typical' hadron momentum along the parton

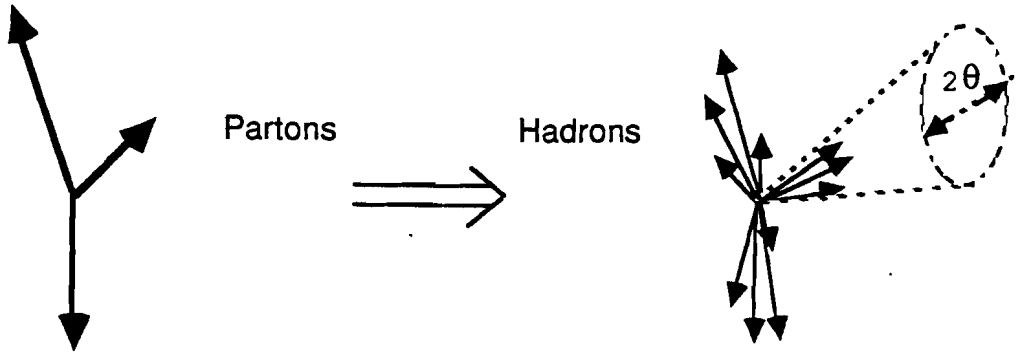

Figure 2.7: Parton fragmenting into 'cone' of hadrons with typical opening angle θ.

direction as $p_h = p/n$ where n is the typical number of hadrons which the parton fragments into, then the opening angle of the 'typical' hadrons about the parton direction will be:

$$\theta \approx \frac{\sigma_\perp}{p_h} = \frac{\sigma_\perp n}{p} \tag{2.17}$$

Now, *typically* we can write the parton momentum as $p_i = f_i W/2$ and also $n \approx f_i N$ where f_i is the same fraction in both cases ($W/2$ using just the forward hadrons). Hence, we can rewrite equation 2.17 using equation 2.16 as:

$$\theta \approx \frac{2.6\sigma_\perp(a + b\ln W^2)}{W}. \tag{2.18}$$

Using the numerical values from EMC we can plot the typical opening angle for a jet as a function of W as shown in figure 2.8. Remember that this is just a rough estimate and in particular does not pay attention to background fluctuations of

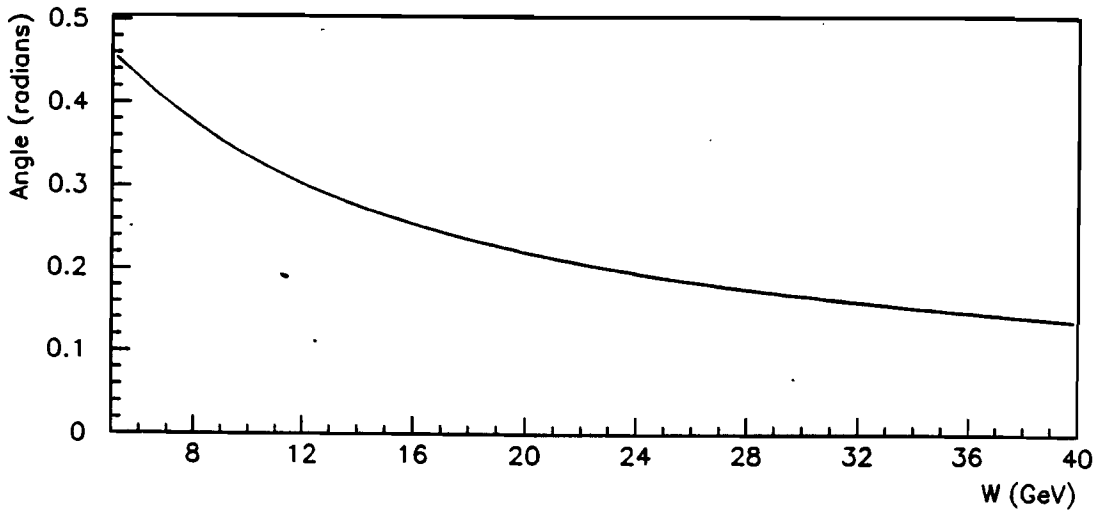

Figure 2.8: Typical opening angle for jet cone as a function of W.

'nonperturbative' fragmentation which will mimic the effect. Certainly, the *very* minimum requirement to be able to tell that there are two forward-going jets is $\theta < 45°$. However, when combined with the potential for background fluctuations and experimental resolution, half of that angle is more realistic. This implies that some separable jets will emerge in the region of $10 < W < 20GeV$ but when combined with the cross section for production, only a handful of events remained in the data of EMC. Functionally, we expect that the 'observable emergence' of jets will occur somewhere in the area of $W = 20GeV$.

Once jets are observed, the challenge is to attempt to relate the measured jet of hadrons to the partons from which they came. QCD makes rather explicit predictions on what the angular distribution and momenta of primordial partons should be and it is interesting to test the theory with observation of jets. A very

large amount of work along this line has been done in e^+e^- collider experiments. Indeed, it seems to me that that these experiments can truly be accredited with the discovery of the gluon [27,28,29,30] – at least as much as we tend to 'discover' things like bottom quarks and heavy vector bosons. The observation of clear 3-jet events which follow the angular distribution and momentum predicted from QCD with fragmentation models must be taken as one of the most significant tests of QCD. In the last decade, the theory has been doubly tested on jet production in both e^+e^- collisions (see for instance [31,32,33,34]) and from hadron colliders with impressive results. (See for instance [35,36,37,38,39,40,41].) In addition, the European Muon Collaboration has been able to demonstrate planar events and the onset of multi-jet structure in deep-inelastic scattering [42,43,24,26]. Their beam energy, however, severely limited their ability to achieve a significant sample of events which was appreciably enriched with multi-jet events. Work at e^+e- machines is continuing at KEK, SLC and LEP while UA1, UA2 and CDF all continue investigating jets from hadron collisions.

Deep-inelastic scattering affords a couple of unique windows of opportunity in the study of jets and the underlying partons and QCD processes. Primary amongst these is the photon-gluon fusion process (figure 2.6c) which simply does not exist in e^+e^- or $\bar{p}p$ colliders. The differential cross section for production of partons by this process is fully calculable to leading order in QCD and will differ from that of

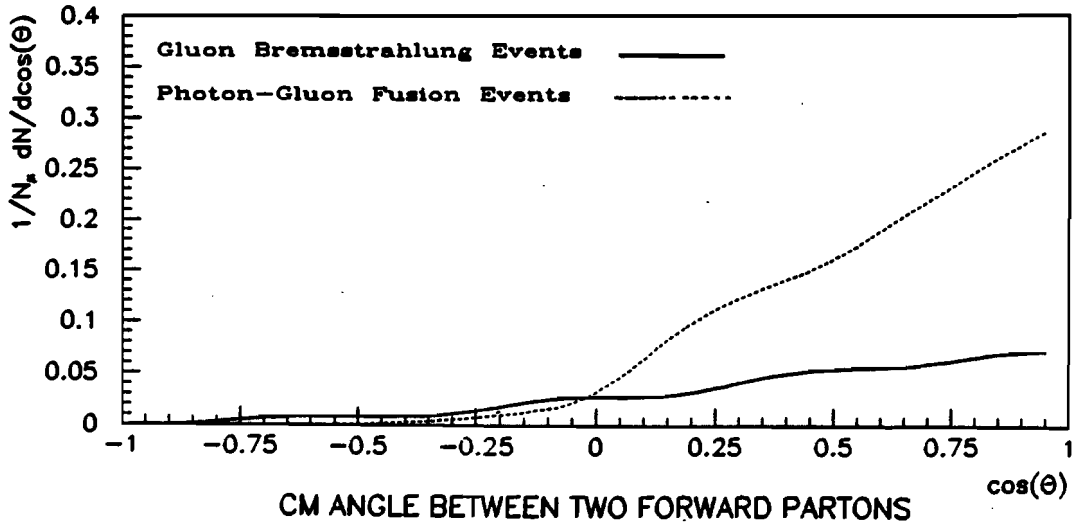

Figure 2.9: Differential cross section (normalized to number of scattered muons) for production of two forward partons as a function of the angle between the two partons in DIS for $20 < W < 30GeV$, $Q^2 > 3GeV^2$, $x_{Bj} > .05$ and parton-pair invariant mass greater than $1.0GeV$. Calculated using Lund Monte Carlo.

the gluon bremsstrahlung process. (See reference [22] for instance for the unintegrated cross section equations for each process.) Figure 2.9 shows the cross section (calculated using the Lund MC) as a function of the cosine of the angle between two forward partons for each process given parton-pair invariant mass greater than $1.0GeV$ and $W > 20GeV$, $Q^2 > 3GeV^2$ and $x_{Bj} > .05$ Figure 2.10 shows the ratio of the magnitude of the parton momenta for the two processes given the same kinematic restrictions. Notice that the photon-gluon fusion process tends to produce events which are more asymmetric than the gluon bremsstrahlung process. This follows from examination of the Feynman diagram for the two processes and the

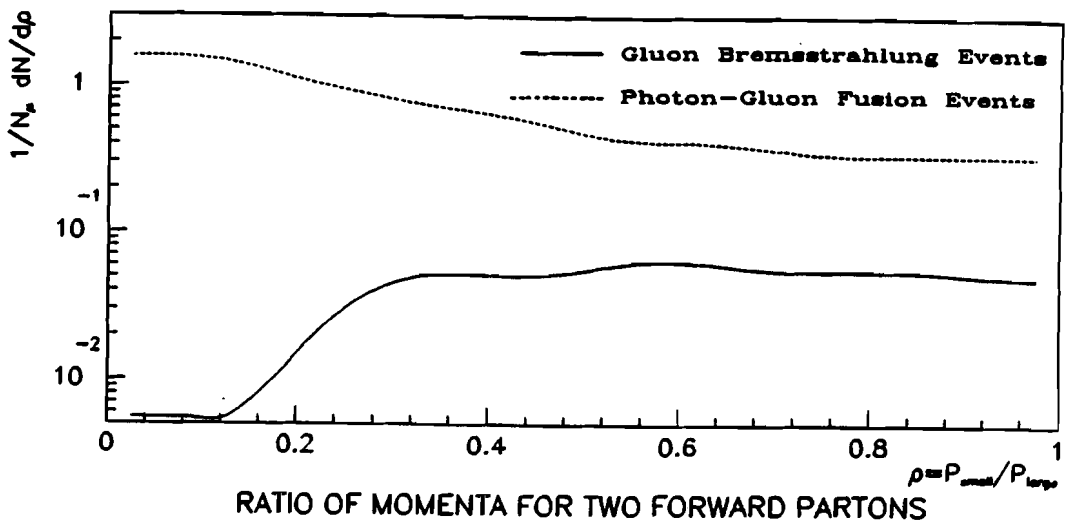

Figure 2.10: Distribution of the ratio of lower to higher momentum parton for two forward partons in DIS for same kinematic range as previous figure. Calculated using Lund Monte Carlo.

imposition of an invariant mass cut. In photon-gluon fusion, one of the final state quarks has a vertex with the very high momentum virtual photon while the other final (anti)quark has an internal propagator between itself and the photon. This will suppress the momentum of this quark relative to its partner. In addition, for gluon bremsstrahlung, the invariant mass cut directly cuts out collinear gluons but this is not the case for the photon-gluon fusion events where the invariant mass is calculated with respect to target remnants. The invariant mass cut simply imposes an effective cutoff in the definition of multi-jet. Effectively it will be difficult (or impossible) to distinguish two forward partons from one if the invariant mass is below that value. Note that although the mass cut does impose a cutoff in the

gluon distribution, that it does not change the overall shapes. The two curves will remain different regardless of the cut. Of course, we wish to actually study the process and verify that the QCD calculation is correct!

Many different experiments rely on the gluon distribution of the nucleon for interpretation. The photon-gluon fusion process has a direct dependence on the distribution of gluons within the nucleon and therefore if understood sufficiently well can help provide information on this important but poorly measured quantity. At some level, there is no real difference between the photon-gluon fusion process and simply scattering off of a sea quark. Indeed, the sea quark scatter can be thought of as the infrared limit of the photon-gluon fusion process. However, in the regime where both of the final state quarks carry sufficient momentum that they are distinguishable in experimental apparatus via separable jets or high transverse momentum final states, it should be possible to measure the gluon distribution. Two different fits to previously available data for gluon distributions, $xG(X)$ are shown in figure 2.11. Superimposed on the same figure with arbitrary scale is the x distribution for E665 data for $Q^2 > 3GeV^2$ and $W > 20GeV$. The gluon distributions are both parameterizations based on data at higher Q^2 – the higher distribution being that of Morfin and Tung [44] and the lower one that of Gluck, Hoffman and Reya [45] (the default for version 1.43 Lund Monte-Carlo) both calculated at fixed $W = 23GeV$. The fit of Morfin and Tung is much more recent and based on a large

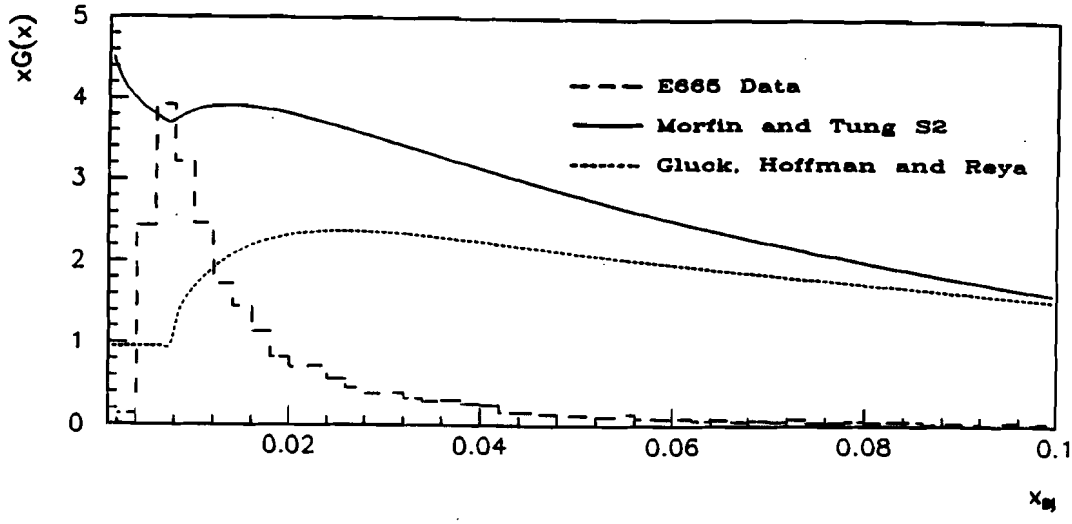

Figure 2.11: Gluon distributions, $xG(x)$ for $W = 23GeV$ for parameterizations of Morfin and Tung and for that of Gluck, Hoffman and Reya. The distribution for E665 data for $Q^2 > 3GeV^2$ and $W > 20GeV$ (average $W \simeq 23GeV$ is superimposed on the plot with arbitrary normalization.

amount of data which was unavailable to Gluck Hoffman and Reya. There are also some differences in the renormalization schemes which will cause a redefinition of some gluons in the nucleon from 'primordial' to 'perturbative'. The discontinuity in each of the distributions is caused when Q^2 (as determined by x and W) drops below $4GeV^2$. Each of the parameterizations has used a minimum $Q^2 = 4GeV^2$ for use in QCD evolution in fitting the data. The implementation of the parameterizations forces $Q^2 > 4GeV^2$ always so that the Q^2 evolution cuts off while some x dependence remains. The point of this plot is not to get picky about Q^2 limits though. Clearly, there is a striking difference between the two distributions in ex-

actly the same region in which E665 has a great deal of data in which it is expected that we can select events with multiple forward partons. According to a calculation using the Lund Monte-Carlo with the gluon distribution of Morfin and Tung, 51% of the E665 events shown in figure 2.11 will result from photon gluon fusion in which the minimum invariant mass of parton pairs is $1GeV$. The equivalent number for the same calculation with GHR is 25%.

The fact that roughly one-half of events will originate due to hard scatter off of a gluon is striking. Essentially, the high W and low x region presents an entirely new dimension in deep-inelastic scattering. Instead of being a minor effect, scattering from gluons becomes the dominant feature! Half of the cross section may be the result of scattering from gluons! Certainly, this has major implications for the hadron production in this region. Scattering from gluons implies that the value of R will be non-negligible. It will be important to either measure R or take it into account via a QCD calculation when calculating structure functions from the measured cross section. In fact, a measurement of the gluon distribution function will in some ways be related to a conventional measurement of R! A particular measurement of the gluon distribution may be influenced by the QCD calculation and fragmentation model which are used to extract it. Further discussion on measurement of the gluon distribution is delayed to chapter 5.

In addition to studying the photon-gluon fusion process, DIS may also be able

to provide unique insight to the gluon bremsstrahlung process. Knowledge of the virtual photon direction will aid in understanding of the overall event. With sufficient statistics it should be possible to make systematic studies of differences (or the lack thereof) between quark and gluon jets. Recent studies from experiments at KEK show a softer fragmentation spectrum for gluons [34] but a very nice analysis done with the TASSO data at two different beam energies shows no difference between quark and gluon jets [46]. Although more experiments seem to observe that the gluon fragments more softly than the quark, the TASSO data seem to be very solid indeed. Perhaps there is an interesting clue in the treatment of jets as the energy changes in the $W = 20GeV$ region? Of course, other issues which can be addressed are the charge and flavor differences (if any) in quark and gluon jets.

An interesting but quite speculative possibility for DIS, is to study the production of gluons and their properties as a function of different nuclear targets. The varying radii of the nuclei may be useful as a means of studying the fragmentation of the gluon over a spatial distance. Such studies have already been done for quark propagation through nuclei [47] and are being done using E665 data. This is certainly not possible in e^+e^- experiments. Of course, it will take a considerable amount of data and good understanding of what the gluons look like off of light targets before a useful comparison can be made. Another possibility for use of heavy targets is to attempt to look for differences in the gluon distribution by studying

the 'jettiness' of the final states.

Another fragmentation area which is uniquely measured in DIS is that of diquark or target fragmentation. Do diquarks fragment like a quark, like two quarks, like a gluon or do they tend to behave differently? We know from EMC that they tend to form baryons and that there is less transverse momentum in the 'backwards' direction where the diquark is fragmenting [48,24]. How do the diquarks act in photon-gluon fusion events where nominally there isn't really a diquark but some other colored object?

Another topic to which DIS may be able to contribute is the matter of coherence in QCD processes. Historically, this is a subject which has actually evolved from the data and from the attempts of fragmentation models to explain the data. However, given that QCD is a quantum theory, it should actually be expected that various coherence effects should arise and be measurable. The challenge is to reliably calculate such effects given the potential traps in use of perturbation theory. Possibly the first (and to this date the only) observed effect of this type is known as the *string effect*. The string effect is most succinctly described as a relatively lower probability that hadrons are produced between the two highest energy jets than between the higher and lowest energy jets in 3-jet events from e^+e^- collisions. The interpretation of the jets in this case is that the two higher energy jets will be fragmenting quarks while the lowest energy jet will have resulted from a hard

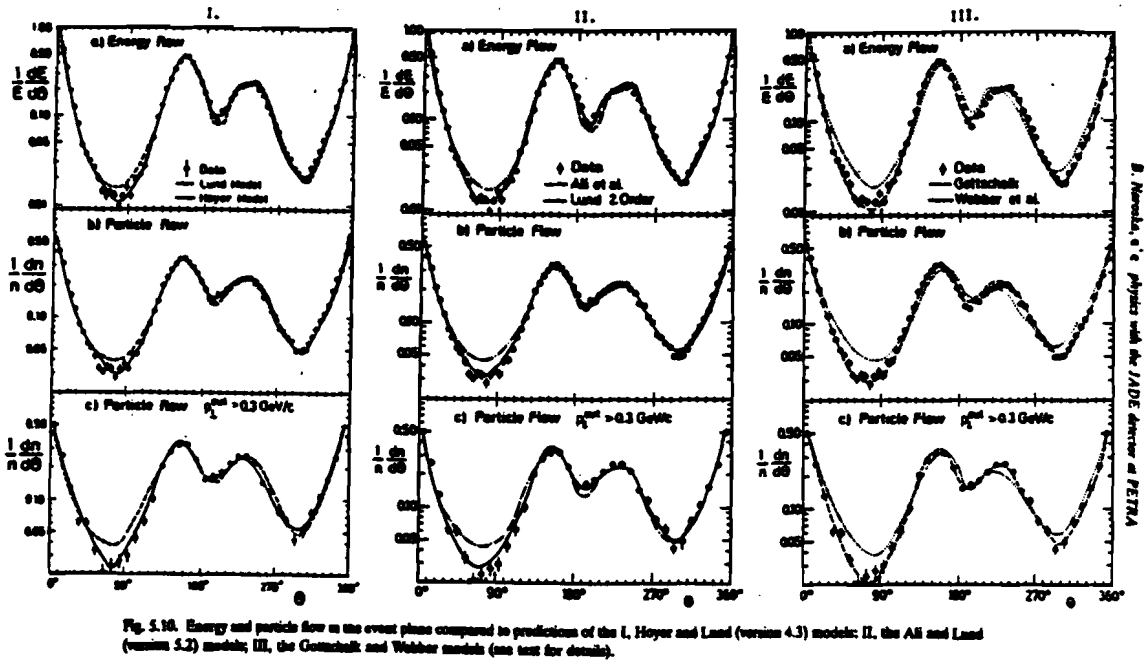

Figure 2.12: Energy and particle flow in the event plane from the JADE detector. The highest energy jet is centered at $\Theta = 0°$. Plot is from reference [33].

gluon. Figure 2.12 shows the effect in data from JADE.

The original explanation for this effect came from the Lund string model of fragmentation and will be more fully described in section 2.3.3. However, the effect was later described equally well in parton shower fragmentation models which will be described more fully in section 2.3.3. Briefly, the string model produces the effect due to strings being broken into hadrons and then boosted to the CM frame while the parton shower models produce the effect due to an *angular ordering* of

subsequent parton emissions as the shower progresses. A recent paper by Ballocchi and Odorico claims that the effect is also adequately described using an independent fragmentation model in which corrections for the average transverse momentum are made for soft hadrons [49].

The angular ordering concept in QCD coherence models is analogous to one which occurs in QED and is known as the Chudakov effect [50,51]. Nominally, this effect is calculable from next-to-leading order terms in QCD (or QED). In fact, a series of papers through the 1980's from a number of different authors have apparently demonstrated that not only can angular ordering be calculated from QCD, but that a number of additional coherence effects can be calculated as well. (See for instance [52,53,54,55,56,57,58]. See [50] for a good review.) The physical basis for the QCD coherence effects and how they impinge on hadron distributions is that hadrons will result from emission of many very soft gluons. When a hard gluon already exists in an event, we expect that there will be interference between it and soft gluons which will alter the cross-section for production of the soft gluons. Hence, the 'lowest order' calculation of such effects involves calculating the interference for one extra gluon in an existing event topology and then extending the resulting probability distribution to the probability distribution for production of hadrons. It will be interesting to see how many of the effects which have been predicted will be supported by experiment.

Before any of the preceding topics can be addressed, we face the task of simply identifying and understanding the basic production process and systematic difficulties for multi-jet events in DIS. Do we even see the basics which we expect from the Monte-Carlo predictions? That is the primary aim of this thesis.

2.3.3 Fragmentation Models

Fragmentation models are typically written as Monte-Carlo programs and include parameterizations ranging from a simple few to several tens in an attempt to precisely simulate data. Clearly, so many parameters, applied in a completely random fashion, could describe almost anything. In general though, only a couple of parameters will apply to a particular question, and the rest will be more-or-less irrelevant. If used carefully, it is hoped that it will be possible to extract knowledge of the fundamental processes which are occurring even though a complete understanding of the system is not feasible.

Independent Fragmentation Models

The first attempt at describing the fragmentation process came from Feynman and Field [59,60,61]. Their attempt was primarily phenomenological – the basic tenet being that hard scattering of a parton was the underlying process and then fragmentation would occur with a few basic assumptions (empirical forms for longitu-

dinal and transverse momentum) and rough conservation of momentum and flavors within the jet. It is amusing to note that in their first paper, they commented, 'The model we shall choose is not a popular one...', when referring to hadron production resulting from fragmentation of partons.

The model of Field and Feynman made no particular attempt at describing the fragmentation process as the result of some fundamental theory. Instead, the hope was to be able to simply apply the procedure in order to obtain quantitative comparison between different experiments or theory and experiment. It is my opinion that this is a healthy attitude in discussing the application of this model (or others) to the data. Indeed, the primary difference between an Independent Fragmentation (IF) model such as that of Feynman and Field and any other model comes mostly in the attempt at providing an underlying explanation for the otherwise completely phenomenological parameters. A cynic might argue that models such as Feynman and Field are simply less hypocritical about taking the parameters to be freely determined.

In independent fragmentation, the starting point is simply a number (any number) of quarks at a vertex all with determined momenta. The quarks fly away from the vertex and as they do they fragment into hadrons. Each quark is assumed to fragment based only on its own momentum in the CM of the system with no other dependence on the initial state. The fragmentation process is an iterative

one. A first $q\bar{q}$ pair is assumed to be produced in the color field. The antiquark is combined with the quark to form what is known as the *first rank* hadron. The longitudinal momentum of the hadron is determined randomly with the probability of any given momentum being determined empirically from data (of course the original momentum is the maximum). The remaining longitudinal momentum of the original quark is assigned to the leftover quark from the $q\bar{q}$ pair. After this, a second $q\bar{q}$ pair is generated and the antiquark combined with the quark from the first pair to form the *second rank* hadron. Longitudinal momentum is determined as before and the process continues. Each quark and antiquark are produced with equal and opposite transverse momentum within the pair. The transverse momentum for a hadron is simply the vector sum of the transverse momenta of the two quarks which comprise it. The probability distribution for transverse momentum is assumed to be Gaussian with a width which comes from an empirical fit to the data. The process of producing new $q\bar{q}$ pairs and forming hadrons continues until the remaining momentum falls below a cutoff value.

Hadrons are produced according to the flavors of quark involved and available spin states and can include an appropriate suppression for mass. Unstable hadrons are allowed to decay according to measured decay modes. The resulting final hadrons will form independent jets with no communication between each jet. In addition, in earliest models, no explicit overall energy conservation was imposed.

Improvements upon the initial work of Field and Feynman include the addition of tree-level QCD and various improvements on the fragmentation (such as explicit overall flavor, momentum and energy conservation using some 'reasonable' prescription. See for instance [62,63,64,65]). Inclusion of tree level QCD clearly requires a prescription for treatment of fragmentation of gluons.

Making very significant objections to the arbitrary mechanisms used to enforce various conservation principles seems mostly unfounded to me. Other models may nominally achieve this in a 'natural' fashion but they lack any rigorous proof that the mechanism has any true physical meaning. Even apparent effects which 'must follow' from one model or another can be tricky. As mentioned in the preceding section, recent work by Odorico and Ballocchi [49] seems to indicate that a simple scaling of transverse momentum to longitudinal momentum (certainly not a silly idea) adequately produces the so-called string effect using an independent fragmentation model.

Lund Model

The Lund (or String) Model of fragmentation [66,67,68,69,70] has grown to be one of the most popular models on the market and with apparently good reason. The model has enjoyed several triumphs in explaining data from both deep-inelastic and e^+e^- experiments. The heart of the model is the conjecture that color singlet

quarks can be treated as having a color flux-tube or 'string' between them. If the quarks have a large relative momentum, they will fly apart and as they do the string will stretch whilst acquiring a characteristic amount of energy per unit length – just as a stretched spring would. The string is not infinitely strong and eventually will break whenever the string tension exceeds a particular amount. This is basically determined by the probability that a quark-antiquark pair (of a particular transverse mass) can be formed from the energy which resides in a particular length of the stretched string. The $q\bar{q}$ pairs are pulled apart by their associated string segments to be combined into hadrons with the neighboring $\bar{q}$ or q on the string. The string continues to stretch and break until insufficient energy remains in any segment of the string to produce any further hadrons.

Clearly, the string will produce communication in the hadronization process of two different jets. For instance, in a two-jet event, it becomes very difficult to associate hadrons very near $x_F = 0$ to one jet or the other. The very center of the string can clearly be thought of as belonging equally to both of the jets and small boosts in either direction for the produced hadrons will mix the two sides together. Only those hadrons which are produced at boosts which are sufficient to overcome fragmentation momentum kicks will clearly appear as belonging to a particular jet.

Production of hadrons from the string is essentially a stochastic process which will be governed by the probability that any given section of the string will produce

a $q\bar{q}$ pair. This is assumed to be a simple quantum mechanical tunneling process with the probability for the process proportional to:

$$\exp\left(-\frac{\pi}{\kappa}m_\perp^2\right) = \exp\left(-\frac{\pi}{\kappa}m^2\right)\exp\left(-\frac{\pi}{\kappa}p_\perp^2\right) \tag{2.19}$$

where $m_\perp$ is the transverse mass which is due to both the particle rest mass m and the transverse momentum $p_\perp$ and κ is the energy constant for the string. Hence, we see that typical transverse momenta will be on the same order as meson masses and that mesons containing heavy quarks will have a suppression factor compared to those containing only light quarks. It is assumed that the string has a flat probability for breaking at any given point with sufficient energy and this means that longitudinal momenta will be governed by the random iterative procedure of breaking the string in a number of locations. Clearly, hadrons with large longitudinal momenta will be produced as a result of the string breaking early in the process near one of the endpoints before that endpoint has had sufficient chance to be deccelerated by the tension of the string. On the other hand, if the string tends to keep breaking nearest to the middle, then much of the string energy will be absorbed in production of hadrons and the leading hadrons will be appropriately degraded in momentum. The typical transverse momentum kick and the string constant κ are left as free parameters in the model. Quark flavors will have suppression factors from their masses given by $u : d : s : c = 1 : 1 : 0.3 : 10^{-11}$

and hence we expect that charm (or heavier quarks) will not be produced from fragmentation.

First order QCD processes are included in the Lund model by allowing gluons to function as kinks in the string at a given location with given momentum. Because the kink will have two strings attached, the kink (gluon) will experience a force which will be twice that of the quarks on the endpoints of the string. This compares well to QCD where the effective ratio of the force acting on the gluons compared to the quarks would be $2/(1-1/N_c^2)$ were N_c is the number of colors [69]. Each string between the gluon kink and it's endpoint quark (diquark, etc.) will fragment in the usual fashion. Once the gluon has expended all of its available energy for stretching strings, it will be broken into a $q\bar{q}$ pair which can either directly form a stiff hadron themselves if the two strings both happen to break early and very near the kink or the pair will be separated to combine with other quarks from each string to form two hadrons. Because the gluon will be fragmenting with two strings rather than one, the Lund model expects that gluon jets should have a softer hadron spectrum than for quark jets. If the gluon carries insufficient momentum to cause the string to break then it will simply produce some extra transverse momentum in the hadrons in its locale and the endpoint quarks will experience a corresponding recoil. Hence, the model provides a natural means for regularizing the gluon field.

The probability for the production of a gluon in an event is determined using the

first-order splitting functions of Altarelli and Parisi. Along with the axis coupling the virtual photon to one of the quarks, this allows for calculation of both the gluon bremsstrahlung process and photon-gluon fusion. In the case of photon-gluon fusion, the gluon is treated as a fluctuation of the original state of the nucleon and is then split into a $q\bar{q}$ pair ala Altarelli and Parisi. Two separate strings are used for the fragmentation – one which connects the quark from the gluon with a diquark remnant in the nucleon and another which connects the antiquark from the gluon with the quark which initiated the gluon radiation. Clearly this is a particular prescription which may or may not have anything to do with the real world.

The so-called string effect which was mentioned in section 2.3.2 arises in a simple fashion from the Lund model. Each string segment on two sides of a gluon is fragmented in the CM frame for that particular segment. The fragmentation will result in a number of hadrons with little momentum transverse to the string direction. However, after fragmentation, the string (or rather the resulting hadrons) are boosted into the event CM frame. Because each string segment will have a velocity component in the direction of the radiated gluon, the hadrons which result from that string will preferentially be travelling in that direction (see figure 2.13). The result will be more hadrons in the gaps between each of the quark jets and the gluon jet than between the two quark jets. This, of course, is precisely what is observed. It remains to be seen whether this or other explanations for the effect

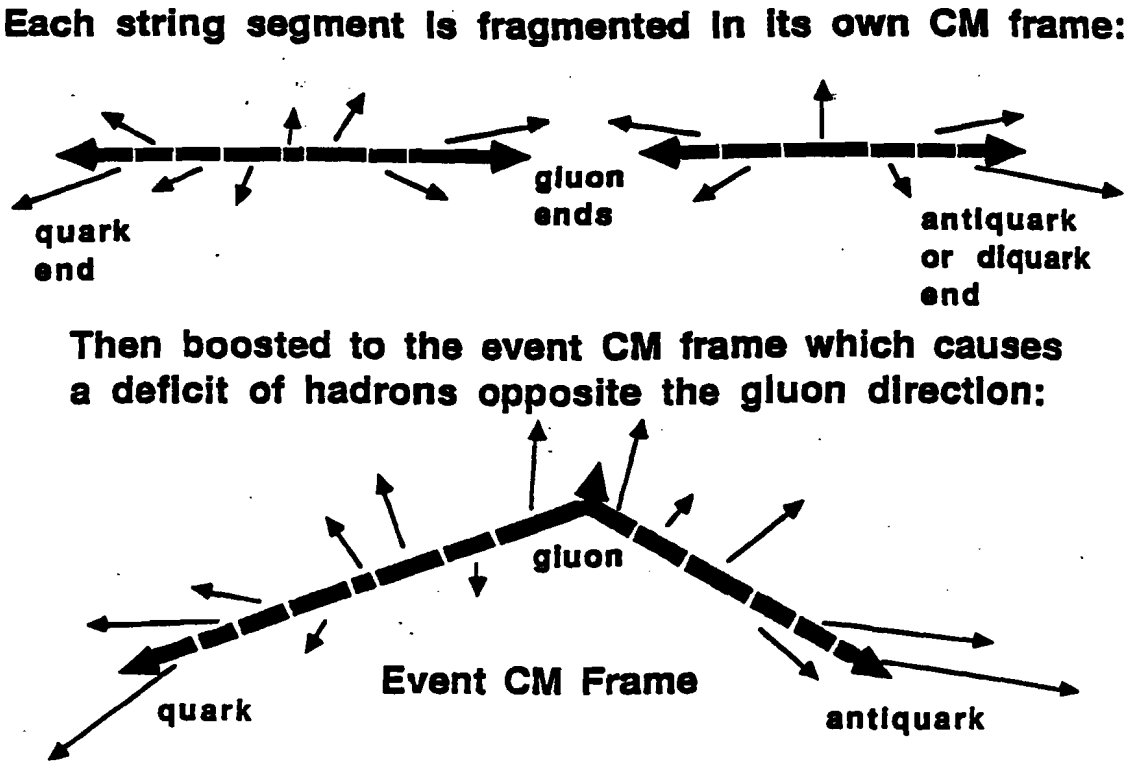

Figure 2.13: Production of the String Effect in the Lund Model.

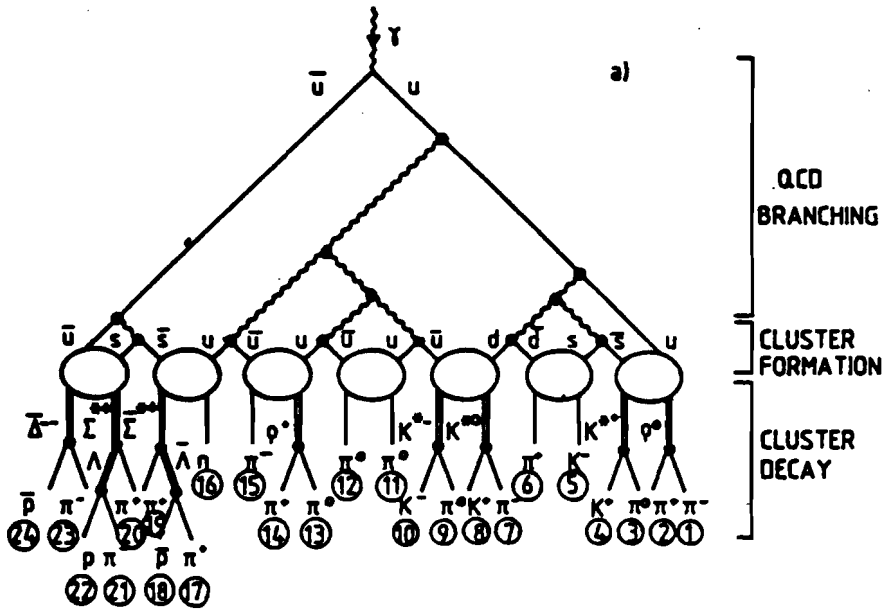

Figure 2.14: Example of a parton shower process. Parton Branchings are calculated using QCD, followed by combination of final partons into clusters which are then decayed into hadrons.

will maintain validity.

Parton Shower Models

Parton shower models were first proposed by Fox and Wolfram in 1979 with later development from Field, Gottschalk, Marchesini, Webber and others [71,72,73,74,75,76,77,78]. The basic picture of the process is shown in figure 2.14. The idea is that initial state partons will be far off mass-shell for the original hard scattering process. The partons will evolve through successive branching into a cascade of partons nearer

to mass-shell. The simplest calculation of the branching probabilities comes from tree-level leading order QCD ala Altarelli-Parisi splitting functions. The branchings are treated incoherently and the process continues until all of the partons have dropped below a *virtuality cutoff* Q_0. Although the cutoff parameter should nominally be given by the region in which perturbative QCD is understood to be valid, it is typically left as a completely free parameter which is to be determined by a best fit to the data. Typically, the cutoff is set around or slightly below $1GeV$. At this point, gluons are forcibly split into $q\bar{q}$ pairs which combine with neighboring quarks to form color singlet blobs with invariant mass which is typically on order $1Gev$. The blobs are subsequently allowed to decay into known hadrons with branching ratios determined by density of available states (takes into account phase space and spin).

In addition to the shower cutoff energy, the models also typically allow the Λ_{QCD} which is used in calculating α_s to be a free parameter. This is tantamount to an admission that the model has not taken account of all possible QCD processes which could have occurred. Presumably, the better the simulation of the actual QCD processes, the closer the parameter will be to the 'true' value. These two parameters form the basis of any of the parton shower models. Further parameters or prescriptions can also be applied. In particular, final $q\bar{q}$ clusters may receive special treatment when they have higher mass and can decay into heavy flavors or

with appreciable relative transverse momentum. Still, the number of parameters is uniformly quite small and very small indeed compared to the number of parameters used in the Lund Monte Carlo.

Since the introduction of the first parton shower models, appreciable work has been done to attempt to include higher order QCD processes into the branching probabilities. Marchesini and Webber [75,76,77] have included a partial treatment of soft gluon coherence effects. Following the work of a number of authors,they have included an angular ordering procedure for gluon emissions. The idea is that tree level coherence for soft gluon emission will be taken into account by requiring an ordering in the variable:

$$\xi \equiv \frac{q_j \cdot q_k}{\omega_j \omega_k}, \tag{2.20}$$

where $\omega_{j,k}$ are the energies of produced partons with four-momenta $q_{j,k}$. For small virtualities $q^2_{j,k}$,

$$\xi \simeq 1 - \cos\theta, \tag{2.21}$$

where θ is the opening angle, and

$$q_i^2 \simeq 2\omega_j \omega_k \xi = 2z(1-z)\omega^2 \xi, \tag{2.22}$$

where z is the energy fraction and ω is the energy of the parent parton i. Each subsequent branching in the shower is required to have smaller ξ than the previous branching. This ordering is then equivalent to q^2 when all parton energies are of the

same order of magnitude but will have a very significant effect on soft partons. It will cause a strong suppression of soft gluons (and therefore the resulting hadrons) in certain regions of phase space. In particular, it does a marvelous job of producing the so called string effect. Here though, the effect is attributed to the inability of long wavelength gluons to resolve individual color charges of partons within the shower.

The parton shower model is attractive from several points of view. First, the process at least attempts to rationally apply QCD to the fragmentation process rather than simply jump to the conclusion that 'its just not calculable'. Of course, the application of QCD in any given model may be completely wrong! However, I think that the question should be at least partially treated as an experimental one. If parton shower models are successful in describing data with only a couple 'physically motivated' parameters, then can we really be so sure that the underlying 'ad hoc' assumptions are so wrong? In particular, given that *any* present fragmentation models make rather major assumptions, it seems reasonable to at least make those assumptions in an attempt at utilizing what we believe to be the underlying theory which is responsible for the process. Perhaps the attempt at applying the theory will ultimately assist in leading us to the correct application. It will be particularly interesting to see if predicted coherence effects are observed in the data.

The parton shower model is also very attractive for use in calculating fragment-

ing systems at very high energies. In these cases, four or more 'hard' jets are not at all uncommon. The parton shower process naturally allows for arbitrarily complicated event structures. The process for production of a 'hard' parton is no different than that for 'soft' partons – only the probability of production is different. Because of this fact, parton shower models are being used extensively for calculations of jets at both present and future proton and electron colliders. The string model becomes unwieldy (at best) when too many partons become involved.

Some comparison has been made between deep inelastic data from EMC and a version of the Webber model by Wilson [78]. In almost all overall aspects, the model reproduces the data quite well. Tests on very specific aspects have not been made. Work continues on development of these models.

2.3.4 A Few Final Comments on Fragmentation

The three basic models presented in the preceding sections comprise the main set of QCD based Monte Carlos in use today. There are also other models such as the Firestring model of Preperatta *et al* [79] (which is not based on QCD but it has to do many similar things!) and simple phase-space fragmentation. I will not (and likely cannot) even start to list all of the subtle variations on the market of the various models. Likely, there are an unlimited number of models which can mostly 'fit the data' which exists today. It all depends upon how arbitrary one is willing

to be in production of a model.

For the data which exists thus far, it is my opinion that most of the QCD based models do an adequate empirical job of describing the basic features of data as determined by hard QCD processes. I think that the jury is still very much out on the specifics of the fragmentation process though. At the bottom of it all, it may be that several models will always be capable of building in whatever new effects may be required. Hence, I think that the number of free parameters becomes of great interest in trying to select a favoured model. As more data becomes available, it will be interesting to see what extra levels of arbitrariness will have to be added to various models.

2

Chapter 3

Beam and Apparatus

3.1 Overview

The E665 spectrometer sits at the end of the approximately 1.5 km long NM (New Muon) beam line at Fermilab. The muon beam is effectively a tertiary beam resulting from the decays in a secondary beam of pions and kaons which have been produced by impinging the primary extracted proton beam from the accelerator onto a beryllium target. Muons are tagged in a beam spectrometer system in the final section of the beamline before emerging into the experimental hall. The beam spectrometer supplies both trigger information and tracking information for the incoming beam, utilizing two stations of scintillators and proportional counters upstream of a horizontal bending magnet and two sets of scintillators and proportional counters downstream of that magnet. The beam is further defined (electronically) by a system of veto 'jaws' scintillators around the beam and a large veto wall of scintillators just inside the Muon Laboratory.

The E665 spectrometer has been designed to allow acceptance which is very nearly 4π steradians (in the CM of the collision) with good momentum resolution and particle identification for practically all secondary particles. (Of 'common' particles only neutrons, neutrinos and K_L^0 are not detected). A plan and perspective view of the spectrometer are shown in Figure 3.1. The spectrometer is built around two large, superconducting, dipole magnets. The first magnet, the 'Cern Vertex Magnet' (CVM) was originally built for use in the NA9 experiment (EMC) at CERN. It was shipped to Fermilab for use in E665. The second magnet is the 'Chicago Cyclotron Magnet' (CCM) which was originally constructed for use as the magnet for the the Chicago Cyclotron. Since that time, it has has been used in past experiments at Fermilab as an analyzing magnet and eventually was converted to a superconducting magnet. For this experiment, the CCM was moved into place first and then the Muon Laboratory was constructed around it.

For this running, the targets were 'thin' (less than approximately one nuclear interaction length) and were located between the poles of the CVM. The targets were also within a large streamer chamber and hence had to be constructed solely from dielectric materials. Hydrogen, deuterium, and xenon were selected as target materials. The streamer chamber permits momentum measurement for high angle and low momentum tracks. In addition, it allows significantly better determination of the primary interaction vertex than can be achieved using just the downstream

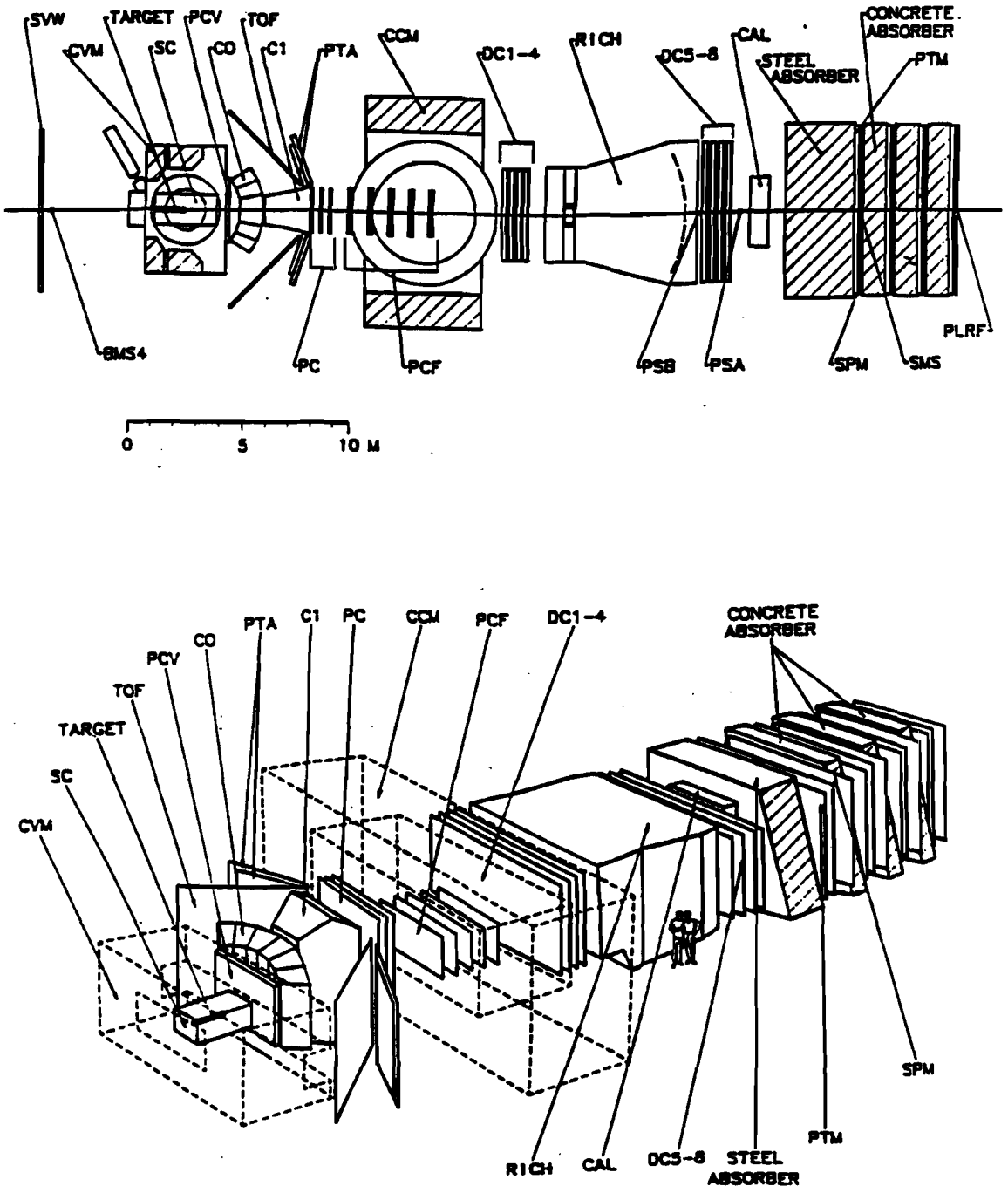

Figure 3.1: Plan and Perspective view of E665 Spectrometer

detectors. Immediately downstream of the CVM is a six plane multi-wire proportional chamber (MWPC) which is designated PCV. This detector provides the anchor for charged particle track segments between the two magnets. At wide angles, two sets of streamer tubes (designated PTA) provide the other end of the track segment and at smaller angles a series of MWPC chambers (designated PC) serve this function. At large angles and in front of the PTA's are two scintillator hodoscopes (designated TOF) which are used to measure time-of-flight of large angle charged particles. Between PCV and PC are two threshold Cerenkov detectors designated C0 and C1. With the exception of the PTA tubes and PC chambers, all of the preceding detectors were part of the vertex spectrometer used for NA9 and were shipped from CERN for use in this experiment.

In between the poles of the CCM are a series of MWPC's designated PCF. These chambers allow tracking of particles as they curve through the magnetic field of CCM. Immediately downstream of CCM are four packages of drift chambers each of which contain two active wire planes. These drift chambers are designated DC1-DC4. These provide the anchor for charged particle track segments in this region and four more drift chambers (DC5-DC8) located 8 m further downstream provide the other end of the track segments. Between the two groups of drift chambers is a large ring imaging Cerenkov detector (RICH) for charged particle identification up to very high momentum. The drift chambers are deadened in the beam region

and two sets of small area MWPC's are provided downstream of the RICH (PSB) and downstream of the second group of drift chambers (PSA) to provide track information in this region and also for trigger purposes.

Through the detectors listed thus far the amount of material to be traversed by particles has been kept to a minimum (about 25% of a radiation length). Next comes a 20 radiation length lead/proportional tube calorimeter (CAL) for detection of photons and electrons. The calorimeter hence provides detection of neutral hadrons which decay into photons such as π^0's. Following the calorimeter is a $3.0m$ wall of steel for absorption of hadrons. The muon detection and trigger apparatus consists of four sets of scintillator planes and proportional tubes interleaved with walls of concrete which are $90cm$ thick. The scintillator planes are divided into two parts– the wide angle SPM's and the small angle SMS's in the beam region where the SPM's have a hole. The SPM's are used primarily just for triggering while the SMS's serve a dual function of trigger devices and position measurement for the beam region where the planes of proportional tubes (PTM's) are deadened or inefficient. The concrete walls provide for absorption of low energy electromagnetic showers generated by beam muons which could cause a high(er) rate of false triggers.

A brief compilation of detectors and their properties is given in Table 3.1.

Chamber Devices						
Detector Name	Detector Type	Active Region h x w (x l) [m]	Number of Planes	Wire Spacing or Resolution	Active Gas † [mg/cm²]	Total Material [g/cm²]
PBT	prop. wire	0.13 x 0.13	4 x (U;Z;Y;V;Z';Y')	1 mm	0.7	–
SC	streamer ch.	0.7 x 1.2 x 2.0	–	850 μm	–	–
PCV	prop. wire	1.0 x 2.8	Y;U;U';V;V';Y	2 mm	2.2	0.49
PTA	prop. tube	2.0 x 2.0	Y;Z;V;U	12.7 mm	5.1	–
PC	prop. wire	2.0 x 2.0	3 x (Y;Z;V;U)	3 mm	1.4	.33
PCF	prop. wire	1.0 x 2.0	5 x (U;V;Z)	2 mm	1.3	2.5
DC1-4	drift ch.	2.0 x 4.0	4Z;2U;2V	<400 μm	1.0	0.05
DC5-8	drift ch.	2.0 x 6.0	4Z;2U;2V	<400 μm	1.0	0.05
PSA	prop. wire	0.13 x 0.13	Z;Y;Z';Y';U;V;U';V'	1mm	0.7	–
PSB	prop. wire	0.13 x 0.13	Z;Y;Z';Y'	1mm	0.7	–
PTM	prop. tube	3.6 x 7.2	4 x (Y;Z)	12.7 mm	5.1	–

Scintillation Hodoscopes					
Detector Name	Material	Thickness [cm]	Array Size h x w [m]	Number of Elements	Photomultiplier
SBT	NE110	0.3	0.18 x 0.14	4 x [26, 13Y;13Z]	R1398
SVJ	NE110	1.0	0.5 x 0.5	3 x 2 [with hole]	RCA6655
SVW	NE110	2.5	3.0 x 7.0	28 [14 x 2 array]	RCA8575
TOF	NE110	1.5,2.0,4.0	1.6 x 4.2	2 x 38	XP2020,XP2230,XP2252
	NE104	1.0	0.2 x 0.2	5 [radial]	XP2252
SPM	GS2030	2.5	3.0 x 7.0	4 x 30 [15 x 2 arrays]	R329
SMS	NE110	1.3	0.2 x 0.2	4 x 32 [16Y,16Z]	R1166

Cherenkov Detectors							
Detector Name	Index of Refraction	Radiator Length [m]	Number of Cells	Detector/ Photomultiplier	Thresholds [GeV/c]		
					π	K	p
C0	1.00141	0.9	144	RCA8854Q,EMI9829QA	2.6	9.3	17.6
C1	1.00052	1.5	58	RCA8854Q	4.3	15.3	31.0
RICH	1.00033	6.0	10800	wire chamber	5.4	19.2	36.5

Electromagnetic Calorimeter						
Detector Name	Detector Type	Active Area [m]	Number of Planes	Number of Cathode Towers	Wire Spacing	Total Thickness [radiation lengths]
CAL	gas sampling	3.0 x 3.0	10 x (Y:Z)	1188	1.04 cm	20

Table 3.1: Summary of detectors and their properties.

3.2 Coordinate System

The E665 coordinate system has been defined to have its origin at the center of the CCM. A right-handed coordinate system has been defined which has the positive x-axis along the direction of the beamline (referred to as $\hat{\boldsymbol{x}}$), the y-axis is horizontal with the positive direction to the west ($\hat{\boldsymbol{y}}$), and the z-axis is vertical with positive z pointing up ($\hat{\boldsymbol{z}}$). The nominal 'zero' time of any event is defined to be the time which the scattered muon passes through the center of the CCM. The standard unit of distance is meters and the standard unit of time is nanoseconds. In this document, *upstream* will refer to the $-\hat{\boldsymbol{x}}$ direction while *downstream* will refer to the $+\hat{\boldsymbol{x}}$ direction which is almost exactly the direction that the beam muons travel.

3.3 Beam

The NM (New Muon) beamline at Fermilab [80] has been designed to deliver a high intensity beam of muons to the muon laboratory while limiting halo (muons which are outside of the useful phase space of the beam but still pass through the detector apparatus) to no more than approximately 10% of the beam flux. A further consideration in the design of the beamline was the capacity for producing a polarized beam (at the expense of intensity). The capacity for polarized running was not used in the 1987-88 running period. In addition to the normal muon beam, it is possible to convert the beamline to provide a calibration beam of hadrons and

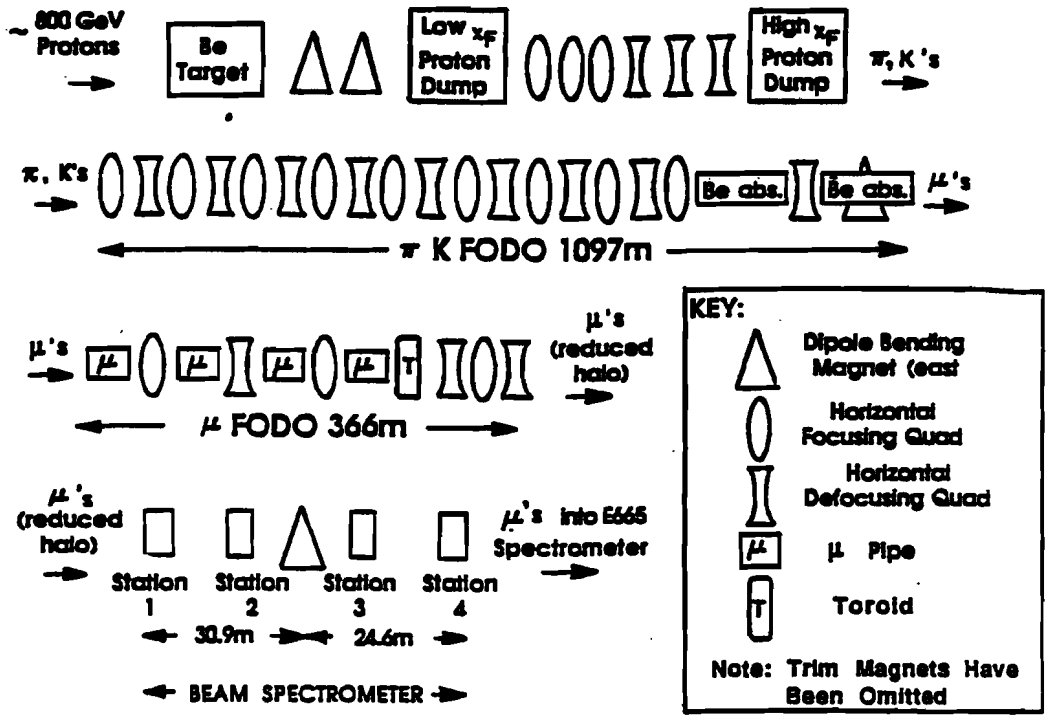

Figure 3.2: Schematic view of the main elements of the New Muon beamline.

electrons.

A schematic of the beamline is shown in figure 3.2. The beamline can be separated into four sections; pretarget, target and front-end elements, parent (decay) FODO and the muon FODO. The pretarget section takes the primary protons from the switchyard and delivers them to the target. Secondary pions and hadrons are produced from the proton beam impinging on the target and the useful phase space is collected by a set of front-end magnets while non-useful phase space and the remaining proton beam are absorbed. The parent FODO is a transport line which gives the pions and kaons time to decay before reaching a beryllium absorber in the beamline, after which only muons (with a small hadron contamination) remain.

The muon FODO is a transport line which allows for removal of halo and provides for focussing of the muon beam on the experiment target in the muon hall. Following the final quadrupole element of the muon FODO is the section used for beam tagging and momentum analysis which includes a horizontal bend and several MWPC's. Wire chambers are utilized at numerous points along the length of the beamline for diagnostic purposes in tuning and operation of the beam.

3.3.1 Pretarget Elements

Protons for the NM beamline are split from the main proton beam using an electrostatic septum followed by a Lambertson septum magnet. After the proton split is sufficiently large, a superconducting dipole magnet (MUBEND) bends the protons at a relatively large angle to their initial direction and into the muon beamline. A switch dipole exists just upstream of MUBEND which is used for changing operation modes from high intensity to polarized running. MUBEND bends the protons mostly horizontally but also vertically downwards. The muons are leveled out by subsequent vertical bends in enclosures NM1 and NM2 (NM... refer to beamline enclosures. I will leave out the word *enclosure* in the following.) which leaves the beamline at $\sim 3m$ underground for the entire length of the beamline. This provides shielding for radiation safety. A doublet consisting of five quadrupoles (FFDDD *F stands for focussing, D for defocussing*) in the upstream end of NM2 (the target

hall) focusses the protons onto the target. The doublet configuration minimizes divergence in the bending plane of the secondary beam and maximizes the spatial separation of the desired secondaries and the primary protons at the beam dumps.

3.3.2 Target and Front-End Elements

The proton beam is focussed onto the target consisting of $48.5cm$ of beryllium. Secondary particles emerging from the target are gathered in a doublet of six quadrupole magnets (FFFDDD) downstream of the target. A set of bending magnets is provided which are used to select the central value of the momentum of the secondary hadrons which are accepted. The primary protons and off-momentum secondary hadrons are absorbed by a beam dump located $\sim 10m$ downstream of the target assembly. In addition, a second beam dump is located in the next enclosure (NM3, the first enclosure of the parent FODO which is $\sim 73m$ downstream of the post-target bend) along with a collimator which can be used to reduce intensity in any mode and is crucial in selecting a momentum bite and achieving polarization in the polarized running mode. Interaction of the various front end elements is dependent on both tune and mode of operation. Further details are presented in [80].

3.3.3 Parent FODO

The Parent (or Decay) FODO is designed to give efficient transmission of the secondary hadrons while giving them time to decay into muons. The relevant considerations in design of the decay FODO are; the decay length for $\sim 800 GeV/c$ pions and kaons, transmission efficiency of the FODO for a given interquad length, phase advance per cell (determines shape of muon beam at the experiment), halo at the experiment, number of quadrupoles and enclosures and physical positions of quadrupoles, enclosures and the Muon Laboratory with respect to other structures.

The basic structure of the FODO consists of alternate focussing and defocussing single quadrupoles spaced at equal intervals followed by a beryllium absorber to remove the undecayed hadrons from the beam. The quadrupoles are a standard Fermilab construction referred to as 4Q120. The beryllium absorber is $11m$ long, $6.2m$ of which is inserted into a large aperture bending magnet which can be used to further select the momentum bite of muons reaching the lab. The length of the absorber is calculated so as to reach a minimal plateau in the remaining hadrons (hadrons are regenerated by muons in the beryllium) while being kept little (or no) longer than this in order to keep multiple scattering of the muons to a minimum.

Minimizing the spot size of the beam at the absorber will minimize the increase of the phase space of the muon beam due to multiple scattering and hence will

increase the flux of muons at the Muon Laboratory. Minimal spot size is achieved by having the phase advance at the absorber be a multiple of 180° and a total phase advance of 540° was chosen. Effect of spacing of quadrupoles on transmission efficiency was calculated and it was decided that a spacing of $61m$ would be acceptable with transmission efficiency only 5% from maximum with that separation. Given the determination of these factors, cost and space are the primary factors which will limit the length of the decay FODO and the final determination was to make it $1.116km$ long.

3.3.4 Muon FODO

The primary reason for not placing the Muon Lab just downstream of the absorber is to provide a distance over which halo muons can be separated from the beam. Hence a FODO with the same periodicity as the parent FODO provides efficient transport for the beam past devices which will remove a large portion of the halo. Because the halo consists of high energy (and therefore very penetrating) muons, it is not possible to absorb it. Instead, a system has been devised which produces a sharp-edged, toroidal, magnetic field around the muon beam. This is accomplished by conventional toroid magnets and with a thick-walled iron pipe referred to as *mupipe*. Muons which are inside the radius of the field will be unaffected, while muons which are just outside of the inner radius of the field will experience a strong

outward radial deflection.

The mupipe is designed to provide the very sharp edge to the magnetic field. Mupipe is cold-rolled iron pipe which has coils carrying current wrapped along the inside length of the pipe and then returning along the outside so as to induce a torroidal field. The field within the pipe is $\sim 2.0T$ while the field just a few millimeters within the inner radius of the pipe is virtually zero. The mupipe is divided into several sections. The first section of pipe is $9.2m$ long and consists of pipe with inner diameter of $11.4cm$ and outer diameter of $17.8cm$. The following three sections have an inner diameter of $12.7cm$ and an outer diameter of $19.1cm$.

Larger aperture toroid magnets continue the process of deflecting halo away from the beam. These toroids are placed downstream of the mupipe and consist of $9.2m$ of $1.73m$ diameter toroid magnets followed by $6.2m$ of $3.05m$ diameter toroid magnets. During the 1987-88 run, the combination of the mupipe and these large diameter toroids resulted in a factor of 5 suppression in the amount of halo compared to beam which enters the experiment downstream. Approximately half of the remaining halo is within $20cm$ or the nominal beam axis and the rest is spread more uniformly across the apparatus.

3.3.5 Beam Performance

The characteristics of the final muon beam depends on a number of factors including the number of incident protons, the tune which is being implemented and the selection of useful phase space by the experiment. In general, the beam has a transverse size at the experiment of $\simeq 4cm$ in the z direction (nonbend) and $\simeq 6cm$ in the y direction. For high-intensity running, with tune of $x > .5$ a muon/proton ratio of 5×10^{-6} is typically achieved. For the 1987-88 running period typically $2\text{-}3 \times 10^{12}$ protons were delivered per spill to the muon beam target which resulted in $10\text{-}15 \times 10^{6}$ muons per spill or instantaneous rates approaching $10^{6}/s$. Significantly higher intensities can be achieved with a lower momentum tune. Rates as high as $10^{7}/s$ can be achieved by use of more primary protons or lower momentum tunes.

The beam retains the RF structure of the accelerator. The RF is $53MHz$ which gives buckets spaced at $\sim 19ns$ intervals with the arrival time of muons having a jitter of only about $1ns$ within a bucket. This fact has been used in the design of the trigger logic for the experiment. At high intensities, as many as 20% of the muons will be in buckets which contain another muon. With this in mind, the beam spectrometer has been constructed with multi-hit capacity.

3.3.6 Calibration Beam

It is possible to produce a calibration beam of hadrons and muons by making several alterations to the NM beam line [81]. For this mode, a secondary target is installed $60m$ upstream of the beryllium absorber. A dipole magnet just downstream of the secondary target sweeps charged particles out of the beam. The beryllium absorber is replaced with 0.1 radiation lengths of lead. Resulting electrons, positrons and hadrons are transported along the muon FODO to the experiment. Beam particles are tagged in the beam spectrometer in the same way as muons, but with a lower current in the tagging magnet. A final dipole magnet, which can be rotated remotely, is used to alter the direction of the beam as it enters the experimental hall. It is also possible to remove all absorbers from the beam and bring primary protons all of the way to the Muon Lab for purposes of alignment of the beamline magnets and other components.

3.4 Beam Spectrometer

The beam spectrometer must not only supply tracking information for the incoming muon but must also provide trigger information which defines a 'good' incoming muon. This is accomplished by two stations of detectors upstream of a horizontal bending magnet and two sets of detectors downstream of the same magnet. Each station of detectors consists of a set of scintillator hodoscopes for trigger in-

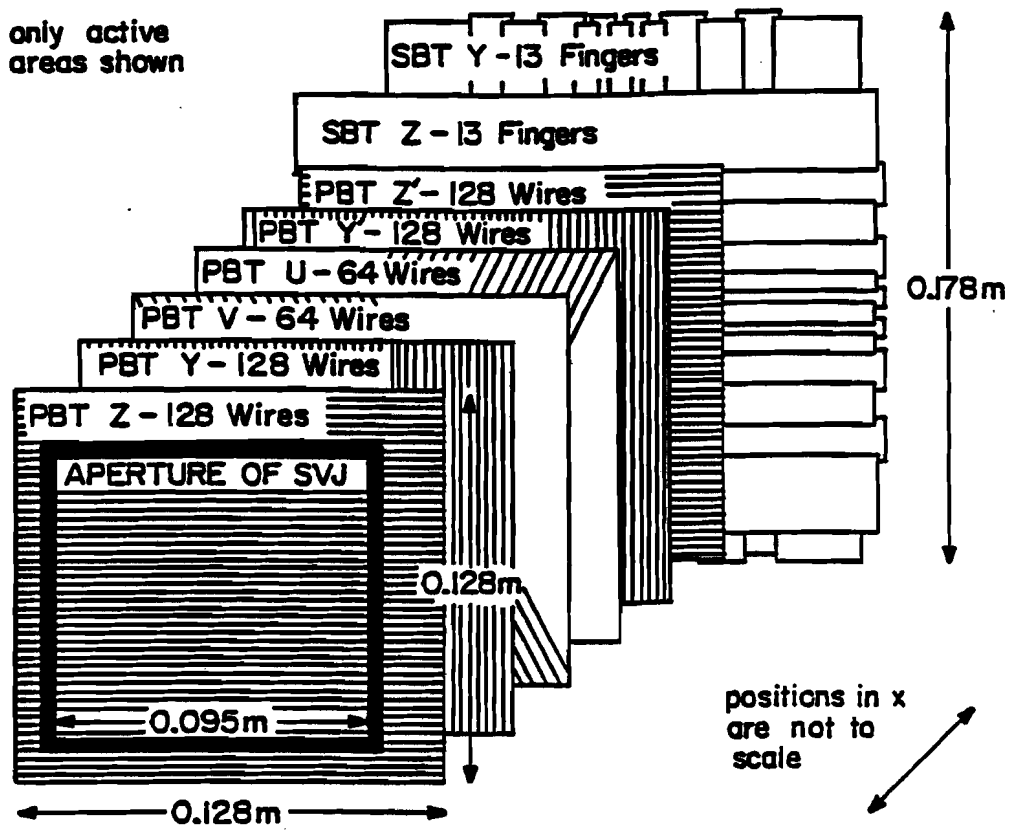

Figure 3.3: Wire planes and scintillators for a beam tagging station.

formation and a package of MWPC's for precision tracking information in offline reconstruction (see figure 3.3). The beam spectrometer is located in enclosures upstream of the Muon Laboratory. The bending magnet is a dipole magnet with a $3mR$ bend (the magnetic field strength is changed to suit the average momentum of the beam). Stations are numbered from 1 to 4 with number increasing along $\hat{x}$. The detector stations provide for $\sim 27m$ lever arms on each side of the magnet position. The system is designed to operate with an instantaneous beam rate of $10^7/s$. Angular resolution is $\sim 10\mu R$ which results in an uncertainty in momentum

of $\sim$ .5%. During the 1987-88 running, reconstruction efficiency for single beam muons was in excess of 99%.

3.4.1 Scintillator Hodoscopes (SBT's)

Scintillator hodoscopes with a y view are provided at all stations and hodoscopes with a z view at stations 1,3 and 4. All of the scintillator hodoscopes consist of 13 small scintillators. All stations but the z-view in station 1 have scintillators which are graded in width in order to give approximately equal signal rates. These hodoscopes have an active area of $17.8cm \times 14.0cm$. The scintillator strips are Bicron BC-400 and are $3.2mm$ thick, $17.8cm$ long and vary in width from $6.4mm$ to $25.4mm$. Narrower counters are used in the central portion of the hodoscope while wider counters are in the wings of the hodoscope. The z view hodoscope in station 1 has equal width scintillators ($9.5mm$) in order to enhance the beam fraction which is available for the small angle trigger (see section 3.11.4). All counters are arranged in two layers with $1.6mm$ overlap. Each scintillator has attached a single Hamamatsu R-1398 phototube with maximum operating voltage of $1.9kV$. Each scintillator is equipped with an optical fiber leading to a common LED for each station which can be used to check basic operation.

Phototube signals are transmitted on fast cables (RG-8U hardline) to a position which is adjacent to the most downstream station. Here, signals are split

with one half being digitized (LRS2249 ADC's) and the other half being discriminated (LRS4416 Discriminators) with resultant logic signals being used in trigger determination and latched for read-out (LRS4448).

3.4.2 Beam Proportional Counters (PBT's)

The beam proportional chambers consist of a specific implementation [82] of a generic design developed by the Fermilab Experimental Areas Department [83]. Each station has a package consisting of six planes of proportional wires with $1mm$ spacing with two planes each at orientations for y readout (vertical wires), z readout (horizontal wires) and one plane each at $\pm 30°$ from vertical. Orientations with two wire planes have the wires offset by $0.5mm$ between the two planes, yielding an effective wire pitch for that view of $0.5mm$. Inclined planes are necessary for reconstruction of events with multiple beams which will be rather common if instantaneous beam rates of $10^7/s$ are achieved. The planes in each package are separated into two gas volumes with independent high-voltage power supplies so that if one plane of wires is not functional, the other set can still provide a space-point.

Sense planes consist of 128 anode wires ($10.2\mu m$ gold-plated tungsten) and mounted on G10 frames. The active area of each plane is $12.8cm \times 12.8cm$. Cathode planes and gas windows consist of $12.7\mu m$ thick aluminum foil. There is a $3mm$ gap between cathode and anode planes. The gas mixture consists of 50% argon and

50% ethane bubbled through ethyl alcohol at $0°C$.

Signals from the chambers are amplified and discriminated at the chambers (Nanometrics N277). Discriminated signals are transmitted through flat pair cable to delay and latch modules in CAMAC crates (LRS 2731A, PCOS III MWPC Readout System).

3.4.3 Halo Veto System

Halo muons are an inescapable part of life in a muon beam and provide a potential source of background for various triggers used in the experiment. Two systems have been implemented to remove the effects of this halo. First, an array of large scintillator counters has been constructed at the most upstream end of the Muon Laboratory and provides a veto for wide halo. Second, several stations of 'jaws' scintillators have been provided which can be closed in around the muon beam to cut out halo muons which are close to the beam but not useful to the experiment. Of course, at some point the halo-veto jaws actually begin to define what is and is not 'useful' beam.

3.4.4 Veto Wall (SVW)

The halo-veto wall (SVW) consists of an array of large scintillators at the beam inlet into the Muon Laboratory ($\sim 5m$ upstream of the CVM center). The active

area of the array is $3m \times 7m$ which effectively covers the entire active area of the downstream spectrometer. A $25cm \times 25cm$ hole is left in the center for the muon beam. The array consists of 28 counters, each $1.5m \times .55m$ and $2.54cm$ thick. These counters were originally built by Rutherford Lab for use in E98 and were resurrected for use in this experiment. A few of the counters had to be rebuilt. The counters are mounted on the downstream side of a $5cm$ thick wall of steel (with a hole in the middle!) in order to discourage false vetoes due to soft photons produced by the beam. The counters are read out using RCA8575 phototubes. Signals from the phototubes are transmitted on RG58 coaxial cable to a location adjacent to the last beam station. There, the signals are split in the same fashion as those for the SBT's with part being digitized and part being discriminated and latched or forwarded via fast coaxial cable to the trigger electronics downstream.

3.4.5 Veto Jaws (SVJ's)

The halo-veto jaws (SVJ 1-3) consists of three pairs of scintillation counters located at beam tagging stations 2, 3 and 4. Each pair covers an active area around the beam of $50cm \times 50cm$ The counters in a pair can be adjusted relative to each other in order to produce an adjustable, rectangular aperture around the beam. This aperture is adjusted so as to cut out 'close' halo which would just miss the target or portions of phase space which produce trigger anomalies (e.g. low momentum

tail). Because of the proximity to the beam, these counters suffer very high rates which can be as much as 5% of the beam. RCA6655 phototubes were used and signals are treated in the same fashion as those for the beam tagging hodoscopes (SBT's) and the veto wall (SVW).

3.5 Targets

For the 1987-88 running period, 'thin' ($\sim$ a few tenths of an interaction length) targets were used in order to minimize re-interaction of final-state hadrons and thus maximize probability for observation of the 'true' hadronic final state. A major consideration which had to be taken into account for this running was that targets had to be designed to live within the streamer chamber environment. This constrains both total target length and requires a dielectric material. With those considerations in mind, selection of target materials was made on the basis of physics interests and ease of analysis. The three materials used in this running were liquid hydrogen, liquid deuterium (actually a mixture of D_2, HD and H_2 with a total of 95% of deuterium) and high pressure gaseous xenon. Hydrogen was selected as the 'most basic target available' and to allow comparison with deuterium. Deuterium was selected as the lightest possible isoscalar nucleus and higher cross section (than hydrogen) for production of hadrons off of a 'fundamental' target. Deuterium also provides the baseline for comparison with heavier targets in searches for A-dependent ef-

fects. Xenon was selected as an element which is a dielectric and has a large atomic number in order to search for A-dependence effects. Given the time available and priorities of the collaboration, no other 'heavy' targets were used in this running period.

The same cryogenic liquid target was used for both the hydrogen and deuterium running. It consists of a cylinder which is $1.1m$ long (along the x-axis) and with a diameter of $9cm$. It is constructed from $1mm$ Kapton which was reinforced with Kevlar threads. From tests of boil off rate it was determined that bubbles in the target would produce a less than 1% effect on the target thickness. The target filled with hydrogen presents $\sim 8g/cm^2$ of material to the beam while filled with deuterium it presents $\sim 16g/cm^2$ of material. The end-walls of the target correspond to 2% of the thickness in grams of the hydrogen filling.

The pressurized gas target used for the xenon running consists of a cylinder which is $1.12m$ long and has a $7.2cm$ diameter. The vessel is constructed from $200\mu m$ mylar reinforced with Kevlar and epoxy. The operating pressure for this target with xenon was 14 atmospheres gauge which results in $9.5g/cm^2$ of xenon in the target. This is comparable to the amount of material in the cryogenic target filled with hydrogen. The thickness of the endwalls in the beam for this target is $0.3g/cm^2$ which is about 5% of the total target thickness.

Some data were taken with each beam and target vessel with the vessel filled

with atmospheric pressure gaseous helium. These *empty target* data are used to statistically subtract effects caused by the target vessel for certain analyses.

3.6 Large Analyzing Magnets CCM and CVM

The two large magnets CCM and CVM form the basis upon which the tracking spectrometer is constructed. The CCM is a large dipole magnet with a $3m$ diameter pole piece and a gap of $1.3m$ between the two poles. It has a superconducting coil which is capable of carrying $\sim$ 900 Amps which corresponds to a maximum field between the pole pieces of $1.5T$. As mentioned above, this magnet was originally constructed as the magnet for the Chicago Cyclotron and has since been converted for use as an analyzing magnet in high-energy experiments. The CCM coils are not equipped with any quench protection. This allows for more windings and smaller coils but will certainly be a disaster if the magnet ever does quench. So far, this has never happened.

The CVM (CERN Vertex Magnet) was originally used in NA9 (EMC) at CERN and was shipped to E665 as part of the 'complete' vertex spectrometer. The CVM is a dipole magnet with $2m$ diameter pole tips which have a cylindrical opening in the center to allow for viewing of the streamer chamber. The poles are separated by a gap of $1m$ The CVM is equipped with a superconducting coil which is capable of carrying a maximum of $\sim 5000amps$ which corresponds to a field of $1.5T$. The

CVM is equipped with quench protecting copper coils which means that less winds can be produced in a fixed volume. Hence, the current required to produce a given field is higher than for the CCM but the magnet will survive quenches.

For the 1987-88 running, the two magnets were operated with fields in opposite directions such as to produce a *focussing* condition. This condition is achieved by setting the field integral for each magnet inversely proportional to the distance of each from the first plane of the PTM's. This corresponded to field integrals of $4.312Tm$ for the CVM and $-6.734Tm$ for the CCM. Neglecting various achromatic effects, the result of this focussing condition is that the impact position at PTM1 for a scattered muon depends only on the scattering direction and not on the muon energy. In addition, focussing ensures that unscattered beam muons hit the SMS1 arrays at the position predicted by a straight line projection from the beam spectrometer. Both of these effects simplify the construction of the large and small angle triggers. Because the target is located in the CVM field, muons change momentum part way through this field resulting in an achromatic effect. This effects the triggers and in particular is one of the primary limitations on the small angle trigger performance.

3.7 Tracking Detectors

3.7.1 Streamer Chamber (SC)

The streamer chamber (SC) consists of a rectangular active volume of 2.0 m along the x-axis, 1.2 m along the y-axis and 0.7 m along the z-axis. The volume of the chamber is divided into three sections by horizontal electrode planes of phosphor-bronze grids which give 80% light transmission. This construction allows for insertion of targets in the upstream half of the streamer chamber and avoids a dead spot for tracks in the forward direction downstream of the target. The walls of the chamber are constructed of 50 mm thick Rohacel coated on each side with 1 mm of Lexan. The chamber is viewed from the top which consists of a clear Lexan plate. The original version of this chamber [84] had a 120 μm mylar foil in place of the Lexan plate. The heavier plate was installed as a safety precaution against possible chamber rupture should the target vessel break. In addition, 'blow out' windows connected to exhaust vents were installed in the sides of the chamber to relieve pressure if such a target catastrophe were to occur. All outside electrodes are at ground while the two inside electrodes are at positive and negative high voltage.

Streamers are produced in the chamber upon application of a 10 ns long, 350 kV pulse produced by a Marx generator and Blumlein system. The memory time of the chamber is controlled by the gas mixture which is nominally 70% Ne, 30% He, .3%

isobutane and a few times $\frac{1}{10}$ ppm of SF_6 (the SF_6 controls the memory time which is between 1.0 and 1.5 μs). The pulse is produced in the Marx generator which has 21 stages each with a capacitance of 22 nF and is charged up to 19 kV. The formation time for the pulse is $\sim$ 400 ns and is originally 100 ns in duration. The Blumlein shapes the pulse and reduces the length to $\sim$ 10 ns. The charging time for the Marx is several hundred milliseconds. This time, required for stability of operation of the Marx, determines the streamer chamber dead-time which is considerably longer than the electronic dead-time for the remainder of the apparatus. Hence, specially selective triggers must be generated for the streamer chamber as discussed in section 3.11.8. The 1 μs or longer memory time typically causes several muon tracks (not necessarily associated with the trigger) to be visible in each picture.

The optical system of the streamer chamber consists of three cameras each with a different stereo angle (15° between cameras 1 and 3, 12° between 2 and 1 or 3). The film is advanced by a vacuum capstan which is capable of operating at the rate of 10 pictures/second. Image intensifiers (Varo type 1248-3 with P11 phosphor) are used in order to minimize the necessary length of the streamers. The image intensifiers offer a light gain of $\sim$ 100 and have a resolution of 55 line pairs/mm. A demagnifying lense (Nikon-Rokor type; 58mm/1.4; located .384 m from the center of the chamber) reduces the image by a factor of 66 which combined with the film resolution provides a minimum track separation of $\sim$ 3mm. Single tracks in the

subset of 1987-88 data which has been analyzed have an $\sim 850\mu m$ spatial resolution which leads to a momentum resolution of $\frac{\delta p}{p} = p \times 10^{-2}$ (p in GeV).

3.7.2 Vertex Proportional Chamber (PCV)

The PCV multi-wire proportional chamber [85] sits immediately downstream of the CVM. Its purpose is to provide for matching of tracks in the streamer chamber with downstream tracks, provide wide angle tracks (both with and without the PTA's) without streamer chamber information, improve resolution of momentum for forward tracks and improve location of the primary vertex for events in which no streamer chamber information is available.

The sensitive area of PCV is 2.80 $m \times 1.00$ m. The chamber consists of six planes of anode wires; two vertical, one each inclined at $\pm 45°$ and one each inclined at $\pm 18°$ from vertical. The signal wires are of 20 μm gold-plated tungsten with a separation of 2 mm. The cathode planes consist of 10 mm thick Rohacel 31 foam covered on each side with a 75 μm thick mylar which is coated with 75 μm of graphite. There is an $8mm$ gap between anode planes and surfaces of the cathode planes. The Rohacel cathodes permit the wire support frames to be kept thin while adding only a small amount of material to the active area. The support frames are constructed from fiberglass FE27. The gas mixture used is 71.8% Argon, 28% isobutane, 0.14% Freon, and trace amounts of isopropyl alcohol.

PCV is a copy of a similar chamber used in the NA9 experiment [84]. With that chamber, a plateau of 400 volts was obtained above 5.1 kV and time resolution permitting a gate width of 50 ns. With these conditions, the r.m.s. point reconstruction was .5 mm in the horizontal and 1.2 mm in the vertical direction. In order to be resolved as individual hits, tracks must be separated by 4 mm in the horizontal direction and 12 mm in the vertical direction.

Signals from the wires travel through a 6.6 m twisted pair cable to preamplifiers which are mounted near the chamber. These amplifiers drive a 65 m length of twisted pair cable which is used as a delay element. The signals are received in the counting-room where they are amplified, discriminated and delayed using a monostable circuit. The data are then latched and encoded. Addresses of hit wires are ready for readout via CAMAC after .8 ms.

Single plane efficiency for detecting halo muons away from the beam region during low intensity running during 1987-88 was typically 90%.

3.7.3 'PC' Proportional Chambers (PC1-3)

The PC multi-wire proportional chambers were used in an earlier experiment [86]. The readout electronics were changed for this experiment. The system consists of three packages each containing four anode wire planes- one mounted horizontally, one vertically and one each at $\pm 28.07°$ from vertical. The active area of each

chamber is 2 $m \times 2$ m. The anode and cathode planes are mounted on 'Stesalit' frames each 6 mm thick which are packed together and stiffened with external iron frames. The anode planes are constructed of 25 μm diameter, gold-plated tungsten wires soldered onto a printed circuit board and spaced $3.0 \pm .1$ mm. The cathodes consist of plastic foils coated on each side with graphite with a single cathode foil separating anode planes. The gap between the anode and the cathode is $6mm$. Two zig-zag mylar strips 5 mm wide are in each gap between cathode foils and anode wires to act as spacers and reduce the free wire length to prevent oscillations caused by electromagnetic forces. A compensating field wire runs parallel to the mylar spacers in order to restore full efficiency to these regions. The distance (along $\hat{\boldsymbol{x}}$) from the first to the fourth anode plane in each package is 36 mm. The total thickness of all 12 planes is $0.33 g/cm^2$ in the active region.

Preamplifiers are mounted directly on the chamber frames and drive twisted pair cables (which act as a delay element) and lead to the so-called RMH readout system [87] in the counting room. The RMH system provides amplification, discrimination and latching for all signals. In addition, it provides a fast OR of each group of 32 wires for use in triggering purposes (see section 3.11.8). RMH modules (consisting of 32 channels each) are housed in crates each containing 22 of the modules. Readout is performed by an encoder in each crate. The crate encoder records the station number for each hit channel and this information is transferred at readout time to a

system encoder which sits in a CAMAC crate and controls readout of the 12 RMH crate encoders. Data transfer is via a DMA transfer to the PDP from the system encoder.

The average efficiency for detecting halo muons in a subset of 1987-88 data examined was $\sim$ 85% per plane. The poor efficiency is believed to mostly be due to degradation of the cathode in the beam region.

3.7.4 Proportional Chambers in CCM (PCF)

The PCF system [88] consists of five triplets of multi-wire proportional chambers distributed in the upstream half of the CCM. Each triplet has one plane of horizontal anode wires and one plane each oriented at $\pm 15°$ with respect to vertical. Each plane has an active area of $1\ m \times 2\ m$. The Anode planes are constructed with 20 μm diameter, gold-plated tungsten wires stretched on G-10 frames. The wire spacing is 2 mm. Cathode planes are constructed from styrofoam-backed aluminized Kapton and are spaced 6.4 mm on either side of the anode wires. There are two support wires in each z plane, one on each side of the beam region. The U and V planes have a single support wire near the center of each plane. Support wires are offset in different planes in order to avoid completely dead regions. Anode planes within a triplet are separated (along $\hat{\mathbf{x}}$) by 6.7 cm. The gas used is a mixture of 80% Argon, 19.7% CO_2 and 0.3% Freon. High voltage is typically $3.8kV$.

The wire signals are amplified and discriminated on the chamber using Nanometrics (N-303) amplifiers. Signal delay is generated by a monostable ($700ns$) for each wire and two monostables for central region wires to reduce the dead-time. Hit wires are recorded as bits in a shift register and a CAMAC based scanner (Nanometrics WCS300) converts these into addresses at readout time.

The average single plane efficiency for detecting halo muons away from the beam region and support wires was greater than 95% for the subset of 1987-88 data examined thus far.

3.7.5 Drift Chambers (DC1-8)

Tracking of charged particles downstream of the CCM is primarily accomplished via two sets of drift chambers [89]. One set is immediately downstream of the CCM while the other set is another four meters further downstream (on the other side of the RICH). The aperture of the upstream chambers is 2 m × 4 m while the aperture of the downstream chambers is 2 m × 6 m. The upstream chambers are numbered 1-4 while the downstream chambers are 5-8. Each chamber contains two parallel planes of drift cells with anode wires for one plane offset by one-half cell from the anode wires in the other plane. Chamber planes with horizontal wires are split vertically into two half-planes (using a G-10 septum) to improve multi-hit capability. Each set of four DC packages contains four planes of horizontal wires

(z view), and two planes each with wires inclined at $\pm 5.758°$ from the vertical.

The drift cells in each plane have dimensions $50.8mm$ along the y-axis and $9.6mm$ along the x-axis. Drift cells in adjacent planes are offset by 1/2 cell width. The central region around the beam in each plane is deadened over a region which is two cells wide and $50.8mm$ along the length of the wires. Cathode and field shaping wires are of $102\mu m$ copper-beryllium wire with electroplated silver coating. Anode wires are of $20.3\mu m$ gold-plated tungsten with rhenium doping for added strength. A special wire placement table was used to achieve an absolute precision in anode wire position of $100\mu m$ over the entire face of each chamber. Wires are mounted on precision drilled printed circuit boards which are laminated with precision drilled stainless steel plates which are all sandwiched together (to form the drift cells) and supported by frames of $35.6cm$ and $45.7cm$ wide by $1.27cm$ thick G-10 fiberglass beams surrounded on all sides by $7.62cm \times 7.62cm$ aluminum angles for strength. The gas volume of the chambers is enclosed by a film laminate of $25.4\mu m$ thick aluminum foil and $50.8\mu m$ thick mylar. The aluminum side of the film is on the inside of the chamber and acts as an electrostatic shield. The gas mixture consists of 50% argon and 50% ethane bubbled through ethyl alcohol at $\sim 0°C$. The electric field is $492V/cm$ which yields a (measured) drift velocity of $4.2cm/\mu s$. Hence, full drift time is approximately $500ns$. Each eight plane package has a total thickness of $.045g/cm^2$ along the beam direction in sensitive areas.

Anode wire signals are amplified and discriminated on the chambers (Nanometrics N-311) which supply a double pulse resolution of $100ns$. The signals are then transmitted along $28m$ of twisted pair cable to a repeater, followed by another $32m$ of cable before reaching the time digitization system. The time digitizing system is 'home-built' and provides a time resolution of $2ns$ with a multi-hit capacity of 16 hits per channel and with a $35ns$ deadtime [90]. This system exists in CAMAC crates and is read out in a standard DMA transfer.

Single hit spatial resolution is $\sim 400\mu m$ per hit. After halo muon calibration, individual wire corrections should improve this resolution to $\sim 250\mu m$. Resolution for double hits is dominated by the $100ns$ front end electronics dead-time and is $\sim 5mm$. Efficiency for detecting halo muons away from the beam region was $95\% \pm 4\%$ per plane for a subset of 1987-88 data.

3.7.6 Small Angle Proportional Chambers (PSA,PSB)

Two small-angle MWPC's have been included for purposes of small angle tracking and triggering (PSA and PSB) [91]. The chambers use the same flexible base design [83] as the beam spectrometer chambers. PSA is located directly in front of the calorimeter while PSB is located just downstream of the RICH which provides a lever arm between the two small angle chambers of $\sim 2m$.

PSA consists of two identical packages of four planes each. The first four plane

package is mounted with orientation z, y, z', y' (primed planes are offset by $0.5mm$). The second package is mounted at 45° with respect to the first yielding u and v views. The planes have $1mm$ wire spacing and an active area of $12.8cm \times 12.8cm$, which is sufficiently large to cover the dead region in the center of the drift chambers. The gap between anode and cathode planes is $3mm$ (as in the beam chambers). The average thickness of each four plane package is $9.3g/cm^2$, including the support frames and electronics.

PSB consists of a single four plane package identical to those used in PSA. It is oriented to yield y and z views.

Both PSA and PSB are operated at $3.1kV$ with a gas mixture of 50and 50Amplifiers and readout system are the same as for the beam spectrometer chambers. Only PSA data has been used for the 1987-88 running. The efficiency for finding at least one space point for the combined package was over 98%.

3.7.7 Large Angle Proportional Tubes (PTA)

At large angles, behind the time of flight hodoscopes, are the PTA detectors which provide a larger lever arm and extra hit information for pattern recognition for charged particles which are either produced at wide angles or swept into large angles (from the $\hat{x}$ direction) by the CVM. The counters have an identical construction and readout as the PTM counters (discussed in Section 3.8.3) but with different

sizes and orientations. Each of the PTA's has an active area of $2m \times 2m$ and provides y, z, u ($+45°$ from vertical) and v ($-45°$) views.

3.8 Muon Detection

High-energy muons are much more penetrating than hadrons, photons or electrons and this fact is utilized in muon detection. A $3.0m$ thick wall of steel ($\sim$ 18 nuclear interaction lengths) is placed behind the electromagnetic calorimeter and acts to absorb all secondary particles other than high-energy muons. Arrays of detectors are then placed behind the steel. Slabs of concrete which are $90cm$ thick are placed between each of four sets of counters used for muon detection. The concrete acts to eliminate spurious hits caused by a soft electromagnetic shower which may emerge with a muon as it passes through matter. The muon detection must not only supply identification of the muon track in the forward spectrometer but must also supply the trigger information for the experiment based on angle of scatter for the muon. To accomplish this, each set of detectors consists of an array of large scintillator counters (SPM's), an array of small scintillator counters in the beam region (SMS's) and large arrays of proportional tube counters (PTM's). These detectors can be combined in a number of different ways for trigger purposes while the PTM's and SMS's yield tracking information to be associated with upstream tracks for identification of muons. A small set of scintillators at the very back of the

experiment produce a $53MHz$ signal which is phase locked to the arriving muons for use in trigger timing.

3.8.1 Large Muon Scintillator Counters (SPM)

The large muon scintillators (SPM's) [92] consist of four planes each consisting of an array of large scintillator counters. The active area of each array is $7.0m \times 3.0m$ with a hole in the center for the beam which is $20cm \times 20cm$. The individual counters consist of $2.54cm$ thick acrylic scintillator (ROHM GS-2030) with area of $0.5m \times 1.5m$. The counters are arranged so that a $12mm$ overlap exists with adjacent counters. Scintillation light is absorbed and re-emitted in wavelength shifter bars (ROHM GS-1919) which run the length of the scintillator and also act as light pipes leading to a single phototube (Hammamatsu R329) for each counter. The counters are enclosed in plywood boxes. The two central counters (above and below the beam hole) consist of $2.5cm$ thick NE110 scintillator with dimensions $.28m \times 1.4m$. An acrylic light guide leads to a single phototube (Hammamatsu R329) at the top end of the upper counters. The lower counters have an air light guide at the top end since this area is in the beam. Phototube high voltage is supplied by LRS HV4032 modules.

The phototube bases for counters with acrylic scintillator are built to integrate for $20ns$ and then discriminate at the level of 2-3 photoelectrons. This helps to

maintain moderatetiming in spite of a two-component output from the shifter bars; one with mean lifetime of $20ns$ and another with mean lifetime of $600ns$. The discriminated signals are transmitted via twisted pair ribbon cables to the trigger electronics which is located on a platform on top of the absorber steel. In addition to the digital signals, analog pulses are digitized and read out for each counter.

3.8.2 Small Muon Scintillator Counters (SMS)

The beam hole in the SPM counters is covered by hodoscopes of small, 'finger' scintillators (SMS 1-4). Each station has a vertical and a horizontal hodoscope which is constructed from 16 scintillators with width of $13.2mm$ except for the outer counters which are $19.6mm$ wide. The edges of the individual scintillators are beveled so that an effective overlap of $\sim 0.3mm$ is created for adjacent fingers. Phototubes (Hamamatsu R1166) are mounted directly on the scintillators and signals are transmitted via RG58 coaxial cables to LeCroy 4413 discriminators which are run in update mode and to LRS2249 ADC's. Discriminator outputs are sent to LeCroy 4448 latches and to the trigger logic. Phototube high voltage is supplied in the same manner as for the SPM's.

3.8.3 Muon Proportional Tubes (PTM)

The purpose of the muon proportional tubes (PTM) is to provide tracking for muons behind the steel. The detectors consist of four sets of proportional wire tube planes, each set being positioned immediately upstream of one of the SPM hodoscope planes. Each set consists of a pair of planes of horizontal and vertical proportional tubes (a total of four planes per set) with active area $3.6m \times 7.2m$. The proportional tubes are constructed from aluminum extrusions and have a pitch of $2.54cm$. Two planes yielding the same view are adjacent to one another and there is an offset of $1.27cm$ between the tubes in each plane so that an effective pitch of $1.27cm$ is achieved with no dead region between tubes. The aluminum walls between tubes are $2mm$ thick which results in frequent hits in both layers of tubes. The anode wires are $50\mu m$ gold plated tungsten. The planes are operated at $\sim 2.7kV$ with a gas mixture of 50% argon and 50% ethane which has been bubbled through ethyl alcohol at $0°C$. This results in a maximum drift time for ionization electrons of $250ns$. Wire signals are amplified, discriminated and latched at the planes (Nanometrics N-272-E). Latch readout is performed in parallel for each plane using a Nanometrics WCS 200 system. Outputs from the monostables at the plane are also available as differential ECL signals. It is intended that these signals will provide the basis for a target-pointing level-2 trigger processor which

was not ready for the 1987-88 running period.

For halo muons away from the beam region, the typical efficiency for finding at least one PTM wire hit per station in a single view was $\sim$ 95% for the subset of 1987-88 data examined.

3.8.4 RF Phase Locking System (PLRF)

The Tevatron RF structure is preserved in the muon beam. During the 1987-88 running period, the frequency was $53.10470 MHz$. A signal source in the Muon Lab is Phase-locked to the arriving muons and used throughout the experiment. Because this signal has less than $1ns$ of time jitter relative to the arriving muons, it is very useful for a number of timing purposes.

The reference phase for the PLRF signal is provided by four $5.08cm \times 5.08cm \times 1.27cm$ NE110 scintillation counters located downstream of the last SPM counter. Two RCA 8575 and two Hammamatsu R329 phototubes are used and high voltage is supplied in the same manner as for the SPM counters. A four fold coincidence between the counters is formed. The output of this coincidence has a time fitter of $1.05ns$ (FWHM) with respect to the accelerator RF. This signal is used to phase-lock the distributed accelerator RF, producing the PLRF signal. The phase lock circuit can track time shifts at a rate of $300ps$ per arriving muon and has a back-up local oscillator.

3.9 Electromagnetic Calorimetry (CAL)

The primary function of the electromagnetic calorimeter (CAL) is measurement of photon momenta. Of course, electron energies can also be measured and the design of the calorimeter allows for reconstruction of neutral hadrons (π^0 for instance) which decay into photons. Indeed, the calorimeter was designed so that hadron reconstruction will be sufficiently complete that a direct photon signal may be visible. In addition, the calorimeter is able to provide a fast signal for use as a component in experiment triggers. Considerable use is being made in a wide variety of analyses of calorimeter information for removal of bremsstrahlung from event samples. Because I spent several years in the planning, construction, testing and operation of the calorimeter, I shall dwell considerably more on the details of its construction and operation than I have on other detectors.

3.9.1 Calorimeter Design Criteria

The idea of the E665 spectrometer is to intercept and detect as many of the secondary particles produced by a deep-inelastic-scatter *as possible* and this rule includes photons. Of course *as possible* includes a number of considerations. A necessary feature of calorimeters is that they contain a large amount of material and hence, must be located behind tracking and particle identification detectors for

various charged hadrons. This relegates the calorimeter to be downstream of the final set of drift chambers and just upstream of the absorber steel. This forces the calorimeter to be more than $20m$ from the target (actual final position is $\sim 24m$ from the target). Given this position, the pole pieces of the CCM determine the effective aperture which will be available to the calorimeter and is $\sim \pm 1.3m$ in the vertical direction. Monte Carlo studies were performed which showed that a square calorimeter of $3m \times 3m$ would (on average) intercept only $\sim 65\%$ of the total number of photons but that these photons carry most of the total photon energy in an event ($\sim 95\%$). Diminishing returns are achieved by attempting to intercept more photons by extending the calorimeter in horizontal directions (Only a small fraction of remaining phase-space can be intercepted by doing so.) and cost scales about linearly with extension in this direction. Hence, it was decided that the calorimeter should be around $3m$ transverse dimension and a square design was chosen for ease of construction.

The calorimeter needs to supply information on the neutral energy flow of an event with reasonable position and energy resolution. A considerably more ambitious goal is to allow reconstruction of neutral hadrons which decay into photons and through this capacity, the ability to discern extra photons which are left over and constitute a 'direct' photon signal. In order to achieve this, good energy resolution, longitudinal shower development information and high segmentation with

good transverse spacial resolution are essential. Given finite amounts of money to spend, the chosen solution was a gas-sampling calorimeter with cathode-pad-tower readout. Size of pads was chosen by Monte Carlo study and for convenience of construction. Three regions of different pad sizes were selected; smaller pads in the center and larger pads in the perimeter. High density is required in order to keep showers as narrow as possible so lead was chosen as the passive absorber material between active elements. Monte Carlo studies showed that 20 radiation lengths of material would be sufficient to keep shower leakage acceptably small (less than $\sim$ 2% for showers up to 50 GeV).

The largest source of limited resolution in a sampling calorimeter is caused by statistical fluctuation due to discrete sampling. Following Rossi [93], Monte Carlo data [94] give the average total number of electron tracks sampled between lead plates each of thickness t (in radiation lengths) as:

$$N \approx \frac{50E[GeV]}{t[X_0]} \tag{3.1}$$

for electrons with kinetic energy greater than $1MeV$ (E is the energy of an incident electron). Assuming a Gaussian distribution for the number of sampled tracks, the fluctuation is given by:

$$\sigma_E[\%] = \frac{1}{\sqrt{N}} = \frac{14\sqrt{t[X_0]}}{\sqrt{E}} \tag{3.2}$$

for lead. This can be generalized [95] to:

$$\sigma_E[\%] = \frac{k\sqrt{\epsilon}\sqrt{t[g/cm]^2]}}{\sqrt{E}} \tag{3.3}$$

where ϵ is the critical energy of the absorber in appropriate units and k is allowed to be material dependent and typically ~ 2. This equation agrees very well with measured data. Gas sampling calorimeters will have worse resolution by about a factor of 2 from the above equations due to Landau and track length fluctuations in the gas Hence, the energy resolution of the calorimeter will improve by increasing the number of active sampling elements (decreases t) along the shower development but cost increases roughly linearly and longitudinal density will be affected. A total of 20 sampling planes (one per radiation length) was decided upon as a good compromise.

A number of different techniques have been employed for construction of gas-sampling calorimeters with pad-tower readout. In this case, it was decided to use so called Iarocci tubes [96] to build planes of proportional tubes with cathode pads on both sides of the plane in order to reduce charge fluctuations due to wire-pad separation. The Iarocci tubes (rather than some other tube construction) were chosen primarily because they were available and inexpensive. It was decided that readout would be performed on sums of sixteen anode wires (a single Iarocci bitube) on all planes to provide longitudinal shower information. Precision position

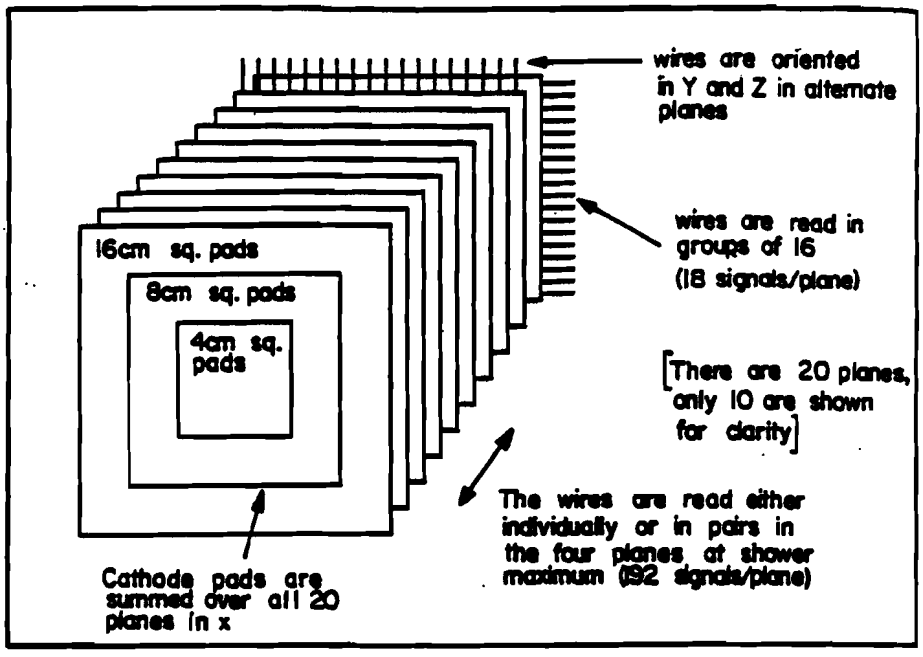

Figure 3.4: Simple schematic for the E665 electromagnetic calorimeter.

information is provided by readout of individual anode wires in four planes which are near shower maximum.

3.9.2 Calorimeter Construction

As noted above, the basic design of the calorimeter is a lead/proportional-plane sandwich with both cathode pad and anode readout. A simple schematic of the calorimeter is shown in figure 3.4 There are a total of twenty planes of lead with twenty planes of proportional tubes interspersed. Each of the lead planes is $3m \times 3m$ and $5mm$ thick (about one radiation length). The lead sheets are backed with aluminum and supported by individual hangers for each plane. The lead sheets are

actually constructed from five pieces of lead, each $62cm \times 363cm$, which are glued side by side onto the aluminum backing (on both sides). Gaps between the lead pieces are less than $0.3mm$ so that this will produce a negligible effect on the energy resolution.

The detector planes each consist of eighteen $3m \times 16.6cm \times 1cm$ plastic proportional tubes layed side by side to create an active area of $3m \times 3m$. The plastic chambers are an early version of the now rather common 'Iarocci' chambers [96]. Each of the chambers consists of two extruded PVC 'profiles' which have eight cells of proportional tube on a $1cm$ pitch. The extrusions are open on one side (the 'top') but in our design we have included a 'top' plastic sheet which is attached to the profile with tape. The inside of each tube and the plastic top is coated with a resistive graphite paint which acts as the cathode for high voltage. The two profiles are enclosed in an outer plastic sheath (creating a 'bitube') which acts as a gas vessel requiring gas to flow through one profile then out through the second profile. The bitubes are strung with a combination of $50\mu m$ and $63\mu m$ copper-beryllium wires (a few are gold plated tungsten). The mixture of wires resulted from an error during the stringing process and was not intentional. It was decided that restringing was not necessary if each plane contained all the same wire diameter (and hence requiring two different high voltages). The wires are strung at $140g$ of tension and are held in place by $1cm$ wide plastic supports at $\sim 50cm$ intervals

along the length of the chamber. The ends of the chambers are sealed by a plastic end-plug which has connections for gas and high voltage. In most chambers, the eight anode wires in a profile are all connected together and a single electrical feed through is provided for each. Four of the planes have chambers which were converted to provide 'individual anode readout'. In these chambers, each anode wire has a separate electrical connection to the outside. The anodes are held at ground while a connection for negative high voltage is provided for each of the profiles (two connections per bitube).

Use of these particular Iarocci tubes has provided a number of challenges in construction and operation. These tubes were of a rather early design (They were extruded and coated in Italy in 1983, strung at CERN in that same year, shipped to Harvard for testing, modification and repair in 1984, and finally shipped to Fermilab for assembly into planes in 1985.) and there have been a number of improvements made in new designs. In particular, it was quite difficult to achieve a reliable gas seal between the outer sleeve of the bitubes and the endplugs. Some high voltage problems occurred due to inconsistencies in the resistive coating. Wire positioning and sealing is not always consistent which leads to high voltage problems (sometimes even after passing many previous tests!). Some high voltage problems have occurred during 'burn-in' periods of operation. These difficulties have resulted in about 12 profiles (out of 720) being inoperable during the first running period. In addition,

half of one of the individual anode planes had its gas flow pinched off during the run which severly effected the gas gain in every other bitube in that plane. Due to the relative inaccessability of the bitubes, it is only possible to make repairs during prolonged down times.

Each plane has eighteen bitubes which are contained in a $4m \times 3.3m \times 2.5cm$ aluminum box. Bitubes are located within the box to within $1mm$ using aluminum locator pieces which are attached to each tube. The aluminum box acts as the physical support for the bitubes, an electromagnetic shield, and as a secondary gas seal. The aluminum boxes consist of two side frames of rectangular aluminum extrusions to which the large sheet-aluminum sides (50 mil thickness) are riveted. The other two sides of the box consist of an FR4/micarta laminate which provides feedthroughs for signals, power and high voltage. These sides have screw connections with the sheet-aluminum sides. Portholes were cut in one of the sheet-aluminum sides for each plane to allow for access to the internal electronics and connections. The portholes have sheet-aluminum covers which are held on with packing tape and a piece of copper tape for electrical connection. Each box is supported by two large steel bolts which are attached to the hanger. The aluminum boxes and lead sheets are supported via their hangers on a very large steel frame. An insulating material is inserted between the hangers and support frame so that the calorimeter will be electrically isolated except for intentional ground, power and signal cables.

Each aluminum box has a ground strap attached to a 'main' ground bus for the calorimeter. Planes of lead or detector can be removed from above (after being uncabled) with the overhead crane in the Muon Lab. Planes can be moved over about a $1m$ distance along $\hat{x}$ to allow limited access to any plane in the stack without having to remove it.

Half of the planes have the bitubes mounted horizontally and half vertically. Horizontal and vertical bitube planes alternate throughout the calorimeter stack. Each profile has a separate high voltage cable but the cables are externally ganged by plane and there is a separate high voltage supply for each plane. High voltage is supplied by HK5900 modules. Although it would be possible to have different high voltages in a single plane, no attempt was made to do this (except for profiles which were completely off due to HV problems). The high voltage is $2000V$ for planes with $50\mu m$ wires and $2150V$ for planes with $63\mu m$ wires. Gas flows serially through each of the bitubes in a single plane. In the individual anode planes, alternating bitubes are reversed in direction and in these planes the gas flow consists of two separate serial systems. Each bitube has an electronics card attached to the endplug which combines all of the wires from both profiles into a single signal and amplifies this signal. In addition, the four individual anode planes have electronics which allow readout of each wire individually in the central $1m$ (six bitubes) and the combined signal of each pair of two adjacent wires in the outer regions (the outer 6 bitubes on

each side). The readout of the bitubes allows for an anode tower readout and for information of the longitudinal development of showers while the individual anode readout permits precision measurement of transverse shower position. The four individual anode planes were located near shower maximum - planes 4,5,6,7 (1 in front) in the stack.

Cathode pads are attached to both sides of the bitubes. The pad pattern is etched onto one side of copper-plated, double-sided FR4 boards ($1.6mm$ thick) and the etched pad side faces the bitube. The pads are held onto the plastic tubes with a combination of double-sided adhesive tape and soldered wires which electrically attach corresponding pads on each side of the bitube to one-another. The back sides of the pad boards act as a ground plane. (Connections to a solid ground on a number of the $16cm \times 48cm$ pad boards are known to be broken on one side of the bitube. This connection is nominally made using copper tape soldered into position but the tape is torn in some places; a fact which was only discovered after installation of most planes. Because the aluminum box is quite near, it is expected that this will result in only a small extra dispersion of pad signals due to capacitive coupling with neighboring pads through the faulty ground plane. Signals are fed through the boards via plated through holes and are transmitted via 100Ω twisted pair cables. No amplification or electronics is provided internal to the aluminum boxes for the pad signals. The size of the cathode-pads is $4cm$ square in the central

$1m \times 1m$ of the calorimeter (a square grid of 576 pads), $8cm$ square in the region $50cm$ wide outside of the central $1m \times 1m$ region (432 pads), and $16cm$ square in the $50cm$ wide strip running around the outside of the acceptance of the calorimeter (180 pads). The pads are aligned from plane to plane in towers and signals from every plane's pads are actively summed externally for each tower so that there is a final total of 1188 pad tower channels which are read-out.

Clearly, dead regions are produced in the calorimeter as a result of profile and bitube walls and wire supports. Overall, about 10% of the total area is dead but only gaps which are large compared to the extent of the core of an electromagnetic shower will produce noticeable inhomogeneities in the response. The worst 'dead areas' occur around the wire supports (which are not very well localized) and at intersections of edges of bitubes (or profiles) in horizontal and vertical planes. These intersection points form a grid of low-gain regions. The worst regions are at bitube intersections where an area of roughly $6mm$ square will be dead. In principle, it should be possible to correct for these regions but in practice it will require very large statistics with careful position measurements using either a calibration beam or actual data in order to determine the size of this effect. At present, no attempt has been made to unfold this effect from the 'average' energy resolution of the calorimeter.

The average thickness of a detector plane is 4.8% of a radiation length. The

thickness of the lead sheets is 95% of a radiation length so that each lead/detector plane iteration is about one radiation length. During operation, the detector planes and sheets of lead are placed as close together as possible in order to maximize density and hence minimize transverse spread of showers. When the planes are all together as close as possible, the total longitudinal depth of the calorimeter is $76cm$ which yields an average longitudinal density of 0.26 radiation lengths per centimeter.

Electronics and Readout systems

There are several major systems of electronics which are associated with the calorimeter. These include the internal and external electronics for summed anodes (high and low gain), internal and external electronics for individual anodes, external electronics for summing pads into towers, trigger logic for producing a fast calorimeter trigger based on summed anode charge, FASTBUS based ADC's for digitizing all signals, readout electronics for the ADC's, CAMAC based control and test-pulsing modules, NIM logic for control of gates and test pulse signals, NIM based high voltage modules and CAMAC based DVM's for monitoring of all voltages (including gas flow, gas gain, high voltage levels as well as power supply voltages) which are used throughout the system.

Amplifier cards for anode signals are plugged into the end of each bitube. A low

input impedance amplifier is provided for the summed signal of all wires within a bitube. The low input impedance is necessary to provide overall proper termination for the signals which travel along the wires in the profiles and are connected to the output sums of the wires via a 50Ω resistor for each wire. The open loop gain of the low impedance amplifier is best described in terms of the output voltage divided by the input current and is $0.4V/mA$ [97](hence it is a transresistance amplifier). In addition to the low impedance amplifier, each bitube card provides a low-noise, high gain FET integrating amplifier for use in calibration using either cosmic rays or halo muons. The output of this amplifier is a shaped pulse with amplitude which is $\sim 1mV/fC$ of input charge. The FET amplifier (with its high input impedance) is always connected to the ganged output of the bitube wires while the low impedance amplifier is only connected when a single pole relay is powered on. When this is the case, the high gain input is effectively shorted out due to the very low input impedance of the other amplifier. Unfortunately, many of the relays failed after a couple of years such that they were stuck closed (low input impedance amplifier connected). This has made the high gain calibration system practically useless but fortunately, the 'normal' data acquisition mode works properly. Signals from both amplifiers are connected to the edge card for the box of that plane via a short length of 100Ω flat cable and then are sent to the external summing and delay electronics via about $5m$ of 50Ω coaxial cable.

In four of the planes, an alteration has been made to the Iarocci tubes to bring signal wires for each of the anode wires out through the endplugs. On these bitubes, special amplifier cards are used which provide a low impedance amplifier for each of the anode wires in the central $1m$ of the calorimeter and for the sum of pairs of adjacent wires in the outer $1m$ sections. These are in addition to the normal pair of amplifiers as described in the preceding paragraph. The outputs from these amplifiers are sent to the external summing and delay cards via 100Ω flat cable.

No internal electronic amplifiers are provided for the cathode pad signals. The pads in each plane are connected to the plane's edge card via pairs (one side grounded) in flat cable. From there more, flat cable transmits the signals to the external summing and delay electronics which will form the sum of corresponding pads from each of the 20 planes to form a pad towers.

The external pad-tower summing cards are located in four crates (sometimes referred to as 'coffins') which are located at each corner of the calorimeter. Each crate contains 37 summing cards, each card capable of producing a summed signal for 8 or 9 pad-towers. Ribbon cables carry signals (single sided with separating ground wires) from pads in each plane to the summing cards. Each crate of sum cards serves the nearest quadrant of the calorimeter. A unity-gain op-amp circuit is employed to provide active summing of the signals. This reduces the total 'pad tower capacitance' so that signal speed will remain as fast as possible (on order

$400ns$ for the complete pulse). Spiradel delays on each output channel provide $400ns$ of delay. Outputs of the sum cards are carried via ribbon cable to ADC's. A complicated mapping of pad tower position to output number exists which calls for careful cabling and decoding of data.

The bottom 'coffin' on each side of the calorimeter also contains 9 cards for receiving signals from the internal anode electronics. Individual anode signals are essentially just sent straight through with delay. Summed anode signals are sent straight through with delay and also are summed to provide anode tower outputs which can be used in constructing a fast trigger based on total energy and/or energy topology in the calorimeter. As for the pads, an active sum is employed which buffers the front end sources from each other. Each anode sum card accepts signals from two bitube towers (20 bitube signals from 10 planes). Individual anode and summed anode signals are transmitted to ADC's via ribbon cables. Fast outputs to trigger logic are via coaxial cable. High gain signals are driven onto a 'high gain tower bus'. This bus provides 10 differential signal lines which are received in a NIM based converter module known as the 'MUX' box. An address bus selects which bitube tower (only one at a time) will drive data onto the output bus. The 'MUX' box provides two sets of single-sided Lemo outputs which are suitable for sending to a LeCroy 2249A ADC and for combining to produce a self trigger for the tower.

With the exception of the anode tower sums, all signals (in normal data acquisition mode) from the external pad and anode sum cards are sent via 100Ω flat cable (one pair per signal) to LeCroy 1885N ADC's [98]. The input to the 1885 is terminated in 50Ωs, so an extra 50Ω precision resistor is included in series with each signal input. The 1885's are operated in 'quasi-differential input' mode which means that at low frequencies, the signal grounds will determine the ground for the front end of the ADC and no ground loop will be formed. The 1885 is a 12-bit dual range ADC with a sensitivity difference of a factor of 8 between the two ranges. This effectively allows 15-bits of sensitivity which permits observation a large range of signals. The low range sensitivity is $50fC$ per count which allows us to (just) observe the Landau peak for single halo or beam muons in a pad tower. The high range sensitivity is $400fC$ per count which will permit observation of showers over $100GeV$ with full linearity. Although the ADC's gains and pedestals are calibrated (along with the rest of the front-end electronics), in practice it was found that for most modules the gain and pedestals were quite stable.

Calibration for the electronics is done for each electronic chain as a unit. For the pads, a CAMAC based programmable pulser provides signals to each of the four pad summing crates. The signals are distributed to each of the sum cards within a crate via a local bus. It is not possible to inject charge directly to the pads (other than real signals in the calorimeter). Capacitance testing was done on all of the

pad channels to ensure that each was connected. A CAMAC based pulser of similar design to that for the pads is provided for charge injection to the high gain anode amplifiers. Charge injection for the low input impedance amplifiers is done using a capacitor on each amplifier card. The capacitor is charged to a voltage which is set by the CAMAC based anode electronics control module and is distributed on a common bus for all planes. Upon a control signal, the capacitor is discharged into the amplifier. Hence, it is possible to describe the gain for the entire electronics chain using two sets (high and low ADC range) of pedestal, slope and width for each channel.

Readout of the ADC's is done using Lecroy 1821 FASTBUS Segment Managers which run special readout microcode and transfer data to LeCroy 1892 memory buffers modules. A brief description of the readout chain is given in section 3.12. Although I spent a large amount of time designing and implementing this system the details are far too extensive to list here. A complete description of the system has been provided in reference [99].

Control and Correction for Global and local Gain

A very important issue in any calorimeter design is controlling and correcting for non-uniformities, both in time and space, of the gain of the device. Two major categories of fluctuation must be addressed; gas gain and electronics gain.

Gas gain is dependent upon a number of different criteria including gas mixture, gas pressure, temperature, high voltage, wire diameter, physical location of wires with respect to cathode surfaces and beam loading effects. Some of these effects can be corrected for in analysis simply by keeping records of fluctuations during data acquisition. However, it is important to minimize effects which can create inhomogeneities in the gain in different planes and across the face of any single plane. Inhomogeneities will produce nonlinearity problems and degradation of energy and position resolution for which it will be impossible (and at best painful) to properly correct in analysis. Still, some inhomogeneities are unavoidable and must be dealt with in analysis as well as can be managed. For instance, as long as temperature changes occur sufficiently slowly that the entire calorimeter essentially always remains negligibly close to thermal equilibrium, then it should be possible to simply apply a global calibration constant for temperature to all of the data with no degradation in resolution or linearity – as long as the temperature is monitored on a time scale which is short compared to the changes and is recorded with sufficient precision and accuracy. On the other hand, temperature gradients are quite another matter. Some gradients will essentially be permanent and correctable. An example is a temperature gradient produced by heat from the internal electronics. It should be possible to make corrections by channel for effects of this sort. On the other hand, gradients created by sun shining on one corner of the calorimeter or

the temperature in the hall suddenly dropping by a few degrees Centigrade would essentially be impossible to correct. Hence, the prudent thing to do is to ensure that such things don't happen. This is the overall spirit of gain control: Do what you can to keep everything constant and where you can't avoid fluctuation, make sure you have a method of correction.

A number of different design features have been included which allow for either keeping gain constant or monitoring changes in gain as they occur. The idea is to limit total fluctuations and inhomogeneities in gain (after correction) to less than about 3% *from all causes*. This is comparable to the intrinsic energy resolution of this construction of calorimeter for a 100 GeV electromagnetic shower. Hence, the design goal was to limit the fluctuations caused by any given source to less than 1%. The two primary sources of changing gains are electronics and gas gain.

Given a fixed mechanical construction, gas gain will be dependent on high voltage, temperature, pressure and gas composition. Dependence on these parameters have been measured by several groups. Mishina has reported several measurements made by Atac [100]. The gain varies with the high voltage according to the equation:

$$\log G = aV + b \tag{3.4}$$

where a and b are constants. Measurements show that a voltage change of $100V$

will result in a gain change of $\sim$ 2.5 which corresponds to a 0.9% change in gain for a $1V$ change in high voltage. Ratios of gains at two temperatures has been measured to be:

$$\frac{G_1}{G_2} = \left(\frac{T_1}{T_2}\right)^{6.7} \tag{3.5}$$

for Argon/Ethane. Hence a $1°C$ change in temperature will result in a 2.3% change in the gas gain. Ratios of gains at two pressures is measured to be:

$$\frac{G_1}{G_2} = \left(\frac{P_1}{P_2}\right)^{-7.7} \tag{3.6}$$

for Argon/Ethane. Hence a 1% change in pressure will result in a 7.7% change in the gas gain. (Mishina observes that the dependence of gain on temperature and pressure are close in magnitude. It is possible that the gain depends only on density. He reported on a sealed module in which gas gain did not change despite temperature and pressure fluctuations.) For a roughly 50/50 Argon/Ethane mixture, it has been measured that a 1% change in the mixture results in an $\sim$ 10% change in the gas gain. Another factor which can effect gain is trace gasses in the mixture such as oxygen (leaks) or various hydrocarbons and chemicals either present in the gas to start with or which are the result of outgassing or chemical recombination of gasses resulting from ionization.

From the above we see that we wish to maintain high voltage to within about 1 Volt. Each of the high voltage modules (10 in all with 20 channels) were calibrated

using the same voltage divider and measuring the voltage with a DVM. Voltages are set via an analog control voltage supplied by a modified BiRa 5408 CAMAC based DAC. The modification consists of changing the normal range of the output to be better tuned to the HK5900 HV units. During running, front panel low voltage outputs (proportional to the HV) are monitored by a CAMAC based DVM system (Joerger ADC-32's with special inputs) in between spills. If the voltage is observed to drift by more than 1 Volt then an adjustment is made via the DAC's.

Temperature is primarily controlled by the Muon Lab air-conditioning system. As long as large doors are kept closed, it has been measured that this system maintains the temperature of the experimental area of the Muon Lab to within about $3°C$ with these changes typically occurring only over long periods of time. If the large delivery door in the building is left open, larger fluctuations can occur. However, a few extra temperature considerations are relevant to the calorimeter. First, the calorimeter has been enclosed in an environmental tent. The tent is needed in order to reduce the relative humidity of the atmosphere around the calorimeter. It was discovered that the electronics feed-through sides of the calorimeter plane boxes are hygroscopic and that large current flows can result in the HV system if the calorimeter is left out in the typical summer-time atmosphere of the Muon Lab (quite frequently exceeding 80% relative humidity). The solution was to build a tent around the calorimeter with a standard 'basement' dehumidifier operating within.

This tent also provides extra thermal insulation from quick changes of temperature within the room but also tends to keep the calorimeter at a higher temperature than the room as a whole. The tent also provides for keeping late afternoon sun from shining on the calorimeter which can happen at just the right times of the year. The result is that the *overall* temperature of the calorimeter appears to be rather rather well insulated from quick fluctuations and indeed is rather stable over long periods of time.

Unfortunately, the calorimeter has some rather significant sources of heat within the planes. All of the internal anode electronics supply considerable amounts of heat. An air circulation system was installed which flows air across the internal electronics cards for cooling purposes and also to possibly prevent the buildup of dangerous concentrations of leaking ethane. The efficacy of this system appears to be limited and it appears that some temperature gradients exist within the calorimeter due to the electronics. Temperature monitors have been installed at a number of strategic locations throughout the calorimeter to attempt to measure these gradients. It is presently unclear how well it will be possible to correct for these temperature gradients. An upgrade for air-conditioning and circulation has been planned for the calorimeter tent to attempt to address this issue.

Pressure of the calorimeter gas is allowed to fluctuate with atmospheric pressure. The outputs of the individual planes are all joined together in a single manifold and

the output of this is connected to the experiment exhaust system via an oil filled bubbler mechanism. The experiment exhaust system has a fan which maintains a negative pressure differential (within the pipe) of -2.0 inches of water compared to atmospheric pressure. The bubbler allows us to maintain a slightly positive pressure differential in the calorimeter bitubes with respect to atmospheric pressure. This was deemed to be necessary to avoid any problems with air leaking into the chambers. After a considerable amount of trial and error we discovered the fine art of building a good bubbler mechanism which will not produce pressure fluctuations due to large bubbles forming at the outlet pipe in the liquid. It is assumed that the entire calorimeter pressure equalizes quickly compared to the rate of fluctuations in atmospheric pressure. Atmospheric pressure was measured using a Microgauge P120 pressure transducer. Drops in pressure across planes due to flow of gas through the serial system and gravity are negligible (as long as gas is free to flow through all of the tubing in the system - which was not the case for one plane during the run).

The gas mixture for the calorimeter was both controlled and monitored. The mixture was produced using a mixing system built by the Research Division at Fermilab. Argon boiling off a dewar was mixed with CP grade ethane using a solenoid controlled system feeding into a $.5m^3$ reservoir at 35 psig. A flow controller for each input is preset for a nominal 50/50 output mixture of argon and ethane. Research

Division experience has shown that the mixing system is capable of maintaining the mixture to within 1% (2% of the argon concentration). Two gas gain monitors were constructed which are capable of measuring the gas gain to within 1%. One gas gain monitor is at the input to the calorimeter while the other is on the output. It was decided that shifts in gas gain due to composition were acceptable as long as the rate of the shift was small compared to a typical calorimeter flushing period (about once per day). It was decided that the nominal performance capability of the mixing system was insufficient to meet this requirement. The solution was to add a very large buffer tank ($\sim 800 ft^3$ at 10 psig) which would dampen any shifts in gas mixture. This tank has a volume which is 20 times that of the calorimeter and hence allows an effective reduction in possible gas mixture fluctuation to less than 0.05%.

Control of the gas mixture as above does not necessarily provide control over trace gasses which can effect gain. The primary sources of such gasses are original contamination of the ethane, leaks in the system, outgassing and (eventually) ionization and recombination of the ethane into other hydrocarbons. Original contamination of the ethane will be damped by the large buffer tank and changes in gain due to this source can be reliably tracked for the entire calorimeter using the gas gain monitor on the input. Effects due to outgassing and leaks can be reduced by maintaining a sufficiently high rate of gas flow through the calorimeter and by

maintaining the calorimeter gas at a positive pressure compared to atmospheric pressure. Ionization effects are also controlled by sufficiently high flow rates. It was decided that a flow rate such that the calorimeter volume would on average be changed once per day was acceptable to eliminate these effects. Unfortunately, it is difficult to control the gain for local problems which may exist in various bitubes within the calorimeter. The bitube high gain readout system was devised to attempt to measure and correct for such problems but electronics problems made this system difficult to use in practice. During the run, a plastic tube carrying the gas to one-half of the bitubes in plane 4 (every other bitube) was pinched off and slowly these bitubes went completely dead presumably from the gas being poisoned by one or more of the above causes. This is proving to be a challenge in analysis of the data. Plane 4 has now been fixed.

3.9.3 Calorimeter Calibration

Calibration of the calorimeter is actually a variety of procedures which are intended to set the absolute energy scale, determine any non-linearities and correct for any variations in shower response both as a function of position and time. Effects such as gains of the amplifiers can be calibrated for by running interspill programs which cause charge to be injected into the electronics and then read out the appropriate channels. Effects such as changes in gain due to pressure can be corrected by making

regular measurements and correcting for the known difference in response during analysis. However, for basic detector response, it is essential to have beam and actual electromagnetic showers with known properties in the calorimeter at some time. Ideally, one would have available a large number of known momentum and position electrons and/or photons illuminating the entire face of the calorimeter throughout the running period. We are forced to settle for less. Many different compromises are possible to the ideal. Because various systematic difficulties are associated with almost each of our calibration options, we have used several different methods in order to cover as much area of the calorimeter as possible and compare results to eliminate systematic errors.

The primary tools which we use for calibration are:

- Interspill test pulsing of electronics.
- 'Empty' events such as beam or halo triggers.
- Interspill monitoring (and later correction) of such variables as temperature, pressure, gain variation due to gas composition and high voltage.
- Special electron calibration beam brought into the Muon Lab.
- Bremsstrahlung and muon-electron scattering events with a tracked scattered muon.

- Position and width of the π^0 peak from DIS events.
- Ionization from halo muons.
- Gain for individual bitubes as determined by running in high gain mode with cosmic rays.

Results for some of the primary calibration techniques are presented in the following section.

3.9.4 Calorimeter Performance

As mentioned above, a number of different checks are useful for determining the functionality of the calorimeter. An ideal test would be a beam of mono-energetic electrons (with several energy tunes possible) which could be used to uniformly illuminate the calorimeter over a short period of time. Although we did some calibration with an electron beam, the quality of the beam was poor and we could only achieve illumination over a small fraction of the area of the calorimeter. Hence, we must rely on an interconnection of a number of different calibration sources.

It should be noted that there were several hardware problems (some of which have already been mentioned) during the 1987-88 running which will effect the resolution and uniformity of response for the calorimeter. I list the most severe problems here:

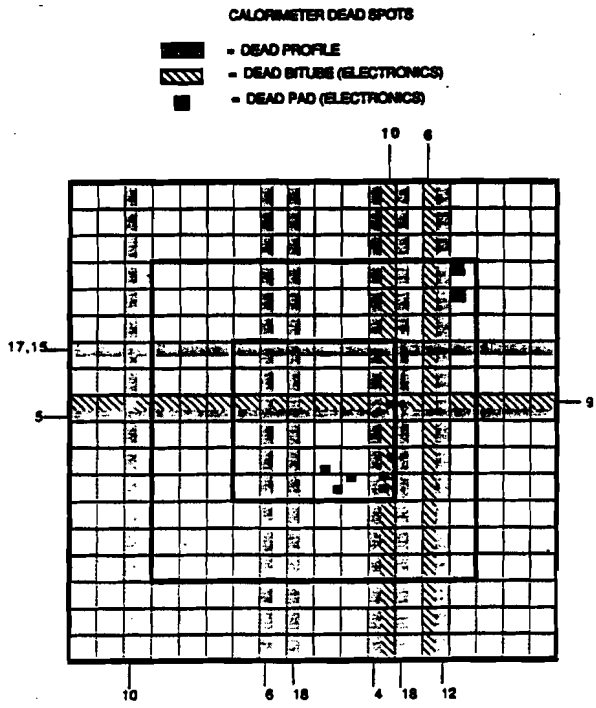

Figure 3.5: Map of dead channels in the calorimeter during the 1987-88 running.

- Several Iarocci tube profiles would not hold high voltage and had to be turned off. These bitubes will produce dead spaces in the calorimeter. In addition to these, every other bitube in plane 4 was gas-gain dead due to the fact that gas flow was cut off during the run as a result of a pinched gas tube. Figure 3.5 shows the positions of dead channels from all effects.

- A few channels of electronics for both bitube and pads were dead. The locations of these are shown in Figure 3.5.

- Bitubes in planes 5 and 7 had very large oscillations on them. These oscillations appeared during the middle of the run. The cause was never completely

clear but it appears to have been related to overburdened power supplies driving the electronics over long cables. The power supplies have been replaced and moved closer to the calorimeter.

- Smaller oscillations exist on most bitubes and pads. In the case of the pads, the oscillations were so small that they are virtually invisible on an oscilloscope. However, because many pads must be summed together to form a single cluster, the sum of the small oscillations (as well as other noise) becomes severe compared to the signal for showers in the few GeV range. It has been demonstrated that replacement of the power supplies and shortening the ADC gates effectively eliminates this source of noise.

- A few ADC channels have 'unstable' pedestal positions which shifted suddenly over a short period of time. In particular, one entire ADC was particularly notorious for shifting its pedestal values over a period of a few hours every few days. Although it is in principle possible to correct for this effect, in practice it is a lot of work and bother.

- High range pedestals for the ADC's were calculated from an intercept using test pulse data. For some channels with large oscillations, it was impossible to get very precise pedestals. Low range pedestals may always be accurately calculated using halo or similar data in which most channels are empty. This

cannot be done for high range however so if the test pulse data is not useable, then it is impossible to get precise pedestal positions. In the future, pedestal positions for high gain will be explicitly measured.

Although the above list appears to be fairly extensive, the reality is that most of the effects are relatively small. Because any given shower is measured by so many different channels, effects tend to wash out and the end result for any given effect is to slightly degrade the energy resolution.

Perhaps a more positive way of looking at the functionality of the calorimeter is to list what *does* work rather than what *doesn't*. More than 98% of the Iarocci tube profiles were functional all of the way through the readout electronics (710 out of 720 profiles). More than 99% of the pad towers were functional (1180 out of 1188 profiles). Furthermore, it is possible to make corrections for dead channels which will largely diminish any deleterious effects. Figure 3.6 shows the measured calorimeter response to actual DIS data for different pad types. (For medium and large pad types, the smaller central pads are summed to form an 'effective' pad of that size.) The response is overall reasonably smooth. Two different shapes are visible in the data. First, there is a rapidly falling distribution which has cylindrical symmetry about the center of the calorimeter. Second, there is energy deposition which runs across the calorimeter in a horizontal band. This is the result of charged

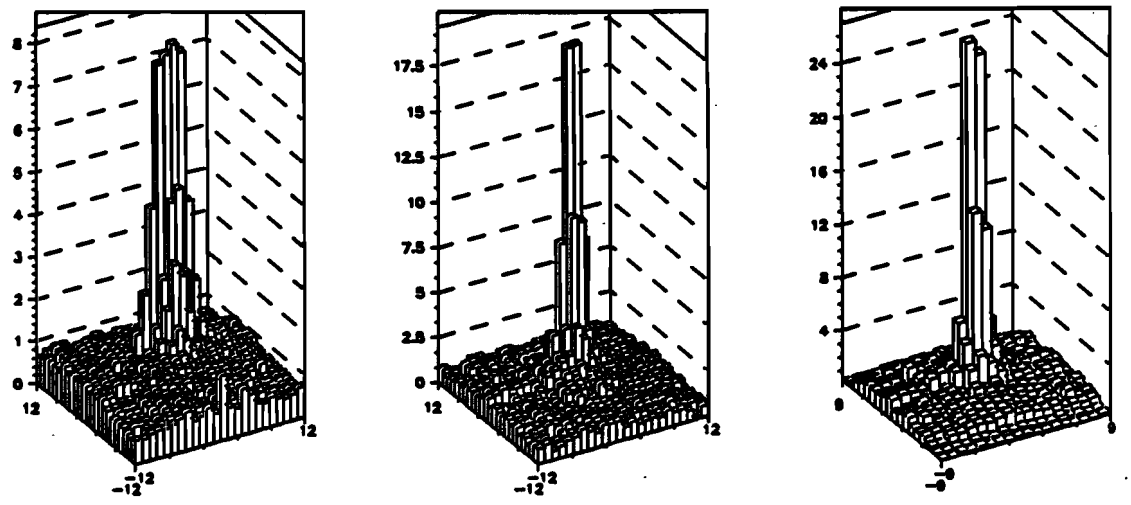

Figure 3.6: Average energy deposition and response in calorimeter pads for deep inelastic data. Vertical scale is arbitrary.

particles which have deposited energy and have been bent by the magnetic field of the CCM. By unfolding the shape for the DIS data it should be possible to use this data to produce a 'bootstrap' calibration for the entire area of the calorimeter. It may be possible to improve the average energy resolution by 5% or more by using this technique.

Since the calorimeter provides a complete energy readout both from cathode pad signals and summed anode signals, a comparison of the energy for the two modes provides a useful check on the calibration of electronics for each branch. Because the 'input' for each event should be identical, then nominally the ratio of the two

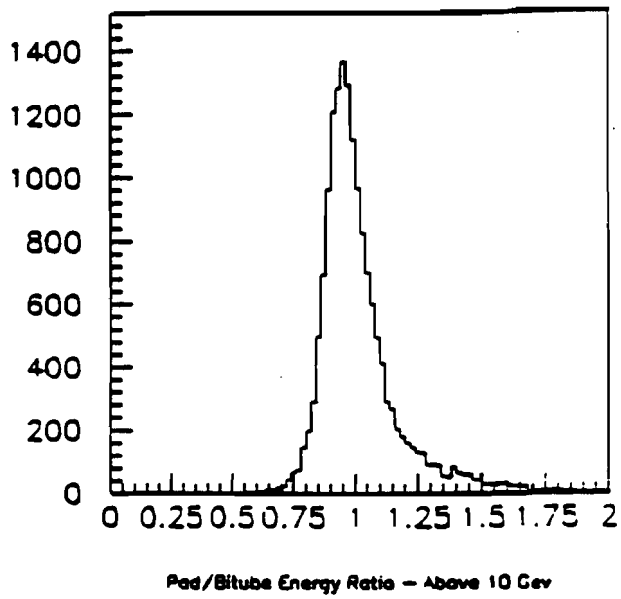

Figure 3.7: Ratio of cathode energy to anode energy for deposited energy greater than $10GeV$.

distributions obtained from many events will ideally be a delta-function at 1. Of course, various electronics difficulties will cause the distribution to have a finite width. Figure 3.7a shows the ratio of pad to bitube energies for electron calibration data with deposited energy in the pads greater than $10GeV$. The width of this distribution can be attributed to a number of problems with electronics. Dead spots caused by regions in which there is no charge multiplication in the bitubes should not contribute to the width of this distribution.

An average longitudinal energy distribution for $15GeV$ electrons is shown in figure 3.8. This distribution is obtained using the bitube signals and one entry is shown for each calorimeter plane. The distribution shown is the average profile for 242 events - a single event will tend to have considerable fluctuations from the

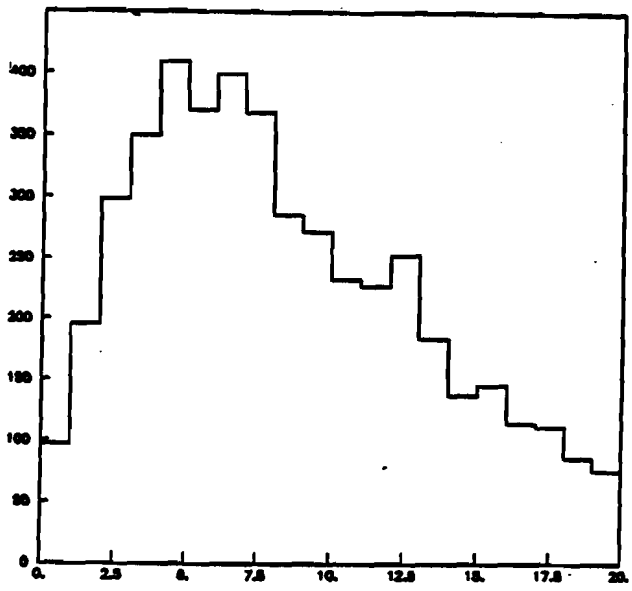

Figure 3.8: Average longitudinal profile for $15GeV$ electrons.

average shape. This distribution comes from a section where all of the bitubes are functioning so that there are no gaps in the profile. As seen in figure 3.5, there will be many areas of the calorimeter than will be missing at least one bitube in the profile. Still, it can be seen that appreciable power exists for making cuts based on the longitudinal development of a shower even if one or two bitubes are missing.

The calorimeter is nominally sensitive to energy depositions less than $1GeV$. Figure 3.9 shows the signal distribution from pad towers in which a halo muon passed through (determined from tracking) compared to a pedestal distribution for pad towers. The muon signal exhibits a clear Landau shaped energy distribution which has the peak clearly displaced from the pedestal position. The peak of the muon signal corresponds to only a few hundred MeV of deposited energy. Because the signal is so near the pedestal, it would be very difficult in practice to use such

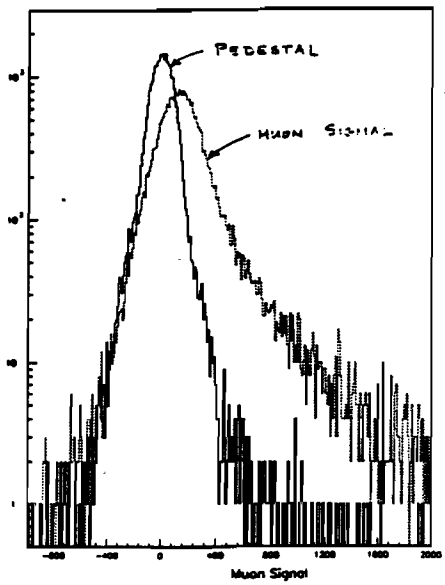

Figure 3.9: Muon signal compared to pedestals for wide halo muons in pad towers.

signals on an event by event basis but averaged over many events they can be utilized to track calorimeter gain. For the 1987-88 running, the halo muon trigger allowed too few halo muons in the exterior regions of the calorimeter for tracking gain but a new trigger should allow this for future running.

Figure 3.10a shows the calorimeter energy response versus the measured track momentum for electrons resulting from $\mu - e$ scattering. The $\mu - e$ scatters are defined from the number of tracks and event kinematics. The sample may include a few pions from DIS which deposit less energy. Figure 3.10 shows the calorimeter energy versus track momentum for charged pions resulting from the reconstructed decay of elastically produced ρ^0s. A very clear difference in energy deposition can be seen but it is also seen that some pions will deposit almost as much energy as an electron. Cuts based on shower shape can be made, in addition to energy ratio,

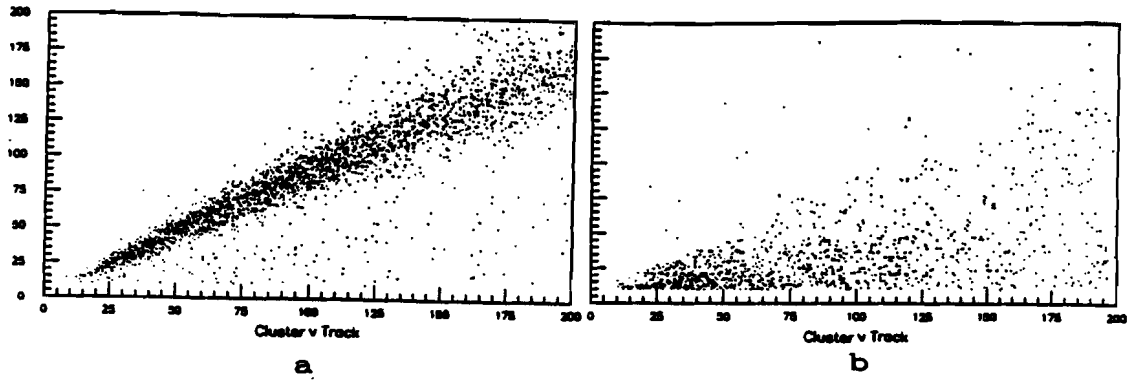

Figure 3.10: Calorimeter energy response versus measured track momentum for a) electrons from $\mu - e$ scattering and b) pions from reconstructed elastic ρ^0 events.

to further distinguish between pions and electrons.

The calorimeter response versus electron momentum (for electrons from $\mu - e$ scattering) is shown in figure 3.11. The response is seen to be quite linear up to about $200GeV$ beyond which space-charge effects and perhaps saturation of amplifiers and/or ADC's cause the response to fall-off. It is expected (and observed) that all photons from DIS lie safely within the linear range. Some account must be taken of the nonlinearity when the calorimeter is used to remove bremsstrahlung events (which is done for many analyses).

The calorimeter energy resolution is shown in figure 3.12 as a function of energy and as a function of $1/\sqrt{E}$. This resolution is obtained using electrons from the calibration beam for the low energies and 'tagged' photons from bremsstrahlung

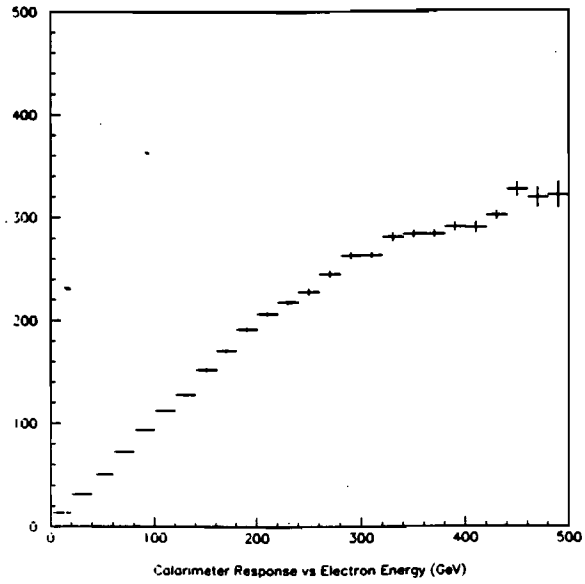

Figure 3.11: Calorimeter energy response versus measured track momentum for electrons from $\mu - e$ scattering.

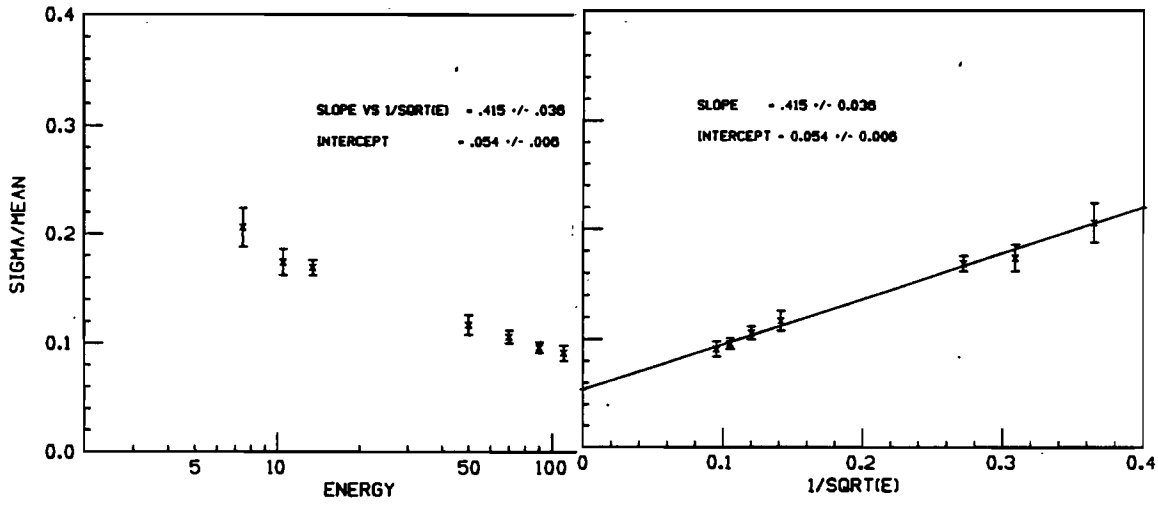

Figure 3.12: Calorimeter energy resolution as a function of energy and as a function of $\frac{1}{\sqrt{E}}$.

events for the high energies. It is seen that a good linear fit is obtained to σ/E versus $1/\sqrt{E}$ such that the calorimeter resolution is:

$$\frac{\sigma_E}{E} = \frac{.42}{\sqrt{E}} + .054. \tag{3.7}$$

The energy independent term is the result of electronic amplifier noise problems and should be reduced in future running. The energy dependent term is larger than the nominally expected $.28/\sqrt{E}$ which has been calculated from Monte Carlo simulation. This is the combined result of many effects including dead channels. Many of these should be improved for future running and it should also be possible to make further improvements in the present data by more extensive gain corrections. The position resolution for showers using pad events with many clusters has been measured to be about $1cm$ [101].

Figure 3.13a shows the invariant mass distribution between calorimeter clusters (assuming that the photon originated from the primary vertex) for a large sample of DIS data from hydrogen and deuterium. Shown on the same plot is 'background' which is produced by combining clusters from different events with similar kinematics for the invariant mass calculation. Figure 3.13b shows the invariant mass spectrum after subtraction of the background. The π^0 peak is obvious in both plots. This provides solid evidence that the calorimeter is functioning sufficiently well to be a useful tool in the data analysis.

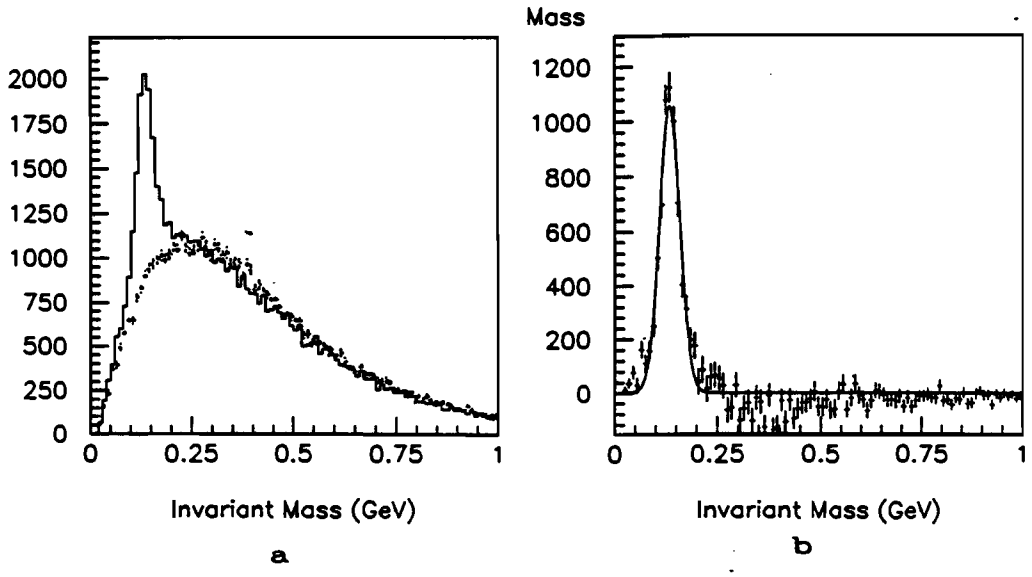

Figure 3.13: Invariant mass distribution between calorimeter clusters for a selected set of data. a) Data shown along with calcuated background. b) Background subtracted distribution.

3.10 Particle Identification Detectors

The particle identification detectors are designed to identify particles over as large a momentum range as possible. The geometrical arrangement of these detectors takes into account both the general correlation between particle momentum and angle (away from the beam) of production and the fact that the CVM will sweep low momentum particles which are produced in the forward direction into larger laboratory angles. Hence, the detectors are arranged with those operating in the lowest momentum region at the highest angles (C0 and TOF) and the higher momentum detectors accepting only more forward particles (C1 and RICH). Figure

3.14 shows the momentum ranges for pion, kaon and proton identification for each of the detectors and for their combined performance.

3.10.1 Time of Flight System (TOF)

The time of flight system consists of two hodoscope walls which are arranged in two 'wings' on each side of the beamline downstream of the CVM (see Fig. 3.1). Each wall has an active area of 4.2 m × 1.6 m and is constructed of 38 scintillator counters. The counters overlap by $\sim$ 10% to avoid dead spots and phototubes are placed at each end of the counters for improved time resolution. The counters vary in width (10cm and 15cm) and thickness (1.5cm, 2cm and 4cm) across the walls with the narrowest and thickest counters closest to the beamline. Valvo Hamburg XP2020, XP2230 and XP2252 phototubes are used.

A very good time resolution hodoscope is placed in the beam upstream of the first spectrometer station. The purpose of this hodoscope is to provide a precise measurement of the incident beam particle time. The hodoscope consists of five scintillators with ten photomultipliers (Valvo Hamburg XP2252) arranged radially. The scintillators were designed so as to measure equal fractions of the incident beam; reducing dead-time in any one counter.

Stability of the TOF detectors is ensured by a laser calibration system. Ultraviolet light pulses (500 ps FWHM) are distributed to each of the counters via a fiber

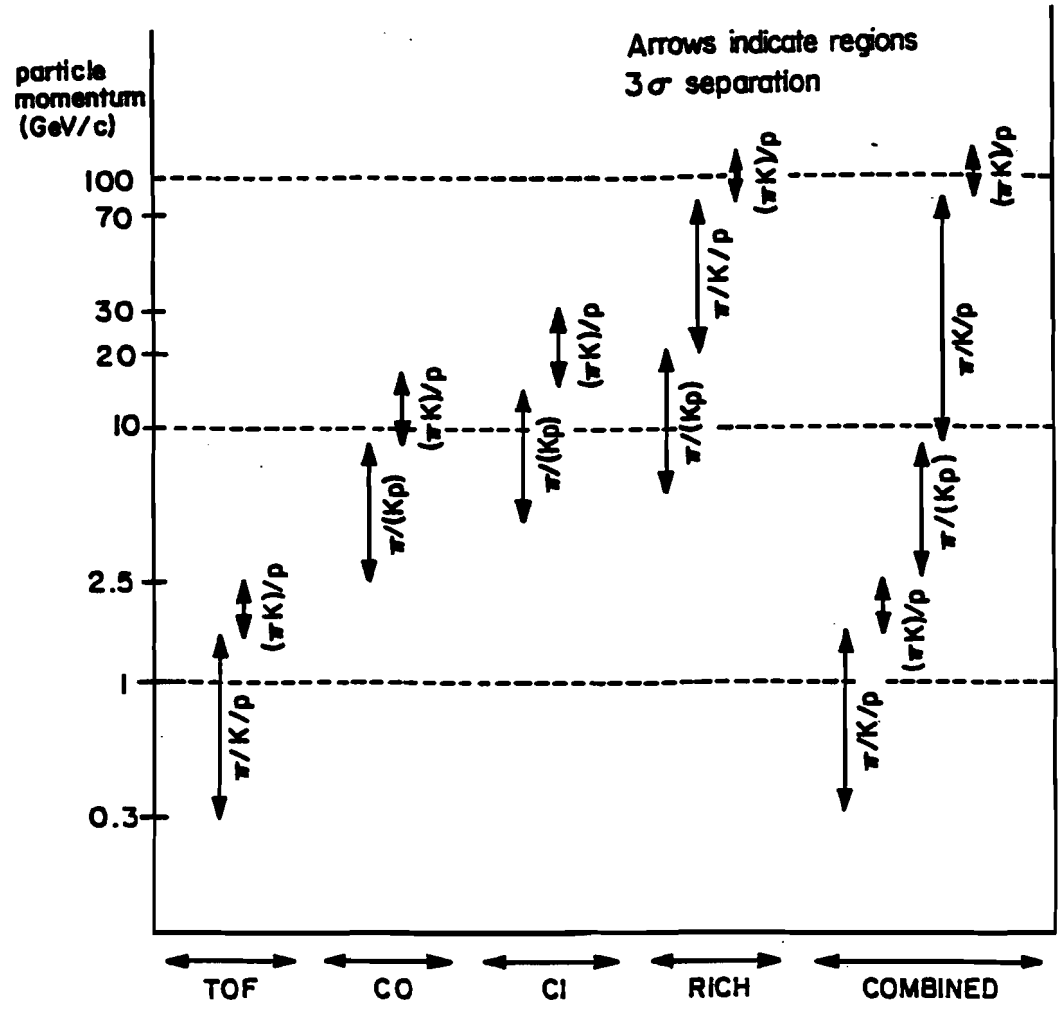

Figure 3.14: Combined momentum ranges for particle identification detectors in E665.

optics system. Light arriving at the scintillators is shifted to the blue by wave-shifter molecules in the scintillator. The intensity of light arriving at a counter can be varied between zero and ten times that produced by a muon passing through the counter. The maximum difference in arrival time of light pulses at the counters is 25 *ps* and is determined by geometrical differences. Counter stability is checked once per hour during data taking. These tests allow correction for 'time-walk' of photomultipliers and other possible systematic effects. Twice per day, a more comprehensive test is performed which includes variation of laser intensity (controlled by reflection off of a piece of chalk before illumination of the individual fiber optics). These tests monitor the stability of pulse-height dependence of the time measurements. A cross check of the laser system is allowed by a variable LED which is also in place on each scintillator. An 'absolute' calibration was performed using a test beam with particles of known momentum impinging on each scintillator.

The TOF system utilizes LeCroy 2228 TDC's and LeCroy 2249A ADC's for readout. High voltage is supplied by LeCroy 4032 modules, which are stable to one volt and contribute only 10*ps* to the time resolution. A VME based microprocessor system continuously monitors the voltages and laser pulse results. If any anomalies are detected, warnings are issued to shift personnel.

3.10.2 Threshold Cerenkov Counter (C0)

The C0 Cerenkov detector is just downstream of PCV and covers essentially the entire aperture of that detector. C0 consists of a radiator with an effective length of $90cm$ and two mirror planes which reflect light above and below the median plane of the detector into 144 Winston-Hinterberger cones. Each cone focuses the Cerenkov light onto a phototube (16 RCA 8854Q and 128 EMI 9829QA). Light from an individual particle may be collected by several phototubes, each of which are sensitive to single photoelectrons. The phototubes are shielded from the CCM and CVM fringe fields by a composite shield built from a Mumetal tube, a soft iron housing and bucking coils. The analog pulses are digitized using LRS2249A ADC's and discriminated with LRS4608Z modules. High voltage is supplied by LRSHV4032 modules. The radiator gas is $C_2Cl_2F_4$ at atmospheric pressure, which has a refractive index of ~ 1.00141. The resulting Cerenkov thresholds for pions, kaons and protons are $2.6GeV/c$, $9.3GeV/c$ and $17.6GeV/c$ respectively. The number of photoelectrons from a $\beta = 1$ particle is approximately fifteen. A subset of the phototubes are equipped with LRS2228 TDC's to record the pulse arrival time.

3.10.3 Threshold Cerenkov Counter (C1)

The threshold Cerenkov counter C1 is located immediately downstream of C0 but with acceptance over a smaller region. The entrance window is $1.09m \times 1.43m$

and the effective radiator length is $\sim 1.5m$. The radiator gas is a mixture of 70% nitrogen and 30% CCl_2F_2 at atmospheric pressure which has a refractive index of 1.00052. The mirror arrangement focuses the Cerenkov light onto 58 phototubes (RCA 3354Q) which have $12.7cm$ diameter photocathodes. The magnetic shielding for the phototubes consists of three mu-metal tubes and a soft iron housing. The phototube pulses are digitized by LRS2249A ADC's and discriminated using LRS623BL discriminators. Arrival time of pulses are recorded using LRS2228 TDC's. High voltage is supplied using LRSHV4032 modules. The number of photoelectrons for a $\beta = 1$ particle is measured to be approximately ten.

3.10.4 Ring Imaging Cerenkov Counter (RICH)

The ring imaging Cerenkov detector (RICH) [102] is designed to permit particle identification up to very high momentum for charged particles which travel completely through the forward spectrometer. The primary components of the RICH are a large radiator vessel, an array of spherical mirrors to focus the radiation onto a smaller area and a wire chamber detector for detection of the reflected photons.

The radiator vessel is a large stainless steel box which is $6m$ along the x-direction and with a front window which is Nm along the y-direction and Mm along the z-direction. The vessel has an inner and an outer skin with a separation of several centimeters. This allows for circulation of nitrogen in the gap which helps to cut

down the amount of oxygen contamination within the radiator volume. (Oxygen is a voracious consumer of ultra-violet photons. A sophisticated radiator gas recirculation system with oxygen scrubbers is also required even with the double skin.) The radiator gas itself consists of an inert gas (e.g. a mixture of argon and helium). The choice of mixture (and hence the index of refraction) depends on a trade-off between number of photons radiated and maximum momentum range of particle identification. For most of the 1987-88 running period, pure argon was used as the radiator which corresponds to an average of $\sim$ 5.4 detected photons per particle and a measured spatial resolution of $2.5 - 3mm$ which is comparable to resolution expected from chromatic aberration. Under these conditions, 3σ π/K separation is possible up to a maximum maximum momentum of $\sim 100GeV/c$.

An array of 33 spherical mirrors at the downstream end of the radiator vessel focuses the radiated photons onto the wire chamber detector. The mirrors are of the same design as those used in the Omega Spectrometer [103] and consist of $70cm$ diameter, hexagonally shaped pieces of glass which are $6mm$ thick. The glass is heat slumped onto a spherical mold of $10m$ radius of curvature then optically ground and polished. Finally, the glass substrate is coated with aluminum and MgF_2 to optimize reflectivity for 1500 Å photons. The mirrors have an average focal length of $485cm$ with a fluctuation as large as $\pm 10cm$ from mirror to mirror. The mirrors are mounted in an array which is $2.7m$ along the z-direction and $3.7m$ along the

y-direction and such that they lie on a common sphere. The entire array points down at an angle of 18.5° with respect to the x-axis to point in the direction of the wire chamber which is mounted in the lower portion of the upstream end of the detector.

The ultraviolet Cerenkov photons enter the wire chamber detector via a $55cm \times 95cm$ array of CaF_2 windows. A stainless steel mesh (which is 80% optically transparent) is mounted on the detector side of the window and held at $-4.0kV$ potential. The gas mixture in the detector consists of 99.3% methane and 0.7% of a photo-ionizing vapor which in this running was triethylamine (TEA). The Cerenkov photons ionize the TEA within a few millimeters, producing a single photo-electron. The electrons then drift through a $50mm$ long drift space between the window mesh and the plane of cathode wires. The drift time is selected so as to be appropriate for the necessary delay to be in time with the trigger.

The cathode wire plane consists of $50\mu m$ copper-beryllium wires with a $500\mu m$ pitch. An anode wire plane is located $3.2mm$ beyond the cathode plane and consists of $20\mu m$ gold plated tungsten wires with a $2mm$ pitch. A plane of cathode pads is located another $3.2mm$ beyond the anode plane and consists of five copper-clad fiberglass boards, each of which have been etched with 2160 rectangular pads (dimensions $3.8mm \times 12.0mm$) and have plated through holes to carry signals through to amplifiers on the other side. Both cathode planes are held at ground while the

anode plane is held at $+3.1kV$ (which results is operation in the proportional mode). In total there are 10800 cathode pads and 480 anode wires, all of which are read-out. It is interesting to note that a minimum ionizing particle will deposit 300 times as much ionization as a single photon and hence, it was important to shield the detector from sources of extra particles. This is effectively accomplished by the several meters of steel in the bottom pole of the CCM.

The read-out of the system is accomplished by a VLSI circuit known as *Microplex* [104]. This system has been developed at SLAC for use with silicon strip detectors. Each Microplex has 128 input channels with an input pitch of $47.5\mu m$. Each chip produces a single multiplexed analog output. In this application, only 48 channels per chip are actively connected and the outputs of 24 different chips are funneled into a single flash ADC for digitizing. A DAC provides a signal for analog pedestal subtraction prior to digitization and suppression of values below a pre-set threshold can be imposed before digitized values are stored in memory. This system is ready for readout in about $300\mu s$.

3.11 Triggers

The primary kinematic criterion which is easily available for use in the trigger apparatus is the difference in direction between the muon going into the target and the muon leaving the target. For deep-inelastic events, this scattering angle (Θ_{scat})

is given by

$$Q^2 = 4EE' \sin^2(\Theta_{scat}/2) \tag{3.8}$$

so that a trigger based on scattering angle accepts events on the basis of a combination of both Q^2 and ν. In practice, an angle cut approximates a Q^2 cut when integrated over the range of ν accepted by the trigger. Clearly, as ν becomes greater, the trigger also becomes more efficient regardless of the value of Q^2. In the 1987-88 running, the triggers based on angle of scatter also made use of the magnet focussing condition (see section 3.6 in order to simplify the triggers. Two different triggers based on scattering angle were implemented. The large angle trigger (LAT) is based on muons which scatter through a sufficiently large angle so as to leave the overall beam phase space. The small angle trigger is based on muons which do not scatter out of the overall phase space but which do scatter through an angle which is sufficiently large so as to be detected as a scatter in the target.

The trigger logic is arranged in two levels. This structure allows trigger decisions to be made on a more sophisticated basis. Level-1 triggers generate the gates and strobes for most of the equipment. Level-1 triggers are based on essential and 'fast-as-possible' components so that signals will not be lost or degraded and delay cables can be kept short for other detectors. Electronics for the trigger is located on top of the absorber steel. A typical amount of time for production of a level-1

trigger after passage of the muon through the absorber is $\sim 220ns$. Wire chamber data and integrated analog signals are available at level-2. If a level-2 trigger does not occur is association with the level-1, the apparatus is cleared without readout. Note that it is not necessary to make any further level-2 requirements upon any given level-1 trigger. Indeed, in the 1987-88 running, extra level-2 requirements were used only for streamer chamber triggers. In future running, PTM information will be included for some triggers. On average, the deadtime incurred as a result of a level-1 trigger without a subsequent level-2 is $2-3\mu s$. Readout of the apparatus takes $2-3ms$. These times limit the level-1 trigger rate to $40k/s$ ($\sim$ 10% deadtime) and the level-2 rate to $80/s$ ($\sim$ 20% deadtime). During the 1987-88 data taking period, the experiment typically operated with 80% livetime.

3.11.1 BEAM Definition

A component in all of the physics triggers used, is a signal that indicates that a muon has entered the target. The definition of a valid beam muon need not be the same for every trigger. The BEAM definition and its associated component in other triggers consists of a hit in all seven of the SBT (beam tagging) hodoscopes in coincidence with a signal phase-locked to the beam RF (PLRF) and with no hit in any of the SVJ (veto jaws) or SVW (veto wall) counters. Three buckets are vetoed by a hit in the veto wall; the bucket preceding the hit in the wall until the bucket

after the hit in the wall are all vetoed. The veto conditions reduce the useful flux by 10%-20%. The phase space of the beam was further limited by removal of a few of the fingers in SBT hodoscopes. This was made necessary by rate considerations in the large angle trigger.

3.11.2 SATBEAM Definition

It is necessary to define a separate valid beam for the small angle trigger. At small scatter angles, the muon may remain within the phase-space of the overall beam. In order to identify such scatters, the incoming muon directions must either be restricted or measured. In this case, the SATBEAM was defined as a subset of the muons which had their incoming direction measured and was useful to the small angle trigger apparatus. This selection was made using signals from the central (highest resolution) portion of the SBT hodoscopes which were routed into an ECL-based look-up table. The table had been pre-loaded with valid *roads* and only scintillator combinations which satisfied those requirements were allowed to be defined as SATBEAM. For some of the 1987-88 data, an additional restriction on the SATBEAM was that no muon be present in the bucket either side of the one which was used.

3.11.3 Large Angle Trigger (LAT)

The large angle trigger (LAT) is a trigger which relies on a muon being scattered with a sufficiently large angular divergence from the overall beam phase space that at the back of the apparatus it emerges from the overall phase space. For this running, this trigger was a combination of hits in the SPM counters with a corresponding valid BEAM signal and a corresponding lack of hit in certain SMS counters. That is to say that the SMS counters act as a veto on this trigger. Unscattered muons should hit the SMS counters and be vetoed. The definition of this trigger was a BEAM signal in coincidence with hits in three out of four planes of the SPM counters and with no hits in any of the SMS-1 (Immediately downstream of the absorber steel) or SMS-4 (Behind the last concrete wall). For muons which start out centered on the SMS array, this corresponds to a $3.3 - 4.7mR$ angle cut; for muon momentum of $500GeV/c$, at $E = E'$ this corresponds to $Q^2 = 2.7 - 5.5GeV^2/c^2$. Figure 3.15a shows the acceptance of the LAT as a function of the kinematic variables.

This trigger produced a typical rate of 2.5×10^{-5} of the muon beam rate. However, only about 10% of those triggers are associated with muons which scattered in the target. The overwhelming background is produced by muons which scatter either in the calorimeter or the absorber steel and other effects such as the

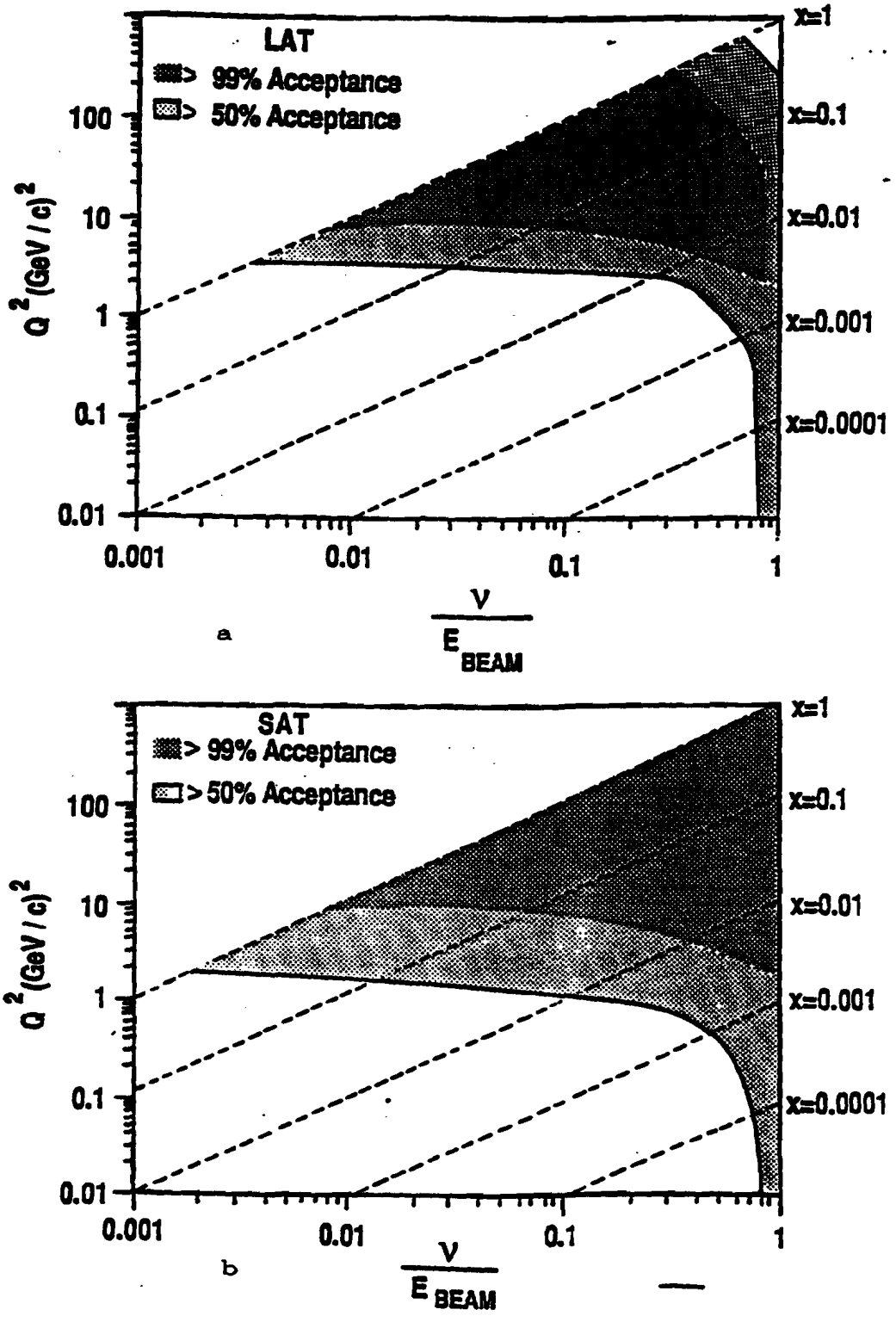

Figure 3.15: Regions of acceptance in kinematic phase-space for a) the large angle trigger (LAT) and b) the small angle trigger (SAT).

off momentum tail of the beam. A future trigger processor is intended to require target-pointing of a scattered muon and hence eliminate this background. For this running, software elimination of this background will be required. An additional concern is that a veto trigger (as opposed to an all-positive trigger) may pose difficulty with normalization as showers accompanying muons will at times cause otherwise valid triggers to be vetoed due to hits in the SMS counters. This problem will behave differently in different kinematic regimes and will have to be modeled by Monte Carlo and comparison of data in overlapping kinematic regions of other triggers.

3.11.4 Small Angle Trigger (SAT)

The small angle trigger (SAT) is designed to trigger on muons which scatter with smaller angles than those detected by the large angle trigger. In particular, SAT is designed to detect scatters for muons which are not scattered outside of the envelope of the overall beam. As described in Section 3.11.2, only a limited fraction of the beam is used for this trigger. Only those muons which point towards the center of the SMS counters are selected as beam triggers. For each of these muons, a projected impact position on the SMS counters is calculated from hits in the SBT counters. A veto region which is a minimum of three SMS counters wide, around the calculated impact counters, is then defined so that if any of the SMS counters in this

road are hit, there will be no small angle trigger produced. An ECL-based hardware look-up table is used in calculation of projected SMS hits which is sufficiently fast to allow for muons in adjacent RF buckets. The effective angle of scatter cut imposed by this trigger is $\sim 1mR$ and corresponds to high efficiency of triggering down to $Q^2 = .5(GeV/c)^2$ with $500GeV$ incident muons. Of course, this trigger suffers from the same problem of potential *suicide* events as other veto based triggers such as LAT. Figure 3.15 shows the acceptance of the SAT trigger as a function of the kinematic variables.

3.11.5 Normalization Triggers (RBEAM and SATRBEAM)

For absolute normalization of cross sections, it is essential to have a measurement of the amount of beam which has been used in producing any given set of events produced from a particular trigger. Because of the very high rates of beam, it is difficult just to be able to count at that rate, let alone readout the apparatus to check for validity of any given beam. One method of measuring the amount of beam is referred to as the *random beam* method [105]. The procedure is to randomly select RF buckets and in those buckets check for a valid beam signal. If a valid beam signal is found, the apparatus is triggered and readout. Note that each beam definition used in the experiment must have its own associated random trigger. Hence, in this running, we had two random triggers; one associated with

the BEAM signal and titled RBEAM and one associated with the SATBEAM signal and titled SATRBEAM. The random selection of buckets is accomplished using an electronic random number generator [106] which is synchronized to the RF. The rate of acquisition of random beam triggers is controlled by prescaling. We typically recorded random events at a rate of about 10% of the associated physics triggers. Note that the true beauty of this method of normalization is that the final *count* of beam used is determined after reconstruction (or the attempt thereof) of the events offline. Hence, any inefficiencies in beam reconstruction caused by the analysis chain or detector inefficiencies will be treated identically for both the set of physics triggers and the normalization triggers!

3.11.6 Electromagnetic Energy Trigger (FCAL)

Fast signals from the summed anodes of the electromagnetic calorimeter can be used to form a trigger based on the total electromagnetic energy in an event. Clearly, this trigger suffers from systematic bias which is inherent in any trigger which relies on the final state hadrons or some fraction thereof. Still, it is hoped that the biases can be modeled and understood sufficiently well that this trigger can act as a *check* on the other physics triggers (where there is kinematic overlap) and can extend the triggering capacity of the experiment to kinematic regions not covered by the other physics triggers. As explained in Sections 3.11.3 and 3.11.4, the veto based triggers

which are the *main* triggers for the experiment will certainly suffer from systematic effects which will have to be corrected for. Any independent trigger which overlaps those triggers should be useful in understanding those systematics.

The FCAL trigger is produced by producing a total energy sum of all of the summed anode bitubes in the calorimeter. The very central bitubes are left out of the trigger due to a high rate of brehmstrahlung and $\mu - e$ scatters (mostly within the calorimeter itself!) which will deposit appreciable energy in the central portion of the calorimeter. Hence, a cross which is $32cm$ wide and centered on the calorimeter is excluded from the energy sum. Hence, the true requirement is dependent on at least some energy deposition which is significantly transverse to the average muon beam direction. The sum of anodes is discriminated and a coincidence is formed with the RF and a fraction of the BEAM signal (prescaled). For this running, the typical energy threshold was $\sim 60GeV$.

3.11.7 Halo Muon Trigger (HALO)

The halo muon trigger (HALO) is designed to provide a trigger when a halo muon passes through the apparatus (surprise!). This is useful for various calibration and alignment purposes. The trigger is produced by a coincidence between an or of all veto counters (SVJ and SVW) and a hit in any three out of the four SPM planes and in time with the phase-locked RF (PLRF). These triggers therefore provide

muons which traverse the entire apparatus with the exception of the central beam region. This region can be covered by beam triggers. This trigger is prescaled during normal data acquisition so that it typically accounts for around 5% of the total trigger rate. Future HALO triggers will likely incorporate separate prescaling for the veto jaws area and veto wall area to provide more balanced rates in these areas.

3.11.8 Streamer Chamber Triggers (PCNLAT,PS(PCNLAT,SAT,LAT))

As mentioned in Section 3.7.1, the maximum rate at which the streamer chamber can operate is $\sim 1.5Hz$. Because the electronic apparatus can take data at a rate approaching $100Hz$ and because neither the LAT or SAT triggers had rates sufficiently low, a special set of highly selective triggers were required for the streamer chamber. The method which was used in this running to enhance the likelihood that a streamer chamber event would be caused by a 'real' scatter in the target was to produce a coincidence between a PCN multiplicity requirement and either the LAT or SAT triggers.

Three of the PCN z planes were selected and fed into a multiplicity unit which was used to select events which had at least two wires hit in three planes. The central $19.2cm$ of each plane was excluded, so that this requirement nominally might correspond to $\frac{2}{3}$ of a track which is likely not associated with just beam passage

through PCN. A coincidence was required between this signal and either SAT or LAT in the level 2 trigger. Approximately 20-40% of the PCNLAT triggers contain target activity according to scans of streamer chamber photographs. Monte Carlo studies indicate that the PCNLAT trigger has little bias for events with $\nu > 40GeV$ and $Q^2 > 10GeV^2/c^2$. The PCNSAT was prescaled to achieve a sufficiently low rate. In addition to these two triggers, a prescaled version of LAT and SAT were also made in coincidence with LAT and SAT at level 2 in order to provide a handle for understanding the biases associated with having PCN multiplicity included in the trigger.

3.12 Data Acquisition and Monitoring System

A schematic of the data acquisition and monitoring system is shown in Figure 3.16 [107]. The basic components are three 'front end' computers (PDP 11/40's) a 'front end' FASTBUS data acquisition system, a microVAX computer and a VAX 11/780 computer. During the 20 second spill, data is collected at a relatively high rate on the front end machines and stored in memory buffers to be read out asynchronously and at a more leisurely pace throughout both the spill and interspill period. This keeps the relatively slow process of concatenating events and writing to tape from immediately effecting the per trigger dead time of the experiment. Events are read into the microVAX where they are concatenated and written to

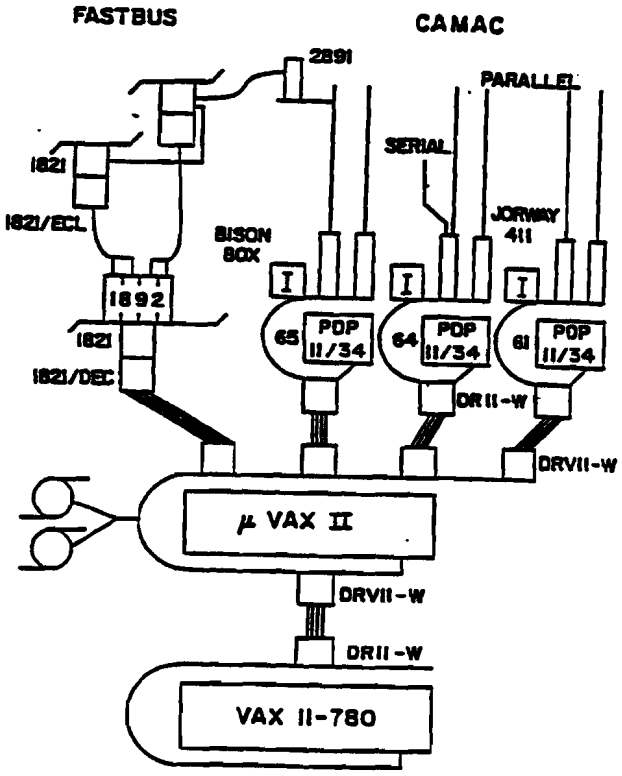

Figure 3.16: Schematic of the E665 data acquisition system.

tape. Concatenation consists of combining the sub-events from each of the front-end systems into a single event prior to writing it to tape. A modest fraction of events (typically 2%-25%) is sent to the VAX 11/780 to be used by monitoring programs to aid in determining the health of the apparatus and validity of the data.

The front end PDP's use an interrupt driven data acquisition system developed by the Fermilab Computing Department [108,109]. Two different interrupt signals are used. The first signal (the A interrupt) is sent a couple of seconds prior to the beginning of the spill and instructs the computer to perform various tasks in preparation for the spill. The second signal (the B interrupt) comes from level

2 experiment triggers. When a B interrupt is received, the PDP's execute code to read in the data from CAMAC via two Jorway JY411 branch drivers on each PDP. The actual readout instructions are written in MACRO to minimize the time required for completion of readout. The readout dead time is determined by the slowest PDP and for this run was typically $2 - 3ms$. Data is written directly to bulk memories on each machine to maximize speed. A data logging task running at lower priority than the acquisition task continuously reads out events from the memories and sends them across a CD link to the microVAX. Deadtime due to readout time is typically 10-20%.

During the interspill period, the PDP's are used to run various monitoring tasks. Some of the monitoring tasks on the PDP's are self contained and send messages if problems are discovered or send results of calculations (on pedestals or gains for instance) into the data stream to be recorded as 'interspill events' on tape. Other PDP monitoring tasks simply acquire raw data to be sent via interspill events to be written to tape and to the VAX 11/780 for further processing. Both CPU time limitations and memory restrictions make it impossible to use the PDP's for all monitoring calculations.

The FASTBUS data acquisition system is used for readout of the electromagnetic calorimeter [99]. The large number of ADC channels for the calorimeter required a faster readout system than would have been allowed via CAMAC read

out directly into the PDP's ($3\mu s$/16-bit word + overhead). The adopted solution is an entirely FASTBUS based system, similar in function to the front end PDP's for data acquisition. Figure 3.17 is a schematic of the FASTBUS readout system. It consists of two crates with LeCroy 1885N ADC's. Each of these crates contains a LeCroy 1821 Segment Manager/Interface. When a level 2 trigger is generated, each of the 1821's execute microcode to read out the ADC's at the rate of one word every $420ns$. This corresponds to a total readout dead time of $1.5ms$ (includes $750ns$ digitization time). The data is written into LeCroy 1892 4MB memories which are in a third FASTBUS crate in the computer room. The 'data logging task' is performed by an 1821 in this crate which reads events out of the memories asynchronously with triggers. This 1821 is under direct control of the microVAX. Although the primitive architecture of the 1821's allows considerable speed in data acquisition, it does not allow for any sort of monitoring function. Hence, monitoring of calorimeter channels is done on a PDP using indirect readout of FASTBUS via CAMAC during the interspill period.

The microVAX and VAX make use of the VMS based VAXONLINE software developed by the Fermilab Computing Department [110]. The system is comprised of several tasks running in parallel. The 'Event Builder' collects pieces of events from the front end machines and concatenates them together into a single event; making use of a hardware event number which is distributed at trigger time to each

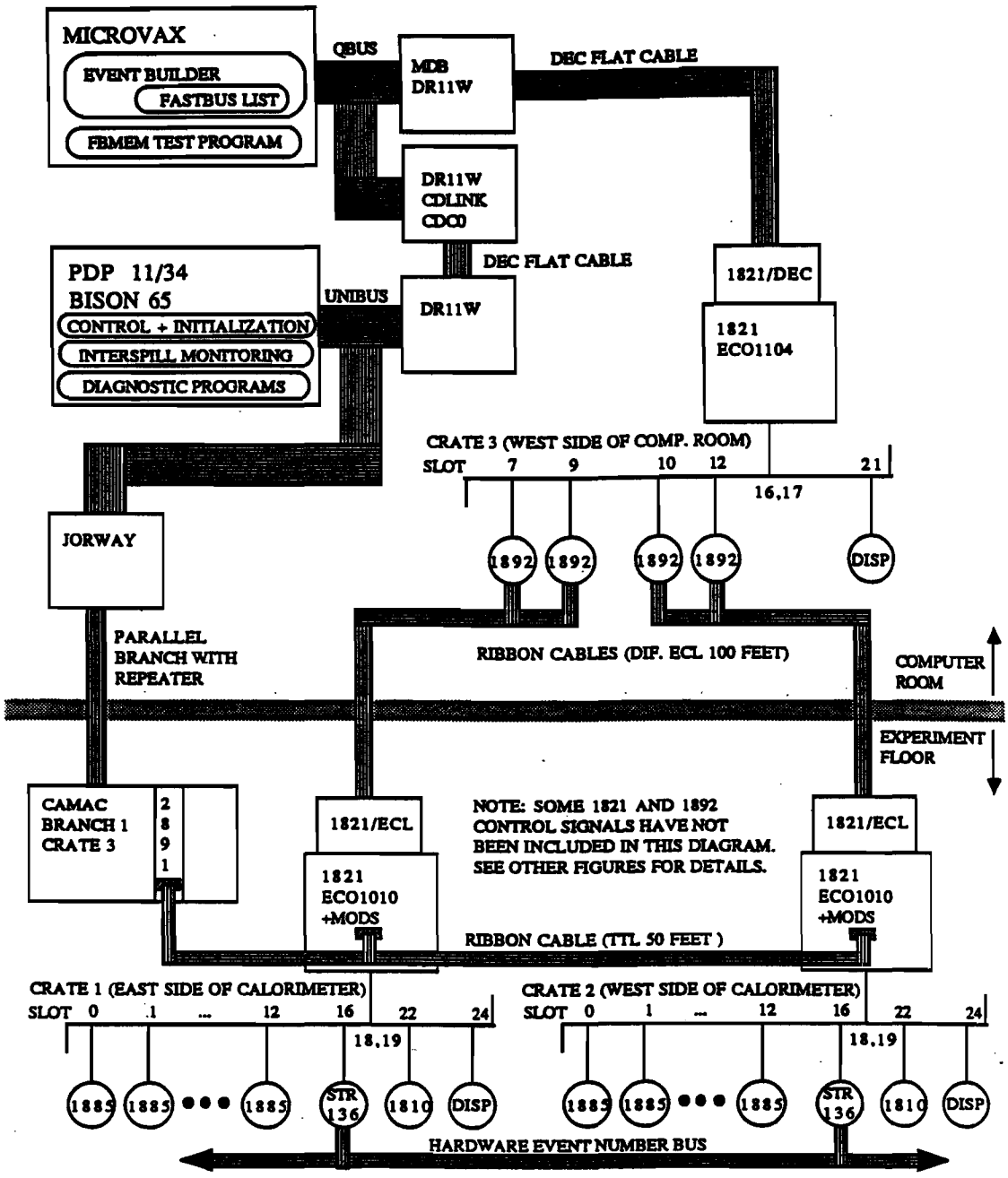

Figure 3.17: Schematic of the FASTBUS portion of the data acquisition system.

of the front ends. These events are then dumped into an 'Event Pool' to be used by 'Consumer' tasks in various ways. Consumer tasks are simply programs which request events from the event pool and then perform any number of manipulations or transfers on those events. Consumers can be tuned to accept only certain types or fractions of events or all events.Two consumers run on the microVAX. The first task is the tape logger which writes all events to tape. The other task is called the 'buffer manager' and is used to send a portion of the events to the VAX for online analysis. The number of events which are sent to the VAX is limited by CPU time on the microVAX and typically was around 5-25 percent of all data (depending on incoming data rate).

The primary tools for determining the health of the experimental apparatus while collecting data reside on the VAX. Here, events from the microVAX (both spill and interspill) are used by a variety of programs to attempt to keep track of changes in detectors or the beam. An Event Builder on the VAX receives events from the microVAX and deposits them in an event pool in the same manner as events are treated on the microVAX. A consumer program exists for each detector subsystem. In addition, there are a couple of more general consumers which keep track of overall features of the data such as scaler information, beam tune, event length, etc. These programs collect events from the event pool and after manipulation produce warning messages and/or sets of histograms. The warning messages are immediately sent

to one of several screens which are monitored by shift personnel. The histogram sets are printed out every several hours and reviewed by shift personnel and by detector experts on a daily basis. Depending on the nature of a problem, most changes or failures in the hardware are then detected within minutes to a few hours of occurrence. It should be noted that a few hours can be a costly amount of time to lose. The dominant limitation on this time is CPU power on the VAX for running the various monitoring programs. Future upgrades plan on increasing the CPU power available for these tasks.

Chapter 4

Event Reconstruction Chain and Monte Carlo

4.1 Reconstruction Overview

Event reconstruction consists of several passes over the data to arrive at data summary tapes with pattern recognized and track fitted events. Approximately 3000 data tapes were written in the first run with a maximum of about 15000 events per tape. The breakdown of data with different main trigger types is shown in table 4.1. Only the last one-third of the deuterium data (when all of the relevant detectors were fully functional) has been used for this analysis. In order to facilitate analysis, raw data tapes were run through a 'split' program to separate events by trigger type onto different tapes. At the time of the split, only data which was clearly not useful for later analysis was excluded (for instance data taken where magnets were in an ill-defined state). No attempts at filtering out background events were made during the split.

Target and Trigger	Number of Triggers
H_2 LAT	2.8×10^6
H_2 LAT SC	0.1×10^6
H_2 SAT	2.4×10^6
D_2 LAT	4.8×10^6
D_2 LAT SC	0.2×10^6
D_2 SAT	3.3×10^6
Xe LAT	3.3×10^6
Xe SAT	2.7×10^6
Xe LAT SC	0.1×10^6

Table 4.1: Number of triggers for different targets (all at $490 GeV$ beam momentum).

The next step in the analysis was to filter the physics trigger data. The physics triggers used in the first run were 'preliminary' and were not completely efficient in triggering only on desired events. At most, about 10% of the events of a given physics trigger which were written to tape were actually due to deep-inelastic scattering in the target. The rest were the result of multiple beams, electromagnetic events in the target and elsewhere, scattering in the absorber steel and calorimeter and so on. Because of scarce CPU time and difficulty in handling large numbers of tapes it was desirable to run an offline filter on the data to eliminate most of the background events prior to attempting full scale event reconstruction. Filters were run on the LAT and SAT data independently. The idea of each filter was to implement a minimal subset of full reconstruction which would allow a determination of whether or not an event was associated with a scatter in the target. If an event could clearly be shown to be due to a muon which did not have an interaction in the target then it was rejected at this point. After filtering, approximately one-third of the LAT events written to tape remain.

Next, data sets were run through an event reconstruction program (known as PTMV). First, the beam track is reconstructed and checked for validity. Following this, a first pass is made through pattern recognition to attempt to reconstruct the scattered muon both through the forward spectrometer and downstream of the absorber steel. Next, a pass is made through pattern recognition to look for other

tracks from charged particles in the event. (Some tracks other than that from the scattered muon may be found in the first pass and vice-versa.) Next, track fitting is done on all reconstructed tracks in an event. Using information from track fitting, tracks from the forward spectrometer are checked for matches with track segments downstream of the absorber steel. Typically only one track will match with a downstream segment and this is then defined to be the scattered muon. Finally, the beam and scattered muon tracks and other fitted tracks are used to reconstruct the primary interaction vertex. Kinematics for the event are calculated using the beam track, scattered muon track and the vertex position. The processors for each of the above tasks are described in more detail in the following sections.

4.2 Pattern Recognition

The task of the E665 pattern recognition program is to take hits from the different sets of wire chambers and reconstruct tracks for the charged particles which produced the hits. Of particular concern to this analysis are the chambers which comprise the forward spectrometer, PC, PCF, DC and PSA. In addition to these chambers, the vertex chamber PCV is useful for helping to constrain the momentum of the tracks and provides improved vertex pointing and determination.

The pattern recognition program is divided into four phases – beam reconstruction, muon projection reconstruction (behind the absorber steel), forward spec-

trometer scattered muon reconstruction, and forward spectrometer reconstruction of all remaining charged tracks.

The beam reconstruction phase uses information from the PBT chambers to reconstruct the beam track. Once the track is reconstructed, correlations between the found tracks and SBT hits are checked to determine which (if any) tracks are in-time.

The muon projection phase makes use of information from the PTM and SMS counters to form projections in y and z. No attempt is made at resolving $y - z$ ambiguities for events in which multiple projections are found. The projections will be lined up with forward spectrometer tracks later on.

Reconstruction of forward spectrometer tracks is done in two stages (so-called *Muon* and *Hadron* phases. The two phases are essentially the same except that the muon phase has stricter tolerances and is particularly concerned with finding candidates for the scattered muon. This is not to say that hadrons cannot be found in the muon phase and vice versa. Splitting the procedure into two parts allows for abandoning further reconstruction if no scattered muon candidate is found and also may assist in reducing ambiguities in identifying the scattered muon. Of course, the muon phase does not attempt to make use of very wide angle chambers such as PTA.

The forward spectrometer reconstruction program consists of a number of dif-

ferent processors. Each processor is designed to either find track segments within a particular detector, combine segments from different detectors or add additional hits to a track using segments from other detectors. The algorithm which is followed in the two phases (with different parameters) is:

a. Find DC space tracks.

b. Find PC space tracks.

c. Link the PC and DC space tracks together, using hits in the PCF's.

d. Find PSA,PSB space points.

e. Follow any unlinked PC tracks through the PCF's, DC's and PSA/PSB's, looking for tracks not found in c. These tracks include small angle scattered muons, low momentum hadrons swept out of the CCM and hadrons that go through the dead regions of the DC's.

f. Find tracks in the PCF chambers using leftover hits.

g. Link the PCF tracks to hits in the PC, DC and PSA chambers.

h. Find PCV track segments.

i. Find PTA space points.

j. Link the PCV track segments to tracks in the PC's. (Note that this is also done after track fitting. Indeed, if an individual track fit is bad the PCV portion will frequently be thrown out.

k. Link outer PCV track segments with PTA space points (not used for this analysis).

Some attempt has been made to reconstruct line segments in the vertex region. However, unless a streamer chamber picture is available, such tracks will rely on being constrained to pass through the primary vertex in order to determine the momentum. Of course, streamer chamber pictures will allow for full reconstruction of these tracks as well as others which will be seen in no other detector. No use of vertex track segments or streamer chamber tracks is made in this analysis.

It is worth commenting that many of the above processors rely heavily on the non-bend view for connecting track segments and points. Tracks can tend to be quite close together in this view in the PC and PCF chambers and this will result in some extra inefficiencies in reconstruction, particularly at large multiplicities. Another difficulty which was encountered and has yet to be properly solved is that tracks which are near the pole tips of the CCM experience a ***kink*** due to the fact that there are non-negligible components of the magnetic field which are not purely in the z direction. Yet another area of difficulty for the pattern recognition is in

the dead region of the drift chambers. Although nominally covered by PSA in the back set of chambers, no equivalent small angle chambers presently exist for the front set of drift chambers. This allows some particles bending at large angles through the CCM to go through this dead region without impinging on the back set of chambers. Hence, for these tracks there will be no chance of any downstream lever arm on the track measurement. There may be similar but more subtle cases near the edges of the PSA and DC dead spaces in the second set of drift chambers. Reconstruction efficiency for Monte Carlo events is discussed in section 4.8.

4.3 Track Fitting

The job of track fitting is nominally a simple one – take tracks from pattern recognition and determine the momentum (actually the momentum/charge ratio!) by virtue of each track's curvature through magnetic fields. In addition to the momentum, the related error matrices are calculated and the goodness of the fit is determined using a χ^2 test. The number of degrees of freedom after the fit is accomplished is also reported. The fit is accomplished using a SPLINE fitting technique.

As it turns out, the track fitting algorithm has effectively taken on a bit of pattern recognition flavor as well. This came about from studying the χ^2-probability for tracks. It was found that a large number of Monte Carlo tracks were being

reconstructed but with very low χ^2-probability. It was further found that in many cases, the bad χ^2-probability was caused by one or just a few hits on the track. In some cases, forward spectrometer tracks would be matched to inappropriate or ghost track segments from the PCV. Because the χ^2-probability is an important tool in elimination of ghost tracks, it is necessary to make a cut on this variable for tracks to be included in the sample for analysis. Hence, a *rescue* algorithm was implemented which attempts to save tracks which will otherwise be discarded due to low χ^2-probability.

The rescue algorithm first iterates over all points on the track to find the single point which is most responsible for the poor χ^2. This point is then eliminated from the track and the track is refitted. If the new track passes the particular χ^2 test then the track is kept and the rescue algorithm terminated. The algorithm will continue throwing points off of the track until either there are no degrees of freedom left or a maximum number of bad points have been removed (typically 6). In addition to a check on individual bad points, the algorithm also checks for the case that an entire segment from a particular detector (especially PCV) appears to be bad. If PCV is found to be the cause of poor χ^2 then it is eliminated from the track. The cost is momentum resolution but the gain is that the track will be kept. Usually, something is better than nothing. Tracks which are rescued tend to have a nearly flat χ^2-probability distribution and generally look very much like other *good*

tracks. According to the Monte Carlo, essentially no disproportionate number of ghosts are added due to the rescue procedure.

4.4 Muon Match

The function of the muon match program is to take muon projections from the SMS and PTM detectors and link them with fitted tracks from the forward spectrometer. In order to do this, forward spectrometer tracks are extrapolated to a point at the downstream side of the absorber steel. The position and slope of the track at the back of the steel has extra errors which come from multiple scattering in the calorimeter lead and absorber steel. The extrapolated position and slope are compared with the position and slope of y and z projections in the SMS and PTM detectors. If a forward spectrometer track matches both a y and z projection within allowed errors, then it is declared to be a muon. Note that the errors will be dependent on the calculated multiple scattering which will be dependent on the track momentum. If more than one forward spectrometer track matches the same pair of y and z projections, then only the 'best' match is declared to be a muon.

The match program offers an additional option which is to link tracks with projections where the track/projection intersection occurs in the calorimeter or absorber steel. For this, extrapolation of the projections is made, taking multiple scattering into account as before, to the nearest point to intersection with tracks in

the calorimeter and steel. If the tracks are sufficiently close in space at the nearest point of approach, the forward spectrometer track is declared to be a muon which has suffered a hard scatter.

If more than one muon is found in an event, it is left to the vertex processor to determine which of the muons was the original scattered muon. This is done by checking which muon is most consistent with a vertex with the beam and if all stands essentially equal, the highest energy muon is taken as the scattered muon.

4.5 Vertex Finding

The task of the vertex finding program is to find and fit vertices between charged particles wherever they may occur in the spectrometer. A vertex is defined to be the point of closest approach for a set of tracks. Tracks are not forced to go through a common point in order to define a vertex. A very important subset of the vertex tasks is to find the primary vertex (defined to be *the* vertex to which both the beam and scattered muon tracks are fitted) and calculate the kinematic quantities for the muon scatter.

The program first determines the primary vertex using only the beam and scattered muon tracks. If there is more than one candidate scattered muon, it will accept the muon which has the highest momentum. Whether or not a vertex will be declared is determined by cutting on the ratio of the distance of closest approach

of the two tracks divided by the error on that distance which is expected given the calculated errors from track fitting. This *primary vertex* will be recalculated using all of the known charged tracks in the event. Although this does not appreciably improve the y or z position of the vertex, it can have a substantial effect on the x position. Note that only tracks which have distance/error ratio less than 4.0 are used in improving the vertex position.

In addition to finding and fitting the primary vertex, the vertex processor also looks for vertices which result from charged particle reinteractions or scattering and vertices which result from decay of hadrons or conversion of photons to an e^+e^- pair. For this analysis, no use is made of particles which arise from secondary vertices except for those charged tracks which are used to *eliminate* energy clusters from the calorimeter. These tracks act only as vetoes and are not actually included with other tracks for analysis.

4.6 Event Selection

In order to eliminate possible systematic difficulties, a number of 'quality' cuts have been imposed on events which have been reconstructed. Note that some of these cuts were made in the filter program while others have been made after full reconstruction. Some of the quality cuts are based on kinematic variables. The quality cuts are:

1. The event must have a primary vertex containing both the beam muon and a reconstructed scattered muon. In order to be declared as a 'legitimate' vertex, the χ^2 probability of the vertex must be greater than 10^{-3}.

2. The primary vertex is constrained to lie within the target vessel to within loose limits. The position cuts are $-13m < x_{\text{vertex}} < -10m$, $-10cm < y_{\text{vertex}} < 10cm$ and $-10cm < z_{\text{vertex}} < 10cm$.

3. The event should have full information from all relevant detectors.

4. Cuts are made to remove bremsstrahlung and $\mu - e$ scattering from the event sample. Although many of these events are removed by the kinematic cuts which follow, there are still a number which remain within 'interesting' kinematic bounds. The cuts to remove these electromagnetic events are based on calorimeter energy and topology. Events will be cut if:

$$\frac{E_{cal}}{\nu} > 0.60 \qquad \text{and} \qquad N_{clusters} < 3 \tag{4.1}$$

or

$$\frac{E_{cal}}{\nu} > 0.80 \tag{4.2}$$

or

$$E_{cal} > 230GeV \qquad \text{and} \qquad N_{clusters} < 3 \tag{4.3}$$

Where E_{cal} is the energy in the calorimeter and $N_{clusters}$ is the number of clusters with energy greater than $2GeV$.

5. The following general kinematic cuts are made:

$$50 < \nu < 1000GeV. \tag{4.4}$$

$$0.01 < y_{Bj} < 0.85 \tag{4.5}$$

$$0.003 < x_{Bj} < 1.0 \tag{4.6}$$

$$3.0 < Q^2 < 10000GeV^2. \tag{4.7}$$

6. For physics purposes, much of the data shown in this thesis will have a $W > 20GeV$ cut applied in addition to the above cuts.

The kinematic cuts tend to overlap one another in functionality. Lower limits on x_{Bj} and Q^2 and an upper limit on y_{Bj} help to eliminate events with very large radiative corrections and/or electromagnetic events. The lower limit on Q^2 also removes a region in which the trigger efficiency is rapidly changing. The lower cut on ν removes events for which the resolution on ν is too bad to be useful while the upper cut on ν removes events for which the total energy is likely questionable (there are not many of these events anyways).

Table 4.2 shows the total number of events which remain after all cuts have been made for the hydrogen and deuterium targets for three different sets of kinematic

Target	$Q^2 > 4, 6.3 < W < 20$	$Q^2 > 3, W > 20$	$Q^2 > 3, W > 20, x_{Bj} > .005$
H_2	7376	3962	3712
D_2	7549	4248	3965

Table 4.2: Number of events passing cuts for hydrogen and deuterium targets with LAT trigger for three different sets of kinematic cuts.

cuts which are used for different physics purposes in this analysis. (Note that the deuterium figures do not include some earlier parts of the run which have some extra analysis difficulties with the calorimeter. Inclusion of this earlier data would roughly double the number of events for deuterium.) The $6.3 < W < 20GeV$ region is designed to emulate the EMC kinematic region and other kinematic cuts similar to theirs have been made on this data. These cuts are: $Q^2 > 4GeV^2$, $20 < \nu < 260GeV$, $.01 < y < 0.9$, $x_{Bj} > 0.01$ and $40 < W^2 < 400GeV^2$. (Some of the plots made to emulate EMC are in the region $100 < W^2 < 400GeV^2$.)

4.7 Track Selection

The charged track reconstruction chain and the calorimeter clustering algorithm inevitably produce some results which do not correspond to the physical reality of the particular event at hand. In the case of charged tracks, this can take the form of tracks which have incorrect momenta or worse yet, tracks which are completely

fictitious. In the case of the calorimeter, some of the reported clusters can be the result of charged particle showers or energy deposition in the calorimeter which definitely should not be treated as photons in the analysis. In addition to clusters associated with charged particles, there can also be clusters which are produced from electronics noise. Another concern for correlating calorimeter clusters to photons is that if photons are sufficiently close together on the face of the calorimeter, then the clustering algorithms will report a single cluster with the combined energy for both photons and the 'average' position. In order to combat deleterious effects to the analysis, various 'quality' cuts are made on reported tracks and clusters before proceeding with analysis.

The quality cuts for charged tracks are:

1. Only tracks which have segments in at least PC and PCF are used.

2. For each track, a distance of minimum approach to the primary vertex and the error associated with that distance are reported. For this analysis, the distance/error must be less than 4.0 and the distance must be less than $2.0cm$.

3. The χ^2 probability for each track must be greater than 10^{-3}. This helps eliminate tracks which have incorrectly fitted momentum due to 'incorrect' hits on the track. There is a fairly large overlap between this cut and the vertex distance cut. Tracks with poor fits usually do not aim very well at

the vertex and vice-versa. Here then, this cut mostly acts to cut out a small number of tracks which have spectacularly bad fits but still get lucky enough to come close to the vertex.

4. Only tracks with momentum greater than $10GeV$ are used. The geometric acceptance plummets rapidly to zero below this momentum. Making a cut defines a clean boundary for both Monte Carlo and data. (The cut for the 'EMC' kinematics set is $6GeV$.)

With the above cuts, a reconstruction efficiency of 65-80% for charged tracks of sufficiently high momentum is achieved (see section 4.8) About 2% of those tracks will be 'ghost tracks'.

There are a considerable number of 'quality' cuts for photons. A number are based solely on calorimeter information and require a given shower to 'look electromagnetic'. In addition, charged track information can be used to further discriminate against clusters which have resulted from interaction of a charged particle. The cuts are:

1. Using bitube information, a ratio of energy deposited in the back-half of the calorimeter to that in the front-half is formed. In order to be retained as an 'electromagnetic' particle, this ratio must be less than 2.0.

2. Again using bitube information, the 'starting point' of a shower is determined. In order to be retained as an 'electromagnetic' particle, the starting point of the shower must be before plane 10. Although considerable overlap exists between this cut and the back/front energy cut, the overlap is not complete. Ambiguities in assignment of bitube energy to the proper pad shower and noise and fluctuations produce clusters which pass one cut but not the other.

3. Using bitube information, a 'longitudinal center of gravity' cut is is made. Only those clusters with center of gravity less than $55cm$ into the calorimeter are accepted. This helps cut out non-electromagnetic energy.

4. Clusters with energy less than $2GeV$ are eliminated. This helps remove false clusters caused by electronics noise or other anomalous effects.

5. Clusters which are anomalously wide are eliminated. Although a number of these could be due to unresolved single photons they can also be caused by 'wild' fluctuations in a single shower and electronics noise problems. A radius parameter is reported by the clustering algorithm. The maximum allowed radius is $10cm$.

6. An impact point on the calorimeter is calculated for each charged track which has been reconstructed. Figure 4.1a shows the distribution for the distance

of separation (at the calorimeter) for each cluster center from the nearest charged track for both data and Monte-Carlo. Clearly, a large number of clusters in the data with a nearby charged track have been caused by that track in some way. In order to be declared a photon, a cluster must have no charged track with an impact point on the calorimeter which is within $8.0cm$ of the cluster center.

7. A cut using drift chamber track segments (not necessarily fully reconstructed tracks) is made using the same approach as the previous cut. This eliminates an important class of pernicious background to the photon signal which is caused by charged particles which experience at least some transverse momentum kick from the CCM. See figure 4.1b for the distribution of separation between cluster centers and impact position of drift chamber segments on the calorimeter. As with the fully reconstructed tracks, there is a clear set of track/cluster pairs which are correlated. Note that this figure contains only clusters which *remain* after all other cluster cuts have been made so these are clusters which otherwise would not be eliminated.

8. In order to eliminate clusters caused by bremsstrahlung in the direction of the incoming beam and possibly clusters due to interactions of preceding beam muons in the calorimeter, an apparent photon must have an angular

separation of at least $3mr$ from the beam direction at the target or it is cut.

9. A calorimeter *fiducial volume cut* is made which eliminates possible difficulties near the edge of the active area. All clusters with centers outside an area $2.8 \times 2.8m^2$ square (centered on the calorimeter) are cut.

10. Photons which have an angular separation (projected to the target) of less than $10m$ are combined into a single photon by adding the energies and taking the average direction of the two. This is done for both Monte Carlo and data. The reason for this is that the clustering algorithm which is used is essentially incapable of separating clusters which are closer together on the calorimeter than would follow from this angular separation. Hence, plots which show distributions for photons are showing the information for *effective* photons.

Momenta are calculated with the assumption that the photon origin is the primary vertex. The calorimeter x position is taken to be exactly $14.0m$ which places showers somewhat inside of the calorimeter as they should be. An error matrix on the photon four-momentum is calculated using the reported errors on the vertex position and nominal resolution errors for calorimeter energy and position. The nominal calorimeter errors which are used for this purpose are:

$$\sigma_E/E = 0.45/\sqrt{E} + 0.07,$$

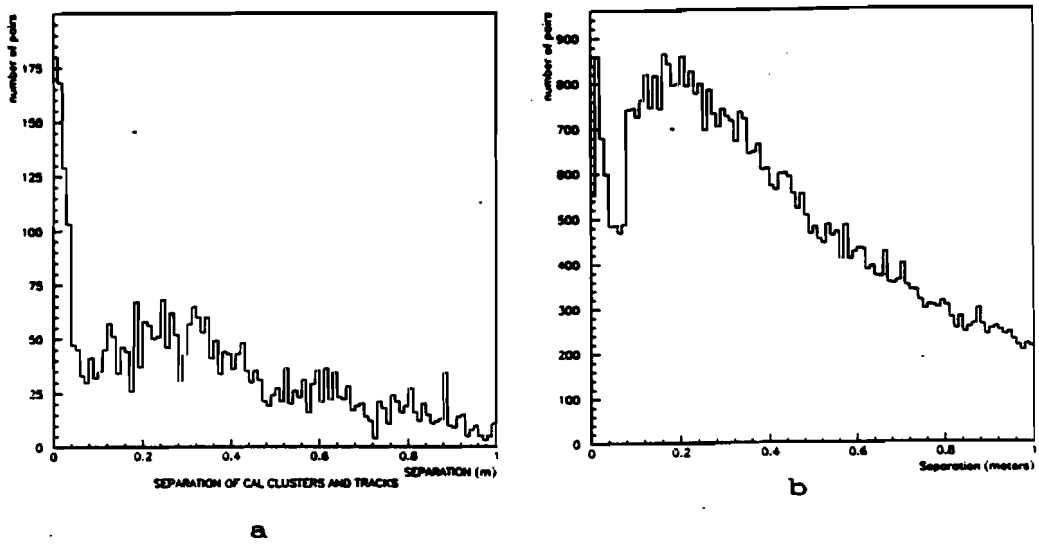

Figure 4.1: Separation of calorimeter clusters and track positions at the calorimeter for a)LSTF tracks and b) drift chamber segments after all other cuts have been made. (Only a small portion of all data is shown.)

$$\sigma_y = \sigma_z = 2cm$$

where E is the energy in GeV. The resolutions here are slightly larger than stated in the calorimeter hardware section. The energy resolution quoted in that section was improved somewhat from the data which is used here by application of new gain corrections. The position resolution has been increased somewhat in order to account for effects due to complicated events with many clusters which can overlap each other and dead regions in a multitude of creative ways that can produce additional smearing.

It should be stated that the cut on events which result from bremsstrahlung

(as described earlier) are made on the actual calorimeter clusters and not on the processed 'photons'. Roughly one-half of the calorimeter clusters are eliminated by making the various cuts. Even more importantly, a large number of clusters which would produce apparently large transverse momentum photons are removed by use of the track pointing cuts. Some small residual effects of charged clusters still remain. This can be seen by looking at the angular distribution of a 'photonic event plane' around the virtual photon direction. Although much reduced by application of the cuts, some tendency still remains for this plane to be more in the bend plane of the magnets rather than orthogonal to that direction. It is interesting to note that the event plane determined solely with the charged particles exhibits a smaller but still noticeable effect. A measure of the magnitude of the effect can be made by examining events from two different alignments of the 'photonic plane'. In all, I estimate that the systematic uncertainty on the summed energy of photons is not greater than $\pm 20\%$.

Table 4.3 shows the total number of charged particles and photons for hydrogen and deuterium targets for the events in two of the kinematic ranges listed in table 4.2. The numbers listed are all after all cuts have been made.

Target	$Q^2 > 4, 6.3 < W < 20$	$Q^2 > 3, W > 20$
H_2Photons	11796	10894
H_2Charged	8844	8953
D_2Photons	12586	12930
D_2Charged	9010	9873

Table 4.3: Number of particles passing cuts for hydrogen and deuterium targets with LAT trigger for two different sets of kinematic cuts.

4.8 Monte Carlo

Monte Carlo in this analysis provides two relatively different needs. First, it is used to test the efficiency of the event reconstruction algorithms and thereby to calculate acceptance corrections for the data. Second, the Monte Carlo is used to provide a 'theoretical model' for new kinematic regimes and measurements by allowing an extension of measurements made at lower energies or from different types of experiments (such as e^+e^-). Nominally, the former need does not require the Monte Carlo to have any particularly physically interesting model for production of particles. It simply requires that the distribution of particles and tracks through the detector be well simulated. However, it will be far more convenient if the same Monte Carlo

meets the needs of both of the requirements. For simple analyses (based for instance on single particle spectra) it will suffice to simply use the Monte Carlo for acceptance. However, for more complicated analyses such as those based on overall event topology, the two purposes become almost inextricably linked. The Monte Carlo can be broken into several logical parts – beam generation, primary vertex generation (kinematics), hadron generation, tracking and reinteraction through the detector, and simulation of signals in the detectors.

The beam generation for the Monte Carlo has actually not been generated at all but are actual measured muons from the beam spectrometer. Files of beam events for different targets have been created and are used as input to the Monte Carlo generation. Some slight difficulties arise from the 'pre-quantizing' of the beam events by the detectors. Overall, the procedure is an easy and reliable method of ensuring that the Monte Carlo beam has the same features as the real beam – because it is real!

Generation of the muon scatter is done according to the standard cross section with input of a particular structure function. The structure function which is used for the standard 'high Q^2' generation is a simple charge weighted summation of the parton distributions fit by Morfin and Tung (fit S2) [44]. This F_2 takes into account data from a large number of experiments including heavy weighting factors from EMC and BCDMS. Favorable comparison in overlapping kinematic ranges has

been made with a structure function parameterization made by Mizuno [111] using EMC data and the F_2 given by Morfin and Tung.

In this analysis, the hadron generation program which is used is the Lund Monte Carlo version 4.3 [69]. This version was 'tuned' using data from EMC and it is therefore expected that it will provide the most accurate description of the E665 data for acceptance correction purposes. Of course, this does not necessarily imply that it provides the best possible model of the underlying physics. Indeed, this is a rather old version of the Lund MC but the basic processes are not significantly changed. It is based on string fragmentation and includes full treatment of first-order QCD processes. In addition, it provides a (rather arbitrary) prescription for treatment of soft gluon effects which was necessary for fitting the EMC data. This Monte Carlo should allow considerable progress in understanding the basics of the underlying physics. Application of newer Monte Carlos and in particular those based on parton shower models would be most interesting. I must admit that the only reason such models are not used in this thesis is that I ran out of time.

Although most of the settings used for the Lund portion of the Monte Carlo are simply the defaults, one very important difference is the gluon distribution function. The default gluon distribution for the version 1.43 Lund MC is that of Gluck, Hoffman and Reya [45]. E665 generation has primarily been done using the gluon distribution given by Morfin and Tung. As has been shown in figure 2.11 there is a

substantial difference between the two gluon distributions in the kinematic region of E665. This will have considerable impact on the MC calculation of multi-jet events. This is by far the most significant difference between the hadron generation of E665 and that of the 'standard' Lund version 1.43.

For completeness, I list here some of the most relevant (for this analysis at least) parameters of the Lund Monte Carlo and the settings used in standard calculation for corrections to E665 data:

- As mentioned above, the parton distributions used are those of Morfin and Tung fit S2.

- Given the above parton distributions, there is no apparent need of the so called 'soft gluons' in this version of Lund. The soft gluon code is essentially an ad hoc prescription for adding extra transverse momentum to the hadrons and most obviously effects the $p_\perp$ distribution as a function of x_F. As will be seen later, the larger gluon distribution of Morfin and Tung more than compensates for lack of 'soft gluons'. It should be noted that more recent versions of the Lund Monte Carlo do not treat soft gluon radiation in the same manner. Soft gluons are turned off.

- The Monte Carlo allows different values for Λ_{QCD} for evolution of structure functions and for production of hard QCD processes. The value for evolution

of structure functions is set to $\Lambda = 0.40GeV$. For production of hard QCD events $\Lambda = 0.30GeV$ is used.

- Although it is allowed to calculate events with $Q^2 < 4GeV^2$, evolution of structure functions and changes in the QCD probability halt Q^2 evolution at $4GeV^2$.

- The width of the (Gaussian) primordial transverse momentum is $\sigma_{k_\perp} = 0.44GeV$.

- The width of the (Gaussian) nonperturbative transverse momentum kick given to hadrons is $\sigma_{p_\perp} = 0.44Gev$.

- The minimum allowed x_F for each jet in a multi-jet system is 0.05.

- The minimum allowed invariant mass (with quark masses included) for a jet system or subsystem is $1.0GeV$. Although this is a somewhat arbitrary setting, it is an attempt to define the 'separability threshold' of a single forward jet from two or more forward jets. In addition, a gluon kink in a string must have $p_\perp^2 > 3.0GeV^2$ with respect to the end points of the string or it is declared 'not viable'.

Of course, the Lund Monte Carlo includes *many* more parameters but most of these will have relatively small effect on the distributions in this analysis. Some

parameters which could have an effect are not listed here as they are not usually considered to be 'adjustable'. In other words they tend to be more an intrinsic part of the model (the string constant for instance).

Although Lund handles all decays of short-lived particles (and some long-lived ones as well if given the chance), little else is done with respect to the multitude of things that can happen to a particle from the time of its production and its exit from the spectrometer. In order to handle the tracking, decay and reinteraction of particles, the GEANT Monte Carlo is used [112]. The E665 detector apparatus has been simulated in considerable detail and many physics processes such as hadronic reinteractions, photon conversions, multiple scattering, etcetera, should be accurately simulated by GEANT. Given a free hand, GEANT will produce prodigious numbers of low energy daughter particles. A $500 MeV$ cutoff has been imposed on all particles produced in GEANT in order to keep the offline software from being overwhelmed by too many particles. Hence, GEANT is not used for production of very low energy particles which will not really produce tracks but just make 'noise' in detectors. On the other hand, any particles of consequence will be fully tracked.

Detector simulation is made using the tracking information provided from GEANT. Hits are calculated given tracks at detector positions. In addition, random noise is added to planes with one component which is proportional to the number of true hits present and another which is independent of the true hits. This has been added

because analysis of the data showed 1-2 times more hits were present in the data than could be accounted for from the Monte Carlo (even using GEANT). Hits in detectors are smeared with known resolution information for the each detector and dead or inefficient regions are accounted for to the best of our knowledge.

Because of the severe time constraints, GEANT simulation is not performed for the electromagnetic calorimeter response to photons. Instead, individual photons are smeared with the nominal energy and position resolution for the calorimeter and momenta are re-calculated. All photons with energy greater than $800 MeV$ after smearing are assumed to be visible. Of course, photons which do not strike the fiducial area of the calorimeter are considered to be lost. In addition, the photons are subjected to the same charged particle cuts as the clusters from the actual data. No attempt is made to cut photons based on individual fluctuations in the longitudinal or transverse energy. Note that a number of studies have been done which show that the energy resolution and longitudinal and transverse shower development is described reasonably well by GEANT.

Monte Carlo events are run through the same PTMV chain as the data. By comparing the reconstructed tracks with the truth tracks, we can measure the Monte Carlo's impression of our reconstruction efficiency. Measurements of the efficiency can then be used to apply acceptance corrections to the data. Checks on the agreement between the Monte Carlo simulation and the data can be made by

examining primitive quantities for the event (such as χ^2 and residuals for track fits) and also by checking that as many different physics distributions as possible behave in the same fashion for both Monte Carlo and data. In addition, by comparing data with EMC in the same kinematic regions, we can acquire confidence that we have at least made the same mistakes they did! Hopefully, this will add to our confidence in the corrections.

One powerful handle on the reliability of reconstruction is the kinematic distributions given by the beam and scattered muon. The cross section for this process is well understood and we should expect good agreement between the shape of our distributions and that calculated from the Monte Carlo. Figure 4.2 shows the corrected distributions for E665 deuterium and hydrogen data combined for Q^2, x_{Bj} and W compared with true distributions from the Monte Carlo for the $Q^2 > 3GeV^2$ $W > 20GeV$ kinematic range. Cuts for removal of bremsstrahlung have been made to these distributions. Clearly, the overall agreement is quite good.

For this analysis, the most significant acceptance corrections will be for low momentum particles. This is primarily due to the geometric acceptance of the PCF chambers in the CCM and the fact that in order to be included, charged particles must have sufficient momentum to make it through these chambers before being bent out of the spectrometer by the CCM. Figure 4.3 shows the calculated acceptance, for the $W > 20GeV$ region, as a function of laboratory momentum for

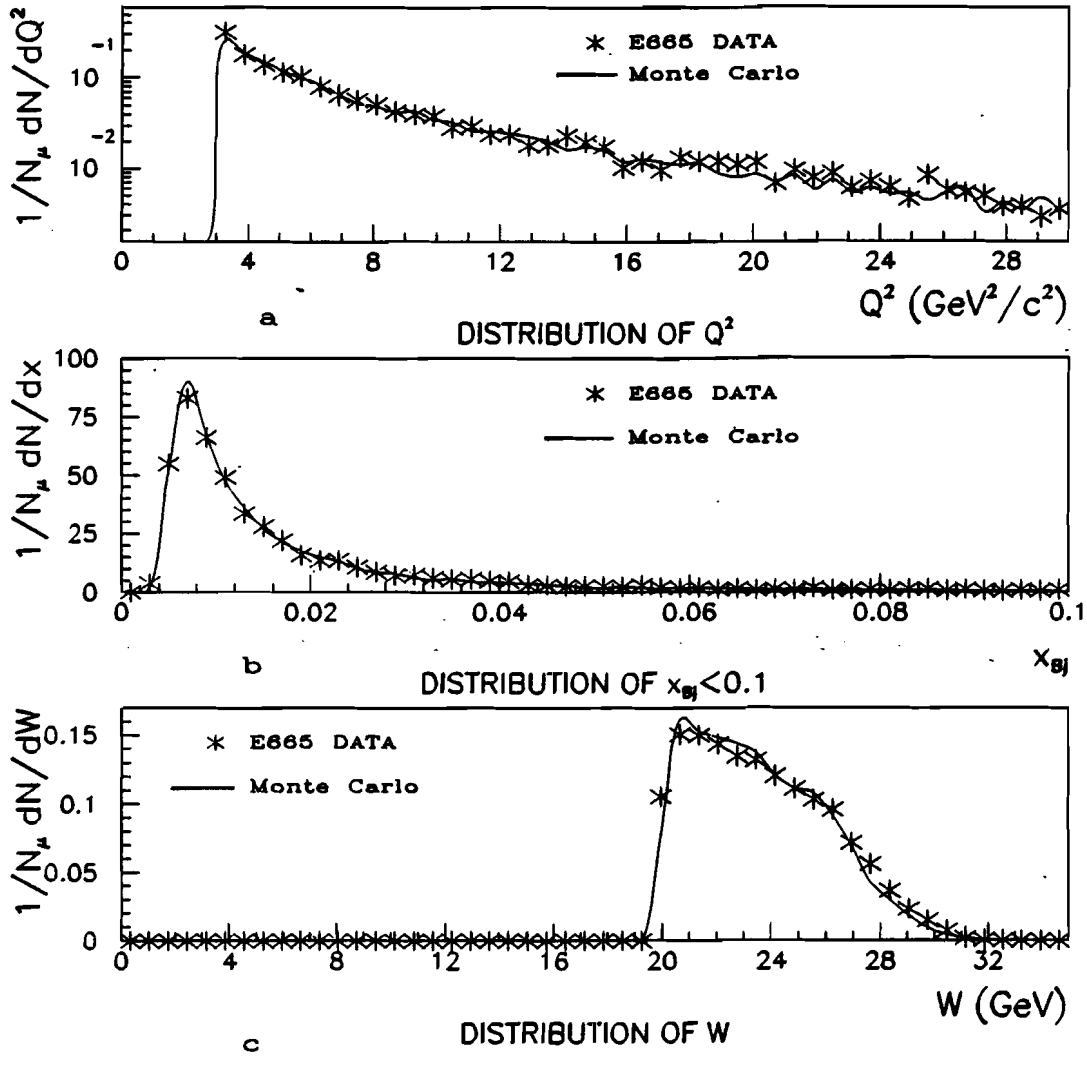

Figure 4.2: Distributions from data and Monte Carlo for a) Q^2, b) x_{Bj} and c) W for the $Q^2 > 3GeV^2$ and $W > 20GeV$ kinematic range.

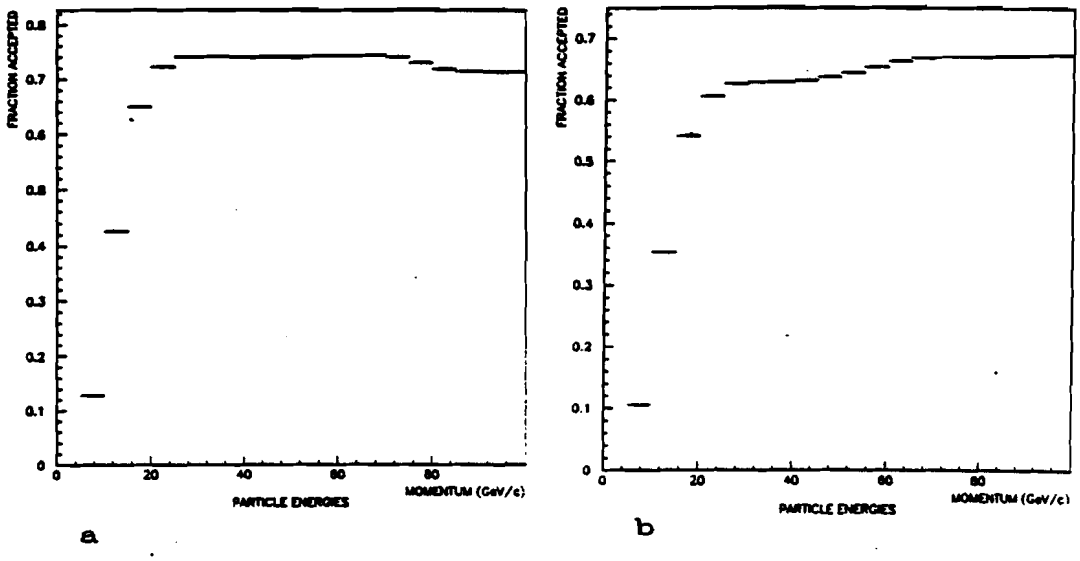

Figure 4.3: Acceptance (reconstructed/truth) as a function of momentum for the $W > 20GeV$ region calculated from the Monte Carlo for charged particles (with momentum greater than $10GeV$. a) Before extra inefficiency is applied. b) After extra inefficiency is applied.

charged particles. The acceptance for charged particles is defined as the number of reconstructed tracks divided by the number of stable charged hadrons at the primary vertex. Hence, tracks which are lost due to reinteractions are counted against the acceptance. The purpose for making the acceptance correction in this fashion is to attempt to have a competely 'detector independent' (but alas not Monte Carlo independent) final result. In order to avoid regions with sufficiently large acceptance correction, only charged tracks with momentum greater than $10GeV$ are used in the analysis and these tracks are removed from both the truth and reconstructed Monte Carlo events prior to calculation of the acceptance corrections.

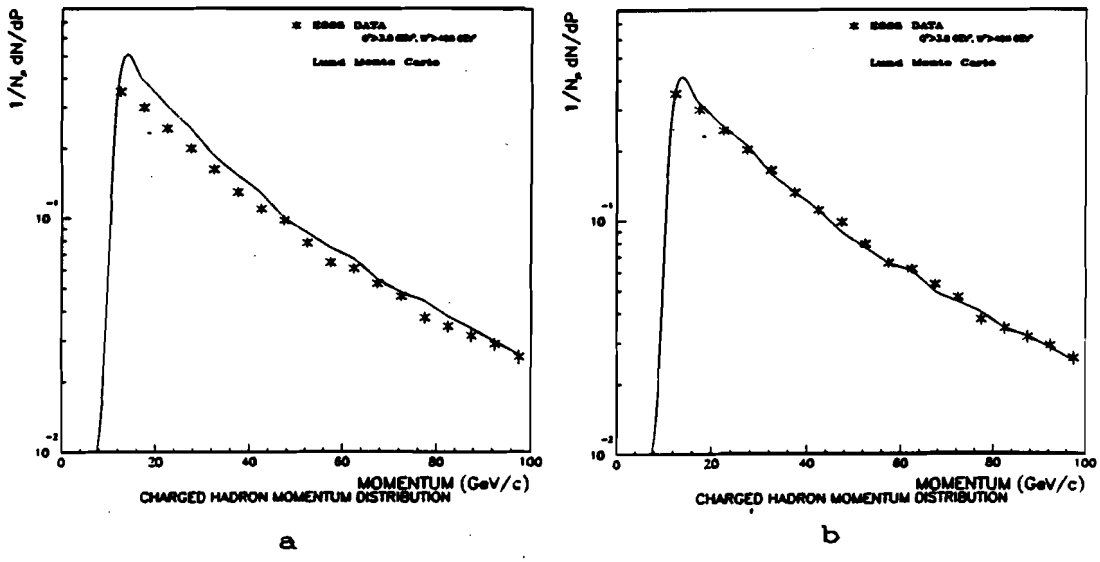

Figure 4.4: Number of reconstructed charged tracks (for the $W > 20$ GeV region) as a function of momentum and normalized to number of scattered muons. a) Monte Carlo before extra inefficiency is applied. b) Monte Carlo after extra inefficiency is applied.

For data in the $W > 20$ region, comparison of reconstructed data to reconstructed Monte Carlo show that there are 12.5% fewer charged tracks for $x_F > 0$ found in the data than in the Monte Carlo. Figure 4.4 shows the number as a function of momentum of all reconstructed charged tracks for both data and Monte Carlo. The 'missing tracks' appear to be roughly evenly distributed throughout the momentum range from 0 to $100GeV$. There is clear momentum dependence. In addition, careful study of the shape of the multiplicity distribution shows that the higher multiplicity events appear to be missing more tracks than lower multiplicity events. Although not shown here, an extension of this plot indicates that there is

no statistically significant loss of tracks for momenta greater than $150GeV$ while there is only a small effect for the range from 100 to $150GeV$. The exact source of this problem is not completely clear. There are a couple of known effects which may contribute. One possible source of this effect may be that there is an extra allignment correction which needs to be made when tracks pass through the drift chambers at large angles. Finally, high W events have lots of tracks and there may still be some extra inefficiencies which result from many tracks in an event which are not simulated in the Monte Carlo. It could also be that *some* of the effect comes from the Monte Carlo being wrong. The overall effect is not too severe. In order to account for this, an extra random inefficiency is imposed on found tracks in the Monte Carlo prior to calculation of the acceptance corrections. The form of the extra inefficiency is given by:

$$\text{Inefficiency} = \frac{150 - p}{150} \times 20\%, \tag{4.8}$$

where p is the track momentum in GeV and only tracks with momentum less than $150GeV$ are cut. (Extra tracks for momentum greater than $150GeV$ are not added!)

Acceptance corrections for each bin of each plot are calculated by taking the ratio of reconstructed Monte Carlo (with the extra inefficiency) to truth Monte Carlo for that bin. The corresponding bin from the data is then divided by this correction factor. In some cases, a smoothing algorithm has been applied to the

Monte Carlo data prior to calculation of the acceptance correction. Although it is possible that the error in the reconstruction efficiency is as large as 15% it is more likely not much worse than 5-10%. This is still unfortunately large. Because the discrepancy between data and Monte Carlo becomes smaller at higher energies, plots which make use of energy weighted results should be less affected by this uncertainty.

There is discussion as to whether the apparent inefficiency could actually be due to the Monte Carlo producing too many tracks. Although this possibility cannot be ruled out at this time, I expect that there are still some effects in the detector which are not accounted for in the Monte Carlo. Therefore, given that the effects observed are consistent with extra loss in the detector, I have chosen to make the extra correction. This fact should be kept in mind when examining the data compared to the Monte Carlo.

Chapter 5

Analysis and Results

5.1 Introduction

The thrust of this analysis is to study transverse momentum and event topology in order to gain understanding into hard (perturbative QCD) processes and resulting fragmentation in deep inelastic scattering. Throughout, the basic approach will be to compare the experimental results with that of the QCD-based Lund Monte Carlo. The analysis proceeds through several layers of sophistication. First, single particle spectra will be presented. Next, basic event topology will be studied using the hadronic event plane. Following this, energy and particle flow for forward particles is studied and various cuts are applied to demonstrate that some events have a 'two-lobed' structure. A jet reconstruction algorithm is applied and cuts are made in order to produce a sample of events which is highly enriched in two forward jet structure. The resulting sample of events should reflect the nature and magnitude of the hard QCD processes. In particular, it will be demonstrated that the overall

structure agrees well with the underlying QCD calculations of the Monte Carlo and that the magnitude of effects may have particular implications for the gluon distribution of nucleons.

Both charged particles and photons will be used throughout the analysis. For single particle distributions or averages over particles, they will be treated separately but they will be used together for practically all of the energy and particle flow analysis. Occasionally, results using the charged particles alone will be presented in order to demonstrate that inclusion of the photons is not producing any particularly large bias. The argument for inclusion of the photons, especially when examining overall event topology, is both simple and strong. The Monte Carlo shows that roughly 67% of the CM energy (W) will be carried away from the primary vertex by stable charged hadrons (mostly pions with a few kaons). Another 26% of the energy will go into π^0's which overwhelmingly decay into two photons. Finally, 7% will go into neutral particles which are invisible to the spectrometer. These include neutrons, K_L^0, K_S^0, Λ, neutrinos, etc. Although it will be possible to reconstruct some fraction of K_S^0's and other neutrals which decay in the detector, this is a tricky business and is unlikely to recover any appreciable fraction of the energy in these channels. We also know from Monte Carlo, that because of reinteraction, scattering, decay, detector inefficiencies and reconstruction inefficiencies that only about 70% of the initial *high momentum* charged tracks will be observed

in high W events. Hence, using charged particles alone, typically less than 47% of the forward energy will be visible (this doesn't even include the 'extra' inefficiency in data compared to Monte Carlo discussed in the preceding chapter). Although the relative resolution is poor, the calorimeter will be highly efficient at observing photons with energies of interest. Hence, inclusion of the photons will bring the sum observed energy up to over 70%, which although not ideal, is workable. Certainly, the fluctuations in the total energy caused by the resolution of the calorimeter are small compared to the effects caused by the inefficiency in charged track reconstruction! It will be shown that this dramatically improves both the number and quality of events which pass 'jet cuts'.

Although some presentation will be made of data in the range of $10 < W < 20GeV$, the primary purpose of this will be to 'touch base' with results from EMC and establish a measure of credibility in the E665 data. Most of the results will focus on the higher W data and the handle which it provides on studying the underlying hard processes. Unless otherwise noted, it may be assumed that any given distribution refers to data in the $W > 20GeV$ region. Also, all distributions are for $x_F > 0$ particles only. Discussion of the analysis methods and presentation of results will be made simultaneously for clarity.

Except as noted, all plots have been corrected for acceptance. In general, only statistical error bars are shown on the plots. I estimate the magnitude of systematic

uncertainty in plots normalized to the number of scattered muons is about 5-10% for charged hadrons and perhaps as high as 20% for photons of energy more than a couple of GeV. The uncertainty on the photons comes from the large number of cuts which had to be made on calorimeter clusters in order to arrive at the nominal photon signal. Keep in mind that these are *effective* photons and not necessarily true single photons. Any photons which have a smaller angular separation than 10 milliradians are combined both in the data and Monte Carlo. For energy flow plots, the systematic uncertainty from missing photons is likely to be considerably less since there it does not matter if two photons are viewed as one.

In many plots, several different Monte Carlo predictions will be presented as smooth curves along with the data points. The predictions are:

1. The E665 standard Monte Carlo using Lund and parton distributions of Morfin and Tung (fit S2). No soft gluon effects are included. This prediction is represented on the plots by a solid line.

2. The Lund Monte Carlo using Gluck, Hoffman and Reya parton distributions with soft gluon effects on. This is the 'best fit', version of Lund tuned on EMC data. This prediction is represented on the plots by the finest dashed line.

3. The Lund Monte Carlo using Gluck Hoffman and Reya parton distributions

but with no soft gluon effects. This is presented in order to illuminate the effects that soft gluons will have on different distributions. This prediction is represented by a medium dashed line.

4. The Lund Monte Carlo with standard parameters but with hard QCD interactions turned off (no gluon bremsstrahlung or photon-gluon fusion). This illustrates how poorly the data are fit without QCD but with the nominal amount of (measured) fragmentation transverse momentum. In some plots, it also shows the background which will pass multi-jet cuts but will not have had at least two forward partons. This prediction is represented by a large dashed line.

5. The Lund Monte Carlo with increased fragmentation $\sigma_{p_\perp} = 0.7GeV$ and with hard QCD turned off. This is the 'best' attempt at making the Monte Carlo fit the data without any QCD processes. This predicition is represented by a dash-dot line.

Some of these 'smooth' curves become noticeably 'wiggly' in the waning regions of some plots. This is due to limited statistics from the Monte Carlo in these regions and the amount of 'wiggliness' may be taken as a measure of the statistical uncertainty. (At first I thought about trying to smooth the curves to get rid of this effect but then I decided that it was better to just leave it in given that error bars

would be confusing.

5.2 Single Particle Spectra

Although single particle spectra provide some sensitivity to the hard processes, one of their main assets is to confirm the overall integrity of the data. In addition, they provide the basis of measurements with which the Monte Carlo must agree before it can believably be extrapolated.

Figure 5.1a is the differential $p_{||}^2$ distribution ($= \vec{p} \cdot \hat{n}$ where $\hat{n}$ is the unit vector in the virtual photon direction) for charged hadrons in the photon-nucleon CM frame for the $W > 20GeV$ kinematic range. Also shown on the same plot is the prediction from the standard Lund Monte Carlo. The data are seen to be consistent with the Monte Carlo which was tuned on EMC data. This plot is relatively unaffected by significant differences in the underlying hard physics processes. Figure 5.1b is the same plot for photons.

Figure 5.2 shows the differential $p_{\perp}^2$ distribution for charged hadrons in the EMC kinematic range (only the deuterium data are used for this plot). The same plots are shown for charged hadrons and photons for events with $W > 20GeV$ in figure 5.3. Note that the transverse momentum is quite limited compared to the longitudinal momentum. Also note that although the effect of having hard QCD on in the Monte Carlo makes little difference to the longitudinal momentum distribution but it has a

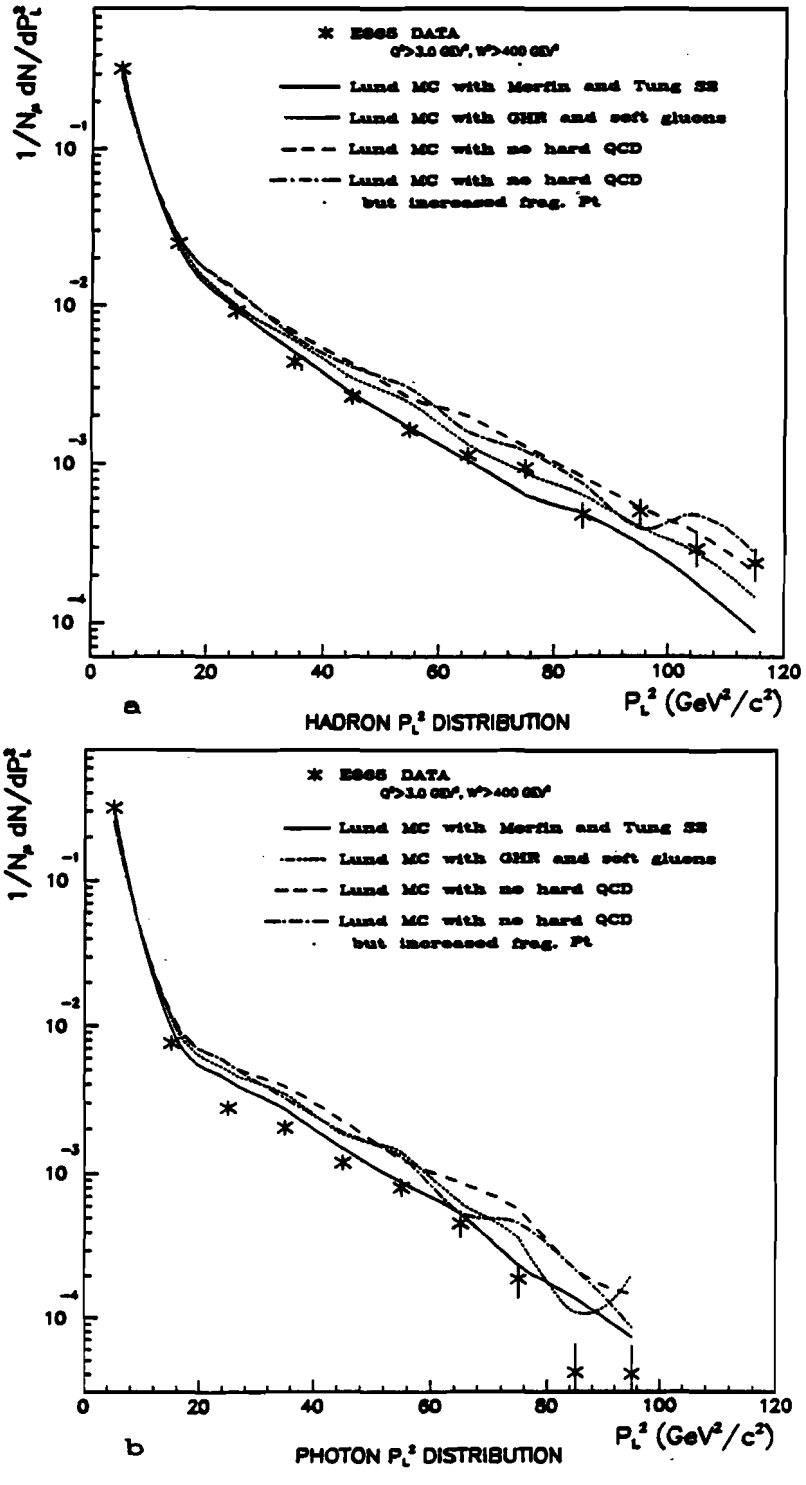

Figure 5.1: Differential $p_{||}^2$ distribution for $W > 20GeV$ for a)forward hadrons and b) for photons. Plots are normalized to number of scattered muons.

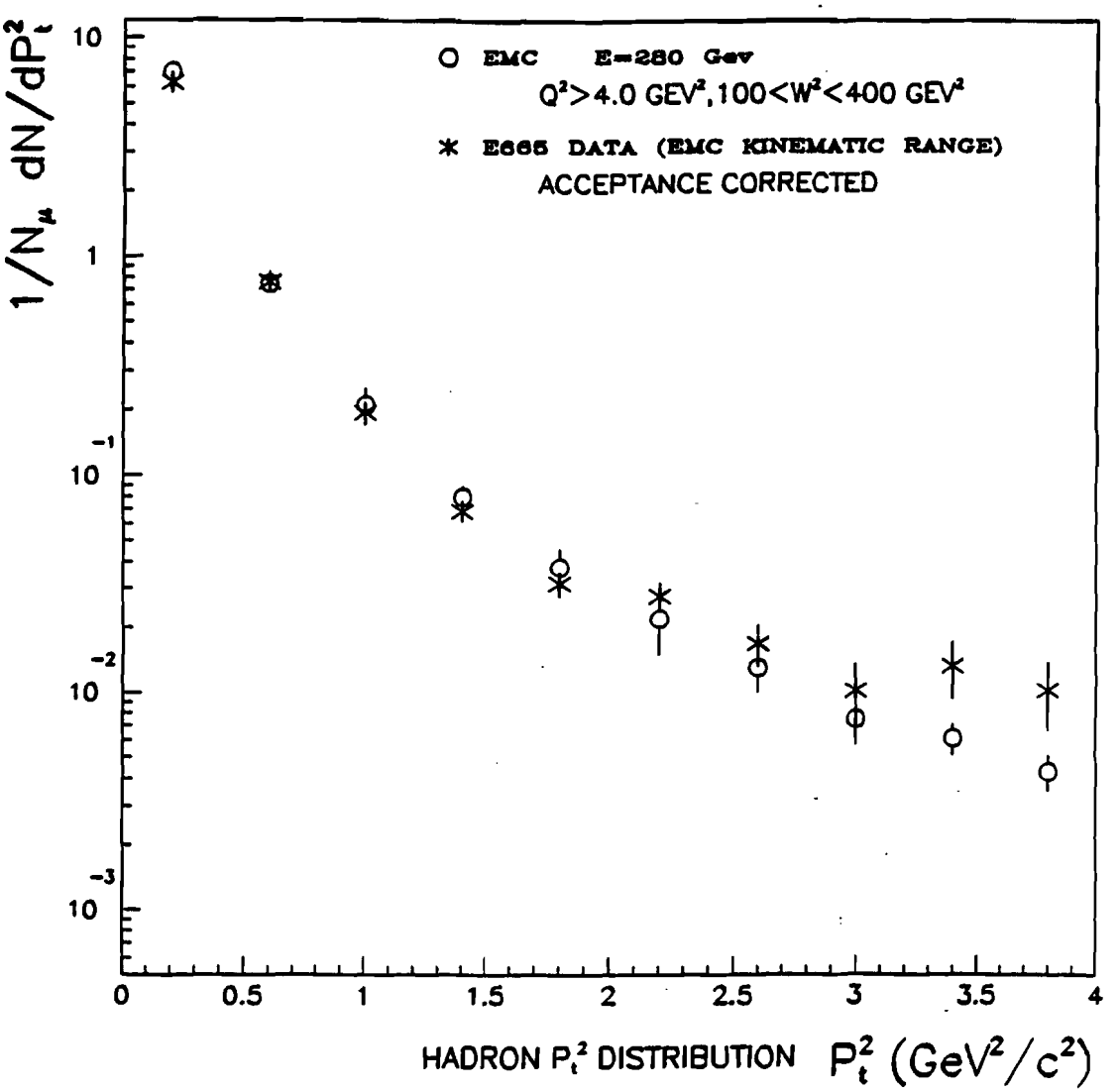

Figure 5.2: Differential $p_{\perp}^2$ distribution for forward charged hadrons for a EMC kinematics. Plots are normalized to number of scattered muons.

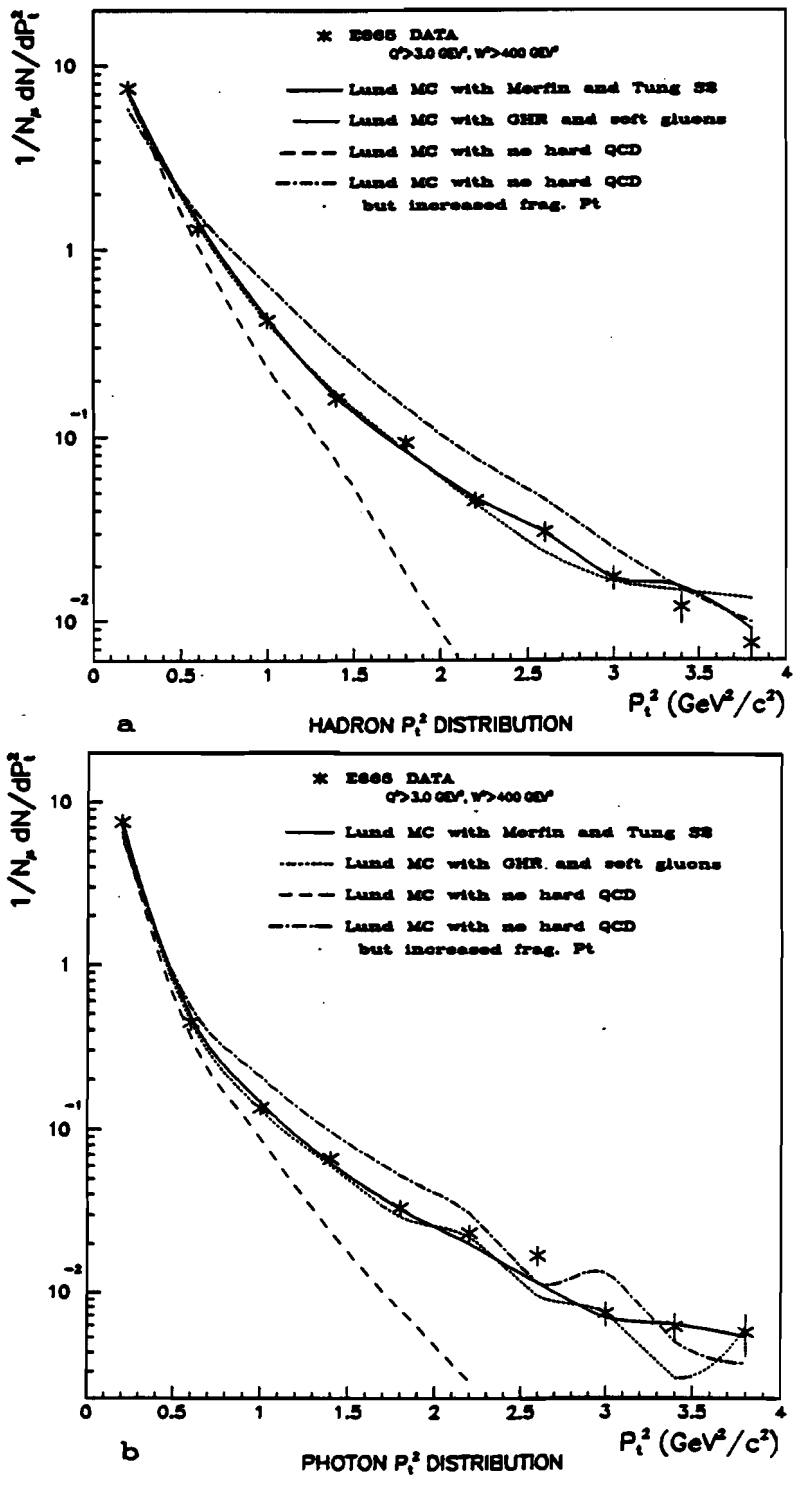

Figure 5.3: Differential $p_\perp^2$ distribution for events with $W' > 20GeV$ for a) charged hadrons and b) for photons. Plots are normalized to number of scattered muons.

considerable effect on the transverse momentum distribution. Although an overall higher $p_\perp^2$ is seen for the higher W range, it is difficult to discern any significant difference in the shape compared to the lower W range for either the photons or the charged hadrons. The Monte Carlo predictions which include hard QCD all fit the data quite well. If QCD is turned off in the Monte Carlo but other parameters are left constant, the agreement with data is terrible. Better agreement is achieved for the Monte Carlo without QCD if the width of the (Gaussian) transverse momentum distribution is increased to $0.7GeV$ from the default $0.44GeV$ but the agreement is still poor compared to the models with QCD. This is the 'best' attempt at fitting a number of distributions with QCD off.

Although there is no EMC data for comparison with the photons, we can take the agreement with the Lund Monte Carlo (tuned using charged hadrons) as validation of the data and vice-versa. Because of the large number of calorimeter clusters which have to be cut, there may be a relatively large systematic error on the photon points - perhaps as much as 20%. The main point is that the overall agreement is quite good so that it is justified to use the photons in combination with the hadrons in later plots. It is also important to always keep in mind that these are 'effective' photons (some may be a combination o two or more real photons).

Figure 5.4 shows the average $p_\perp^2$ as a function of x_F (the forward half of the 'seagull plot') in the $W > 20GeV$ kinematic range for E665 data compared to sev-

eral different Monte Carlo predictions. The highest two data points may have an extra systematic uncertainty due to low statistics in this region in the Monte Carlo acceptance corrections. In addition, the corrections in this region are relatively large. For most of the plot, the acceptance corrections are about 10%. However, for the highest two x_F bins, the acceptance corrections are on the order of 20%. The Monte Carlo indicates (with poor statistics for the highest points in x_F) that the tendency is to over-estimate the average transverse momentum when calculated from the reconstructed tracks. Note that even before acceptance correction, the data fall monotonically in the $0.7 < x_F < 1.0$ range. The extra acceptance correction for the highest two points (in x_F) pulls these points down slightly more than for the lower x_F points. Note that even if the nominal correction of 10% (the same as the medium x_F range points) is applied that these highest points still fall monotonically compared to the distribution at medium x_F. In other words, even though there is additional uncertainty in the acceptance corrections for the highest points, I think that the uncertainty does not allow room for the highest points to continue the rising trend as is seen for the points below $x_F = 0.7$. The additional uncertainty in the acceptance correction is shown by an extension of the error bars on the plot. The solid curve shows the *standard* Lund prediction as described in section 4.8. Although it tends to overestimate the average $p_\perp$ at low x_F, there is overall good agreement between this prediction and the data. Although agreement

is not perfect in the high x_F region, the curve for the Monte Carlo with GHR (Gluck, Hoffman and Reya parton distributions) with soft gluons turned on is consistent with the data. An overall measurement of the 'goodness of fit' for each plot can be defined by:

$$\chi^2 = \sum \frac{(\langle p_{\perp data} \rangle - \langle p_{\perp MC} \rangle)^2}{\epsilon^2} \tag{5.1}$$

where the sum is over all of the data points and ϵ is the error on each data point. The value of χ^2 for the Monte Carlo with Morfin and Tung S2 parton distributions is $\chi^2 = 27.7$ while the Monte Carlo using Gluck, Hoffman and Reya parton distributions and soft gluons turned on gives $\chi^2 = 16.6$.

The seagull plot has an interesting history involving the so-called *soft gluons*. When first measured by EMC, it was very difficult to reproduce the shape of the rise for the forward particles using the Lund Monte Carlo with any adjustment of the relevant parameters. In particular, it appeared that hadrons at large x_F carried more transverse momentum than could be explained using a combination of perturbative QCD, nonperturbative fragmentation and primordial transverse momentum. The solution was to include extra transverse momentum in the system which was generated by *soft gluons*. The idea was that along the string, soft gluons would be generated which would be incapable of forming their own jet but which would cause a local transverse kick to the string. Summation of the effects from these soft

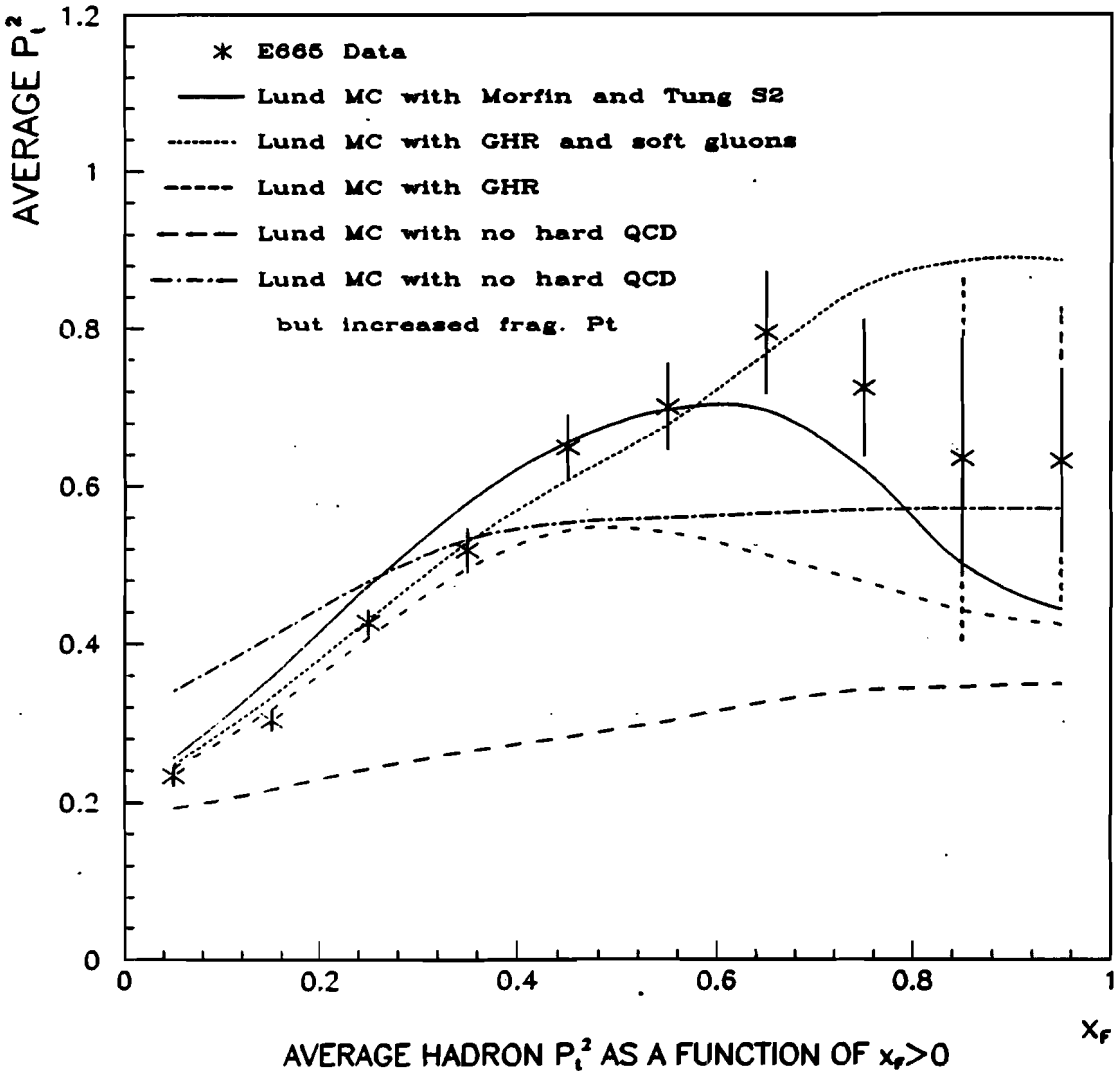

Figure 5.4: Average $p_\perp^2$ as a function of x_F for charged hadrons for $W > 20GeV$.

gluons would cause the end points of the string to pick up relatively larger amounts of $p_\perp$ as they recoil against the rest of the string. This would result in extra $p_\perp$ for the large x_F hadrons.

The implementation of the soft gluon effects is rather ad hoc. No real calculation is made. Rather, extra transverse momentum kicks are just added in according to an arbitrary (settable) parameter. Although it seems to be motivated by the preceding pseudo-physical argument, it really boils down to an arbitrary method of just adding in extra transverse momentum because it needs to be there to fit the data! Perhaps both the argument and the model are completely correct, but maybe not.

Recall that the 'standard' Monte Carlo makes use of the gluon distribution of Morfin and Tung fit S2 rather than that of Gluck, Hoffman and Reya which was originally used in tuning the Monte Carlo and comparison with EMC data. Also recall that the standard *does not include the soft gluon effects.* The dashed line on the plot shows Lund using GHR without soft gluons on while the dotted line shows Lund using GHR with soft gluons. Clearly, the soft gluons have a large and important effect in this plot. It would appear that increasing the primordial gluon distribution will affect the seagull plot in a very similar manner to the inclusion of soft gluons. The real difference occurs in the high x_F region where we see that the data tend to choose a path between the curve with soft gluons included and that

with an increased gluon distribution. Soft gluons may not be the full (or possibly even correct) story in this plot – at least in the style and magnitude as included in the Lund Monte Carlo. More evidence supporting an increased gluon distribution is presented later.

5.3 Transverse Momentum and the Hadronic Event Plane

In addition to studying the transverse momentum spectrum of individual particles and the averages with respect to kinematic variables, it is possible to extract further information on the nature of the underlying strong interactions by studying momentum correlations and topology of the final state hadrons. One of the more useful concepts in this realm is that of the *hadronic event plane.*

Clearly, theories such as QCD which provide limited transverse momentum from 'typical' fragmentation with relatively infrequent hard radiation (or generation) of high transverse momentum particles can be expected to produce some events in which the hadrons will lie roughly in a plane. That is to say, it should be possible to find a plane in space such that there will be a substantial imbalance between the transverse momentum within the plane and that which is out of the plane. In e^+e^- experiments, this plane is typically defined by diagonalizing what is known as the

sphericity tensor [113,114]:

$$S_{ij} = \sum_f \left[\delta_{ij}\mathbf{p}_f^2 - p_{fi}p_{fj}\right] \tag{5.2}$$

where f indicates a sum over all final state particles and i and j run over the three spatial dimensions. The eigenvectors which correspond to the two smallest eigenvalues will define the hadronic event plane.

In muon scattering, the direction of the virtual photon is (nominally) known from the incoming and outgoing muon. In the γ-proton CM frame, for a 2-jet event, the struck parton will be travelling almost exactly along the photon direction while the remnant diquark (or whatever) will be travelling in the opposite direction. (Of course, primordial k_T will cause a small rotation in the axes of the jets compared to the photon direction.) In the case of gluon bremsstrahlung or photon-gluon fusion, two of the partons will acquire significant transverse momentum with respect to the photon axis. Conservation of momentum clearly requires that this transverse momentum be balanced between the two partons on opposite sides of the photon direction so that the hadronic event plane will be constrained to contain the direction of the virtual photon. Hence, it is only necessary to use the component of momentum of final state particles which is transverse to the direction of the virtual photon in order to determine the hadronic event plane. The three dimensional problem in e^+e^- experiments is reduced to a two dimensional problem.

Hence, in this analysis, I define a *Planarity Tensor* which has the same definition as the sphericity tensor but is only two dimensional:

$$S_{ij} = \sum_f \left[\delta_{ij}\mathbf{p}_{tf}^2 - p_{fi}p_{fj}\right] \tag{5.3}$$

where now i and j are two orthogonal directions perpendicular to the virtual photon axis and the sum is over particles in the CM frame with $x_F > 0$ or some other reasonable cut in x_F. The eigenvector which corresponds to the smaller of the two eigenvalues for this matrix will be perpendicular to the virtual photon direction and will lie within the hadronic event plane (for forward going particles). Events for which the two eigenvalues are nearly equal show only slight 'planarity' while those in which the two eigenvalues are quite different will have substantial imbalance of p_t in and out of the plane. Figure 5.5 shows the angle between the event plane determined from final state particles and as determined by the initial partons for the Monte-Carlo for a sample of events with two, identified, forward-going jets. It is seen that for these events, the alignment of the hadronic event plane and the partonic event plane is quite good. The alignment for events resulting from gluon bremsstrahlung is better than that for photon-gluon fusion as would be expected from the differences in collinearity.

Figure 5.6a-c shows the orientation of the hadronic event plane around the virtual photon direction for data using charged hadrons and photons, data using

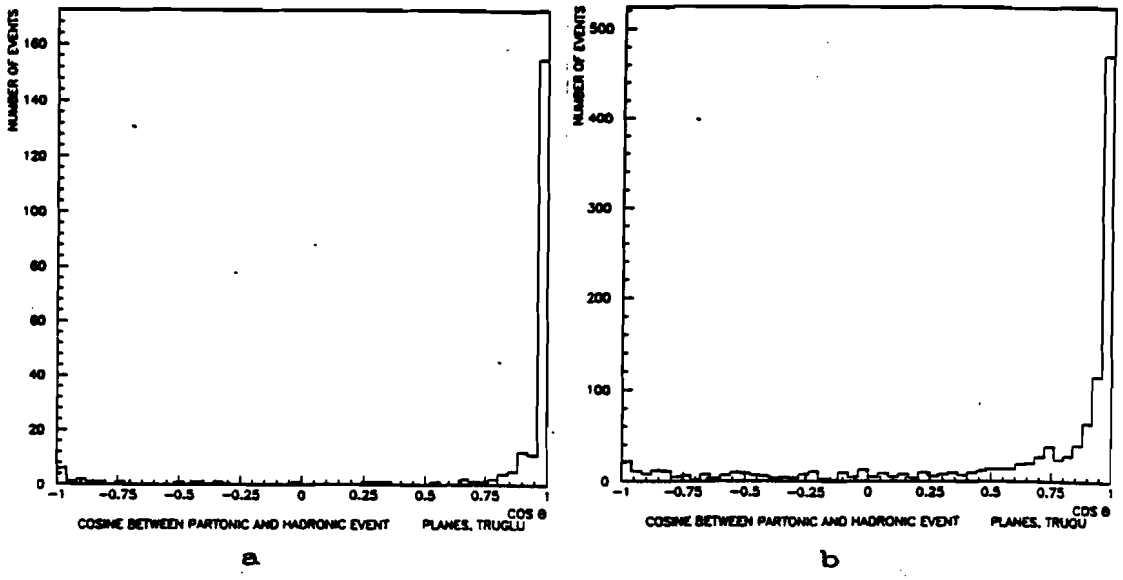

Figure 5.5: Angle between hadronic event plane determined using charged particles and photons compared to the plane determined by two forward partons a) gluon bremsstrahlung events and b) photon-gluon fusion events. (from MC)

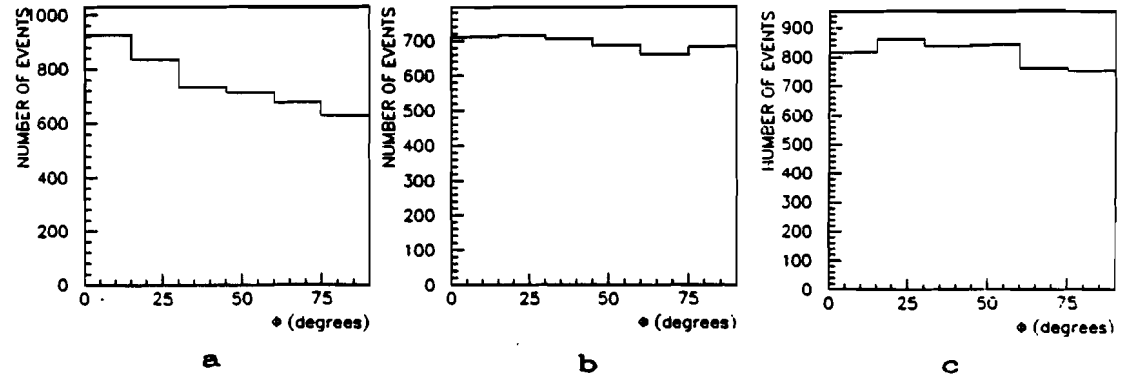

Figure 5.6: Orientation of hadronic event plane about photon direction for a) data using both hadrons and photons, b) data using only charged hadrons and c) Monte Carlo using hadrons and photons.

just charged hadrons, and Monte Carlo using reconstructed charged hadrons and photons. The value of the angle (ϕ) runs from 0° (roughly corresponding to the xy plane) to 90° (roughly corresponding to the xz plane). Note that the virtual photon axis is *not* exactly the laboratory x axis but for high ν events it will be quite close to it. It appears that there must still be some showers in the calorimeter which originate from charged particles which are bent in the magnetic field so that the event plane prefers to be horizontal. The magnitude of the effect is rather small though and is drastically reduced compared to the effect if no charged particle cuts are made on calorimeter clusters. It is interesting to note that there is also a slight tendency for the found plane to be horizontal using only charged particles in the data. There is no asymmetry in the event plane orientation found using the Monte Carlo. The effect of the slight asymmetry using the photons has been investigated and been found to be small. In particular, all physics plots have been studied for the region in which $\phi > \frac{\pi}{4}$ and the differences are unnoticeable in most plots. There is a difference of about 7% in the number of events which pass jet cuts for events in which the event plane is near vertical compared to the total sample. There may also be a slight effect on the order of a couple of percent in the overall shape. Attempts at getting a very precise measurement of multi-jettiness for purposes of measuring gluon distributions should take this into account.

Figure 5.7 shows the normalized sum of $p_\perp^2$ distribution in and out of the

hadronic event plane for charged hadrons in the EMC kinematic range. For this plot, only charged hadrons were used to find the hadronic event plane and only events with at least four charged hadrons are used. This is the way that the EMC analysis was done and the purpose of this particular plot is to show the agreement between the EMC and E665 data. This particular plot also makes use only of about half of the available hydrogen data.

Figure 5.8 shows the normalized sum of $p_\perp^2$ distribution in and out of the hadronic event plane where both charged hadrons and photons have been used to determine the plane. No minimum multiplicity requirement has been set. Also shown on the same plot are predictions from the Lund Monte Carlo. Figure 5.9 shows the same plot for photons. Of course, by definition there will be more transverse momentum within the plane than out of the plane. Hence, the actual shape and slope of the distributions is important. As can be seen from the figures, agreement between the data and Lund MC with hard QCD is quite good for both the charged particles and photons. The data points for the highest summed $p_\perp$ values are slightly lower than the Monte Carlo pdictions. This appears in both the hadrons and photons. As mentioned before, the photons have a sufficiently large systematic uncertainty that it is difficult to argue that any problem exists. However, it is difficult to explain this for the charged hadrons. The data have been studied for the effect that photons will have on the hadronic event plane and it was found that

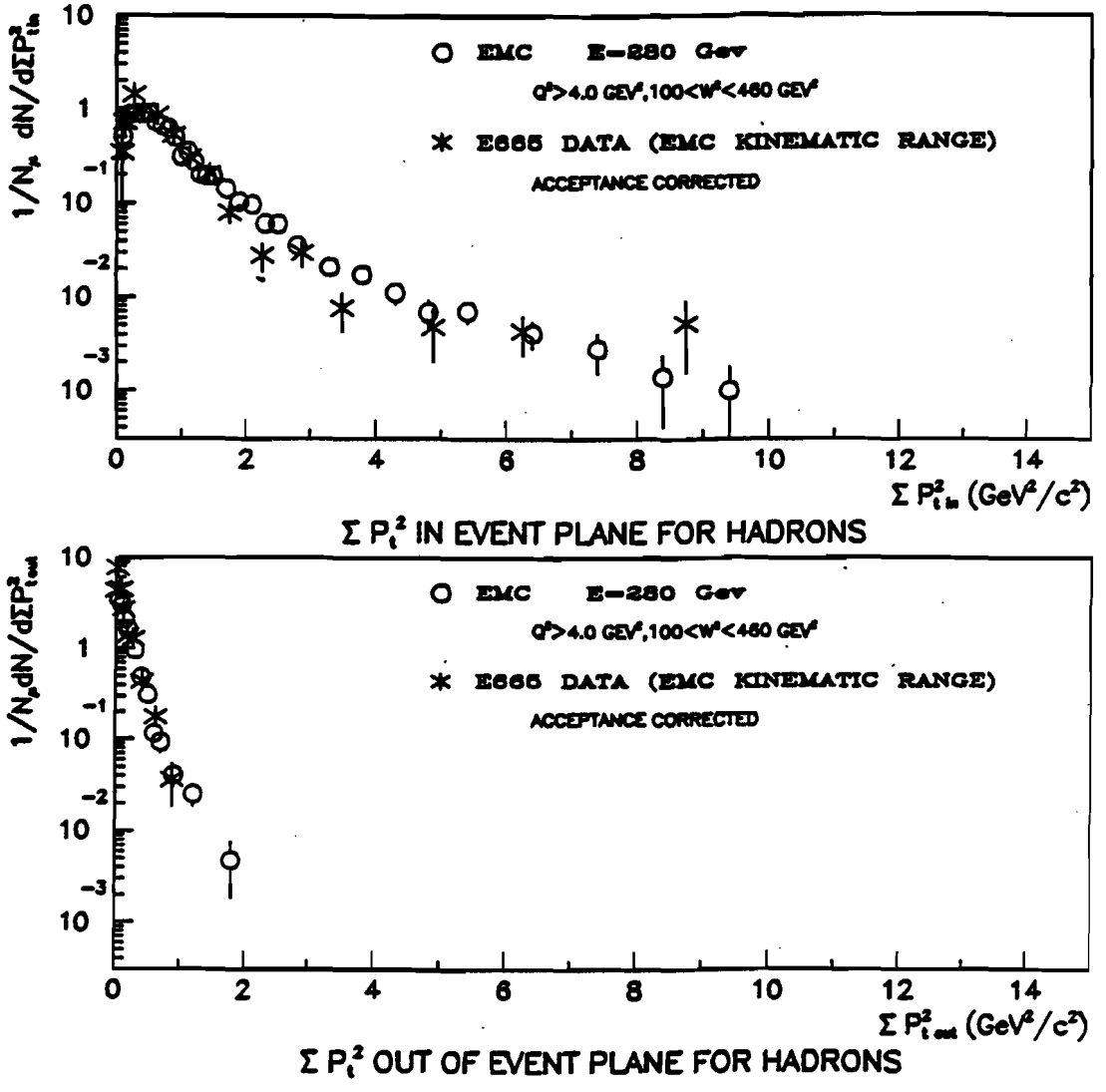

Figure 5.7: Normalized sum of $p_\perp^2$ in and out of the hadronic event plane for charged hadrons only for events with at least 4 charged hadrons. EMC kinematic range.

forcing the plane to be vertical had no effect on the points while using only charged hadrons for determination of the event plane caused the points to move upwards only by a couple of percent. (Note that the definition of the plane *requires* that they move somewhat when only the charged hadrons are used.)

Clearly, there is a tendency for events to have a planar structure. The agreement between the data and the Monte Carlo with hard QCD is quite good while the Monte Carlo with no hard QCD (even with increased fragmentation $p_\perp$) fails rather spectacularly in describing the data. Note also that in addition to an overall higher spectrum, the higher W data exhibit a more pronounced tail in the distribution of $p_\perp$ within the event plane compared to the lower W data. This is consistent with the picture we expect from hard QCD processes.

5.4 Energy and Particle Flow

Once the hadronic event plane is determined, it is possible to construct various ways of looking at the flow of particles within the plane to look for indications of two forward-going jets. Two of the simplest (and illuminating) distributions are the differential distribution for the number of particles as a function of the angle away from the photon direction within the event plane ($\frac{dN}{d\theta}$) and the scaled-momentum-weighted angular distribution ($\sum_i \frac{E_i}{W}\frac{dN}{d\theta}$) which I refer to as the *energy flow* within the event plane relative to the photon direction. Figures 5.10a and 5.10b show these

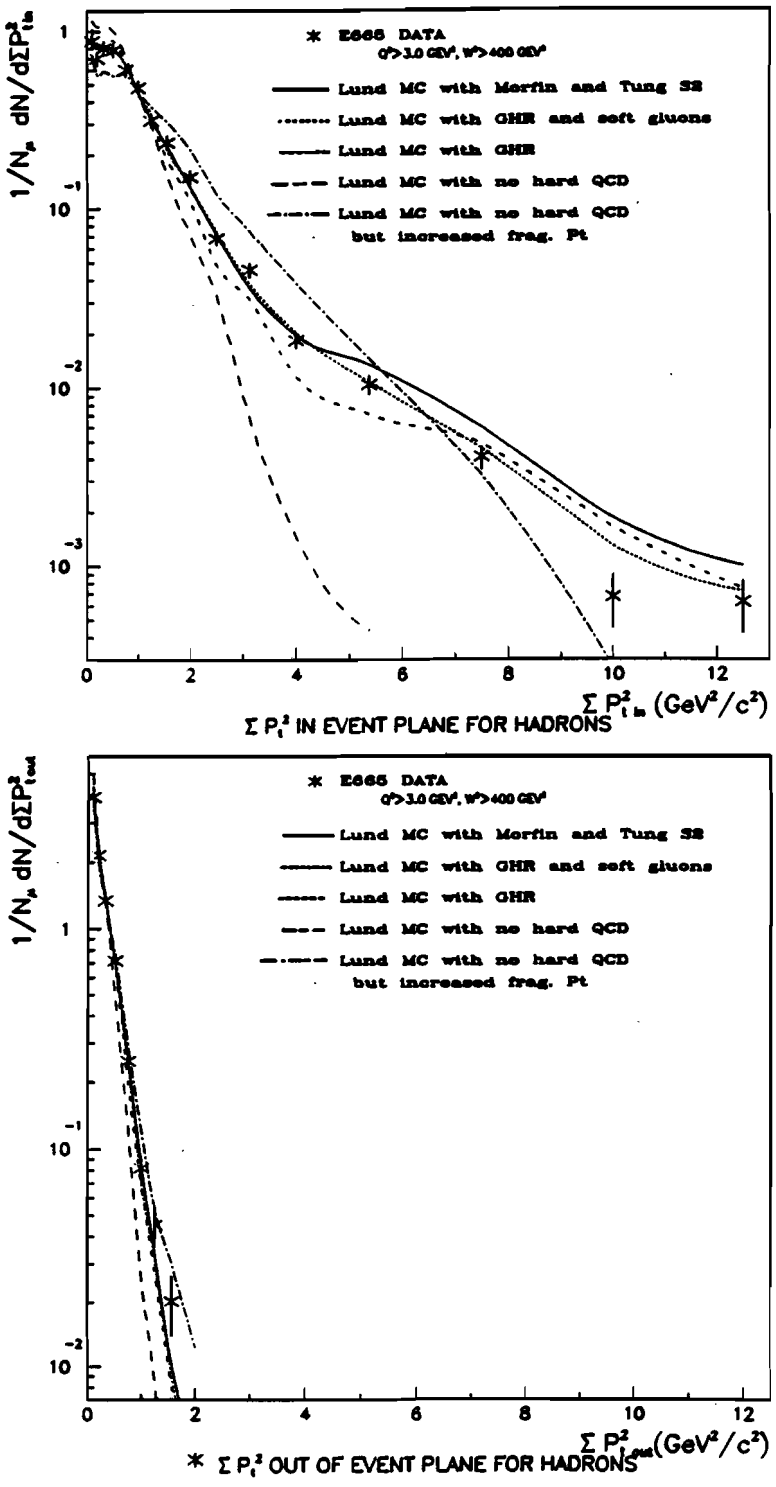

Figure 5.8: Normalized sum of $p_\perp^2$ in and out of the hadronic event plane for charged hadrons in the $W > 20GeV$ range. Event plane determined using both hadrons and photons.

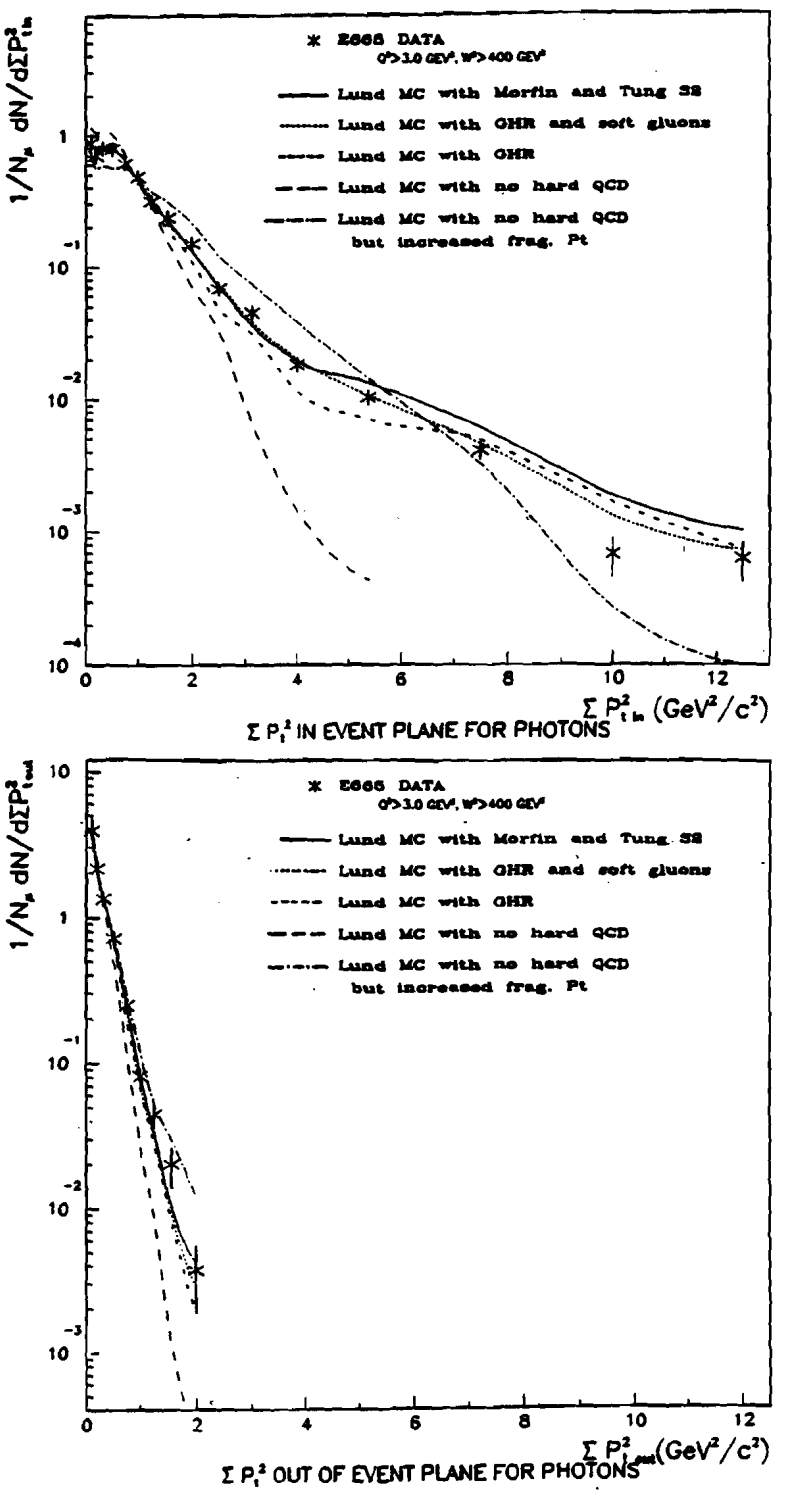

Figure 5.9: Normalized sum of $p_\perp^2$ in and out of the hadronic event plane for photons in the $W > 20GeV$ range. Event plane determined using both hadrons and photons.

two distributions for all events within the $W > 20GeV$ sample. Figures 5.11a and 5.11b show the same distributions but with a cut so that events are included only if they have at least one particle with $p_\perp^2 > 1.5(GeV)^2$. All of these plots have been made so that the particle with leading $p_\perp$ in the event plane will be at negative angle with respect to the photon direction ($\theta = 0$). With this cut, two distinct lobes on each side of the photon direction begin to appear. Figure 5.12a shows the energy flow when a cut is made on the smaller planarity tensor eigenvalue $Q_1 < 0.1$ with total multiplicity in the event greater than 4. This cut will select only events which are particularly planar without introducing specific transverse momentum requirements within the event plane. Figure 5.12b shows the energy flow when a cut on the sum of the squares of the transverse momenta in the event plane is greater than $2GeV^2$ (includes only events in the tail of the distribution in figure 5.8). Expectations from the Lund Monte-Carlo are also shown on these figures. Clearly, the energy flow is more sensitive to event structure than the multiplicity flow in any of these distributions.

It appears that in order to observe a two-lobed structure, some sort of cut on the transverse momentum in the event plane is required. Without such a cut, there are events which are quite planar but have no clear sign of a forward two-lobed structure. Although imposition of cuts on the transverse momentum in the event plane leaves events which exhibit a clear two-lobed shape, it is not clear that the

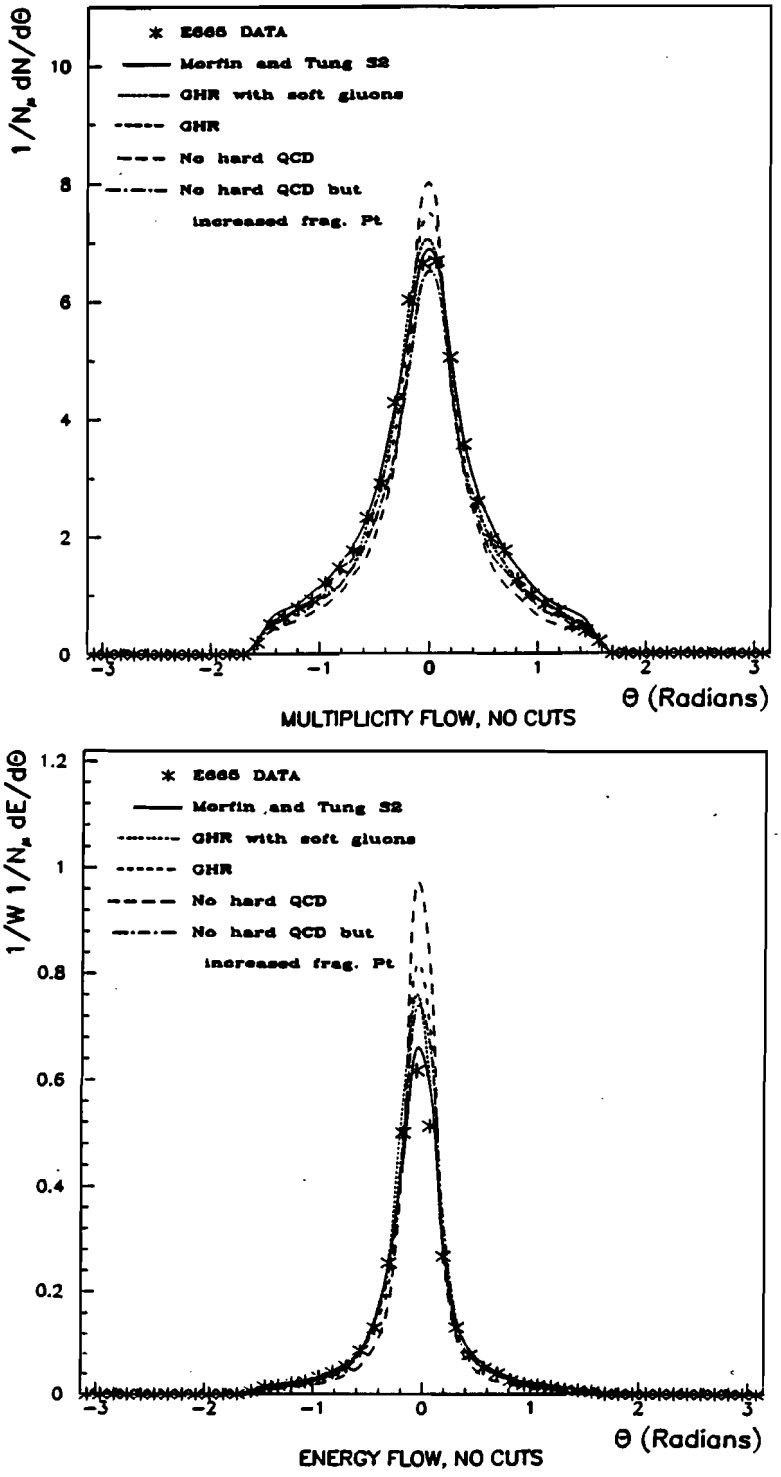

Figure 5.10: Angular particle flow and scaled energy flow for the CMS system for hadrons and photons for all $W > 20GeV$ events.

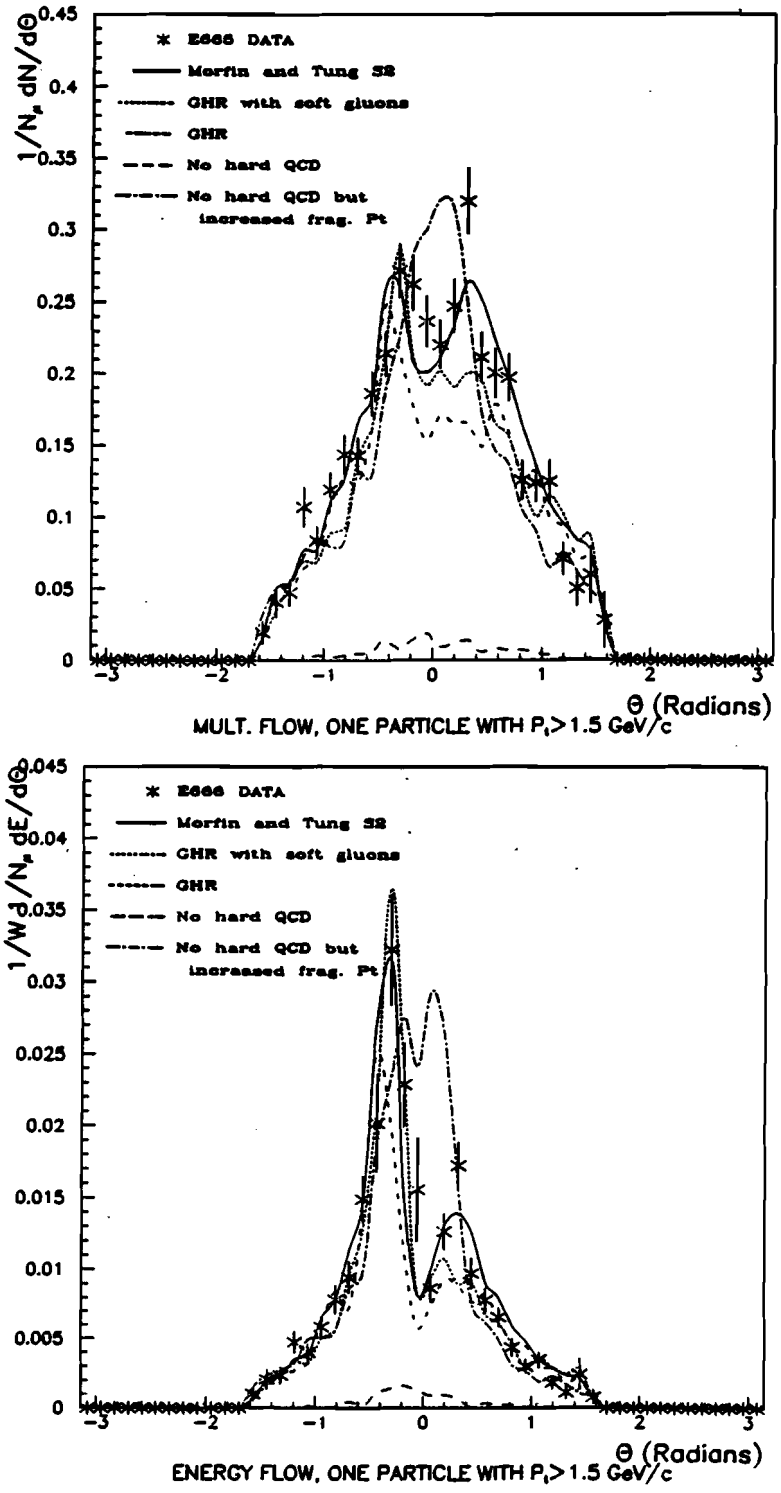

Figure 5.11: Angular particle flow and scaled energy flow for the CMS system for hadrons and photons for events in which at least one particle has $p_\perp > 1.5GeV$.

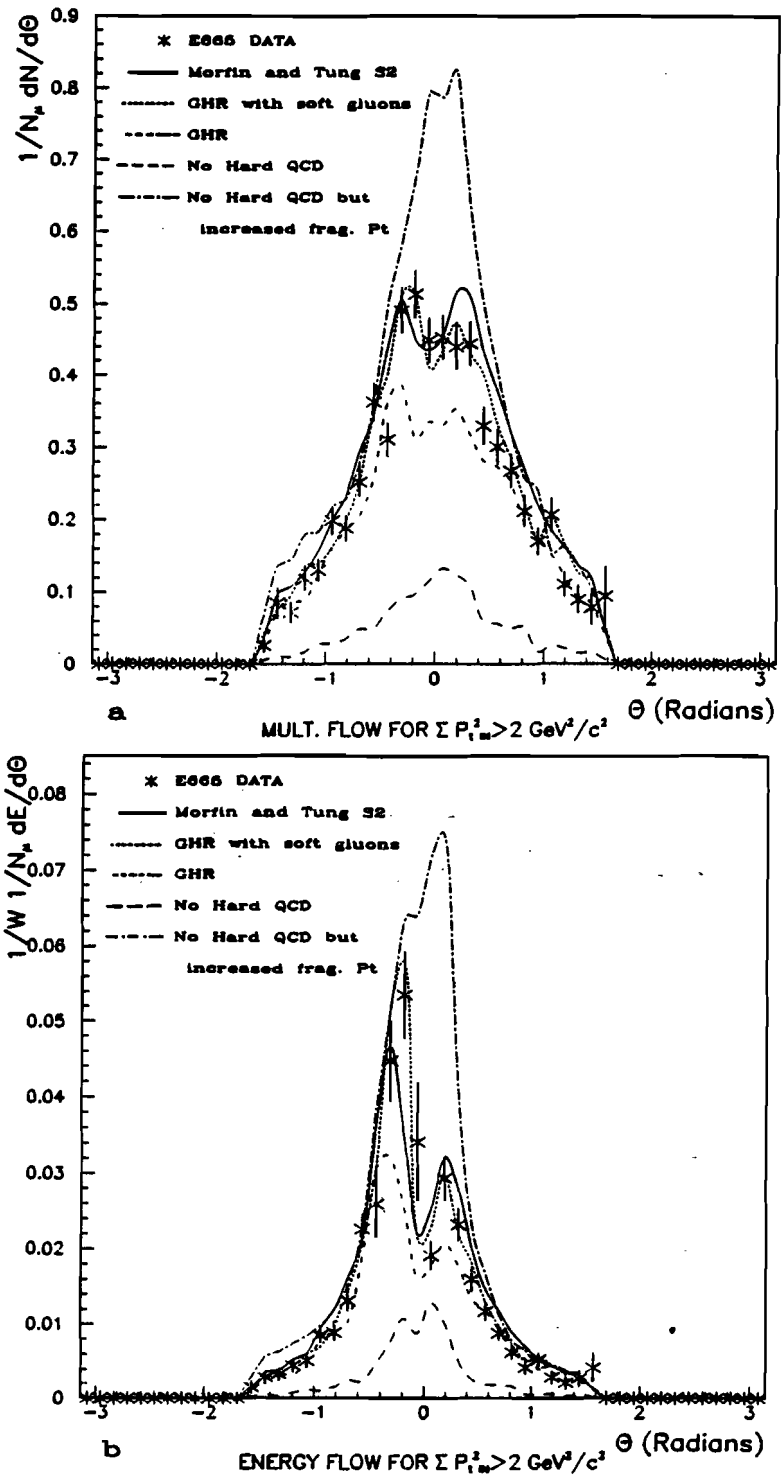

Figure 5.12: Scaled energy flow for the CMS system for hadrons and photons for a)events (uncorrected) with the smaller planarity eigenvalue $Q_1 < 0.1$ and multiplicity> 4 and b) events with $\sum p^2_{\perp in} > 2GeV^2$.

shape in and of itself obviously defines that these events originated from two initial 'hard, forward' partons. The nature of fluctuations in the fragmentation process will be such that events which pass the cuts will typically have a two-lobed structure regardless of the origin. The structure may look different but will still have some of the general qualities of the two-lobed structure from hard partons. As can be seen in the curves for the Lund Monte Carlo without hard QCD in the preceding plots, there are tremendously fewer events which pass the cuts but the ones which do still exhibit much of the same general shape as those which originated from an initial hard QCD process. It is important to consider not only the shape but the relative number of events which pass a given cut. Increasing the fragmentation transverse momentum will tend to increase the number of events which pass a given cut but is not consistent with the overall structure of events seen in earlier plots and the relative size and shape of the lobes is quite different than the data or the hard QCD models. The combined effect of shape and relative numbers of events which pass cuts, along with previous plots, requires that the two-lobed structures cannot simply be the result of fluctuations in the soft fragmentation. Some hard process must be occurring in these events and we can see that QCD seems to predict the shape and magnitude of the effect quite well. As can be seen from the different 'models' with hard QCD there are extra subtleties to the preceding statement. This discussion will be continued after introduction of the jet finding algorithm and the

results which it provides.

With sufficiently complete reconstruction of the hadronic final state and separated lobes of energy flow, it should be possible to reconstruct jet momenta which will correlate both in direction and magnitude with the momenta of the initial partons in the events. In addition, it will be possible to retain a higher proportion of events with multi-jet structure by explicitly cutting for that feature. Numerous algorithms have been developed for this purpose for e^+e^- and $p\bar{p}$ colliders. However, it would appear to make sense to once again utilize the knowledge of the hadronic event plane and photon direction in DIS in order to make the reconstruction easier. With that in mind, I have developed the following clustering algorithm (see figure 5.13

1. Particles with $x_F > 0$ (or higher x_F cut) are used to determine the hadronic event plane as described above.

2. Proceeding on a 'two forward jet' hypothesis, all forward particles on each side of the photon direction in the event plane are vectorially added to yield two 'jet momentum vectors'. In some cases it may be desirable to use only particles with x_F greater than some particular cut value in order to reduce confusion from the fragmentation region at $x_F = 0$. A similar cut which has more to do with the acceptance than a particular physics argument is a

minimum momentum cut.

3. The transverse momentum of each particle *relative to each jet axis* is calculated and particles may be reassigned to the two jets according to which jet offers the minimum p_T for that particle.

4. The preceeding step is iterated a couple of times. Monte-Carlo study shows that for true two-forward-jet events, that typically no more than two or so particles are reassigned on the first iteration, perhaps one on the second and rarely one on the third. On the other hand, if the two-jet hypothesis is incorrect, then two or more particles may be exchanged on every iteration. Hence, it appears that there is little reason to ever iterate more than 3 times.

5. Cuts are made using various quantities associated with the 'final' jet momentum vectors to separate events which will be designated as two-jet events from those which are one-jet events. The quantities which are used for making cuts are the angle between the two jet vectors (θ), the angle between each jet vector and the photon direction (ψ_1 and ψ_2) the magnitude of the momentum of each jet and the ratio of the magnitudes. In addition to removing single forward jet background, the cuts can also be manipulated to help separate different topologies of the final state jets (and therefore hopefully initial parton configurations).

Note that the combination of angle and momentum cuts will result in an effective cut on $p_\perp$ in the hadronic plane. However, because it is designed to look for 'jetty' events, it is far more efficient at obtaining an enriched sample of events without such a severe cut that little data remains. When applied to the true final state particles from the Monte Carlo, the above algorithm can be used to produce a set of events which is highly enriched in two forward-going jets. Figure 5.14a shows the enrichment of two jet events in the remaining data sample as a function of the angle between the two reconstructed jet axes for the true stable hadrons and photons from the standard Monte Carlo for events in the $W > 20GeV$ range. The same plot shows the percentage of the total multi-jet events which remain in the sample and the total percentage of all events which are retained after cuts. A 10 to 1 ratio of true multi-jet to single-jet events is obtained while over 30% of the available multi-jet events are retained. Using the parton distributions of Gluck, Hoffman and Reya moves the starting multi-jet fraction to $\sim 30\%$ and the final enriched fraction to $\sim 80\%$. Figure 5.14b shows the same curves for the range $10 < W < 20GeV$ where it is seen that it is impossible to achieve very good enrichment even with very severe cuts. Hence, we see that the *potential* for jet separation in the $W > 20GeV$ range is very impressive indeed.

Real detector efficiencies and smearing will result in a decrease in the signal-to-noise ratio. Clearly, if efficiency is sufficiently low, it will be practically impossible

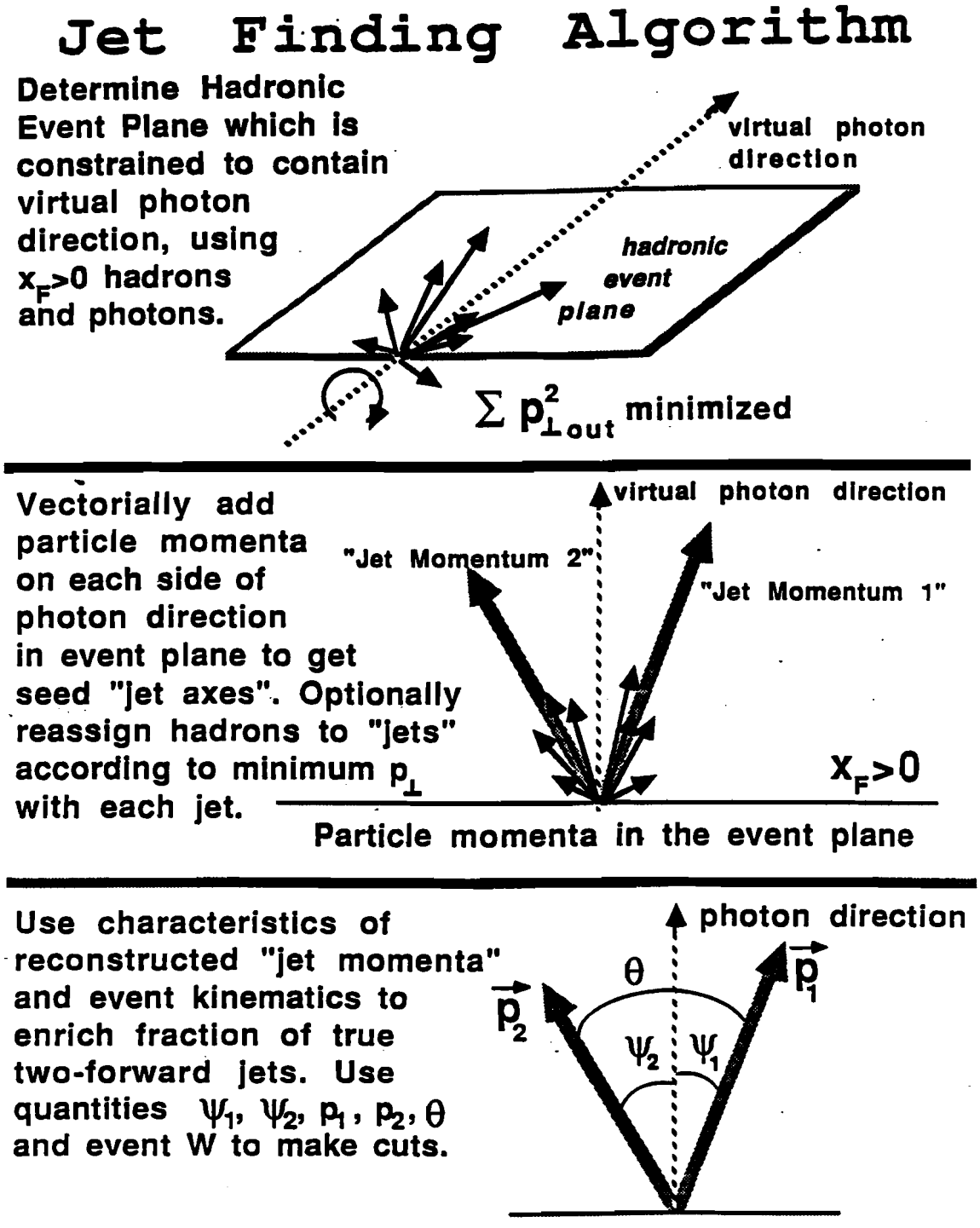

Figure 5.13: Jet finding algorithm.

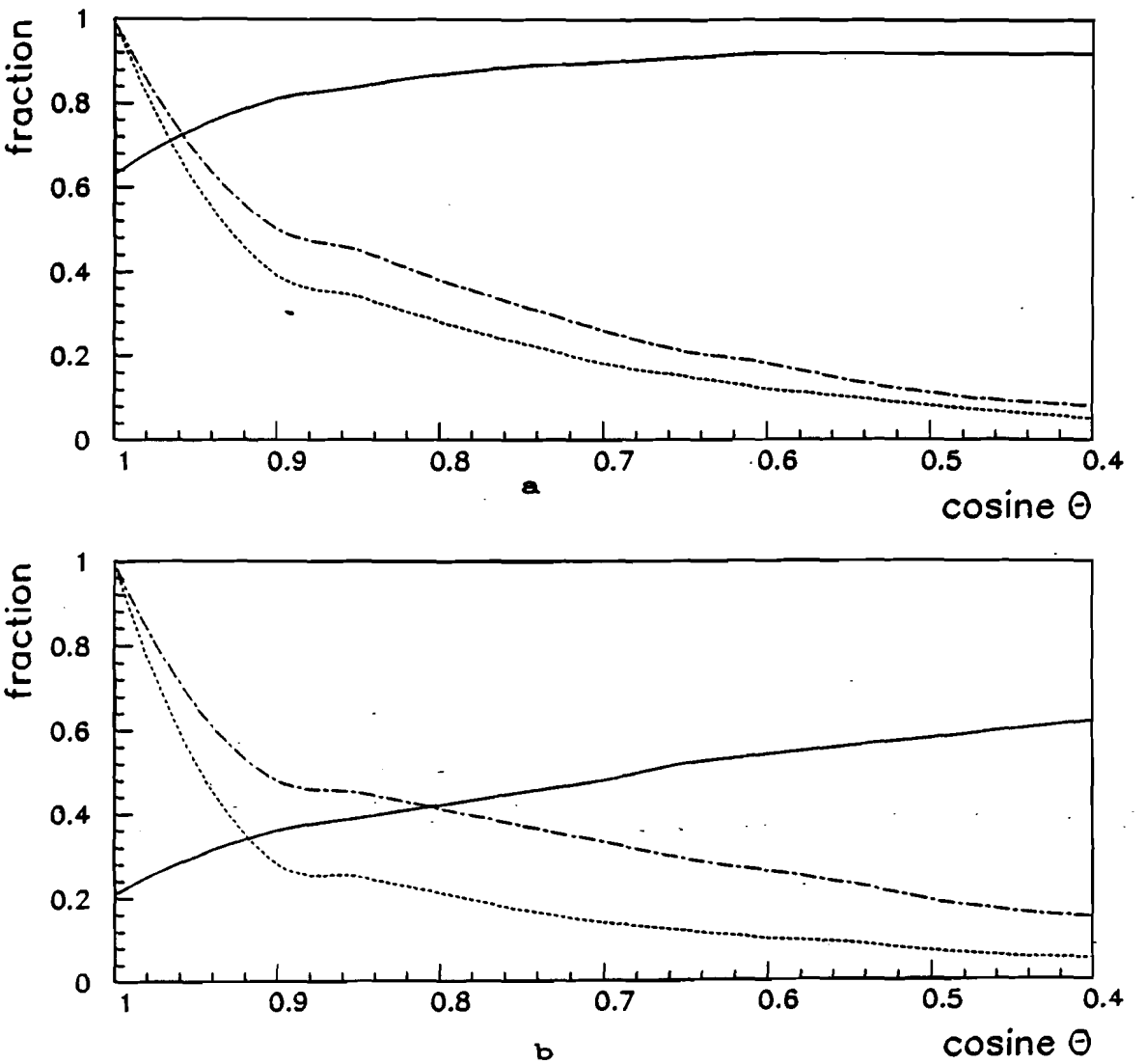

Figure 5.14: Fraction of multi-jet events in retained sample (solid line), fraction of all events retained (dashed line) and fraction of multi-jet events retained (dash-dot line) as a function of the angle between jets for a) $W > 20GeV$ and b) $10 < W < 20GeV$ truth Monte Carlo using Morfin and Tung S2 parton distributions.

to reliably reconstruct jet momenta or directions. As discussed in section 5.1, it is important to include both charged hadrons and photons if the average visible energy is to be over 50%. Figure 5.15 shows the fraction of true multi-jet events and fraction of events remaining for realistic detector geometric acceptance, efficiency and smearing for Monte Carlo events as a function of angle between forward 'jet' axes. Figure 5.15a shows the result when both photons and charged hadrons are used while figure 5.15b shows the same result for charged hadrons only. We see that considerably fewer events pass the cuts using only the charged particles. Later, it will be shown that the quality will be poorer as well. In the analysis which follows, a 'standard jet cut' will be used except as noted. The parameters for the standard cut are:

- The cosine of the angle between the two jet axes must be less than 0.7 (the angle greater than $\sim 45°$).
- The cosine of the angle between each jet axis and the virtual photon direction must be less than 0.98 (the angle greater than $\sim 11°$).
- The ratio between the magnitude of the smaller to larger jet momentum must be greater than 0.25.
- A cut on 'expected opening angle' for the reconstructed momentum is applied. This angle is simply given by $\phi = 0.4/p_{jet}$. The cut value is $\phi < 0.6$ radians.

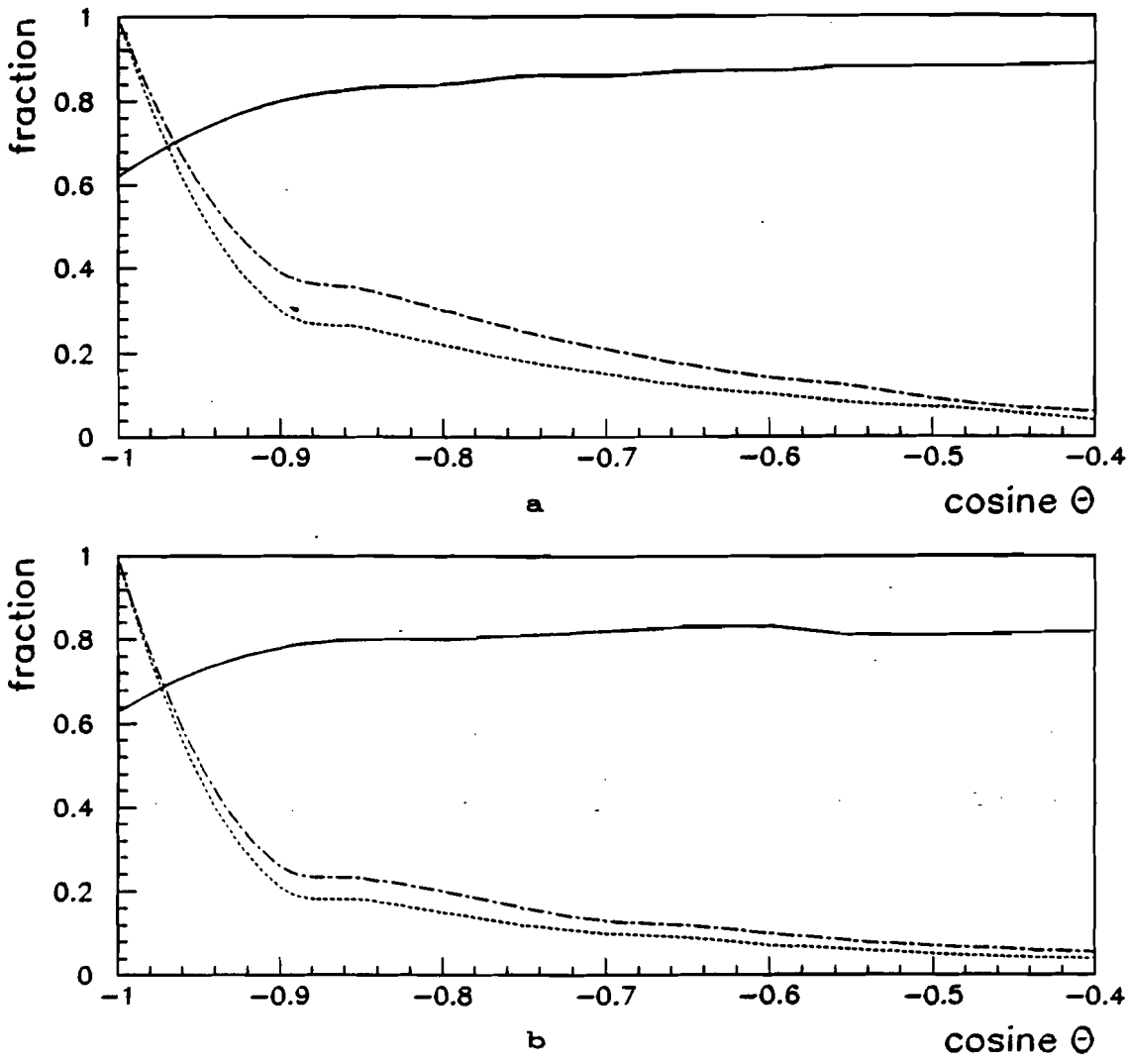

Figure 5.15: Fraction of multi-jet events in retained sample (solid line), fraction of all events retained (dashed line) and fraction of multi-jet events retained (dash-dot line) as a function of the angle between jets using a) charged hadrons and photons and b) using only charged hadrons (using Morfin and Tung S2 parton distributions).

The idea is to eliminate events where one jet momentum is so small that it is likely to have simply resulted from a fragmentation fluctuation. In practice, given the other cuts, this cut is practically never enforced.

- No explicit cut on particle multiplicity is required (other than the implicit one that there must be at least one particle on each side).

- No explicit cut is made on jet momentum (other than the implicit cut that is imposed by the momentum ratio cut combined with the kinematic range and the opening angle cut which corresponds to quite low momentum).

Using these cuts, 1146 events remain from the initial sample of 8211 events (14%).

Figures 5.16a and 5.16b show the particle and energy flow around the virtual photon direction for events which pass the standard jet cut. Notice that the two-lobed structure is more distinctive than when a $p_\perp$ cut was applied. In addition, over twice as many events passed the cuts. Monte Carlo shows that 85% of these events actually contain two hard forward partons. Figure 5.17 is the same as 5.16b but plotted such that negative angles will correspond to the side of the plane which contained the higher momentum jet. Clearly, this way of plotting these events is more in the spirit of the earlier plots than plotting the events with the highest $p_\perp$ particle on the left. Once again, we see that the jets will tend to be asymmetric and that the Monte Carlo prediction with hard QCD supplies a good description

of the data.

Although the previous figures show a two-lobed structure, the true width of the jets has been smeared out because of the angular distribution. By plotting the energy flow around the reconstructed jet axes we can see the true width of the reconstructed jets. Figure 5.18 shows the particle and energy flow plotted around the reconstructed jet axes for the higher momentum jet while figure 5.19 is for the lower momentum jet axis. In each case, the reconstructed jet axis is placed at 0 radians while the other jet falls in the region of positive angle. These plots have been acceptance corrected in the standard, bin-by-bin fashion. The acceptance correction causes the sharpness of the peaks to be degraded somewhat compared to those of the uncorrected data. This is due to the fact that the acceptance for lower momentum particles (small x_F) is low. For a two-lobed event, the high momentum particles will lie in the region of the lobes. The edges of the lobes (and this includes the central region around 0 radians) will be relatively more populated with lower momentum particles for which the detector has a low acceptance. Figure 5.20 shows the same energy flow plots but without any acceptance correction applied. In fact, it is possible to actually make an explicit cut on the x_F of used particles which is higher than the standard cut of $x_F > 0$. This produces an even greater apparent separation of the jets and by cutting out events where the jet is not very well determined also improves the correlation between the initial parton directions and

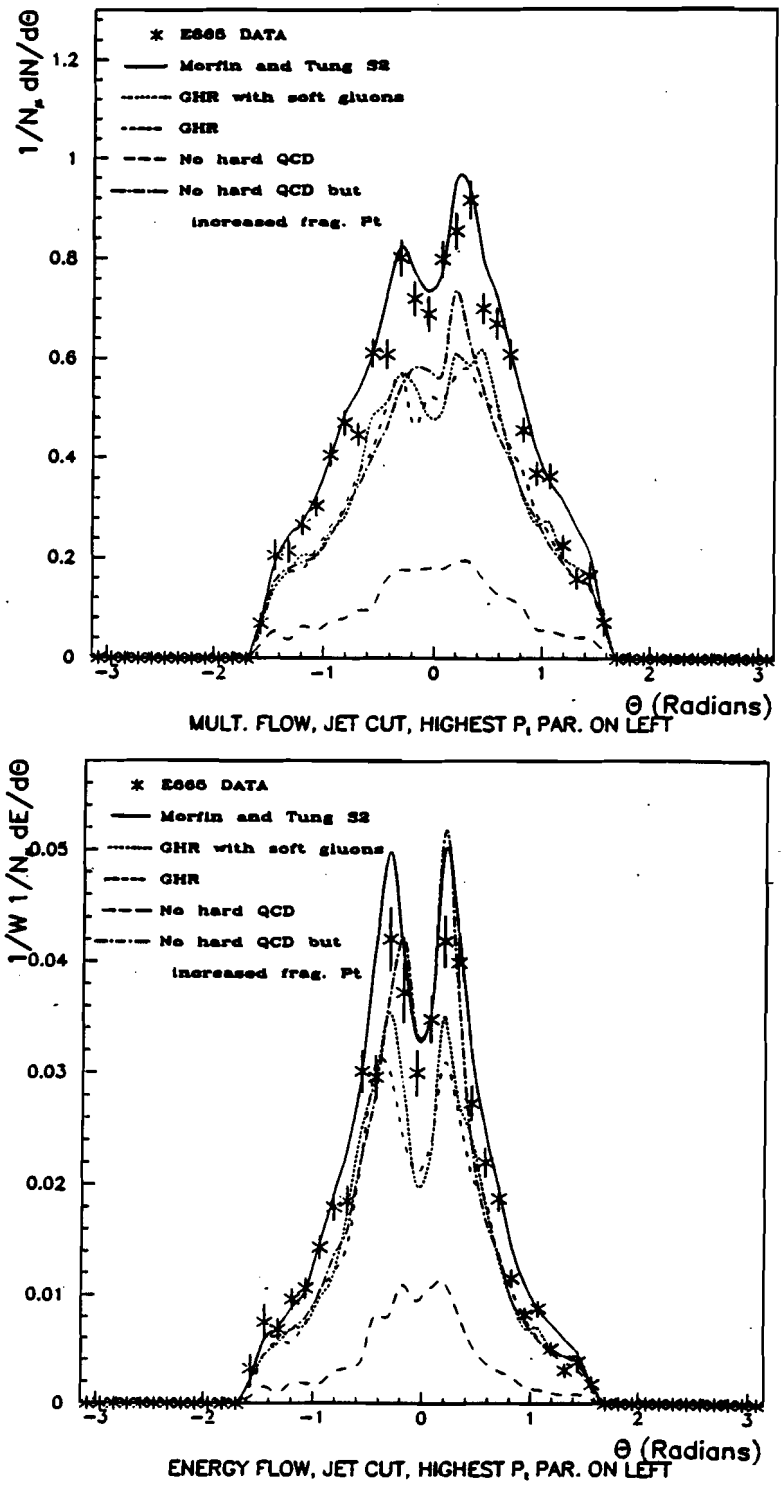

Figure 5.16: Angular particle flow and scaled energy flow for the CMS system for hadrons and photons for events which pass standard jet cut. The plots have the photon at 0 radians with the highest $p_\perp$ particle at negative angle.

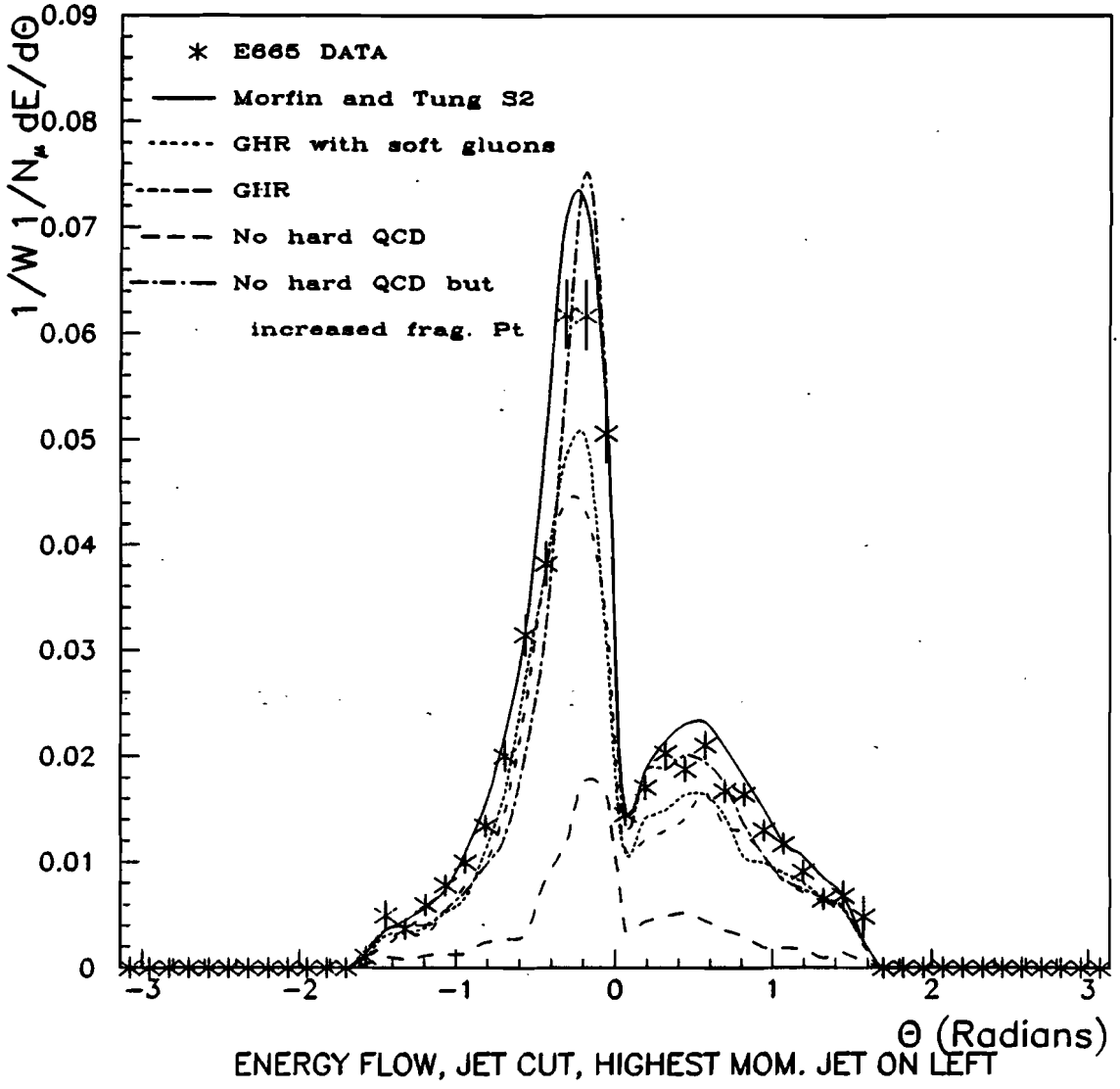

Figure 5.17: Scaled energy flow for the CMS system for hadrons and photons for events which pass standard jet cut with the highest momentum jet at negative angle.

the direction of the final jet axes (according to the Monte Carlo). These plots show that there are jets which are quite well collimated and separated from each other. Figure 5.21 shows the energy flow plots if only charged particles have been used in the analysis. In this case, not only have fewer events passed the jet cut, but as can be seen, many of those events will have a single particle in one of the two jets which produces a spike in the energy flow at zero radians. Even if it is the truth, it is difficult to convince oneself of the jettiness of an event when there is only one particle in one of the jets.

The overall number and shape of the jets appears to be in good agreement with the predictions from the Lund Monte Carlo with hard QCD. The prediction without hard QCD but increased fragmentation $p_\perp$ actually reproduces the overall shape and number of these events quite well but it fails just about everywhere else. Notice that the number of such events differs for the Monte Carlo using the parton distributions of Morfin and Tung (standard) and using those of Gluck, Hoffman and Reya. The data would appear to fall between the two Monte Carlo distributions. It is very interesting now to consider the overall impression from all of the different energy flow plots with different cuts. We see that the plots which explicitly require some high $p_\perp$ are fit best by the prediction using the parton distributions of Gluck, Hoffman and Reya with soft gluons included. In addition, we see that the soft gluons had a very important effect in order to achieve this relative agreement. Although

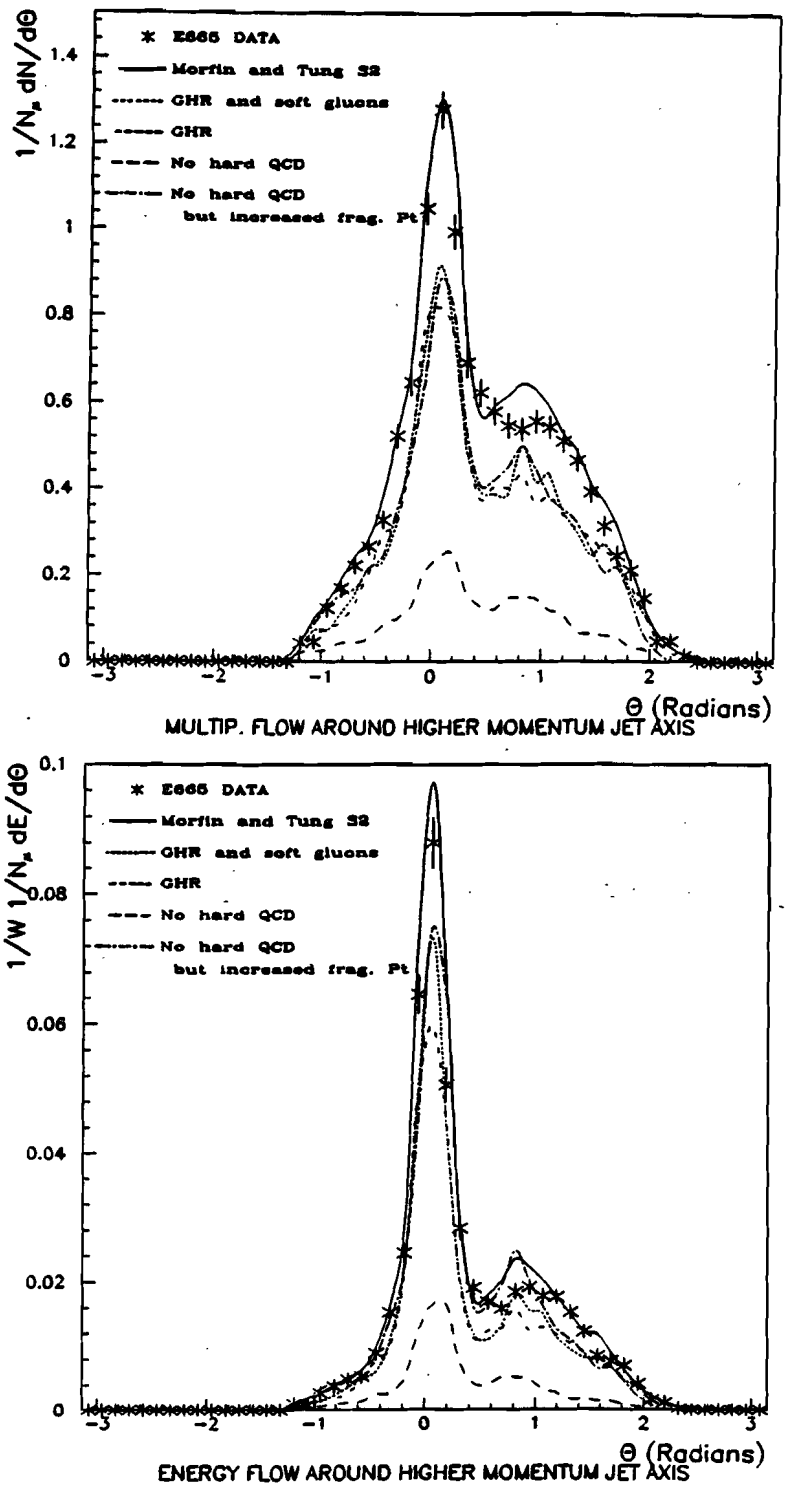

Figure 5.18: Angular particle flow and scaled energy flow for the CMS system for hadrons and photons for events which pass standard jet cut. The plots have the the higher momentum jet axis at 0 radians with the other jet at positive angle.

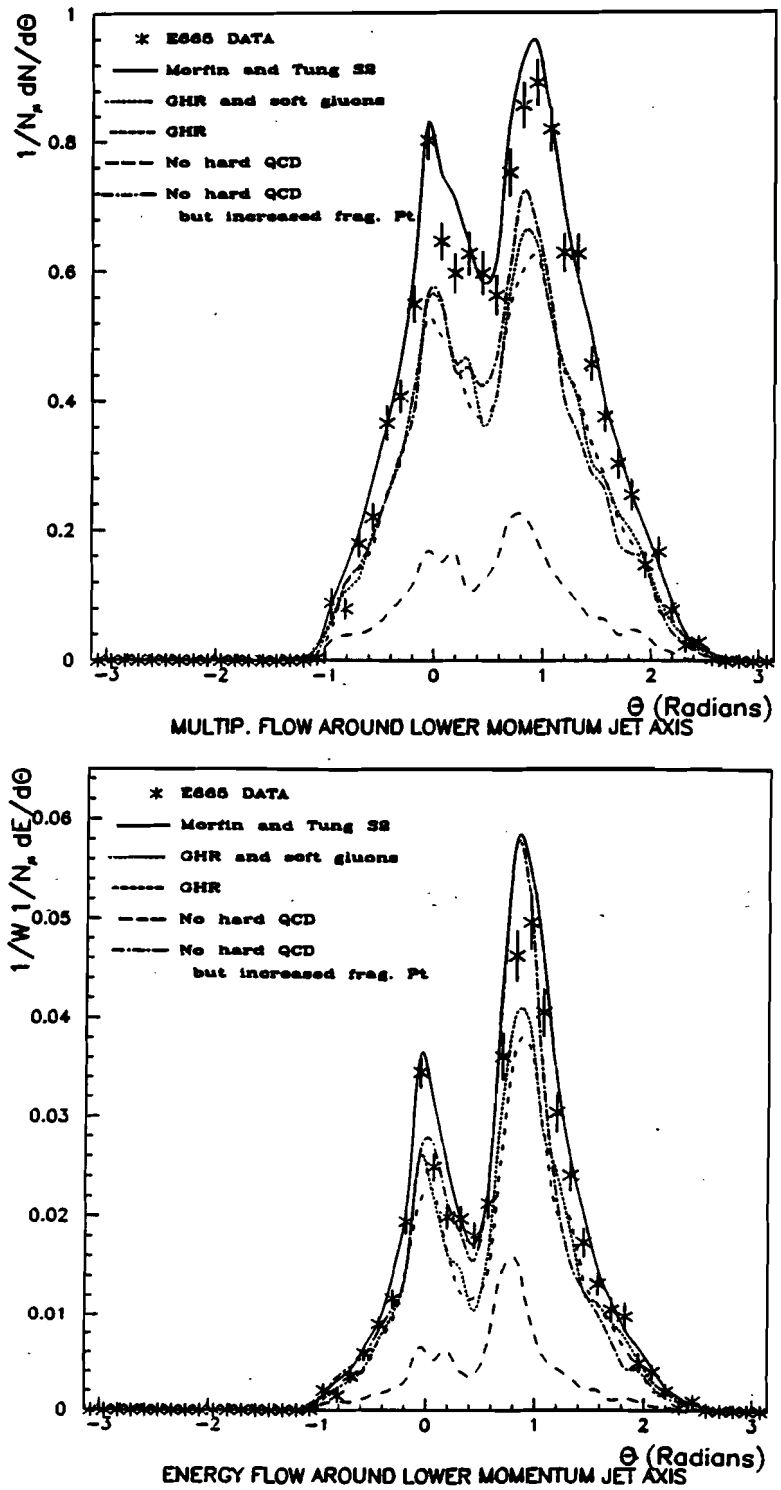

Figure 5.19: Angular particle flow and scaled energy flow for the CMS system for hadrons and photons for events which pass standard jet cut. The plots have the the lower momentum jet axis at 0 radians with the other jet at positive angle.

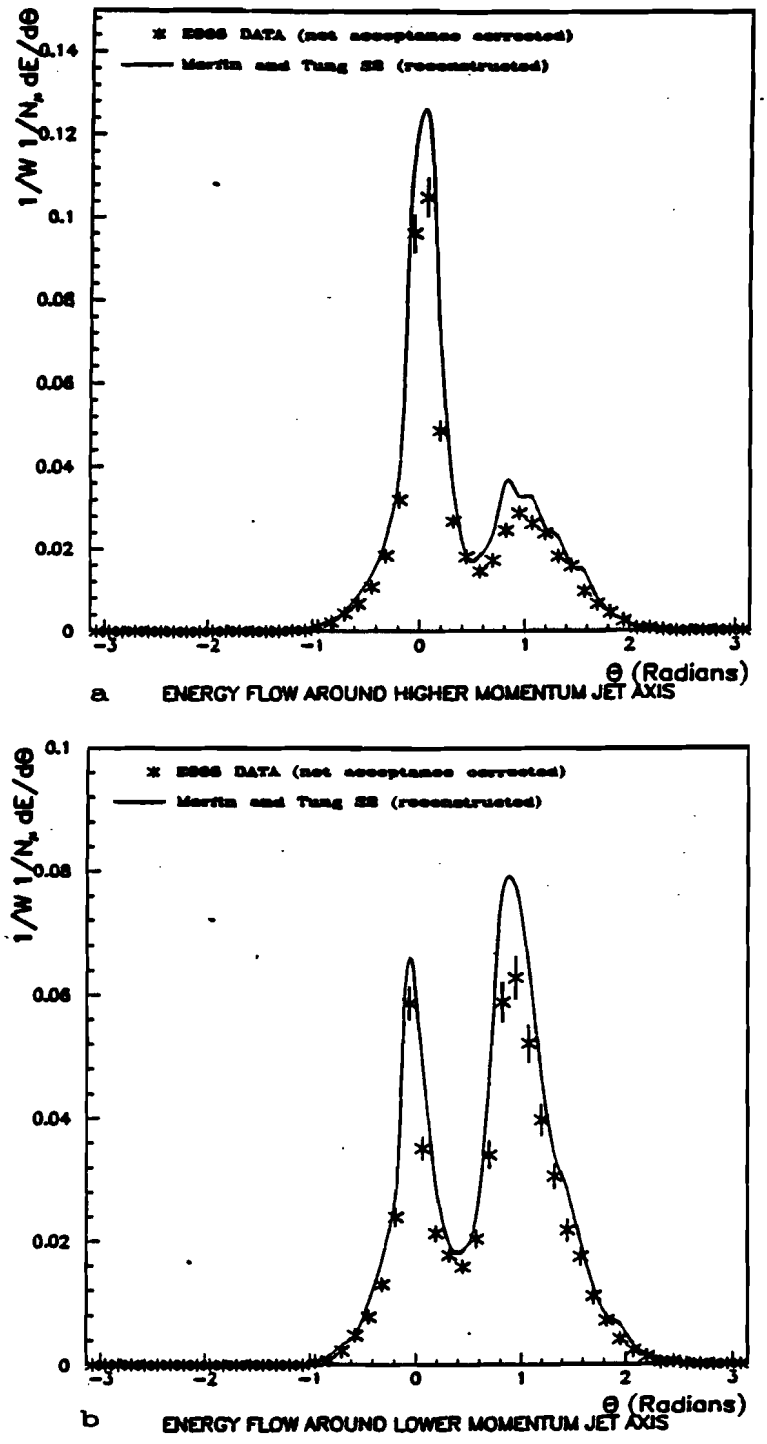

Figure 5.20: Scaled energy flow (without acceptance correction) for the CMS system for hadrons and photons for events which pass standard jet cut. Plotted for a) higher momentum jet axis at 0 radians and b) lower momentum jet axis at 0 radians.

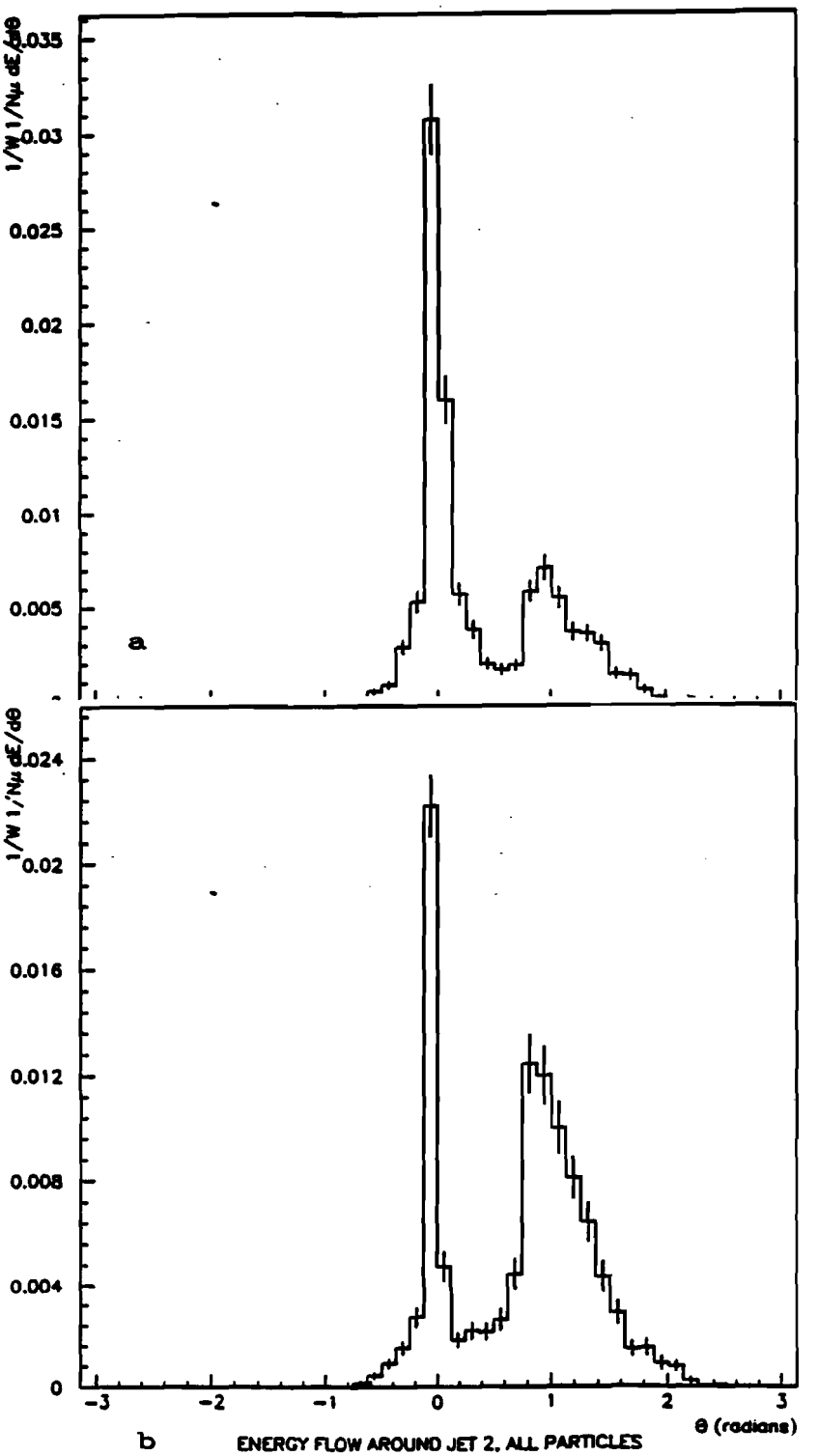

Figure 5.21: Scaled energy flow (without acceptance correction) for the CMS system for charged hadrons only for events which pass standard jet cut. Plotted for a) higher momentum jet axis at 0 radians and b) lower momentum jet axis at 0 radians.

the prediction using Morfin and Tung parton distributions is too small for the larger magnitude lobe, it is gives the best fit to the smaller lobe and none of the models really matches the smaller lobe properly. When the jet cut is applied, we see that the data now fall between these two predictions. Aside from the question of the gluon distribution and soft gluons, it is also possible that some adjustment to the QCD calculation for photon-gluon fusion could account for the observed differences in shape with different cuts.

Recall that the Monte Carlo indicates that over 80% of the events in the plots with jet cuts will actually have two forward partons. In other words, at most 20% of the events will be background which has resulted from fluctuations in the fragmentation of a single forward quark. According to the Monte Carlo, these events will have shapes not terribly different from many of the 'true' multi-jet events. The energy flow for background events is also shown in figure 5.18. The fact that such events exist is simply a fact of life which must be dealt with in attempting to examine 'jets' from partons. The relative fraction of such events which can believably be produced given the known typical fragmentation $p_\perp$ will always be the criterion which must be considered. Clearly, in the highest energy e^+e^- and $p\bar{p}$ colliders, there is no question that the events exhibit multiple separated jets. Nobody believes that these are simply fluctuations in the fragmentation process because it is known that such fluctuations would be ridiculous given the known typical trans-

verse momentum of fragmentation. Here, we still have *some* background in our data for $W > 20GeV$ but it appears that we have finally crossed the threshold into the region that it is clearly silly to attempt to blame all of the multi-jet effects simply on fluctuations from fragmentation. This fact has been demonstrated in several plots where the Monte Carlo is run without hard QCD but with an increased fragmentation $p_\perp$. With this in mind, we can proceed to study the reconstructed jets.

5.5 Properties of Reconstructed Jets

Given a sample of events which have two separated forward jets of hadrons, we can ask what are the properties of those jets and how do those properties correlate with the partons which initiated them? Even if all of the events are guaranteed to contain two hard, forward partons the fragmentation process can still make the final hadron jets look quite different from the initial parton momenta. Clearly, some of the initial longitudinal momentum of the partons will be converted into transverse momentum and mass of the hadrons so that it is not expected that the reconstructed jet momenta are exactly the same as those of the initial partons. Still, we can take the approach that what we are studying is the properties of the hadron jets and then make use of the Monte Carlo in order to interpret those results in terms of partons.

We can fully characterize the differential cross section for production of two jets (at a fixed energy scale) by two variables, the angle between the two jets (θ) and the ratio of the magnitudes of the momenta (R). Figure 5.22 shows the distribution of the cosine of the angle between the two jet axes for events which pass the standard jet cut. Shown on the same plot are the predictions from the various versions of the Lund Monte Carlo. Note that this plot is normalized to the number of events which pass the cut rather than the total number of events. Any of the QCD-based predictions appear to do a fine job of fitting the distribution while the predictions without QCD fail to match the data. It is particularly interesting to see that the model with no QCD but increased fragmentation $p_\perp$ does not fit the data even though the total number and average energy flow which passed the cuts was in fairly good agreement. Figure 5.23 shows the ratio of the smaller to larger jet momentum for the events which pass the standard jet cut along with the Monte Carlo predictions. The falloff of the distribution at low ratios is due to the jet cut. Once again, we see here that any of the models which include hard QCD fit the data well while those without do a relatively poor job. Figure 5.24 shows the distribution of the magnitude of the momentum for each reconstructed jet.

Although I think there are probably no great truths to be learned from them, for completeness, I present a number of plots on the multiplicity of the multi-jet events and individual particle properties with respect to the jet axes. Figure 5.25 shows

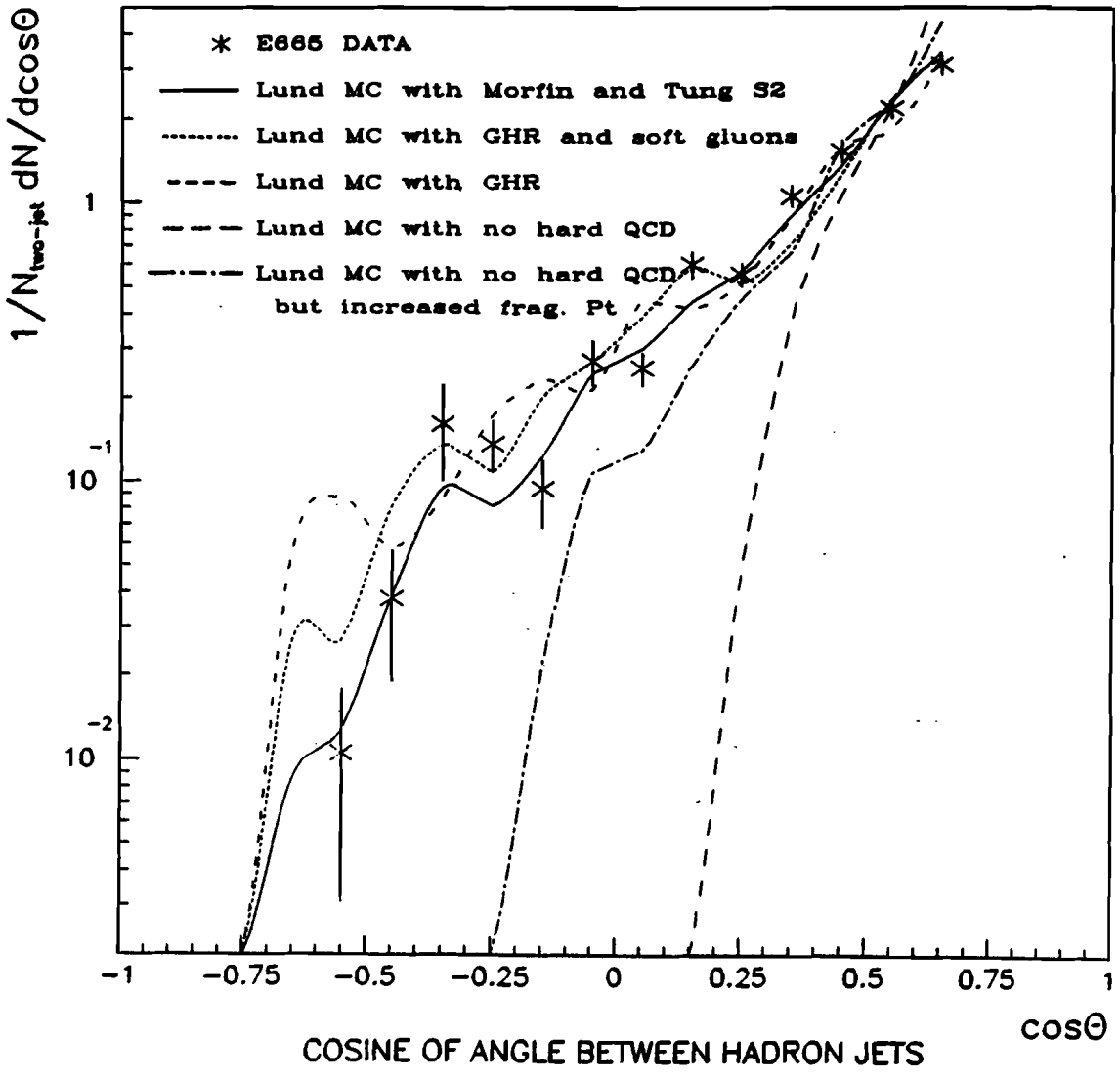

Figure 5.22: Distribution of the cosine of the angle between the two forward jets for events which pass jet cuts. The cutoff at 0.7 is due to the jet cut.

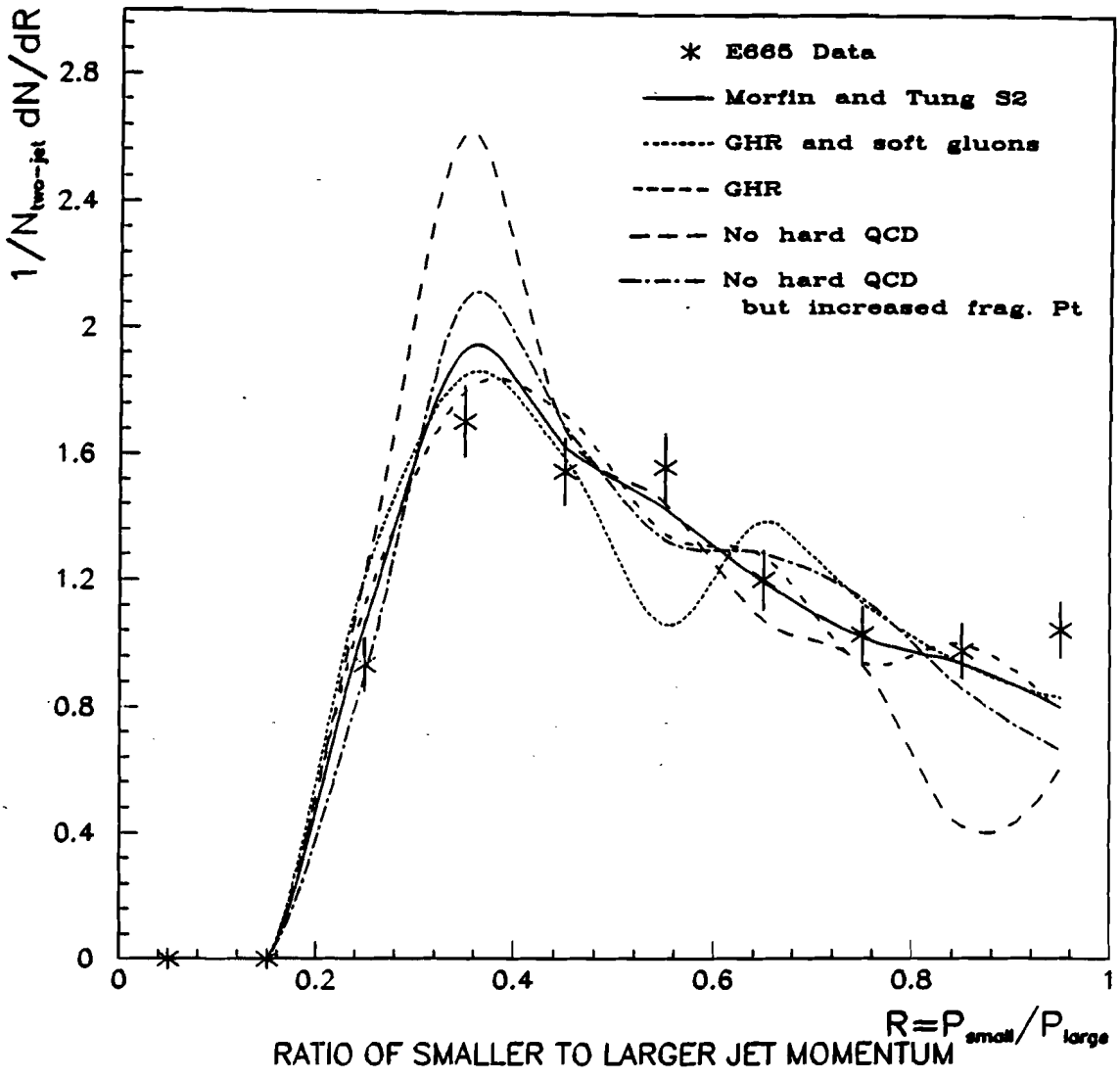

Figure 5.23: Distribution of the ratio of smaller to larger momentum for the two forward jets for events which pass jet cuts. The cuttoff at 0.25 is due to the jet cut.

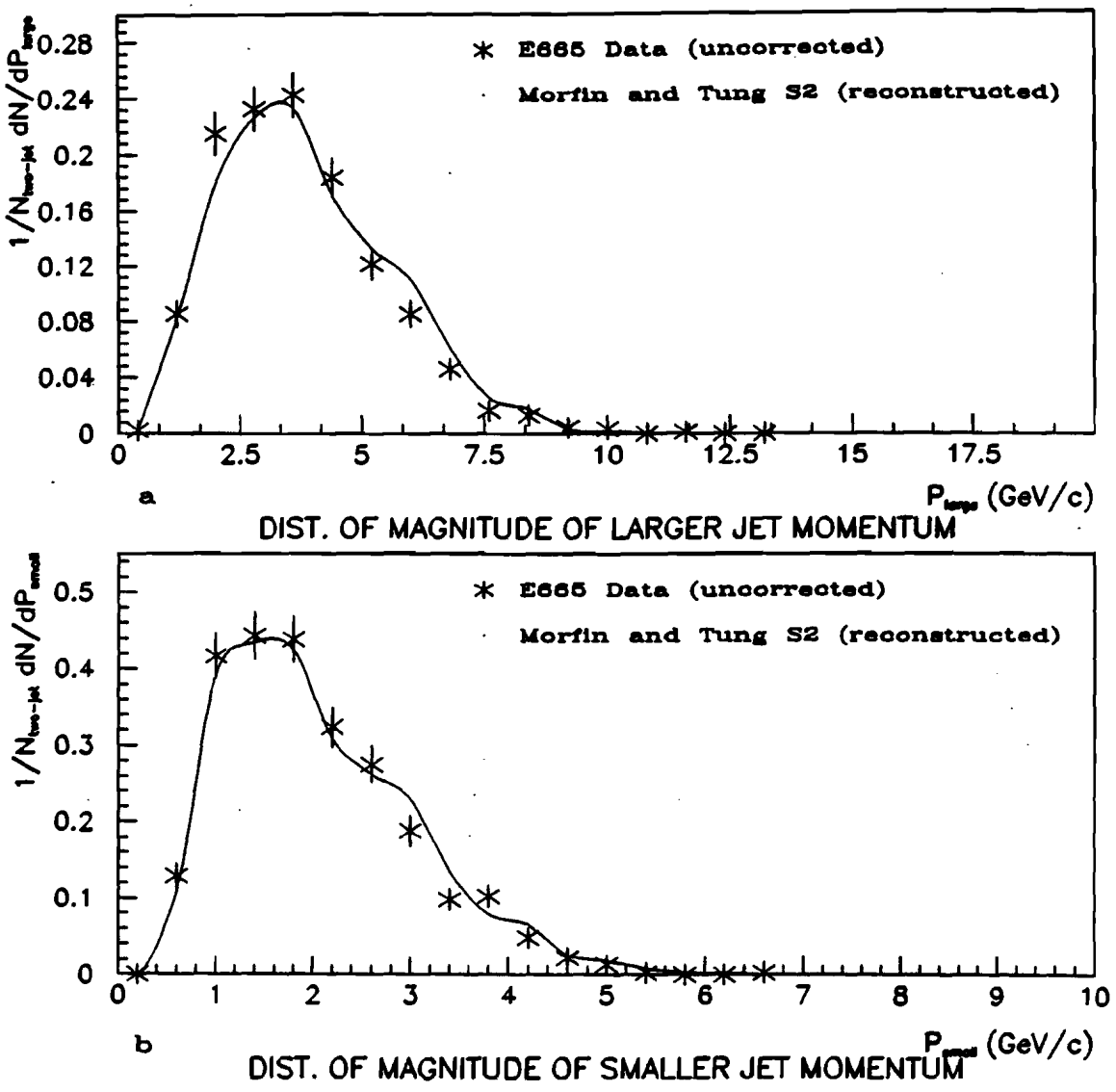

Figure 5.24: Distribution of observed momentum (not acceptance corrected) for a) the larger jet and b) the smaller jet for events which pass the standard jet cut. The relatively sharp cutoff on the lower jet momentum is due to the jet cut.

the total, charged and photon multiplicity for all events and for those events which pass the standard jet cut. Figure 5.26 shows the same set of figures but for each jet's assigned particles. These are not acceptance corrected and the Monte Carlo comparison is made with reconstructed Monte Carlo. Overall good agreement is seen between the data and Monte Carlo. Note that a large number of events have one or the other jet with a charged multiplicity of only 0 or 1. Inclusion of the photons is once again seen to be important.

Figure 5.27 shows distributions of $p_\perp^2$ with respect to each jet axis for all of the particles in the event. Figure 5.28 shows the same plots but including only the particles assigned to that jet for each axis. Clearly the plots with only assigned particles must have lower average $p_\perp$ than the other plots by definition. Still the Monte Carlo without hard QCD but increased fragmentation $p_\perp$ does not fit these very well...one more nail in the coffin.

Figure 5.29 shows the longitudinal momentum squared distribution for the particles assigned to each jet. Once again, by definition, jet 2 will have smaller longitudinal momenta. There appears to be no power in these plots to differentiate between the different models presented here. Figure 5.30 shows the z with respect to the total jet momentum distribution for the assigned particles for each jet. The small spike at $z = 1$ in the lower momentum jet is due to those events in which this jet was defined by a single particle. There is no discernable difference between

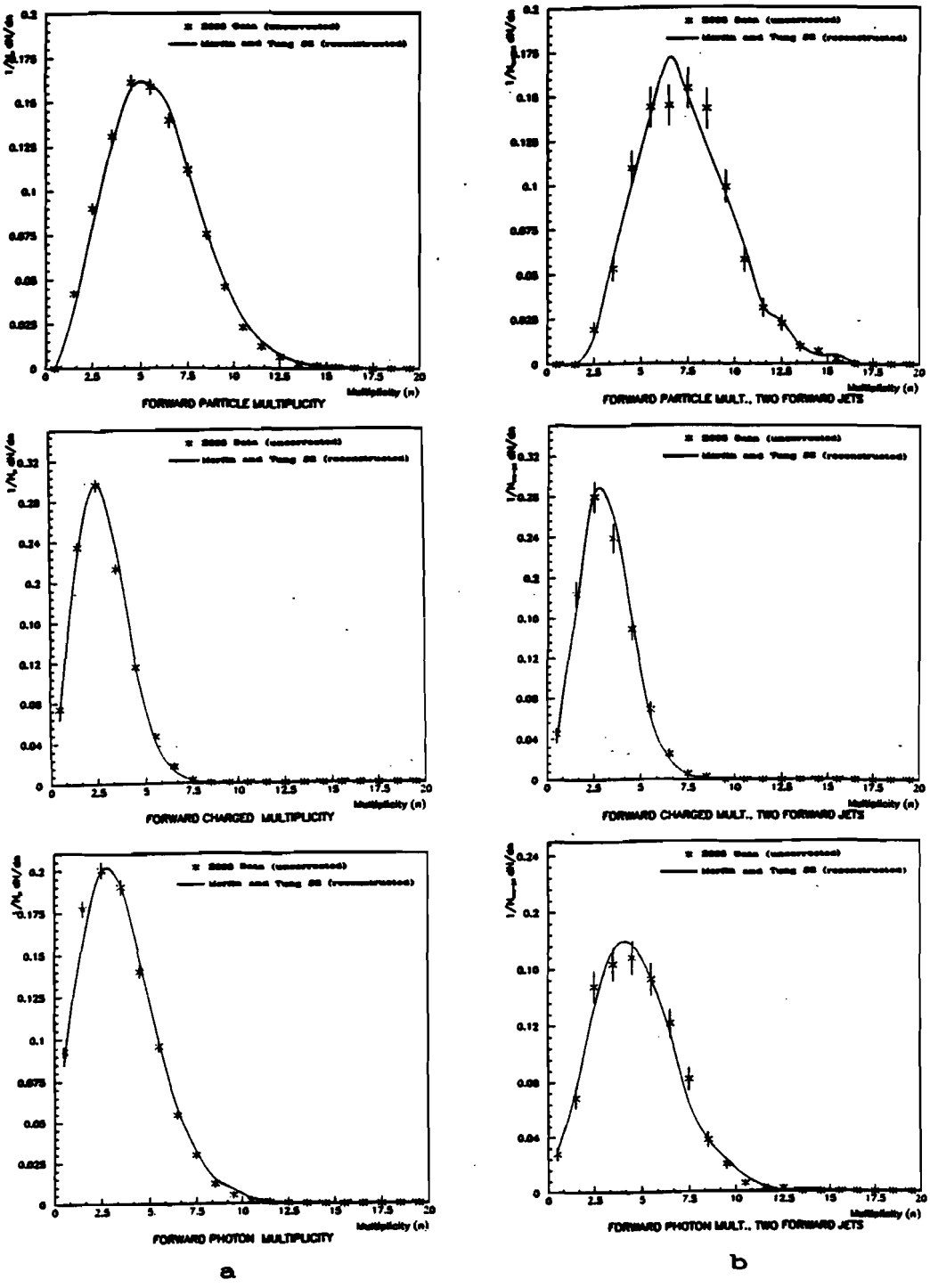

Figure 5.25: Total, charged and photon multiplicity for a) all events and b) events which pass the standard jet cut. (Not corrected for acceptance.)

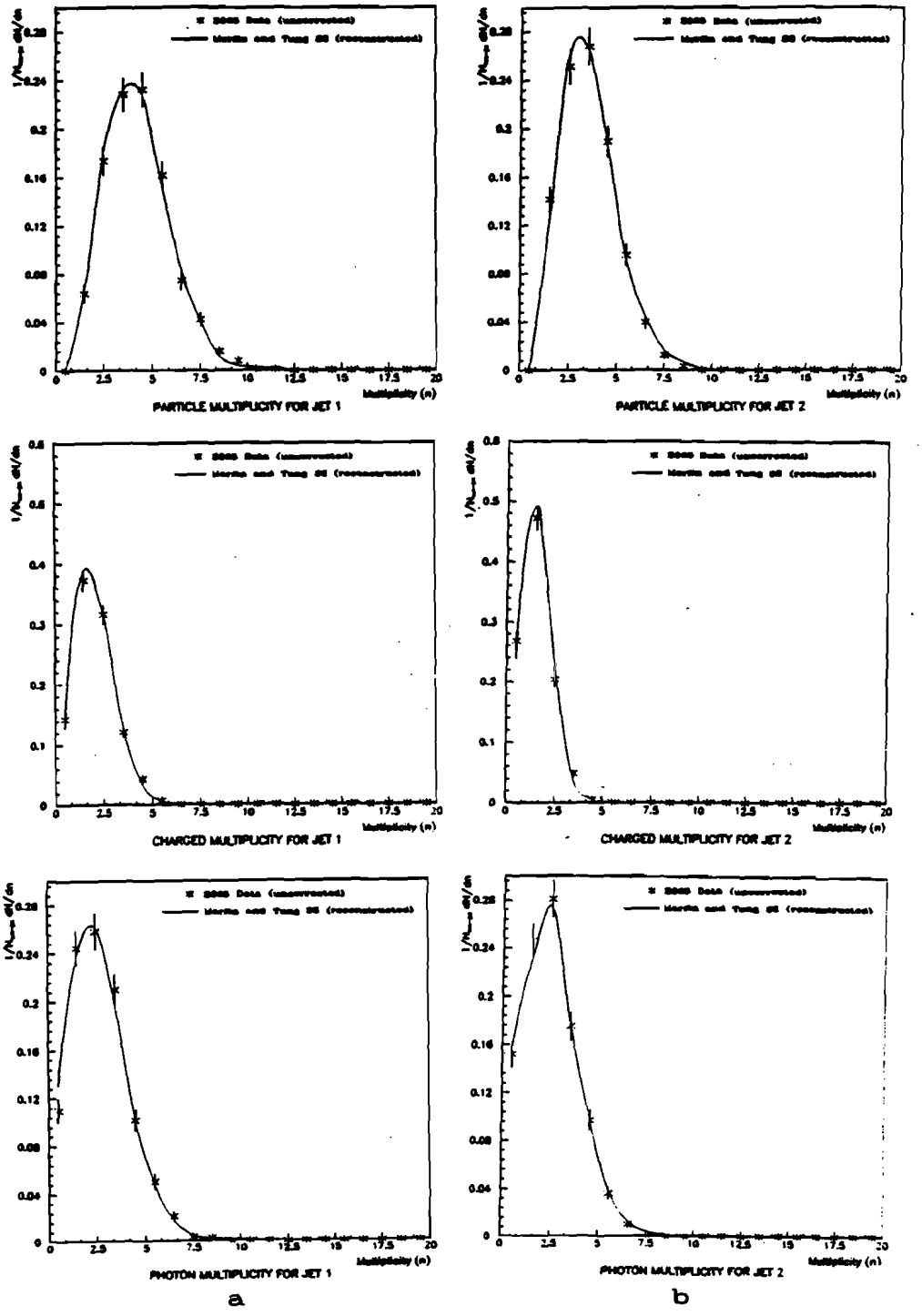

Figure 5.26: Total, charged and photon multiplicity for a) larger momentum jet and b) smaller momentum jet for events which pass the standard jet cut. (Not corrected for acceptance.)

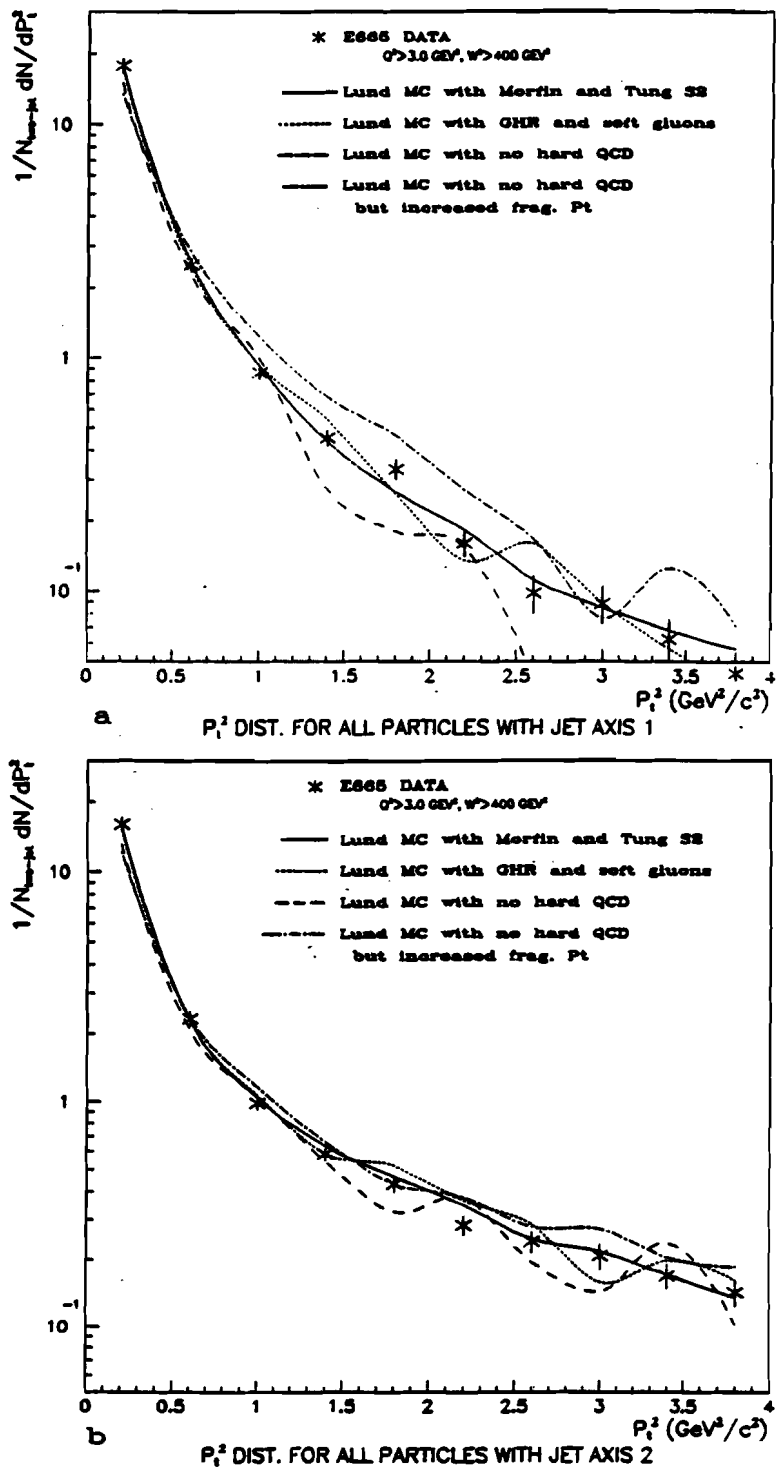

Figure 5.27: Transverse momentum distributions for all particles with respect to a)the larger momentum jet axis and b) the smaller momentum jet axis for events which pass the standard jet cut.

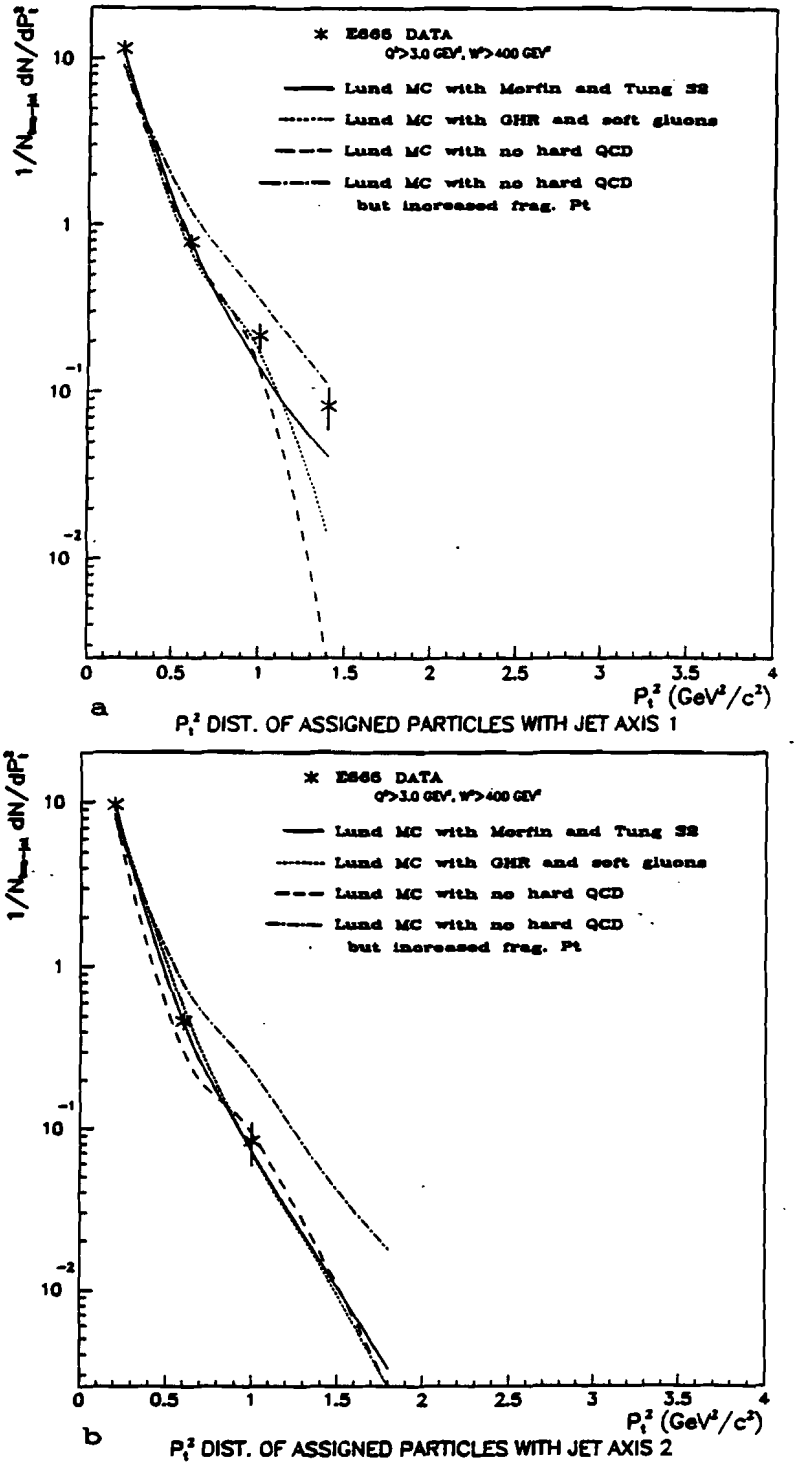

Figure 5.28: Transverse momentum distributions for assigned particles only with respect to a)the larger momentum jet axis and b) the smaller momentum jet axis for events which pass the standard jet cut.

the distributions for the two different jets. As discussed in chapter 2, some models would have gluons fragment more softly than quarks but here we expect that there is only a relatively small fraction of gluon jets anyways. Perhaps we can take the fact that these two plots are so similar as confirmation of that speculation? As can be seen, any of the models agree with the data for these plots.

Although Monte Carlo study shows that a very high percentage of the events which pass the standard jet cut really do contain two 'hard' forward partons, care must be taken in relating the specifics of the reconstructed 'jets' to the initial partons. Differences between gluon bremsstrahlung and $q\bar{q}$ events are subtle and most of the data is thrown away in an attempt to achieve a pure sample of one or the other. In order to achieve a sample of events which was 50% gluon bremsstrahlung, it was necessary to apply cuts in the angle, momentum and x_{Bj} and the resulting sample of events is in the neighborhood of 50 (out of 9000). Studies which attempt to separate a gluon bremsstrahlung signal from the predominant $q\bar{q}$ signal will require significantly higher statistics. In addition $q\bar{q}$ events include a large number of soft, nearly collinear pairs which pass the cuts but tend to reconstruct 'final jets' which do not correlate very well with the initial partons. It is possible to make more restrictive cuts on the data by using only events with larger angles or more balanced momenta to improve the correlation with initial partons but at high cost to the number of remaining events. This too will require more statistics. According

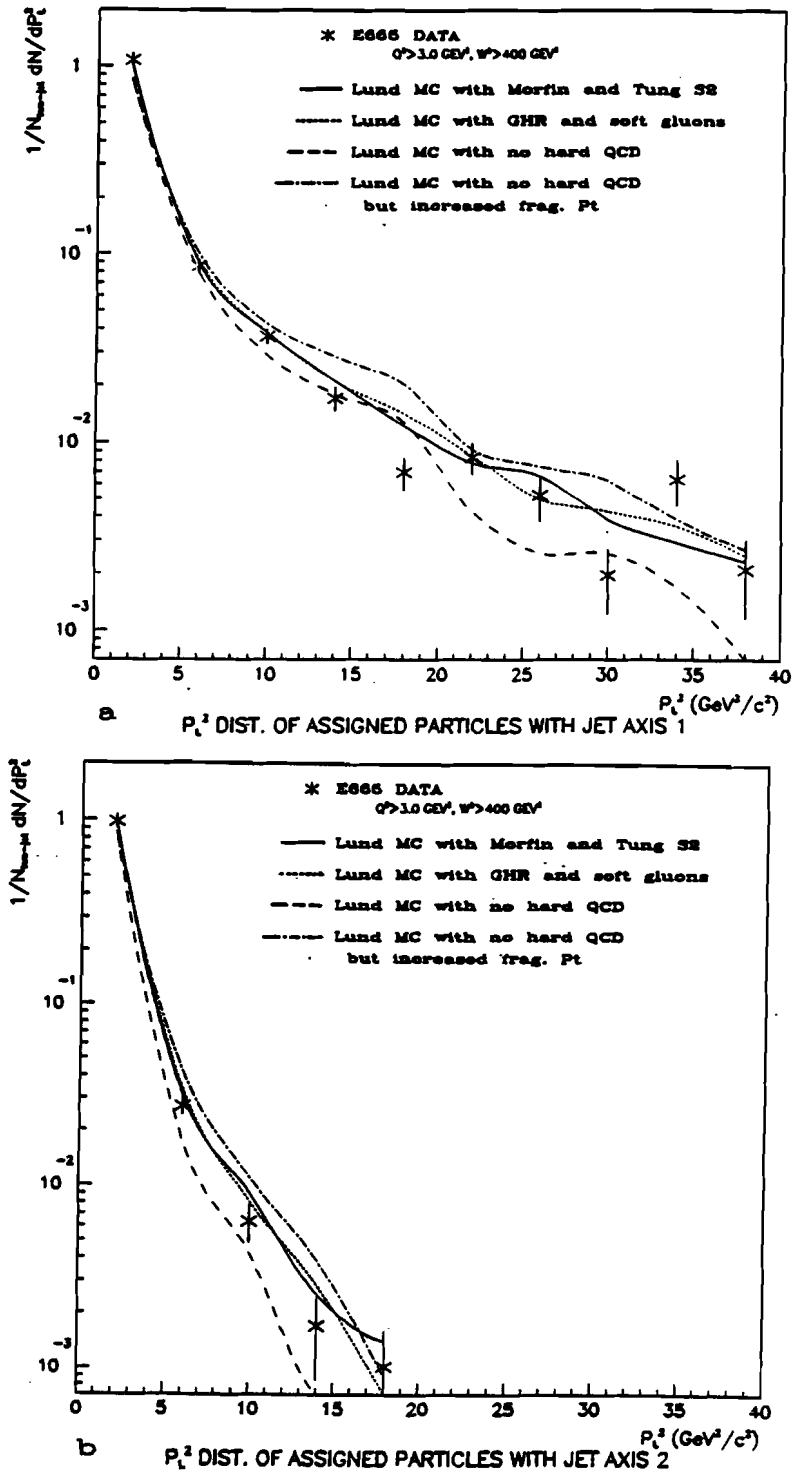

Figure 5.29: Longitudinal momentum distributions for assigned particles only for a)the larger momentum jet and b) the smaller momentum jet for events which pass the standard jet cut.

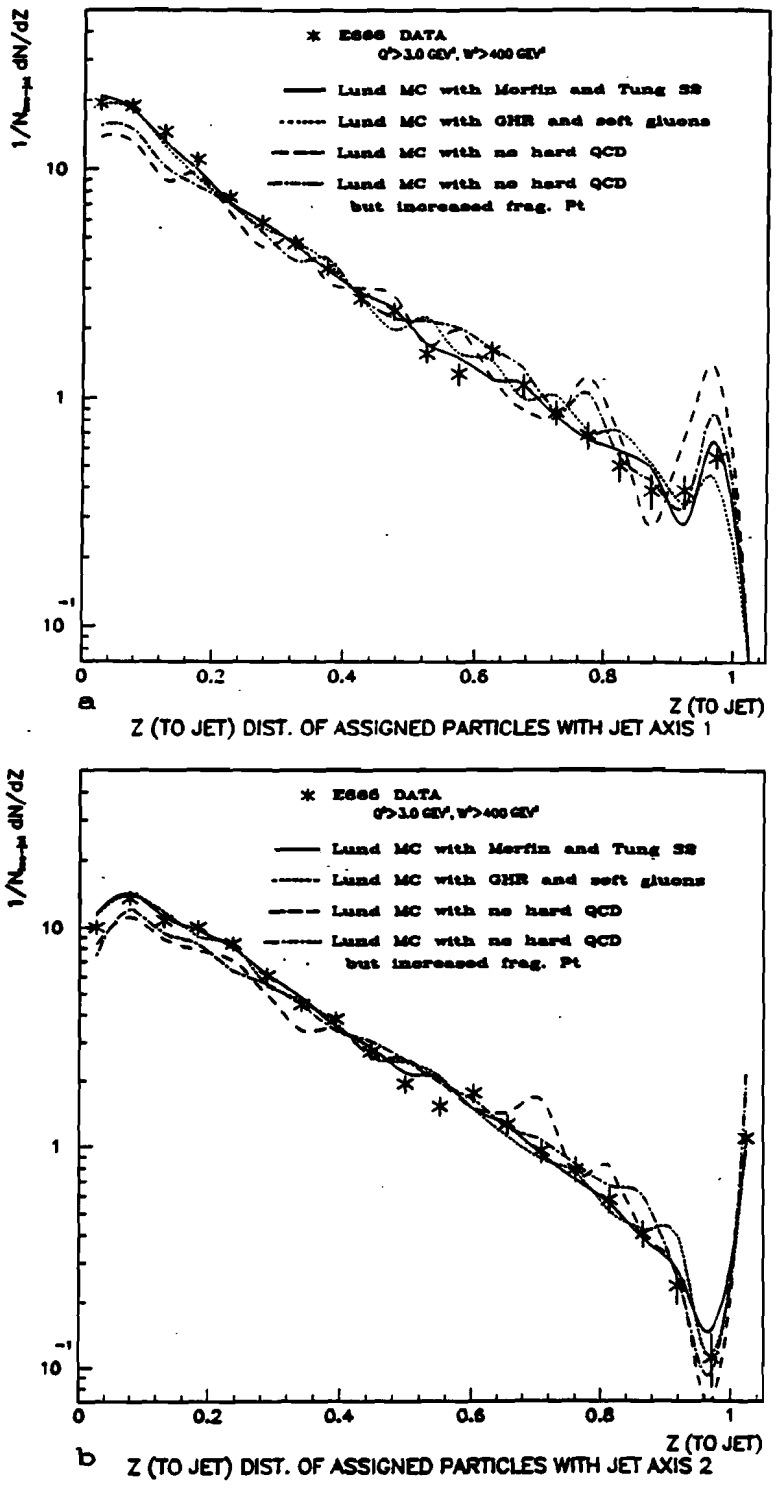

Figure 5.30: Z distributions (with respect to total jet momentum) for assigned particles only for a)the larger momentum jet and b) the smaller momentum jet for events which pass the standard jet cut.

to the Monte Carlo, bremsstrahlung events already have quite good correlation between the initial partons and the final jets.

5.6 Measuring Gluon Distributions using the Hadronic Final State

As has been seen several times in plots in the preceding sections, it appears that a number of the E665 distributions are sensitive to the value of the gluon distribution of the nucleon. Although this has been demonstrated by showing the results for the Monte Carlo using different input distributions, we would like to reverse the process and actually measure the distribution given our data. As was seen in figure 2.11, our high W data falls in a region in which gluon distributions are poorly understood and it is just this data which gives us the ability to make a measurement. At this time, there are still a number of effects which have not been studied and which may produce large systematic errors.

Assume that we measure a distribution of the number of events as a function of x_{Bj} for a data sample given some particular kinematic cuts (e.g. $W > 20GeV$). Now, we assume that this distribution can be written as the sum of two unknown sub-distributions which result from scattering off of different initial parton constituents so that we can write:

$$S(x) = g(x,\xi) + q(x,\xi) \tag{5.4}$$

where $S(x)$ is the given (measured) distribution and g and q are the sub-distributions for initial gluons and quarks respectively. I have purposely called the measured distribution S rather than the cross section σ because the absolute normalization is irrelevant to the problem. What counts is the *fraction* of events of a given type. Clearly, S will be purely a function of x but g and q will depend on an extra parameter ξ which is an effective cutoff in the definition of scattering from a gluon. Such a cutoff is an intrinsic part of any such measurement since the infrared limit of scattering from gluons will be scattering from sea quarks. What we wish to do is to define the cutoff such that the result makes both theoretical and experimental sense. Hopefully the intersection between those two goals will not be a null set. Given a reasonable cutoff, we can treat the two distributions as the fraction of events, as a function of x, which result in scattering off of either an intrinsic gluon or intrinsic quark from the nucleon.

The probability for scattering off of an intrinsic gluon will be given by the relative magnitude of the gluon distribution for the nucleon and by the probability of the resulting photon-gluon fusion process which allows the scatter to occur. If the scale of the photon-gluon fusion process is sufficiently large, we believe that it should be calculable using perturbative QCD. In reality, we will have to take care in the selection of the cutoff parameter ξ given the limits of the validity of the perturbative QCD calculation. This is simply equivalent to defining a 'sliding

scale' for what we define as 'intrinsic gluons'. If we can't calculate it then we call it intrinsic!

In order to determine distributions g and q we need some means of discriminating between the two types of event. The obvious handle on this is the 'multi-jettiness' of the forward hadrons. By definition, every photon-gluon fusion event will contain two 'hard' partons which resulted from the gluon splitting. On the other hand, most of the quark scatters will have only one 'hard' parton which participates in the scatter. An obviously important source of background to the intrinsic-gluon-produced multi-jettiness will be the bremsstrahlung of a hard gluon from the struck quark. Clearly, almost any cut which is meant to select events which resulted from photon-gluon fusion will also select events which resulted from radiation of a hard gluon. This will make it very difficult to measure a gluon distribution in regions where the magnitude of the two effects is similar. At low x, we expect that multi-jet events will be dominated by photon-gluon fusion simply because there will be so many gluons from which to scatter. If the gluon distribution really does rise, then we should be able to demonstrate that the fraction of multi-jet events at low x is inconsistent with pure gluon bremsstrahlung (which has been well measured in e^+e^- experiments).

Once a cut for multi-jettiness has been applied, we can proceed in a couple of different ways to determine the fraction of events which resulted from photon-gluon

fusion and therefore the gluon distribution which that implies. *Any approach will be dependent on the application of some fragmentation model in order to determine the relative acceptance of events which pass a given cut.* The fragmentation process is inseparable from the basic measurement. Before we can believably measure a gluon distribution, we must be reasonably convinced that whatever fragmentation model we apply agrees with the features of the data. Although it cannot be assured to be *the correct model* the preceding sections give us confidence that the Lund model at least stands a chance of providing a legitimate model for measurement of a gluon distribution. It will be necessary to study any measurement with regard to different fragmentation models and different sets of cuts and variations in the experimental data. For this analysis, I will proceed under the assumption that our default Lund model provides a sufficiently correct model for the fragmentation. (The arbitrary treatment of the strings and parton-pair invariant mass cutoff which that implies is one of the outstanding potential systematic errors that may arise in this assumption. It should be possible to study any error which this introduces by using a parton shower model Monte Carlo.)

I will describe here two possible basic approaches to extraction of a gluon distribution. The first approach assumes a known input distribution for quarks and using that distribution will calculate an apparent excess of multi-jet events as a function of x. Scattering from intrinsic gluons will be blamed for the excess and

hence an x distribution is extracted. The second approach will attempt to be free of any bias caused by an assumption of a shape for any input distribution. Each approach presents its own set of biases and difficulty.

Making use of a *given* quark distribution has the advantage of adding a constraint to the problem. We assume that good measurements of these distributions have been made in a series of other experiments and that extrapolation of the results is not too wild. The fixed shape of the distribution may help to constrain the gluon distribution so that it will be easier to measure. On the other hand, it will also provide a potential bias to the measured distribution. In addition, if the derived gluon distribution is not consistent with the input model, it will be necessary to iterate, changing the input each time.

The approach will be to apply some cut to the data to arrive at a distribution $S'(x)$ which will be enhanced in gluon induced events so that:

$$g'(x) = S'(x) - q'_{MC}(x) \tag{5.5}$$

where q'_{MC} will be the fraction of events which remain in the sample as calculated with the Monte Carlo. The idea of the cut will be to maximize the number of gluon events compared to the number of quark events as calculated using the Monte Carlo. The better the separation, the better statistical accuracy will be achieved. Clearly, if only a small fraction of gluon induced events are in the sample S' then the gluon

distribution will be the difference of two relatively large quantities and the errors will be large.

In order to avoid bias from an input quark distribution, we can apply a cut on the distribution $S(x)$ to arrive at a new distribution:

$$S'(x) = a(x)g(x) + b(x)q(x) = g'(x) + q'(x) \tag{5.6}$$

where a and b are the acceptance as a function of x for each type of event through the applied cut. The Monte Carlo is used to calculate a and b from:

$$\begin{aligned} a(x) &= \frac{g'_{MC}}{g_{MC}} \\ b(x) &= \frac{q'_{MC}}{q_{MC}}. \end{aligned} \tag{5.7}$$

Given the 'known' values of a and b we can solve the two equations with two unknowns to get:

$$\begin{aligned} g(x) &= \frac{S' - bS}{a - b} \\ q(x) &= \frac{aS - S'}{a - b}. \end{aligned} \tag{5.8}$$

It is immediately obvious that unless a is appreciably greater than b that g will be poorly determined. Hence, it is important that whatever cut is applied should be as efficient as possible at selecting only the desired events. At the same time, it must retain as much data as possible in order to keep statistical precision. As

has been seen in the preceding section, the most effective means of doing this is to apply a jet cut. The errors on the measured fraction $g(x)$ will be given by:

$$\frac{\sigma_g}{g} \approx \frac{\sigma_{S'}}{g(a-b)}. \tag{5.9}$$

Typical values for the acceptances for the standard jet cut used in this thesis are $a = 0.2$ and $b = 0.1$ and for these values with $g \approx 0.4S$ we get:

$$\frac{\sigma_g}{g} \approx 3 \times \frac{\sigma_{S'}}{S'}. \tag{5.10}$$

Of course, this last equation is valid only for the particular set of cuts involved and it may well be necessary to make more severe cuts for purposes of reducing systematic uncertainty.

Nominally, a and b determined from the Monte Carlo will not depend on the input parton distributions used for the calculation. This is because the ratio is sensitive only to the fraction of events which pass in any given range of x and not on the absolute number of events in that range. However, this will only be true if we do not integrate over too large a range of 'hidden' variables such as Q^2 or W. It may be necessary to severly restrict the integration range for these variables or equivalently, simply treat the full two dimensional problem where g is a function of both x and Q^2.

Figure 5.31 shows the acceptance as a function of x for gluon initiated and quark initiated scattering calculated using the standard Lund Monte Carlo for the

standard jet cut as described in the preceding section. Two different input parton distributions have been used and the two results are shown. There are some nontrivial differences between the acceptances using the two inputs. This underscores the need for better statistics so that smaller integration ranges can be made in the hidden variables. Until this can be done, such differences must be taken as systematic error. It is seen that the overall acceptance is relatively flat and that the acceptance for the gluon-initiated scatters is typically about twice that for quark-initiated scatters. Figure 5.32 shows the two contributions to the quark-initiated scattering - simple quark scattering with a single forward jet and gluon bremsstrahlung. Although the gluon bremsstrahlung is quite suppressed in the initial distribution, it has such a high acceptance for the jet cut that it approximately doubles the number of quark-initiated scatter events which pass the cut. It will be difficult to remove this background using any sort of cut for the same reasons that it is difficult to achieve a very pure sample of events which are gluon bremsstrahlung. (Of course, one can go to lower x but the whole point is to maintain an x distribution for a measurement!) Hence, it is likely difficult to significantly improve the ratio of a/b to much better than this factor of 2. Note that it may be possible to improve the systematic effects within the remaining sample by making stricter cuts.

Figure 5.33 shows the distributions for S, S', g and q as determined for the combined hydrogen and deuterium data where a cut of $x > .005$ has been imposed

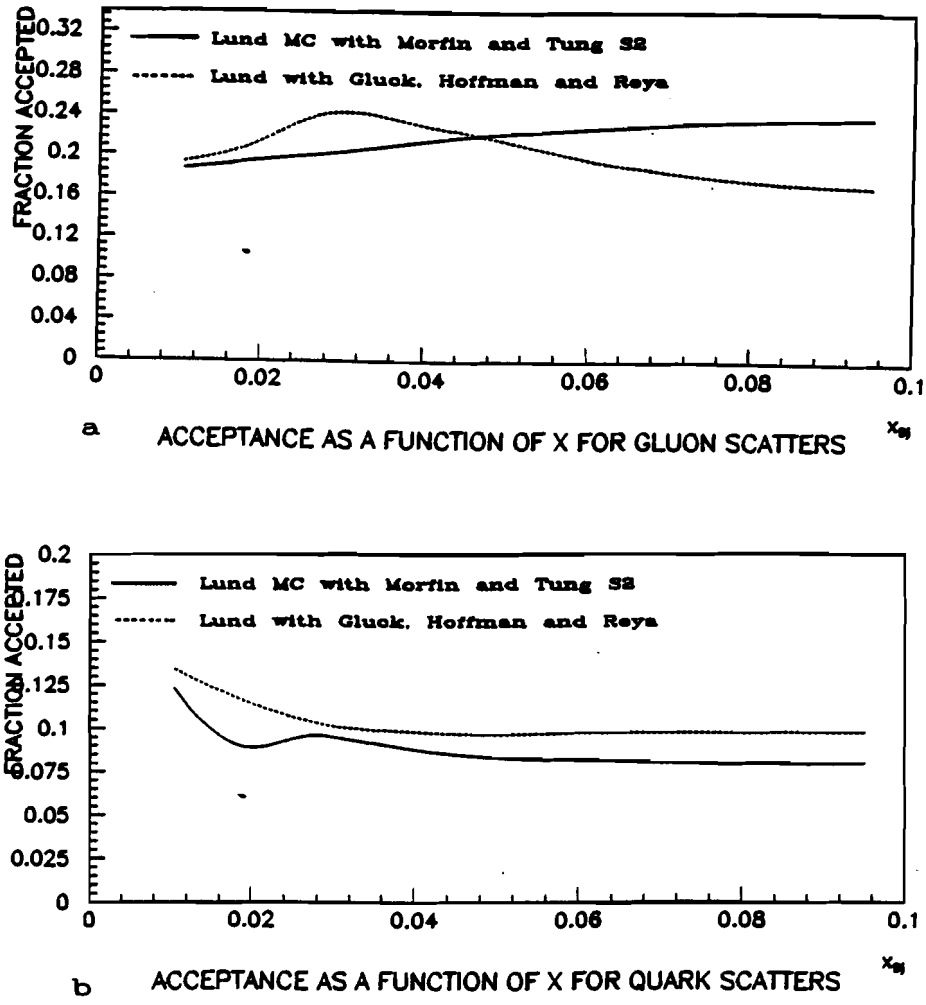

Figure 5.31: Acceptance as a function of x for a) gluon-initiated scattering and b) quark initiated scattering for standard jet cut.

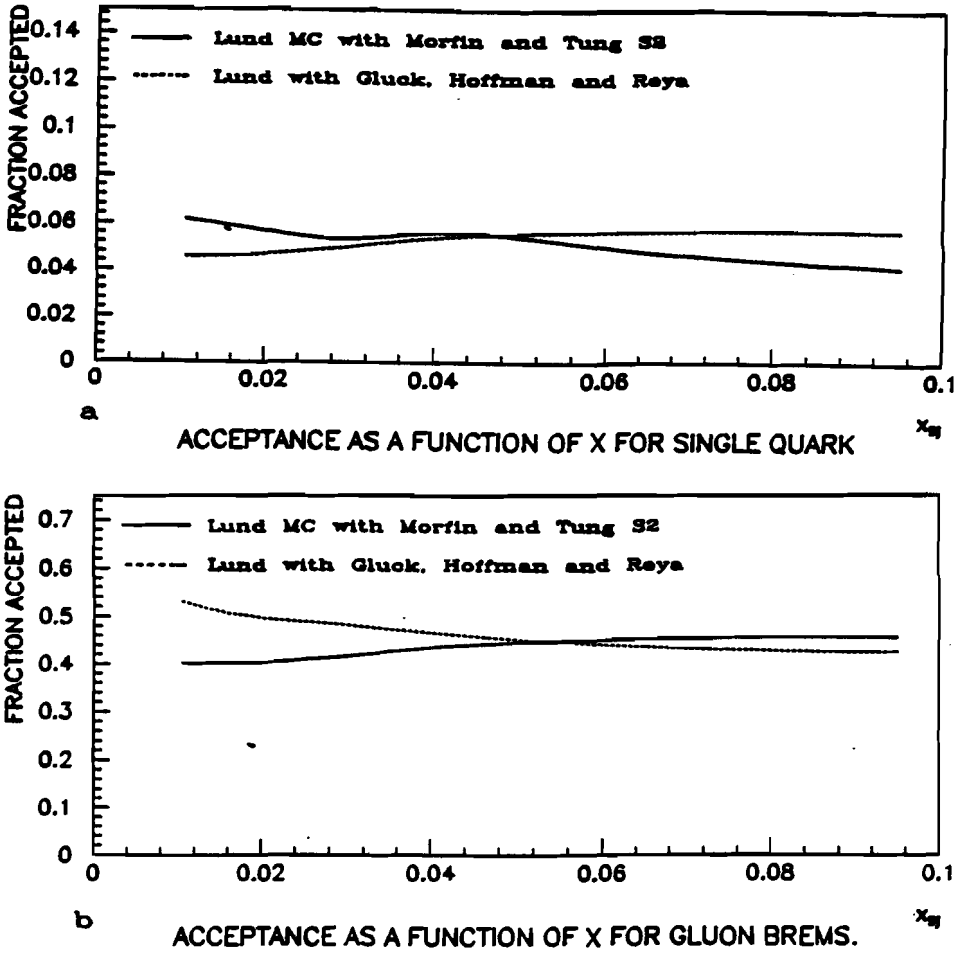

Figure 5.32: Acceptance as a function of x for a) single forward jets and b) gluon bremsstrahlung events for the standard jet cut.

in addition to the normal $Q^2 > 3GeV^2$ and $W > 20GeV$ cuts. The purpose of the x cut is to remove data where the trigger acceptance is changing very rapidly (just in case). The acceptances a and b as shown in figure 5.31 for Morfin and Tung were used for calculating the fractions g and q. In order to convert these fractions into the gluon distribution $xG(x)$, we use the Monte Carlo to 'reverse the process' by comparing the ratio of gluon distributions to fraction of gluon-initiated scatters in data and Monte Carlo. The x as measured using the kinematics of the virtual photon will be related to the fraction of the proton momentum being carried by the struck quark. The x for the gluon will be something larger than that value. The Lund Monte Carlo uses a prescription for the relationship of the gluon x to the scattered quark x of:

$$x_{gluon} = \frac{x}{x + (1 - x)R} \tag{5.11}$$

where x is normal Bjorken x and $0 < R < 1$ is a splitting fraction which simply defines how much of the gluon momentum the struck quark received. Hence for the x_{Bj} regime of E665, we can write $x_{gluon} \approx x/R$. The probability for any given R can be calculated from leading-order QCD. Hence, measuring the fraction of multi-jet events at a given x will be probing the gluon distribution integrated over some region with average R given by $\overline{R}$. Practical considerations will largely constrain the range over which R can vary. First, QCD will tend to force a pile-up of R

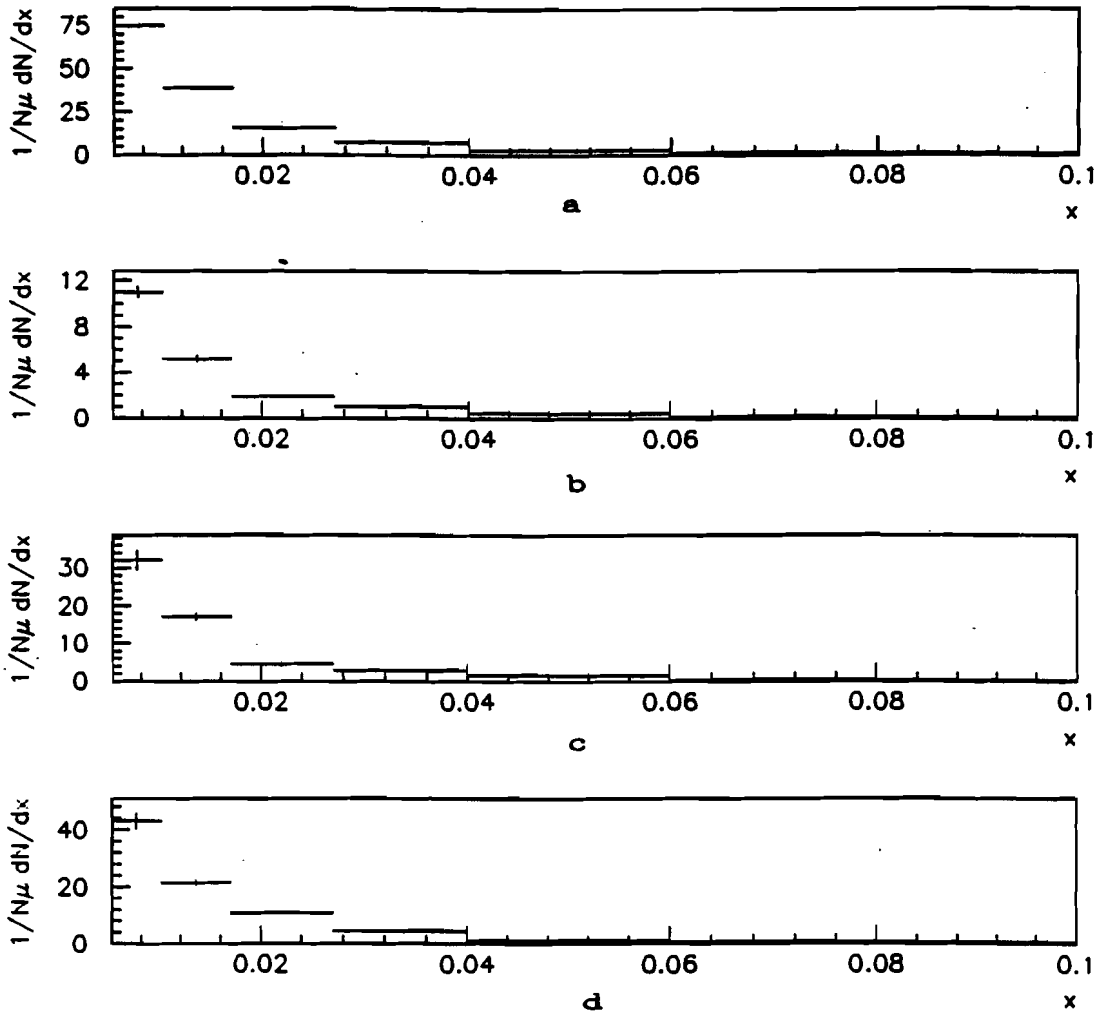

Figure 5.33: Distribution of events as a function of x for a) $S(x)$, b) $S'(x)$, c) $g(x)$, and d) $q(x)$. All distributions are normalized to number of scattered muons.

near 0 and 1. At the same time, it is unlikely that events will be detectable as multi-jet-like outside of the region $.1 < R < .9$. (Recall that the standard jet cut algorithm requires that the ratio of smaller to larger jet momentum is greater than 0.25.) Further, if we assume a falling gluon distribution (which is almost certainly true) values of R near 0 will be highly improbable since these would require the gluon to be at high x. Hence, the effective region over which the gluon distribution will be probed will be approximately given by $1.2x < x_{gluon} < 2.5x$ with $\overline{R} > 0.5$. The gluon distribution is given by:

$$G(x/\overline{R}) = G_{MC}(x/\overline{R})\frac{g(x)}{g_{MC}(x)}. \tag{5.12}$$

Because this equation is being applied to the 'uncut' distribution, no further systematic error should be suffered because of the fragmentation model. We are simply making use of the Monte Carlo result to do the QCD integration over the particular x-bins in question. The crosses on figure 5.34 shows the gluon distribution calculated using $\overline{R} = 0.7$ for three different bins in x. The errors shown in the figure are statistical only with the exception of the upwards extension of the error bar on the first point. The acceptance for quark initiated scatter events jumps up in the lowest x-bin as can be seen in figure 5.31. The 'cause' of this appears to be a sudden shift in the relative number of single quark and gluon bremsstrahlung events in this bin from the Monte Carlo. I suspect that there is something which

is not quite right but have not been able to verify this. My guess is that the point will properly be moved upwards. The circles on the plot show the gluon distribution calculated using the acceptances as determined using the Monte Carlo with the gluon distribution of Gluck, Hoffman and Reya. The statistical errors on these points is the same as for the crosses. Clearly, there are important systematic errors as can be seen by the fact that the distribution for the two different input parton models produce different results. There may be appreciable systematic errors due to the fragmentation model and associated with the definition of the cutoff variable ξ as well. Overall, I estimate that the systematic uncertainty in this particular measurement is at least as large as the statistical uncertainty and probably even larger.

Full treatment of the systematic errors involved with this type of measurement will be a big job and in itself would comprise a full thesis. Here, I wish to mainly point out two features. First, it is seen that E665 has appreciable statisitical power for measurement of the gluon distribution in this region. Given increased statistics from future running it should be possible to make a strong measurement in which the systematics are controlled and well understood. Second, even though the systematics are poorly understood, the measured distribution makes pretty good sense. The E665 data suggest that the gluon distribution should be higher than that given by the 1982 paper of Gluck, Hoffman and Reya and it looks reasonable

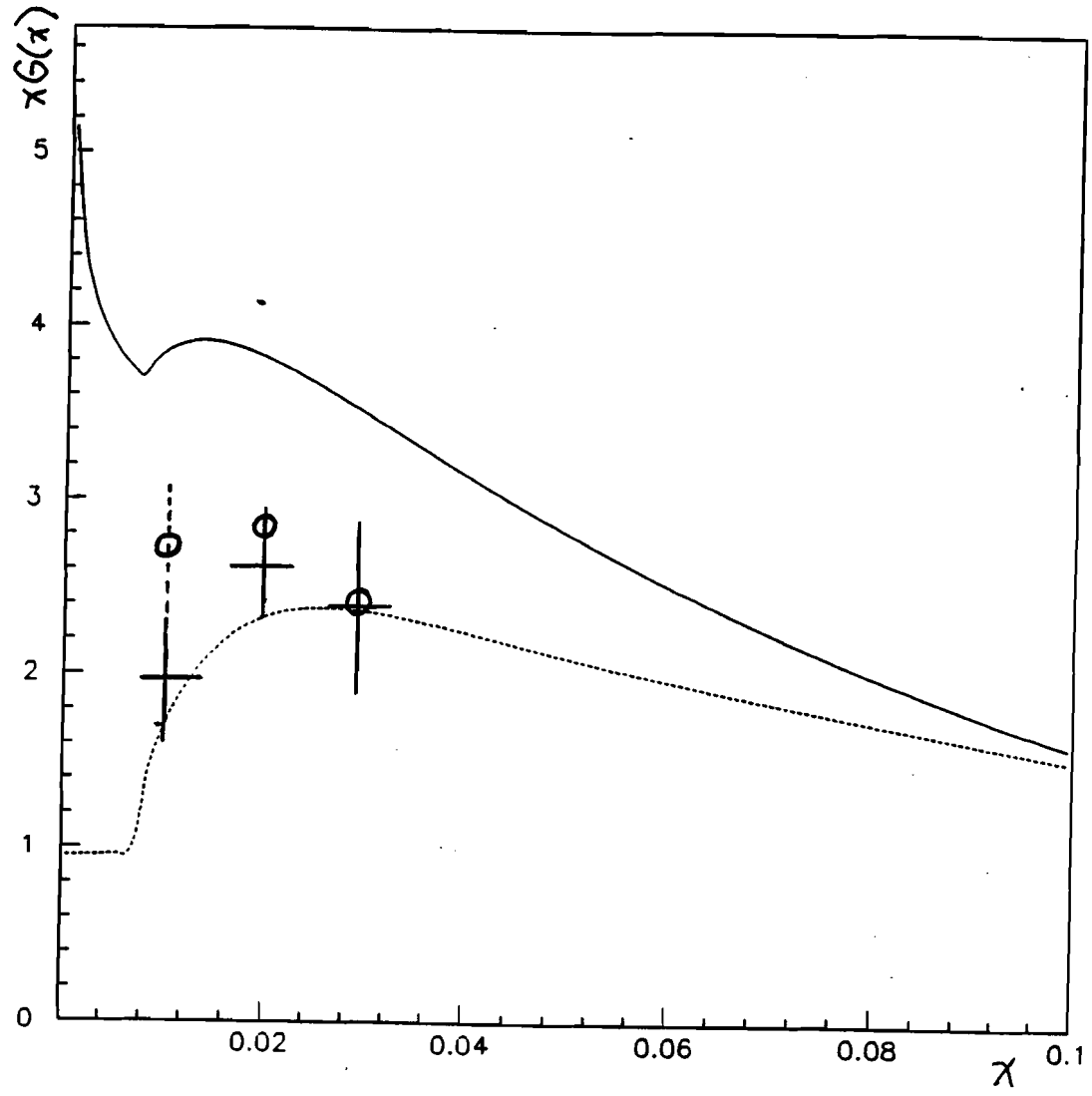

Figure 5.34: Gluon distribution extracted using Lund Monte Carlo with Morfin and Tung parton distributions (crosses) and Gluck, Hoffman and Reya parton distributions (circles) to determine jet acceptances and with a cutoff of $1GeV$ in the Monte Carlo for parton pairs in the photon-gluon fusion process. The crosses are the data. The dashed line is Gluck, Hoffman and Reya and the solid line is Morfin and Tung S2. See text for further description.

that it may be somewhat lower than that of Morfin and Tung S2. Of more questionable status is the shape of the distribution as a function of x for the few bins shown. I think that it will require further study before this is certain. Still, the measurement already supplies interesting information.

5.7 One Last Pass

Just as I was completing this thesis (and I mean *just*), Jorge Morfin (of Morfin and Tung) came to me with a new set of parton distributions which is based on what he calls the $\overline{MS}$ renormalization scheme for the gluon distributions (fit S2 used the *DIS* scheme. As he explained it to me, the difference in these two schemes is that the DIS scheme throws all dependence caused by the possibility of perturbatively produced initial-state (prior to the hard scatter) gluon bremsstrahlung into sea quarks. In this case, the gluon distribution must do all of the work in producing gluons at small x within the nucleon. The $\overline{MS}$ scheme on the other hand expects that extra low x gluons will be added to the initial state via an explicit QCD calculation. These extra gluons can either appear themselves if sufficiently hard or could (if the calculation allows it) participate in a photon-gluon fusion themselves. In this case, the gluon distribution does not need to supply all of the initial state gluon component. Hence, the 'gluon distribution' will be lower than in the DIS model. Here we are simply applying the 'sliding scale' which I mentioned in the

last section in defining what is and is not the primordial distribution.

The reason for all of this is not just to think of how many ways we can redefine the same thing. The point is that the gluon distribution which is used for the Monte Carlo should attempt to be consistent with the method of calculation for the QCD cross section. The $\overline{MS}$ scheme parton distributions of Morfin and Tung are an attempt to treat the cross section in the same way as Gluck, Hoffman and Reya. Since the default for the Lund Monte Carlo is Gluck, Hoffman and Reya this would seem to make sense. The tricky part though may come in that Lund is far more than a coded QCD cross section equation and in particular the way in which cutoffs are imposed and strings routed is (as mentioned earlier) somewhat arbitrary. By plugging in the 'wrong' gluon distributions (DIS) what we are doing is tuning the gluon distribution to be high compared to the 'right' one. Of course, 'right' here will require that extra gluons will explicitly be generated by Lund if they are taken out of the primordial distribution. The new distribution is closer to that of Gluck, Hoffman and Reya but is still somewhat higher and continues to rise at low x in the same fashion as the DIS scheme. It is more consistent with the data points in figure 5.34.

Figure 5.35 shows the average $p_\perp^2$ as a function of x_F for the E665 high W data compared to the prediction of Morfin and Tung $\overline{MS}$ (hereafter referred to as MTMS) where soft gluon effects have also been included in the Monte Carlo. The

fit to the data is quite good; with the overall 'goodness of fit' (as defined earlier) $\chi^2 = 8.1$. In particular, we see that the fit at higher x_F is better than for GHR. The extra primordial gluons (and there aren't that many more in MTMS compared to GHR) may tend to increase the average transverse momentum at medium x_F by effectively depleting the high x_F region somewhat. The fit without soft gluons turned on is now obviously bad (not shown). Figure 5.36a and b show however that the reduced primordial gluon distribution (i.e. MTMS compared to DIS Morfin and Tung) does not provide enough 'jettiness' to satisfy the energy flow in the hadronic event plane either when we impose a high total transverse momentum requirement or when we impose a jet cut. Does this require more 'primordial' gluons or more 'calculated' gluons? Are they really different? Good questions. I think though that the data says 'more gluons'. At this point I must leave it to others to pursue the answers.

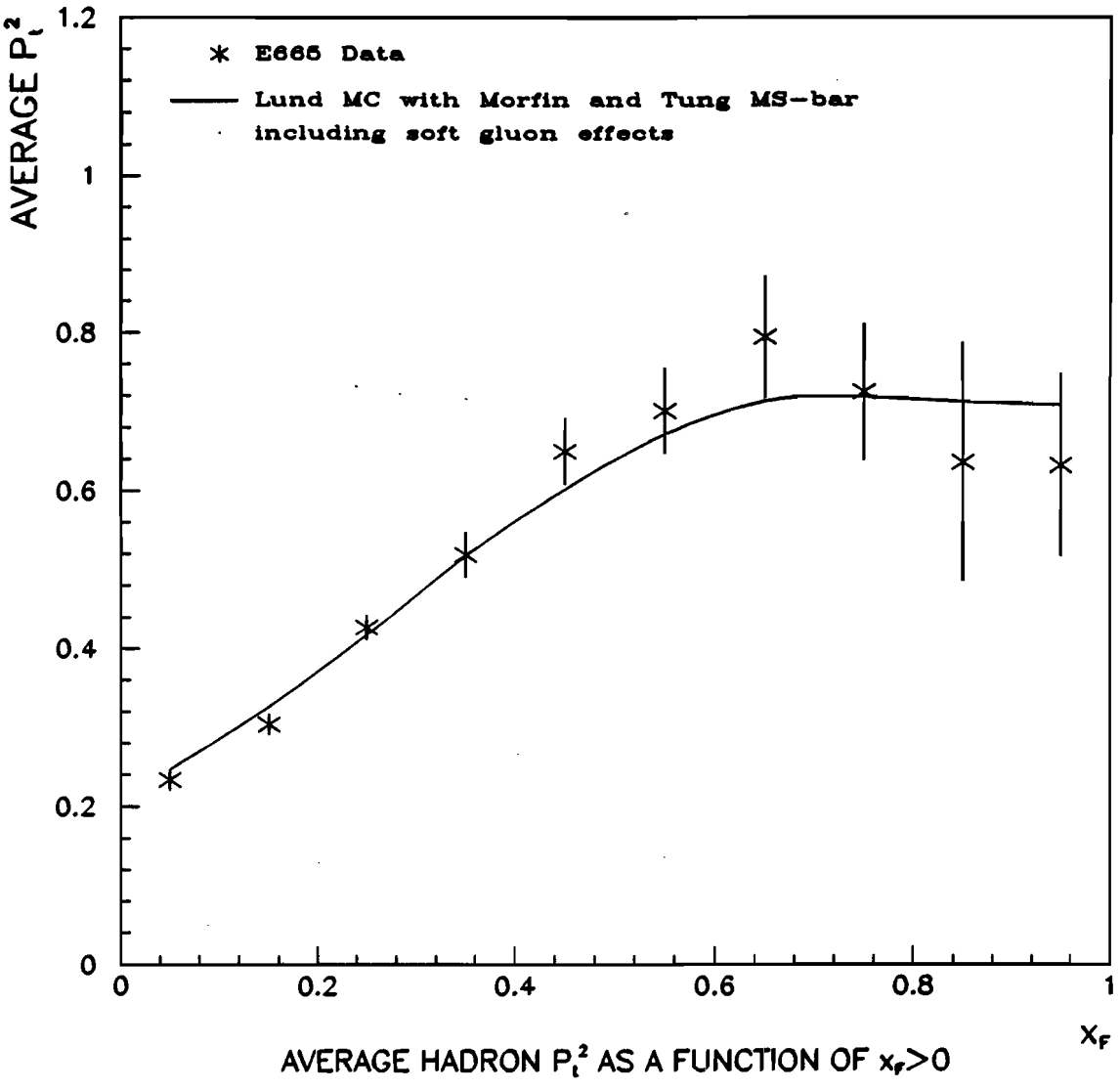

Figure 5.35: Average $p_\perp^2$ versus x_F for high W data compared to prediction from Lund Monte Carlo using Morfin and Tung $\overline{MS}$ parton distributions with soft gluon effects turned on.

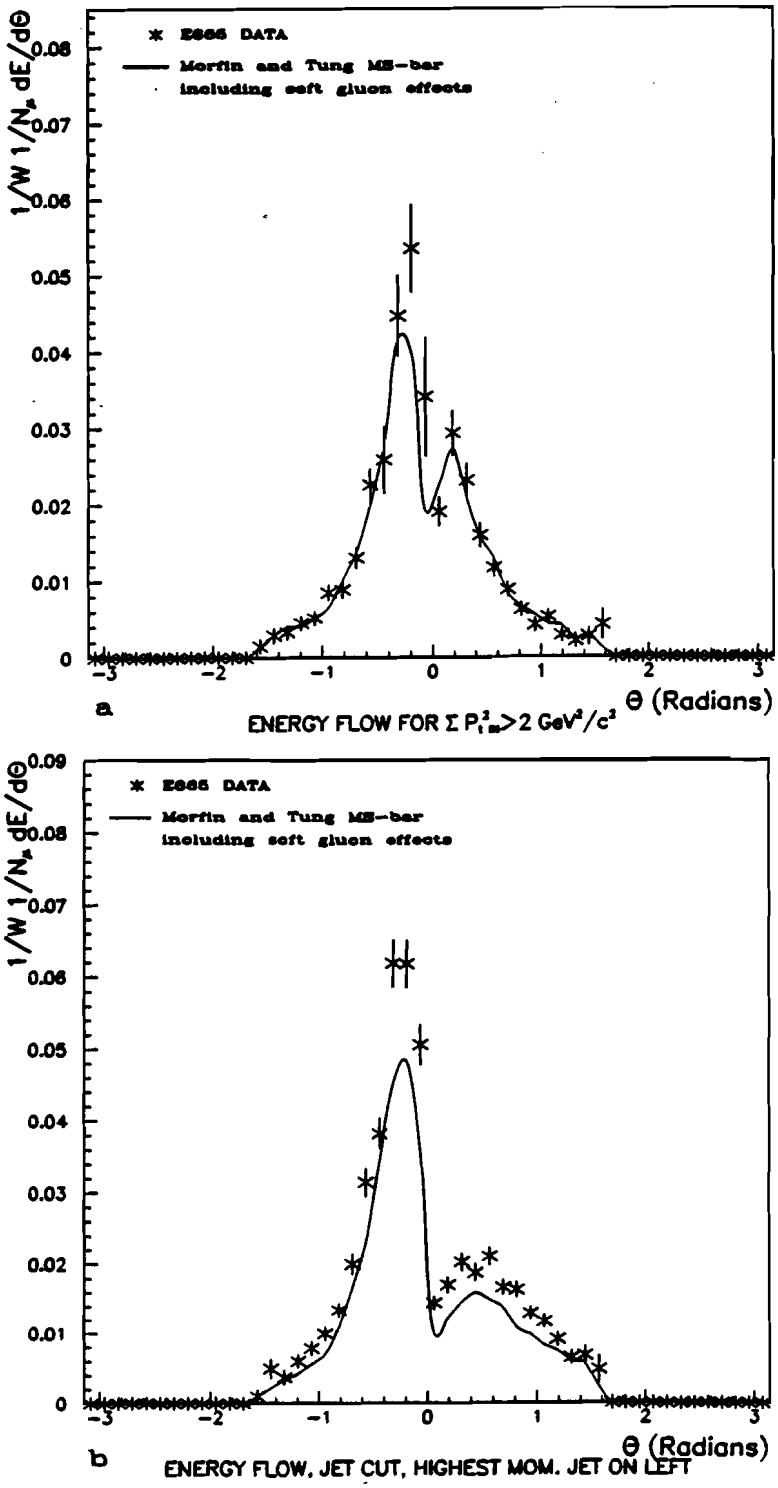

Figure 5.36: Scaled CMS energy flow for high W data compared to prediction from Lund Monte Carlo using Morfin and Tung $\overline{MS}$ parton distributions with soft gluon effects turned on. a) Sum of $p_\perp^2$ cut applied and b) jet cut applied with largest jet plotted on left.

Chapter 6

Conclusions

In this thesis, transverse momentum and event topology has been studied using both photons and charged hadrons. Single particle transverse momentum spectra have been shown to be in good agreement with data from a previous experiment (EMC) and with the standard Lund Monte Carlo with hard QCD effects included. Poor agreement is seen between the Lund Monte Carlo without hard QCD, even with an increase in transverse momentum from fragmentation.

It was shown that the average transverse momentum as a function of x_F agrees with previous measurements and with Lund Monte Carlo predictions. The $p_\perp^2$ distribution as a function of x_F requires that either an increased primordial gluon distribution be used or that a prescription for inclusion of 'soft gluons' be included if using the 'Lund default' parton distributions of Gluck, Hoffman and Reya. It was observed that the gluon distribution of Morfin and Tung (S2) allowed the Lund Monte Carlo to produce results which are consistent with the data without inclusion

of a soft gluon prescription.

The data were studied for events with a planar structure and such events were found and consistent with predictions from the Lund Monte Carlo with Hard QCD. If QCD is not included, the discrepancy between data and Monte Carlo is spectacular even with increased fragmentation $p_\perp$. The hadronic event plane was then used to search for events with a two forward jet structure. Various cuts were made on events and energy flow within the event plane was studied. The overall shape of the forward energy flow was shown to be in good agreement with the Lund Monte Carlo but there are subtle differences which may be associated with the photon-gluon fusion cross section, the inclusion (or not) of soft gluon effects and the gluon distribution of the nucleon.

A clustering and jet reconstruction algorithm which makes explicit use of the virtual photon direction was applied to the data. The resulting shape and numbers of the jets was found to be in overall good agreement with the Lund Monte Carlo with parton distributions from Morfin and Tung (S2) but the data shows slightly less jetiness than this prediction. The number of jets was underestimated if the gluon distribution of Gluck, Hoffman and Reya is used. Distributions for the magnitude of the momentum and the angular separation were studied for the reconstructed jet axes. Excellent agreement was seen between the data and the Monte Carlo. In addition, individual particle spectra for each reconstructed jet were shown to be

in good agreement with the Monte Carlo. Attempts to study differences between gluon and quark jets or to carefully relate jet properties to initial parton properties will require higher statistics.

Finally, many plots suggest that a gluon distribution higher than that used for tuning the Lund 4.3 Monte Carlo to the EMC data is required in order to achieve a good fit with E665 data. The ability to even make that statement implies that the data allow a measurement of what the gluon distribution *really* is! An alternative possibility is that the photon-gluon fusion cross section needs to be adjusted. Improvements in the systematic uncertainty in the x and Q^2 distributions should reveal more information. Although the measurement presented here is still quite rough, the technique appears to show great promise. From heavy particle production at hadron colliders to mysterious numbers of muons in ultra-high-energy air showers, the need for measurements of the gluon distribution at wee x is becoming ever more pressing. It will be very interesting to see what can be done with higher statistics from E665 data and with data from HERA in the not-too-distant future.

Appendix A

The Fermilab E665 Collaboration

D. F. Geesaman, R. Gilman, M. C. Green, H. E. Jackson,
S. Kaufman, S. Tentindo-Repond
Argonne National Laboratory, Argonne IL USA

R. D. Kennedy, H. G. E. Kobrak, A. Salvarani, R. W. Swanson
University of California, San Diego, USA

A. Eskreys, P. Malecki, K. Olkiewicz, B. Pawlik, P. Stopa
Institute for Nuclear Physics, Crakow, Poland

J. Bartlett, G. Coutrakon, J. Hanlon, H. Melanson, T. Kirk,
H. E. Montgomery, J. G. Morfin, S. A. Wolbers
Fermi National Accelerator Laboratory, Batavia, IL USA

M. Erdmann, J. Haas, W. Mohr, H. E. Stier, M. Wilhelm
University of Freiburg, Freiburg, W. Germany

J. M. Conrad, D. G. Michael, R. B. Nickerson,
F. M. Pipkin, M. Schmitt, R. Wilson
Harvard University, Cambridge, MA USA

M. R. Adams ,C.Halliwell, S. Magill, D. McLeod
University of Illinois, Chicago, IL USA

S. Aid, S. Kunori, S. O'Day, E. J. Ramberg, A. Skuja, G. Snow
University of Maryland, College Park, MD USA

P. L. Anthony, M. D. Baker, W. Busza, T. Lyons, L. Osborne, J. Ryan
Massachusetts Institute of Technology, Cambridge, MA USA

I. Derado, V. Eckardt,H. J. Gebauer, G. Jancso, A. Manz, N. Schmitz,
H. J. Seyerlein, S. Soldner-Rembold, P. Strube
H.-J. Trost, M. Vidal, W. Wittek, G. Wolf
Max-Planck-Institute, Munich, W. Germany

A. A. Bhatti, R. Davisson, W. Dougherty, D. M. Jansen,
J. J. Lord, H. J. Lubatti, J. Wilkes, T. Zhao
University of Washington, Seattle, WA USA

H. M. Braun, U. Ecker, A. Roeser
University of Wuppertal, Wuppertal, W. Germany

S. K. Dhawan, V. W. Hughes, K. P. Schuler, H. Venkataramania
Yale University, New Haven, CT USA

Bibliography

[1] J. Drees and H.E. Montgomery. Muon scattering. *Annual Review of Nuclear and Particle Science*, 33:383, 1983.

[2] I.J.R. Aitchison and A.J.G. Hey. *Gauge Theories in Particle Physics.* Adam Hilger Ltd., Bristol, 1982.

[3] E.D. Bloom et al. High-energy inelastic e-p scattering at 6° and 10°. *Physical Review Letters*, 23(16):930, 1969.

[4] M. Breidenbach et al. Observed behavior of highly inelastic electron-proton scattering. *Physical Review Letters*, 23(16):935, 1969.

[5] J.D. Bjorken. Asymptotic sum rules at infinite momentum. *Physical Review Letters*, 23(16):935, 1969.

[6] R.P. Feynman. *Photon-Hadron Interactions.* W.A. Benjamin, Inc., 1972.

[7] C.G. Callan and D.J. Gross. Crucial test of a theory of currents. *Physical Review Letters*, 21(5):311, 1968.

[8] L. Whitlow et al. A combined analysis of SLAC experiments on deep inelastic *ep* and *ed* scattering. Contributed to Europhysics Conf. on High Energy Physics, Madrid, 1989.

[9] S. Dasu et al. Precision measurement of $R = \sigma_L/\sigma_T$ and F_2 in deep inelastic electron scattering. *Physical Review Letters*, 61:1061, 1988.

[10] M. Gell-Mann. A schematic model of baryons and mesons. *Physics Letters*, 8(3):214, 1964.

[11] D.J. Gross and F. Wilczek. Ultraviolet behavior of non-abelian gauge theories. *Physical Review Letters*, 30(26):1343, 1973.

[12] H.D. Politzer. Reliable perturbative results for strong interactions? *Physical Review Letters*, 30(26):1346, 1973.

[13] H Fritzsch, M. Gell-Mann, and H. Leutwyler. Advantages of the color octet gluon picture. *Physics Letters B*, 47(4):365, 1973.

[14] V.D. Barger and R.J.N. Phillips. *Collider Physics.* Addison-Wesley Publishing Company, 1987.

[15] G. Altarelli. Partons in quantum chromodynamics. *Physics Reports*, 81(1), 1982.

[16] F. Wilczek. Quantum chromodynamics. *Annual Review of Nuclear and Particle Science*, 32:177, 1982.

[17] The AMY Collaboration, I.H. Park, et al. Experimental evidence for the non-abelian nature of QCD from a study of multijet events produced in e^+e^- annihilations. *Physical Review Letters*, 62(15):1713, 1989.

[18] S. Bethke. An experimental approach to optimise and test perturbative QCD to $O(\alpha_s^2)$. *Zeitschrift fur Physik C*, 43:331, 1989.

[19] The MARK II Collaboration, S. Komamiya, et al. Determination of α_s from a differential-jet-multiplicity distribution in e^+e^- collisions at $\sqrt{s} = 29$ and 91 GeV. *Physical Review Letters*, 64(9):987, 1990.

[20] G. Kramer and K. Lampe. DESY Report number DESY-86-119 (unpublished), 1986.

[21] G. Altarelli and G. Parisi. Asymptotic freedom in parton language. *Nuclear Physics B*, 126:298, 1977.

[22] G. Altarelli and G. Martinelli. Transverse momentum of jets in electroproduction from quantum chromodynamics. *Physics Letters B*, 76:89, 1978.

[23] The European Muon Collaboration, J.J. Aubert, et al. Transverse momentum

of charged hadrons observed in deep inelastic muon scattering. *Physics Letters B*, 95:306, 1980.

[24] The European Muon Collaboration, M. Arneodo, et al. Jet production and fragmentation properties in deep inelastic muon scattering. *Zeitschrift fur Physik C*, 36:527, 1987.

[25] The European Muon Collaboration, M. Arneodo, et al. Multiplicities of charged hadrons in $280GeV/c$ muon-proton interactions. *Nuclear Physics B*, 258:249, 1985.

[26] The European Muon Collaboration, Arneodo, et al. Comparison between hadronic final states produced in μp and e^+e^- interactions. *Zeitschrift fur Physik C*, 35:417, 1987.

[27] Mark J Collaboration, D.P. Barber, et al. Discovery of three-jet events and a test of quantum chromodynamics at PETRA. *Physical Review Letters*, 43(12):830, 1979.

[28] Tasso Collaboration, R Brandelik, et al. Evidence for planar events in e^+e^- annihilation at high energies. *Physics Letters B*, 86(2):243, 1979.

[29] PLUTO Collaboration, Ch. Berger, et al. Evidence for gluon bremsstrahlung in e^+e^- annihilations at high energies. *Physics Letters B*, 86(3):418, 1979.

[30] JADE Collaboration, W. Bartel, et al. Observation of planar three-jet events in e^+e^- annihilation and evidence for gluon bremsstrahlung. *Physics Letters B*, 91(1):142, 1980.

[31] S.L. Wu. e^+e^- physics at PETRA – the first five years. *Physics Reports*, 107(2), 1984.

[32] P. Mattig. The structure of jets in e^+e^- collisions. *Physics Reports*, 177(3), 1989.

[33] B. Naroska. e^+e^- physics with the JADE detector at PETRA. *Physics Reports*, 148(2):68, 1987.

[34] The AMY Collaboration, I.H. Park, et al. The physics of jets produced in electron-positron collisions at center of mass energies from 50 GeV to 56 GeV. KEK Preprint 88-45, Submitted to XXIV Int. Conf. On High Energy Physics, 1988.

[35] The UA1 Collaboration, G. Arnison, et al. Measurement of the inclusive jet cross section at the CERN $p\bar{p}$ collider. *Physics Letters B*, 172(3):461, 1986.

[36] The UA1 Collaboration, G. Arnison, et al. Angular distributions for high-mass jet pairs and a limit on the energy scale of compositeness for quarks from the CERN $p\bar{p}$ collider. *Physics Letters B*, 177(2):245, 1986.

[37] The UA1 Collaboration, G. Arnison, et al. Measurement of the inclusive jet cross section at the CERN $p\bar{p}$ collider. *Nuclear Physics B*, 276:253, 1986.

[38] The UA2 Collaboration, J.A. Appel, et al. Measurement of the $\sqrt{s}$ dependence of jet production at the CERN $p\bar{p}$ collider. *Physics Letters B*, 160(4):349, 1985.

[39] The UA2 Collaboration, J.A. Appel, et al. A study of three-jet events at the CERN $p\bar{p}$ collider. *Zeitschrift fur Physik C*, 30:341, 1986.

[40] The CDF Collaboration, F. Abe, et al. Measurement of the inclusive jet cross section in $p\bar{p}$ collisions at $\sqrt{s} = 1.8TeV$. *Physical Review Letters*, 62(6):613, 1989.

[41] The CDF Collaboration, F. Abe, et al. Dijet angular distributions from $p\bar{p}$ collisions at $\sqrt{s} = 1.8TeV$. *Physical Review Letters*, 62(26):3020, 1989.

[42] The European Muon Collaboration, J.J. Aubert, et al. Evidence for planar events and a forward double jet structure in deep inelastic muon scattering. *Physics Letters B*, 100:433, 1981.

[43] N.I. Geddes. *Properties of Jet Fragmentation in Deep Inelastic μp Scattering at* $280Gev/c$. PhD thesis, Oxford, 1985. RAL-T-017.

[44] J.G. Morfin and W.K. Tung. Parton distributions determined from a global QCD analysis of deep inelastic scattering and lepton-pair production. Fermilab/IIT Preprint to be submitted to Zeitschrift fur Physik C, 1990.

[45] M. Gluck, E. Hoffman, and E. Reya. Scaling violations and the gluon distribution of the nucleon. *Zeitschrift fur Physik C*, 13:119, 1982.

[46] TASSO Collaboration, W. Braunschweig, et al. Comparison of inclusive fractional momentum distributions of quark and gluon jets produced in e^+e^- annihilation. *Zeitschrift fur Physik C*, 45:1, 1989.

[47] W.J. Womersley. *A study of forward hadron production in deep inelastic muon-nucleus scattering.* PhD thesis, Oxford, 1986. RAL-T-037.

[48] The European Muon Collaboration, M. Arneodo, et al. Studies of quark and diquark fragmentation into indentified hadrons in deep inelastic muon-proton scattering. *Physics Letters B*, 150:458, 1985.

[49] G. Ballocchi and R. Odorico. The string effect and independent fragmentation models: lore and facts. CERN-EP/89-162, Dec. 1989.

[50] Y. Dokshitzer et al. QCD coherence in high-energy reactions. *Reviews of Modern Physics*, 60(2):373, 1988.

[51] A.E. Chudakov. *Isv. Akad. Nauk SSSR Ser. Fiz.*, 19:650, 1955.

[52] A. Bassetto, M. Ciafaloni, and G. Marchesini. Inelastic distributions and color structure in perturbative QCD. *Nuclear Physics B*, 163:477, 1980.

[53] A.H. Mueller. On the multiplicity of hadrons in QCD jets. *Physics Letters B*, 104:161, 1981.

[54] A. Bassetto et al. Jet multiplicity and soft gluon factorization. *Nuclear Physics B*, 207:189, 1982.

[55] Y.L Dokshitzer, V.S. Fadin, and V.A. Khoze. Coherent effects in the perturbative QCD parton jets. *Physics Letters B*, 115:242, 1982.

[56] A. Bassetto, M. Ciafaloni, and G. Marchesini. Jet structure and infrared sensitive quantities in perturbative QCD. *Physics Reports*, 100(4):201, 1983.

[57] Y.L Dokshitzer, V.A. Khoze, and S.I. Troyan. Coherence and physics of QCD jets. DESY preprint 88-093, 1988.

[58] B. Andersson et al. Coherence effects in deep inelastic scattering. Lund Preprint LU TP 88-14, 1988.

[59] R.D. Field and R.P. Feynman. Quark elastic scattering as a source of high-transverse-momentum mesons. *Physical Review D*, 15(9):2590, 1977.

[60] R.P. Feynman, R.D. Field, and G.C. Fox. Correlations among particles and

jets produced with large transverse momentum. *Nuclear Physics B*, 128:1, 1977.

[61] R.D. Field and R.P. Feynman. A parameterization of the properties of quark jets. *Nuclear Physics B*, 136:1, 1978.

[62] R. Odorico. Simulation of QCD in hard hadronic processes including gluon radiation effects. *Nuclear Physics B*, 228:381, 1983.

[63] A. Ali et al. A QCD analysis of the high-energy e^+e^- data from PETRA. *Physics Letters B*, 93:155, 1980.

[64] P. Hoyer et al. Quantum chromodynamics and jets in e^+e^-. *Nuclear Physics B*, 161:349, 1979.

[65] F. Paige et al. ISAJET 5.30: a Monte Carlo event generator for pp and $\bar{p}p$ interactions. In *Snowmass Summer Study*, page 320, 1986.

[66] B. Andersson, G. Gustafson, and C. Peterson. A semiclassical model for quark jet fragmentation. *Zeitschrift fur Physik C*, 1:105, 1979.

[67] B. Andersson and G. Gustafson. Semi-classical models for gluon jets and leptoproduction based on the massless relativistic string. *Zeitschrift fur Physik C*, 3:223, 1980.

[68] B. Andersson, G. Gustafson, and T. Sjostrand. On soft gluon emission and the transverse momentum properties. *Zeitschrift fur Physik C*, 12:49, 1982.

[69] T. Sjostrand. The Lund Monte Carlo for jet fragmentation. Lund Preprint LU TP 82-3, 1982. Although this nominally has the same name as the published version, it is in fact a somewhat different program and corresponds to the so-called version 1.43 which is actually used for E665.

[70] T. Sjostrand. The Lund Monte Carlo for jet fragmentation. *Computer Physics Communications*, 39:347, 1986.

[71] G.C. Fox and S. Wolfram. A model for parton showers in QCD. *Nuclear Physics B*, 168:285, 1980.

[72] R.D. Field. The production of partons and hadrons in e^+e^- annihilations and in hadron-hadron collisions – quark and gluon jet models. Invited paper presented at the 1981 Isabelle Summer Workshop, 1981.

[73] T.D. Gottschalk. A realistic model for e^+e^- annihilation including parton bremmstrahlung effects. *Nuclear Physics B*, 214:201, 1983.

[74] R.D. Field and S. Wolfram. A QCD model for e^+e^- annihilation. *Nuclear Physics B*, 213:65, 1983.

[75] G. Marchesini and B.R. Webber. Simulation of QCD jets including soft gluon interference. *Nuclear Physics B*, 238:1, 1984.

[76] B.R. Webber. A QCD model for jet fragmentation including soft gluon interference. *Nuclear Physics B*, 238:492, 1984.

[77] G. Marchesini and B.R. Webber. Monte carlo simulation of general hard processes with coherent QCD radiation. *Nuclear Physics B*, 310:461, 1988.

[78] H.R. Wilson. Simulation of QCD jets including soft gluon interference. 1988.

[79] L Angelini et al. Fire string theory of e^+e^- annihilation. *Riv. Nuovo Cim.*, 3:1, 1983.

[80] A. Malensek and J.G. Morfin. *The Tevatron Muon Beam: A High Intensity Beam With Well Defined Polarization.* Technical Report TM1193 2966.00, Fermilab, July 1983.

[81] J. Conrad, A. Malensek, and J.G. Morfin. *An electron/positron calibration beam for the Tevatron Muon Spectrometer.* Technical Report TM 1652, Fermilab, November 1988.

[82] H.E. Montgomery. *Beam Tagging for E665.* Technical Report BT007, E665 Internal Report, July 1984.

[83] H. Fenker. *A Standard Beam PWC for Fermilab.* Technical Report TM-1179, Fermilab, Feb 1983.

[84] The European Muon Collaboration, J.P. Albanese, et al. The vertex and large angle detectors of a spectrometer system for high-energy muon physics. *Nuclear Instruments and Methods*, 212:111, 1983.

[85] H.J. Gebauer. The vertex proportional chamber PCV. E665 Internal Report VS012, October 1985.

[86] M. DePalma et al. *Nuclear Instruments and Methods*, 217:135, 1983.

[87] J.B. Lindsay et al. A fast and flexible data acquisition system for multi-wire proportional chambers and other detectors. *Nuclear Instruments and Methods*, 156:329, 1978.

[88] A. Bhatti et al. Seattle MWPC System (PCF Detector). E665 Internal Report FS011, October 1985.

[89] T. Kirk, H. Melanson, and S. Wolbers. E665 Internal Report FL027 and FS010, 1985.

[90] T. Kirk. E665 Internal Report FS017, 1978.

[91] Mark Adams. SAT MWPC's. E665 Internal Report BT020, July 1986.

[92] Hans Kobrak et al. E665 scattered muon detector and trigger processor. E665 Internal Report BT014, October 1985.

[93] B. Rossi. *High Energy Particles.* Prentice Hall, New York, 1964.

[94] H.H. Nagel. Electron/photon cascade showers in lead: Monte Carlo computations of primary electron energies between $100MeV$ and $1000MeV$. *Nuclear Instruments and Methods*, 212:111, 1983.

[95] S. Iwata. Calorimeters (total absorption detectors) for high-energy experiments at accelerators. Nagoya Univ. Report DPNU-3-79, Review for TRISTAN Workshop, 1979.

[96] Iarocci. Plastic streamer tubes and their applications in high-energy physics. *Nuclear Instruments and Methods*, 217:30, 1984.

[97] J. Oliver. *E665 Calorimeter Anode Wire Electronics.* Technical Report EMCAL-58, Harvard University, Aug 1984.

[98] *1880 Series ADC Manual.* LeCroy Instruments Corporation, Spring Valley, New York, 1985.

[99] D.G. Michael. *The FASTBUS Data Acquistion System for E665.* Technical Report PN-378, Harvard Univ./Fermilab Computing Department, 1989.

[100] Y. Fukui, M. Mishina, et al. Sources for proportional tube gain variation; what to do about it. In *Proceedings of the Gas Sampling Calorimetry Workshop*, Fermilab, 1985.

[101] E.J. Ramberg. *Neutral Pion and Eta Production in Deep Inelastic Muon Scattering at* $480GeV$. PhD thesis, University of Maryland, 1989.

[102] G.B. Coutrakon et al. The Ring Imaging Cerenkov Detector for Fermilab Experiment 665. E665 Internal Report RC009, 1987.

[103] R.J. Apsimon et al. The design of the optical components and gas control systems of the CERN OMEGA ring imaging Cerenkov detector. *Nuclear Instruments and Methods A*, 241:339, 1985.

[104] G. Anzivino et al. First results from a silicon strip detector with VLSI readout. *Nuclear Instruments and Methods*, A243:153–158, 1986.

[105] R.P. Mount. *Nuclear Instruments and Methods*, 187:23, 1979.

[106] W. Hill and P. Horowitz. *The Art of Electronics.* Cambridge University Press, Cambridge, 1980.

[107] D.F. Geesaman et al. Data acquisiton for FNAL E665. In *Proceedings of the Conference on Real Time Computer Applications in Nuclear and Particle Physics*, 1989.

[108] David M. Berg. *Customizing the RSX-11M Data Acquisition System.* Technical Report PN-209, Fermilab Computing Department, February 1984.

[109] D.M. Berg, L. Quigg, and P. Heinicke. A high-speed data acquisition system for PDP-11. *IEEE Transactions on Nuclear Science*, 32:1368, 1985.

[110] V. White et al. The VAXONLINE software system at Fermilab. *IEEE Transactions on Nuclear Science*, 34:763, 1987.

[111] Mizuno. Parameterization of Structure Functions Using EMC Data. Talk given at Fermilab, To be published?, 1989.

[112] R. Brun et al. GEANT3 users guide. CERN DD/EE/84-1, 1986.

[113] S.L. Wu and G. Zobernig. *Zeitschrift fur Physik C*, 2:107, 1979.

[114] G. Hanson et al. *Physical Review Letters*, 35:1609, 1975.